

The Surface Energetics of Low Dimensional Nanomaterials

Auren Ferguson

A thesis presented for the degree of
Doctor of Philosophy



Supervised by Dr. Shane Bergin & Prof. Jonathan Coleman
School of Physics
Trinity College Dublin
September 2016

For my grandmother Maud

Declaration

I declare that this thesis has not been submitted as an exercise for a degree at this or any other university and it is entirely my own work.

I agree to deposit this thesis in the University's open access institutional repository or allow the library to do so on my behalf, subject to Irish Copyright Legislation and Trinity College Library conditions of use and acknowledgement.

Elements of this work that have been carried out jointly with others or by collaborators have been duly acknowledged in the text wherever included.

Auren Ferguson

Abstract

Over the past two decades, there has been great interest in the discovery and research of low dimensional nanomaterials. These materials, such as carbon nanotubes and graphene, are amongst the strongest and most conductive materials ever discovered and show great promise for applications such as, electronics, renewable energy and polymer composites. Great strides in their understanding have been achieved, however, one material property that isn't well understood is their surface energy. Surface energy is a measure of the energy required to produce a unit area of surface and it controls how a material interacts with its environment. Therefore, understanding the surface energetics of low dimensional materials is very important, particularly in the case of the exfoliation of layered 2D materials in liquid, e.g. the exfoliation of graphite to produce graphene. This thesis develops a framework for the measurement and analysis of the surface energy of layered materials, revealing information such as the material's intrinsic surface energy and information about the type and amount of defects found on a sample surface.

The surface energy of commercial graphites were measured using coverage dependent inverse gas chromatography (IGC), as it allows the mapping of the surface energy of materials as a function of surface coverage, called surface energy profiles. This method allows the examination of both high and low energy sites on a surface. At low coverage, high surface energy is measured, which reduces with increasing surface coverage and eventually plateaus, where surface energy becomes coverage independent. These profiles were empirically fitted to a stretched/compressed exponential function, allowing the extraction of the zero-coverage surface energy ($\gamma_{d,\phi=0}$, this corresponds to high energy sites found on the surface), the full-coverage surface energy ($\gamma_{d,\phi=1}$) and the decay constant (ϕ_0). Computer simulation showed that there are three types of graphite surface sites: the graphite

basal plane, basal plane defects and edge defects. Simulation also showed that ϕ_0 is related to the fraction of high energy sites on a surface. This allowed us to assign $\gamma_{d,\phi=1}$ to the basal plane surface energy of graphite, which was measured as $\langle \gamma_{d,\phi=1} \rangle = 63 \pm 7 \text{ mJ/m}^2$, independent of graphite flake size. Analytical models allowed the separation of the basal plane defect and edge defect contributions to $\gamma_{d,\phi=0}$, which varied from $\approx 120 \text{ mJ/m}^2$ for small, edge rich samples to $\approx 180 \text{ mJ/m}^2$ for larger flaked samples, where basal plane defects are more prominent. This allowed an estimate of the basal plane defect density of graphite to be of the order $10^{15} \text{ defects/m}^2$.

Following on from the graphite study, the surface energy of size selected, liquid exfoliated graphene was examined. The nature and shape of surface energy profiles differed greatly than that found for graphite, with $\gamma_{d,\phi=0}$ having lower values, which varied from $\approx 120\text{-}140 \text{ mJ/m}^2$, depending on flake size. This was attributed to edge defects far outnumbering basal plane defects due to the higher edge density of graphene. As a result, surface energy profiles decreased very slowly with surface coverage. The basal plane surface energy of graphene was found to be $\langle \gamma_{d,\phi=1} \rangle = 62 \pm 4 \text{ mJ/m}^2$, independent of nanosheet size; this is consistent with $\langle \gamma_{d,\phi=1} \rangle$ of graphite and our interpretation of the nature of $\gamma_{d,\phi=1}$.

Graphite and graphene surface energy measurements were directly compared and were found to be consistent, allowing us to calculate the percentage area of basal plane defects found on the graphite/graphene surface to be less than 1%. Analytical models developed for graphite were shown to be applicable to graphene and were consistent with graphite data.

Bacterial cellulose (BC) was dispersed to its constituent bacterial cellulose nanofibrils (BCN) by sonication in various organic solvents. This was done to show the effects of solvent surface energy has on the dimensions and nature of BCN and films made from BCN. Firstly, we showed that it is possible to debundle BC to individual BCN by sonicating it in the solvent N-Methyl-2-pyrrolidone (NMP); an important result, as there are currently very few avenues to solubilise BC. BC was then sonicated in a range of solvents with BCN diameters found to range from 10-16 nm; values consistent with individual BCN. By measuring the concentration of BCN in dispersion spectroscopically and comparing it to the solvents surface energy, it was possible to infer the surface energy of BC to be ≈ 75

mJ/m². This is a higher surface energy than typically found for materials where dispersive interactions dominate the surface energy, such as graphite, graphene and MoS₂. This was attributed to hydrogen bonding within the BC matrix. To confirm this, the total surface energy (both dispersive and specific) of BC was measured by IGC and its full coverage surface energy was found to be \approx 75 mJ/m². This further supports previous findings that the full-coverage surface energy is a measure of the intrinsic surface energy of materials. BCN films were produced by vacuum filtration of BCN dispersions from various media whose mechanical properties showed a clear correlation with the degree of BCN dispersion, i.e. solvents that produced the smallest diameter BCN had the best mechanical response. Therefore, we have shown a novel method of controlling the properties of BCN films via solvent surface energy.

Publications

- [1] A. Ferguson, U. Khan, M. Walsh, K.Y. Lee, A. Bismarck, M. S. P. Shaffer, J. N. Coleman and S. D. Bergin. Understanding the Dispersion and Assembly of Bacterial Cellulose in Organic Solvents *Biomacromolecules* 17 (5), 1845-1853, 2016.
- [2] A. Harvey, X. He, I. Godwin, C. Backes, D. McAteer, David, N. C. Berner, N. McEvoy, A. Ferguson, A. Shmeliov, M. Lyons, V. Nicolosi, G. Duesberg, J. Donegan and J. N. Coleman. Production of Ni(OH)₂ Nanosheets by Liquid Phase Exfoliation: From Optical Properties to Electrochemical Applications. *Journal of Materials Chemistry A*. 4 (28), 11046-11059, 2016.
- [3] A. Ferguson, I. Caffrey, C. Backes, J. N. Coleman and S. D. Bergin. Differentiating Defect and Basal Plane Contributions to the Surface Energy of Graphite Using Inverse Gas Chromatography. *Chemistry of Materials*. 28 (17), 6355-6366, 2016.
- [4] A. Ferguson, A. Harvey, S. D. Bergin and J. N Coleman. The Dependence of the Measured Surface Energy of Graphene on Nanosheet Size. *2D Materials*. 4 (1), 015040, 2017.

Acknowledgements

Firstly, I would like to thank Dr. Shane Bergin for taking the risk and bringing me on board to conduct this Phd and also for his guidance. I would also like to sincerely thank Prof. Jonathan Coleman for his help and encouragement along the way. Without either of you this would not have been possible.

I would like to thank the people who helped get me started on my research when I hadn't a clue; Big Pete, Arlene and Mustafa. To all the support staff in the school of Physics, including the finance office who were always helpful. I'd like to thank Neal from CMA for his SEM and TEM knowledge, along with his saint-like patience when teaching me how to use the equipment. Special thank you to Claudia and Keith for all the help and advice over the years.

A big thank you to all past and present members of the Coleman group who made me feel welcome and made the last 4 years so enjoyable. In no specific order: Big Pete, Little Pete, Paul, Sophie, Arlene, Umar, Tom, Graeme, Paul, Conor, Seb, Adam, Sonia, JB, Dave, Andrew, Damo and Shane. Another special thanks to my fellow Berginer Ivan for the science talk, simulations and often inappropriate behaviour that would lighten the mood. I'd also like to thank the summer students who have helped out over the years: Áine, Brian, Yuri and Tobias.

Outside of the research I'd like to thank my friends of which there are too many to name but roughly correspond to the Malahide, PCAM/Physics and Bath Avenue crew who helped keep my sanity throughout this process; mainly in the form of pints.

To my parents Tom (Tombo) and Barbara, I would like to thank you from the bottom of my heart for all the help and support over the years and for always encouraging me to follow my passions. Id like to thank my brother Steven for all his advice over the last 4 years. To my Grandmother Maud, who just celebrated

her 90th birthday, I'd like to thank her for putting up with me and going to quite frankly outrageous lengths to get me to eat when I was younger; to allow me to become the person I am today. She will be happy to know that finally, at the age of 27, I will be getting my first real job. Last but not least, I would like to thank my girlfriend Aoife for providing love, support and putting up with me giving out and moaning over the last few years. There is no way I would of gotten through this without her.

Contents

1	Introduction	1
1.1	Motivation	1
1.2	Thesis Overview	2
2	Materials and Background	6
2.1	Overview	6
2.2	Graphite	7
2.3	Low Dimensional Carbon Nanomaterials	11
2.4	Graphene	12
2.5	Bacterial Cellulose	19
2.6	Solubility Theory	27
2.7	Surface Energy	30
3	Methods and Theory	39
3.1	Overview	39
3.2	Inverse Gas Chromatography	39
3.3	Spectroscopy	50
3.4	Microscopy	55
3.5	Exfoliation Methods	63
3.6	Tensile Testing	68
4	Differentiating Defect and Basal Plane Contributions to the Surface Energy of Graphite Using Inverse Gas Chromatography	71
4.1	Overview	71
4.2	Introduction	72

4.3	Experimental Methods	74
4.4	Results and Discussion	76
4.5	Conclusion	103
5	The Dependence of the Measured Surface Energy of Graphene on Nanosheet Size	104
5.1	Overview	104
5.2	Introduction	104
5.3	Experimental Methods	105
5.4	Results and Discussion	108
5.5	Conclusion	120
6	Comparison of Graphite and Graphene Measurements	121
6.1	Overview	121
6.2	Results and Discussion	122
7	Understanding the Dispersion and Assembly of Bacterial Cellulose in Organic Solvents	127
7.1	Overview	127
7.2	Introduction	128
7.3	Experimental Methods	129
7.4	Results and Discussion	132
7.5	Conclusion	146
8	Conclusions and Further Work	147
8.1	Conclusions	147
8.2	Further Work	149

List of Figures

2.1	Diamond and graphite structure	8
2.2	Primary industrial applications of graphite	10
2.3	The family of carbon nanostructures	12
2.4	Graphene: The building block of carbon nanostructures	13
2.5	The absorbance of graphene with number of layers	14
2.6	Graphene production methods	16
2.7	Functionisation and reduction of graphene oxide	18
2.8	Liquid phase exfoliation of graphene	19
2.9	Structure of bacterial cellulose	21
2.10	Crystal structure of plant and bacterial cellulose	24
2.11	Transparent BC-polymer composite	27
2.12	Bulk vs Surface atoms	31
2.13	London dispersive interactions	33
2.14	Specific interactions	34
2.15	Explanation of surface coverage	36
2.16	Contact angle, wettability and surface energy	37
3.1	The principle of IGC	40
3.2	Example IGC elution curves	42
3.3	Example Schultz and Dorris-Gray plots	44
3.4	Schultz and polarisation methods for calculating ΔG_{sp}	46
3.5	Adsorption isotherm and BET plot	48
3.6	Schematic of SEA	49
3.7	Lambert Beer Law and Cary Varian UV-VIS Schematic	51
3.8	Raman scattering energy level diagram	53

3.9	Raman spectra of graphite and graphene	54
3.10	TEM schematic	57
3.11	TEM and SEM electron-sample interactions	58
3.12	SEM schematic	59
3.13	AFM schematic	61
3.14	Sonication process	64
3.15	Silverson shear mixer	66
3.16	Cascade centrifugation schematic	68
3.17	Example stress-strain curve	70
4.1	Initial characterisation of purchased graphite	77
4.2	Graphite platelet model	79
4.3	SEM characterisation of graphite	80
4.4	Raman spectra of commercial graphite	81
4.5	I_D/I_G - length relationship for graphite	82
4.6	Example γ_d graphite profiles with fitting parameters	83
4.7	Graphite γ_d profiles	84
4.8	Simulations of surface energy profiles (single surface site)	88
4.9	Simulations of surface energy profiles (two surface sites)	91
4.10	Simulations of surface energy profiles (three surface sites)	93
4.11	γ_d parameters as a function of flake length and Raman I_D/I_G	95
4.12	parametrised specific surface area and IGC data	98
4.13	Comparison of measured $\gamma_{d,\phi=1}$ with literature	101
5.1	Basic graphene characterisation	109
5.2	Graphene length distributions	110
5.3	Raman spectra of size selected graphene	111
5.4	Graphene IGC data	113
5.5	γ_d profiles of each graphene sample	114
5.6	Modelling of graphene surface energy data	117
6.1	Comparison of measured graphite and graphene surface energy . . .	123
6.2	Comparison of graphite and graphene data with developed models .	126

7.1	Successfully dispersion of bacterial cellulose	133
7.2	UV-vis spectrum of bacterial cellulose	134
7.3	BCN diameter AFM statistics	136
7.4	BCN solubility study	138
7.5	BC surface energy profile	139
7.6	Photo and helium ion image of BCN films	141
7.7	Example BCN stress-strain curves	142
7.8	Relationship between BCN film density and Young's modulus . . .	143
7.9	Tensile properties of BCN films as function of BCN junction density	144
1	Column preconditioning curve	152
2	Simulated γ_d profiles	153
3	γ_d simulations showing stretched exponential fits data better . . .	154

List of Tables

4.1	Fitting parameters of the γ_d profiles from commercial graphites . . .	86
5.1	Fitting parameters of the γ_d profiles size selected graphene	115
7.1	Concentration of BCN in successful organic solvents	135
7.2	Unsuccessful solvents for BC dispersion	135
7.3	Density and porosity of BCN films	141

Chapter 1

Introduction

1.1 Motivation

Finding, understanding and exploiting properties of materials has been one of the key drivers in the advancement of technology throughout history. From the smelting and casting of metals in the bronze age, through the industrial revolution, to modern times, where the development of integrated silicon chips have heralded in the computer age. These advancements rely on finding new materials with specific mechanical, electrical and thermal properties, which can then be applied to, for example: transistors, optoelectronic devices and high preference composites. Exploiting the properties of these materials often requires manipulation on the smallest of scales. These factors have driven the field of nanoscience over the last half century, spurred on by the words of Richard Feynman during his now famous talk "There's plenty of room at the bottom".

The interdisciplinary field of nanoscience has been working together to solve both fundamental and practical problems. For example, there has been great strides in the discovery and understanding of carbon nanostructured materials over the last 30 years; with the discovery of fullerenes, then carbon nanotubes and finally graphene (along with many other 2 dimensional nanomaterials). These superlative rich materials have the capacity to revolutionise our lives with the creation of better transistors, solar cells, polymer-nanomaterial composites, super-capacitors and batteries.

The main aim of this thesis is to extend the understanding of low dimensional nanomaterials by measuring and understanding their surface energy. Surface energy is an often overlooked but very important material property, as it controls how materials interact with their environment. For example, it has been shown, amongst others, that the exfoliation of graphite to graphene can be optimised by matching its surface energy to a solvent's surface energy using liquid phase exfoliation. This thesis establishes a framework for the measurement and analysis of the surface energy of low dimensional nanomaterials. This was achieved by mapping the surface energy of materials as a function of surface coverage using inverse gas chromatography, which gives insights into defects (both basal plane and edge) and the intrinsic surface energy of the basal plane. In order to achieve this, new analytical models were developed that describe, for example: how the decay constant measured from dispersive surface energy profiles are related to the fraction of high energy sites found on a surface and how the surface energy of defects scales with platelet/nanosheet size. This analysis was applied to graphite and shear exfoliated graphene but could also be applied to any 2D layered material such as boron nitride, MoS₂ and black phosphorous. A further study of the dispersion of bacterial cellulose by liquid phase exfoliation showed the diameter and mechanical properties of bacterial cellulose nanofibrils (BCN) and nanofibril films could be controlled by solvent surface energy. The best solvents for this were found to have the similar surface energy to that of bacterial cellulose, measured by inverse gas chromatography. It is hoped that this thesis, along with future work, can be used to optimise solvent choice for the ever expanding list of 1 & 2 dimensional nanomaterials, which in turn can be applied to devices as mentioned above.

1.2 Thesis Overview

Chapter 2: Materials and Background

An overview of the history, structure and properties of the materials used in this thesis is given. Several methods of producing graphene (these methods can also be applied to other 2D materials) are explored including liquid phase exfoliation; a method that is extensively used in this thesis. From previous work within the

group, it was found that understanding the surface energy of these materials is crucial to successful exfoliation. Therefore, surface energy, what it is, how it arises and its effects are explored. Several commonly used methods of measuring surface energy are examined with the pros and cons of each method explored and an explanation of why coverage dependent inverse gas chromatography was chosen for the measurements in this thesis.

Chapter 3: Methods and Theory

This chapter explores the experimental methods as well as the underlying theories used to characterise the materials in this thesis. Particular attention is given to inverse gas chromatography as it's the central characterisation technique used. Other characterisation techniques such as spectroscopy, microscopy and tensile testing are explored.

Chapter 4: Differentiating Defect and Basal Plane Contributions to the Surface Energy of Graphite Using Inverse Gas Chromatography

The dispersive surface energy of commercially available graphite is measured using inverse gas chromatography. Using a mix of Raman spectroscopy, scanning electron microscopy and simulation it was possible to separate and examine the different surface energy sites of graphite using newly developed models from both simulation and experiment. We find the surface energy of graphite can be described by three types of surface sites, which we attribute to the basal plane surface energy, basal plane defects and defects due to edges.

Chapter 5: The Dependence of the Measured Surface Energy of Graphene on Nanosheet Size

The dispersive surface energy of size selected, liquid exfoliated graphene was measured. Results show excellent consistency with that of graphite, its parent material. The key difference is that the defect content of graphene is overwhelmingly due to edge defects rather than a combination of edge and basal plane defects as seen with graphite.

Chapter 6: Comparison of Graphite and Graphene Surface Energy Measurements

A comparison of the measurements from the graphite and graphene chapters which shows results consistent with the models developed in the previous chapters.

Chapter 7: Understanding the Dispersion and Assembly of Bacterial Cellulose in Organic Solvents

Bacterial cellulose was exfoliated/debundled from its bulk state to bacterial cellulose nanofibrils. This is interesting because bacterial cellulose is the first material to be exfoliated where hydrogen bonding is prominent, showing that liquid phase exfoliation is applicable to this kind of material. Bacterial cellulose nanofibril films were produced whose mechanical properties were shown to scale with the degree of exfoliation.

Chapter 8: Conclusion and Future Work

This chapter summarises the key results from this thesis and discusses some of questions arising from it, with a view to future work on the topics.

Chapter 2

Materials and Background

2.1 Overview

This chapter introduces the materials studied in this thesis: graphite, graphene and bacterial cellulose. Specifically their history, structure, properties and applications will be explored. Graphite is introduced first, a material that has been used for thousands of years and is still widely used in a variety of applications, such as steel making and in electric car engines. In 2004, single layers of graphite, known as graphene were isolated and it was found that this material was the strongest, most absorbing of light and most conductive material ever. Graphene production methods are explored, including liquid phase exfoliation, a method widely used in this thesis. Bacterial cellulose is introduced, a type of cellulose produced by certain bacteria, characterised by its high purity and strength in comparison to plant cellulose. This thesis heavily involves the exfoliation of these materials. Therefore, the thermodynamics of exfoliation are examined. From this it becomes apparent that understanding the surface energy of these materials is key for their successful exfoliation. Therefore, surface energy, what it is, and how its measured are also explored.

2.2 Graphite

Graphite is the most stable allotrope of carbon and one of the most common minerals found on earth. It has a layered planar structure of carbon atoms arranged in a honeycomb lattice, with each layer stacked on top of each other. It has had a wide variety of uses throughout history, spanning millennia, from the neolithic age where the Marita people used graphite in ceramic paint for decorating pottery [1] to being used to mark sheep in the 1500's in England.[2, 3] Later, it found many uses as a engineering material such as being used as a refractory for moulding cannonballs during the reign of Elizabeth I, making them smoother and able travel longer distances; giving the English navy an advantage over their rivals.[4] Into the industrial revolution and modern times, graphite has been used for refractories, steel making, pencils,[5] lubricants and in batteries.[6] One of the reasons graphite is studied in this thesis is because it can be exfoliated to get graphene, a monolayer of graphite.[7]

2.2.1 Structure and Properties

As stated, graphite is the most stable and abundant allotrope of carbon found on Earth. However, it is just one of the many allotropes found that include diamond, graphene,[8] fullerenes [9] and carbon nanotubes.[10] By comparing the atomic structure of diamond (the second most common naturally occurring carbon allotrope) to graphite, it can be shown why materials made of the same element can have such radically different properties.

Figure 2.1 illustrates diamond and graphene with their atomic structures. The striking differences in how they look as well as their properties can be explained by the different types of bonds found in each material. Diamond is composed of sp^3 hybridised bonds that form a tetrahedral structure as shown in figure 2.1. In diamond, all carbon atoms are covalently bonded to 4 other carbon atoms with a bond length of 0.154nm and bond angle of 109.5° . The hardness of diamond, along with its high refractive index is due to all electrons being tightly bound by the sp^3 bonds. This is in stark contrast to graphite, which has a layered planar structure of sp^2 carbon. In plane carbon atoms are covalently bonded with bond

length 0.142 nm and angle 120° , which forms the characteristic hexagonal graphite lattice. With only 3 of 4 bond sites satisfied, the remaining electrons form delocalised π bonds above and below the plane which gives rise to the conductivity and optical properties of graphite.[11, 12] Graphene layers in graphite have a separation distance of 0.335nm and are held together by weak Van der Waals [13] forces allowing the planes to easily slide over each other; this is the reason graphite is used as a dry lubricant. This property of graphite has also been exploited to produce graphene [8] and is one of the reasons why the surface energetics of graphite is examined in detail in this thesis.

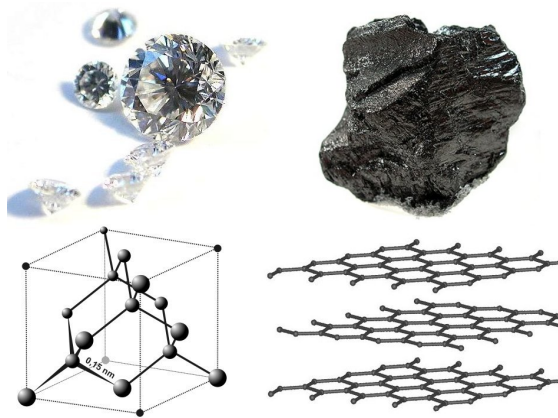


Figure 2.1: Diamond and graphite with their atomic structures.[14]

2.2.2 Types of Graphite

There are two main types of graphite, natural and synthetic. As the names imply, natural graphite can be mined and isolated from ore by using methods like floatation while synthetic graphite is man made from graphitisation which involves the heat treatment of non-graphitic carbon at very high temperatures (>2000 K).

There are 3 main forms of natural graphite: Flake, crystalline/vein and amorphous graphite. Flake graphite occurs as flat, plate like particles ranging in size from fine flakes ($>80 \mu\text{m}$) to large flakes ($\approx 1\text{mm}$). Flaked graphite is mined from metamorphic rocks [15] and has a higher carbon purity levels than amorphous graphite but is far less common. Its high purity makes it appealing for applications such as anode material in lithium ion batteries.[16] Amorphous carbon is

the most abundant form of natural graphite but has a far lower carbon content than flaked graphite and has no or very little crystallinity, making it unsuitable for most applications. High crystalline or vein graphite is extremely pure and a highly crystalline form of graphite. As a result, it has higher thermal and electrical conductivity than the other two mentioned but is very scarce, making it very expensive and not viable for most commercial applications.

Synthetic graphite is graphite that has been produced by higher temperature processing of amorphous carbon.[17] It is characterised by high purity but often lower crystallinity than flaked or vein graphite. Synthetic graphite is used in batteries, electrodes in electric arc furnaces and moderator rods in nuclear power plants. One notable synthetic graphite is highly ordered pyrolytic graphite (HOPG) which is very pure and ordered, meaning that individual graphite crystallites are well aligned. It is produced by heat treatment of pyrolytic carbon or by chemical vapour deposition above 2500 K. HOPG has been studied extensively and is often used as a standard for calibration of scanning tunnelling microscopes.[18] In this thesis, HOPG was used for calibration of the Raman spectrometer due to its low defect concentration.[19]

2.2.3 Graphite Applications

As previously mentioned, graphite has been used for many applications throughout history. This section explores what graphite is used for at present. The pie chart in figure 2.2 shows the breakdown of the main applications and sectors graphite was utilised in 2012.[20] Refractory uses and the steel industry are still the largest consumers of graphite. A refractory material maintains its strength at high temperatures. As graphite has excellent thermal stability, it makes it an ideal material for this function and has been used since the industrial revolution for lining of furnaces and for making crucibles. Today, it is mainly used in refractory magnesite bricks that line furnaces. Graphite has been also been extensively used directly in steel production to increase and control the carbon content of steel.

Over the last quarter century, graphite has been used more and more in clean technology applications such as lithium ion batteries and less as refractories and steel production. According to figure 2.2, battery making consumed a quarter of

graphite produced in 2012. Graphite is used as the anode material in batteries because of its conductivity and low cost. Battery demand is expected to increase massively in the wake of electric cars becoming mainstream, considering it has been estimated that each electric car will have in order of tens of kilograms of graphite in each engine.[21]

Graphite has long been used as a lubricant due to graphite layers being able to easily slide over each other due to the weak Van der Waals forces holding them together. Graphite is generally used as speciality lubricants for use in extreme temperatures, as a anti-seize agent, gear lubricant for mining machines and to lubricate locks. Graphite is also used as a foundry facing which is a water based paint containing graphite, it is used to help easily separate the cooled metal from the mould.

The majority of people will know graphite from the "lead" in pencils. Pencil lead is a mixture of graphite and clay, the ratio of which depends on the type of pencil required.

Since the discovery of graphene in 2004 [8], routes for large scale production of it has been sought after. One such method involves using graphite as the starting material and exfoliating it to mono and few layer graphene. Graphene and production methods are explored in detail later in this chapter.

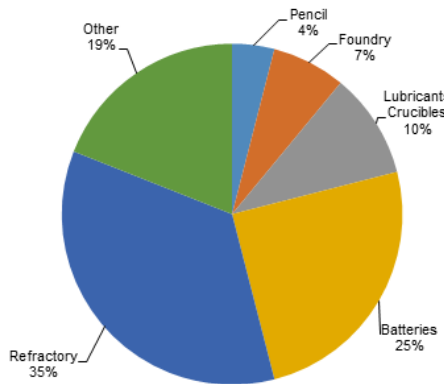


Figure 2.2: Primary industrial applications of graphite in 2012.[20]

2.3 Low Dimensional Carbon Nanomaterials

As discussed in section 2.2, carbon allotropes such as graphite and diamond have been studied and used for a long time, with their structures and properties being well understood. These along with amorphous carbon were once thought to be the only allotropes of carbon. This changed significantly with the discovery of fullerenes by Kroto *et al* in 1985 [9], which kick started interest into the research of synthetic carbon allotropes. The most well known fullerene, C₆₀, shown in figure 2.3 is composed of 60 sp² hybridised bonds arranged in hexagonal and pentagonal rings, resembling a modern football. C₆₀ or the Buckminsterfullerene (Bucky-ball) is considered a 0D carbon structure, owing to all dimensions being on the nanoscale (>100 nm). Like all carbon allotropes discovered over the last 30 years, initially, it was very difficult to produce sufficient quantities for meaningful applications, until a method involving the evaporation and re-condensation of graphite using an arch discharge method was developed.[22] Since then, fullerenes have found many applications depending on their functionalisation ranging from biomedical applications [23] to electronics, specifically as an electron acceptor in organic solar cells.[24]

The discovery of C₆₀ and other fullerenes renewed interest in carbon allotropes that eventually led to the discovery of carbon nanotubes (CNT's) in 1991 by Iijima *et al.*[10] CNT's are considered 1D carbon nanostructures, due to the diameter of the tube to be in the order of 1nm [26] but can have lengths of up to 550mm.[27] CNT's were found to have outstanding electronic and mechanical properties. Depending on their configuration, they could be either metallic or semiconducting in nature [28], with semiconducting CNT's having electron mobility of 100000 cm²/Vs at room temperature.[29] At the time, CNT's were the found to be the strongest material known to man with a Young's modulus of 1 TPa and tensile strength of 60 GPa [30]; making them 60 times stronger than steel.

Research into carbon allotropes was once again revolutionised in 2004 with the successful isolation of monolayer graphene [8], which is a 2D material comprising of single graphite layers that are one atom thick.

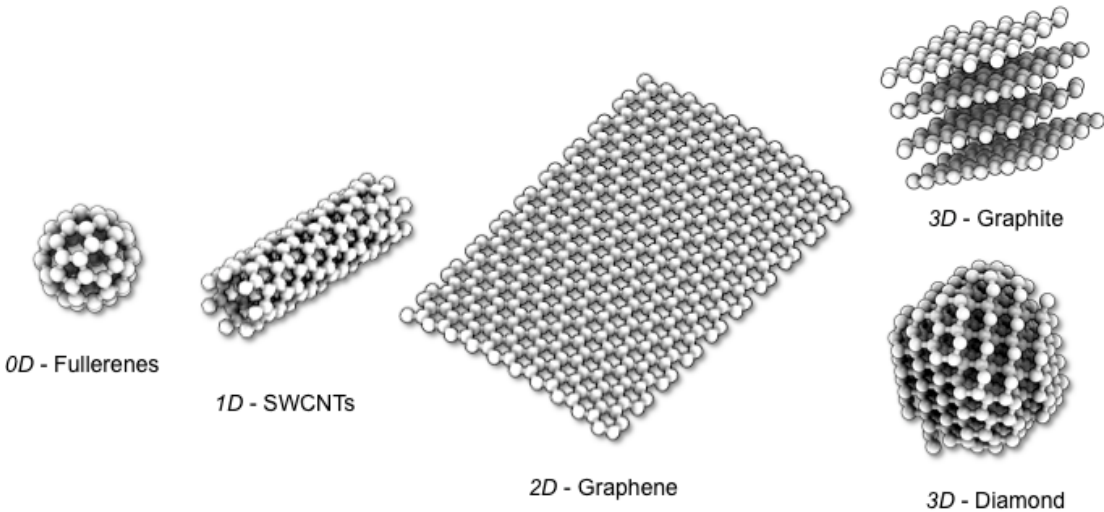


Figure 2.3: The family of carbon nanostructured allotropes showing fullerenes (0D), Carbon nanotubes (1D), graphene (2D), graphite and diamond (3D). Reproduced from [25]

2.4 Graphene

Since the discovery of graphene, there has been an explosion its research. The idea of, or the name graphene is not a new one, having being used in the literature for some time, but was mainly viewed as a theoretical construct or a name used to describe electronic decoupled layers within graphite intercalated compounds.[31] Monolayer graphene was assumed to be unable to exist in nature because the flat monolayer would be thermodynamically unstable [8] if unsupported, causing planes to buckle and roll up.[32] However, ripples in its lattice caused by thermal fluctuations were found [33], allowing it to be thermodynamically stable. Since it was first observed, it has gone on to rack up many superlatives, including the strongest [34], most absorbing [35] and most conductive [36] material known to man.

Graphene can be considered the building blocks of most carbon allotropes, considering graphite is just many graphene layers stacked together, bound by Van der Waals interactions. Fullerenes can be thought of as a graphene sheet wrapped up while CNT's are just a rolled up graphene sheet as shown in figure 2.4. The

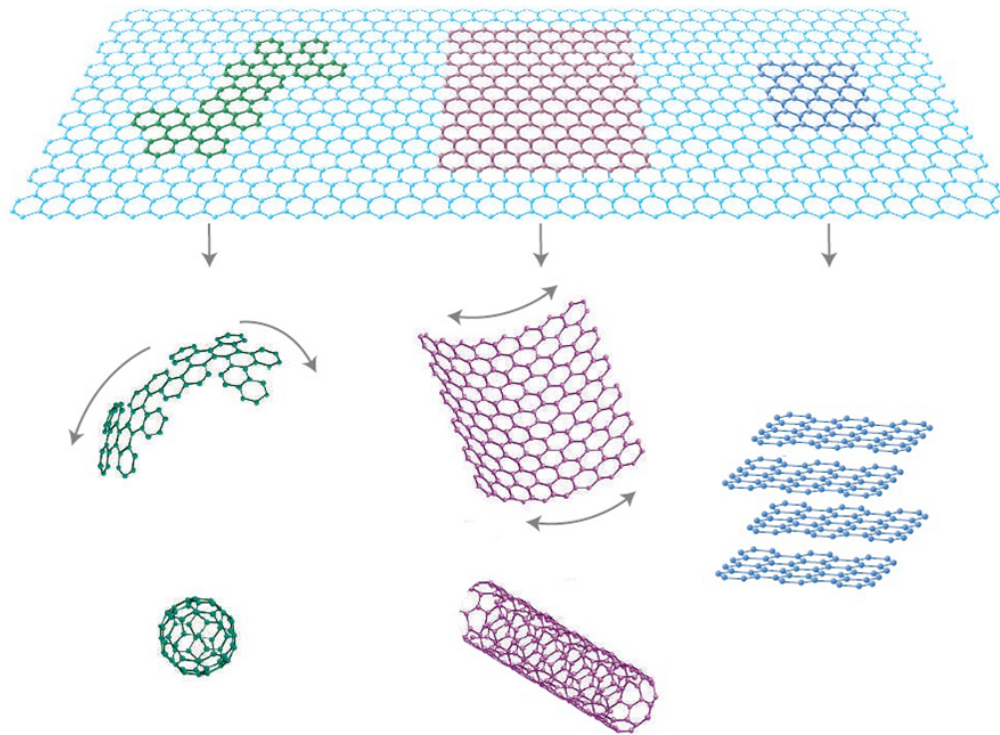


Figure 2.4: Graphene: The building blocks of carbon nanostructures. It can be wrapped to form fullerenes, rolled up to become carbon nanotubes and stacked to form graphite. Reproduced from [33].

properties and production of graphene is discussed in detail below.

2.4.1 Properties

Monolayer graphene consists of sp^2 hybridised carbon atoms that are covalently bonded with a bond angle of 120° with π bonds perpendicular to the plane that are responsible for the optical, electrical and stacking of graphene layers. Considering that graphenes in plane bonding is very strong and intra plane bonding so weak, it allows graphene to be exfoliated to monolayer or multilayer while maintaining much of its lateral size, i.e. graphene sheets can have large lateral dimensions in relation to their thickness.

Graphene is considered the most absorbing material of light currently known. A graphene monolayer can adsorb 2.3% of incident white light [35] as shown in

figure 2.5. Along with its electrical properties, this makes it an ideal material for transparent electrodes in LED's and solar cells.[37]

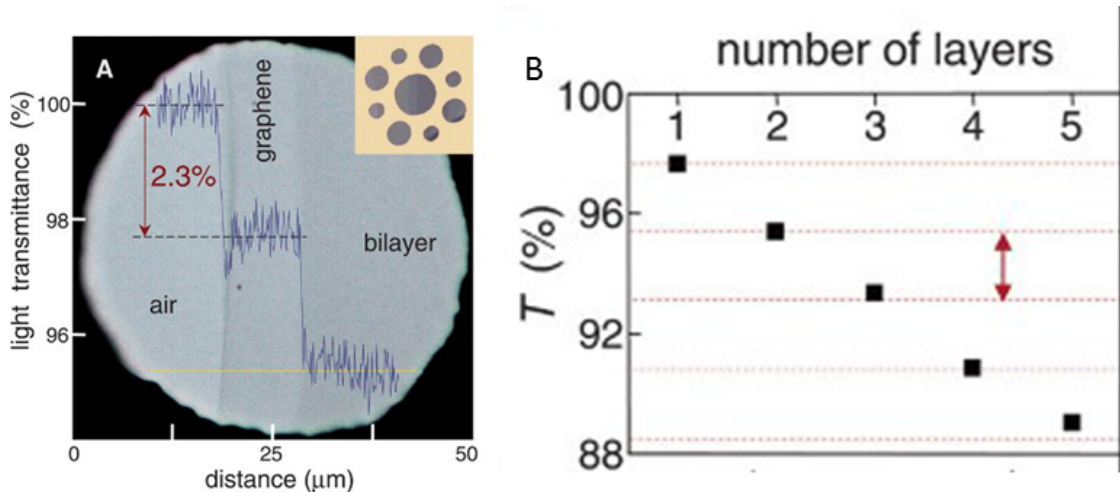


Figure 2.5: A) Photograph showing the absorbance of monolayer graphene and bilayer graphene. B) Graph showing the transmittance of graphene as a function of number of layers.[35]

The electrical properties of graphene are what initially sparked the large interest in it as it has a unique band structure, where the valence and conduction bands touch at points, called the Dirac points. Graphene is defined as a semimetal or zero bandgap semiconductor.[38] This is different from a semiconductor which has an appreciable gap between bands and a metal, where the valence and conduction bands overlap. At the Dirac points in graphene, electrons behave like relativistic quasiparticles, called Dirac fermions with zero effective mass [39] that travel at an "effective speed of light" of 10^6 m/s, as a result, the charge mobility of graphene is exceedingly high with measured values exceeding $200000\text{ cm}^2/\text{Vs}$ for monolayer graphene; 2 orders of magnitude higher than modern Silicon chips.[36] Charge transport in materials is usually limited by defects which act as scattering centres but due to the high quality 2D lattice structure of graphene this isn't observed. Owing to this and other novel electronic properties of graphene such the ambipolar field effect [40], room temperature quantum hall effect [38] and a quantised minimum conductance make graphene one of the most intriguing and exotic materials on Earth.[39]

Coupled with its optical and electrical properties, graphene is also the strongest material known to man. Lee *et al* measured the mechanical properties of mono-layer graphene by nanoindentation using atomic force microscopy. They measured the Young's modulus and tensile strength to be 1TPa and 130GPa respectfully [34], making it approximately 200 times stronger than steel. These amazing mechanical properties, along with its electrical and thermal properties make graphene ideal as a filler in composite materials [41] for applications such as mechanical reinforcement [42], energy storage applications [43] and transparent electrodes.[44] There is no doubt the exotic and remarkable properties of graphene, however there has been considerable trouble in producing large quantities of defect free graphene. The following section explores some of the fabrication methods that have been used to produce graphene.

2.4.2 Fabrication methods

Like most other newly found allotropes of carbon, there was a lack of high quality production methods.[45] Until new fabrication techniques could be established, the superlative properties of graphene couldn't be exploited on a meaningful scale. This section will examine the most widely used methods of graphene production, from techniques used to get large, high quality graphene for electronic applications to other methods, such as mass production for composites and ink printing.

Mechanical Exfoliation

Graphene was first isolated and characterised by mechanical exfoliation.[8] This remarkably simple technique uses scotch tape to peel apart the layers of oxygen plasma etched HOPG. The "peeling" was repeated over and over until mono and few layer graphene was isolated and transferred to a silicon substrate for characterisation. The flakes produced by this method are of the highest quality [46] and are ideal for studying the fundamental physical and chemical features of graphene. As one might imagine, this method produces a very low yield and is expensive, as shown in figure 2.6. Therefore, other production methods needed to be developed.

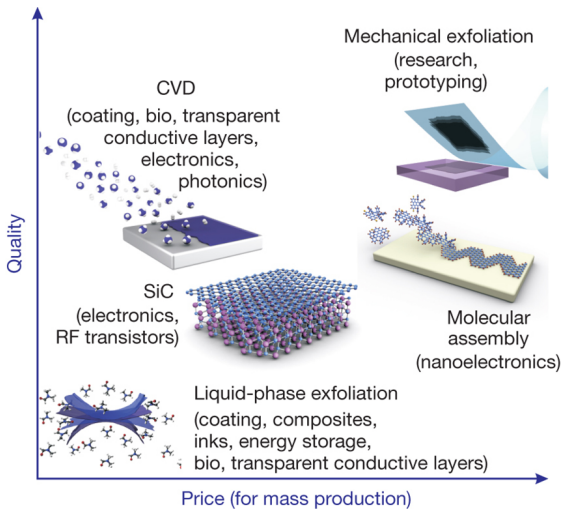


Figure 2.6: Graphene production methods showing the quality of the graphene as a function of price ranging from high quality, expensive mechanically exfoliated graphene to cheaper, lower quality liquid phase exfoliated graphene. Reproduced from [47]

Epitaxial Growth and Chemical Vapour Deposition

Bottom up fabrication is a method that could be used for high end electronic applications involving graphene. Silicon carbide is a common material used in high power electronics. Graphene is generally made using this method at high temperatures to produce a graphitised surface, which initially was used to grow a stack of randomly orientated polycrystalline layers.[48] But now, the number of layers can be controlled.[49] This method produces very high quality graphene with crystallites being able to be grown to sizes in the order of hundreds of micrometers.[50] The downside to this method is that it is costly.

Chemical vapour deposition (CVD) has been used to grow high quality, large area polycrystalline graphene films.[51] CVD involves the decomposition of hydrocarbons, usually methane onto a metal substrate (usually copper) at high temperatures, forming a film of material on the substrate. One problem with this method is that there usually needs to be a substrate transfer from the metal to a dielectric substrate. Saying that, square meter graphene sheets have been produced [52] with up to 95% monolayer coverage.[53] The graphene produced by CVD is of extremely high quality that exhibits the quantum hall effect and high carrier

mobilities found in mechanically exfoliated graphene.[37] Therefore, it is envisaged that graphene made from this method will be used in high end electronics that require large monolayer graphene crystals [54] and isn't suitable for fillers in composites or for ink printing due to scaling costs as seen in figure 2.6. As a result, lower cost methods had to be developed.

Chemical Exfoliated Graphene

The electronic structure of graphite allows it to participate in many types of chemical reactions with reducing agents or oxidisers. As a result, the surface chemistry of graphite can be altered in order to change its properties to make it easily dispersible in aqueous solutions to produce large amounts of graphene.[41, 55]

The functionalisation of graphite to make thinner platelets is nothing new as graphite oxide was prepared by Brodie in 1859 [56] by treating graphite with potassium chlorate and fuming nitric acid to make paper like foils of graphite that were 0.05 mm thick. However, this method proved rather dangerous and inefficient. Hummer *et al* [57] improved on this method by developing a safer and more efficient method of producing graphite oxide by using strong oxidising agents to attach hydroxyl and other functional groups to the basal plane of graphite, altering its affinity to water. This method later became known as the Hummer method. Upon the discovery of graphene, it was thought that the Hummer method could be applied to exfoliate graphite oxide to graphene oxide (GO) in a scalable manner. This was realised in 2006 by Stankovich *et al* who used a modified Hummer method to produce liquid exfoliated GO in water with the addition of sonication to disperse the stacked layers of Graphite oxide.[41] The hydrophilicity of the modified basal plane allowed water to stabilise the dispersion of GO. Problems with this method are that by functionalising the basal plane, it makes it non-conductive, thus removing one of the most promising properties of the material.[58] This was somewhat overcome with the reduction of GO by treating it with hydrazine hydrate and thermal annealing to remove the oxide groups on the surface to produce reduced graphene oxide (rGO) as shown in figure 2.7. Even with the reduction of GO, many defects from the process still remain [59, 60] which can have detrimental effects on the properties of the graphene.[61] The presence of these defects limit the use of rGO in applications that require high strength and conductivity

such as conducting inks and spray coating.[62, 63] Therefore, a scalable method of producing pristine graphene was needed to fit these needs.

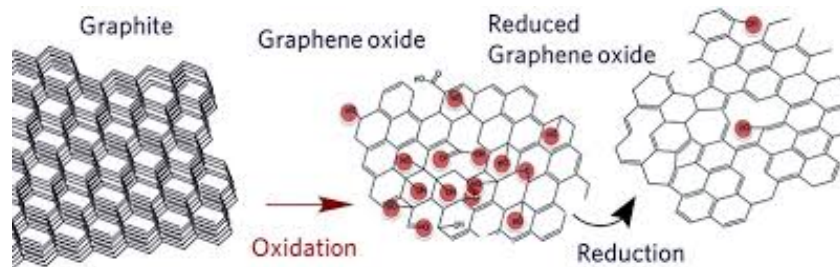


Figure 2.7: The functionalisation of graphite is used to exfoliate it to graphene oxide which can then be reduced by removing most of the functional groups, but not all, to get reduced graphene oxide. Reproduced from [64]

Liquid Phase Exfoliation

Liquid phase exfoliation (LPE) is a scalable and cost efficient method of production of pristine graphene, first shown by Hernandez *et al* in 2008.[7] In this work, graphene was exfoliated in organic solvents such as N-Methyl-2-pyrrolidone (NMP) or N-Cyclohexyl-2-pyrrolidone (CHP) by sonication to produce polydisperse graphene sheets that included a monolayer content of about 1%, which with controlled centrifugation could be increased. The energy provided by sonication is enough to disperse the weakly bound graphene sheets which are then stabilised in an appropriate solvent whose surface energy matches that of graphene.[65] If the solvent has the same or similar surface energy to the dispersed graphene sheets, they will preferably interact with the solvent rather than each other (reaggregate), as is the case for a 'bad' solvent whose surface energy doesn't match as is shown in figure 2.8.

This is a similar approach to previous work, where carbon nanotubes were de-bundled in a similar manner.[66] Initially, concentrations of graphene were low, at around 0.01 mg/mL [7] but after further refinement of the technique, it was possible to get concentrations of up to 63 mg/mL where indefinitely stable dispersions at 28 mg/mL were observed. TEM and Raman spectroscopy showed that the graphene exfoliated by LPE was defect free, unoxidised, pristine graphene.[67] Graphene made by this technique has been used in a variety of applications such



Figure 2.8: Liquid exfoliation of graphene: graphene is sonicated in a solvent. If the solvent is 'good' it will form a stable dispersion while a 'bad' solvent will result in reaggregation.[76]

as a reinforcing agent in polymer composites [68, 69] to transparent conductors [70] and sensing applications.[71] LPE is not exclusive to graphene and has been used to exfoliate a host of other 2D layered materials [72, 73, 74] in solvents and aqueous solutions, using surfactant to stabilise the dispersion.[75]

One of the disadvantages of LPE is that sonication can't be scaled up to produce g/hour or kg/hour required for industrial scale production. Therefore, a large scale exfoliation method had to be developed. Paton *et al* used industrial shear mixers to scale up graphene production.[77] Here, high shear rates were applied to a graphite-solvent system to produce few layer exfoliated graphene whose output scales with volume. Shear exfoliation was used in this thesis to produce appreciable amounts of size selected graphene for surface energy characterisation, the theory of which can be found in section 2.6. Another disadvantage of LPE is that the graphene produced is polydisperse, with a low monolayer content, making it unsuitable for high end electronics. In some cases, it is possible to greatly increase the monolayer population but requires a complicated centrifugation regime.[78] Still, the flakes produced are too small for those applications. This makes LPE suitable for applications that don't require large monolayers as discussed above.

2.5 Bacterial Cellulose

Cellulose is probably the most abundant polymer found naturally on Earth [79] and also one of the most widely used. It represents about 1.5×10^{12} tons of total annual biomass production and is considered nearly inexhaustive.[80] It has been used for thousands of years for ropes, timber for housing and paper. Wood is by far the most used material containing cellulose but it also features heavily in other

materials like cotton and plant fibers. It is not far-fetched to say that cellulose materials have heavily shaped human history.

Cellulose was first isolated by French chemist Anselme Payen in 1838 when he described a resistant fibrous solid that remained behind after treatment with various acids and ammonia.[81] He determined its molecular formula to be $C_6H_{10}O_5$ by elemental analysis. Cellulose has no taste, is odourless, hydrophilic, is insoluble in water and most organic solvents, and is biodegradable.[82] Cellulose has excellent thermal stability for a biopolymer with a melting temperature of 467 °C. Cellulose is primarily sourced from wood and plants but can also be produced by types of bacteria, called bacterial cellulose (BC). BC is considered a very pure, high performance cellulose which has garnered great interest over the years from the materials science community. BC has a wider variety of applications such as in optoelectronics [83], electronic paper displays [84], supercapacitors [85] and medical applications such as wound dressings.[86] BC, and more generally all cellulose types, have a hierarchical structure [87], where smaller sub-structures have extremely promising properties compared to the macroscopic material, but these properties are limited by their tendency to aggregate.[88] This thesis demonstrates a controllable method to break down and isolate the sub-structures, called BC nanofibrils (BCN).

2.5.1 BC Structure and Properties

Certain types of bacteria have been found to secrete cellulose of extremely high purity, giving it promising properties over other cellulose sources. BC was first described by Brown in 1886 [89, 90] when he discovered an organism in the *Mycoderma aceti* ("mother of vinegar") which produced extremely strong membranes when cultivated in a medium containing fructose [91], that he named *A Xylinam*. Since then, many other forms of bacteria have been found that secrete cellulose such as *Acebacter*, *Sarcina ventriculi* and *Agrobacterium*. In this thesis, BC produced by *Glucanobacter Xylinum* (previously known as *Acebacter Xylinum*) was used. Exactly why some bacteria produce cellulose isn't fully known and is still debated in the community. Some suggestions are it is produced for protection from UV light [92], to protect against heavy metal ions and improve nutrient transport by diffusion [93] or to maintain close proximity to the surface

of the culture medium where oxygen concentration is highest.[94]

BC, like all other types of cellulose are carbohydrate polymers made up of β -glucose monomers as shown in figure 2.9A. Glucose has 2 primary isomers, α and β , that differ by the position of the hydroxyl group attached to C1 in the glucose ring. In α -glucose, the hydroxyl group attached to C1 and the group at C5 are on opposite sides of the rings plane, whereas in β -glucose, they lie on the same side of the plane as shown in figure 2.9A.

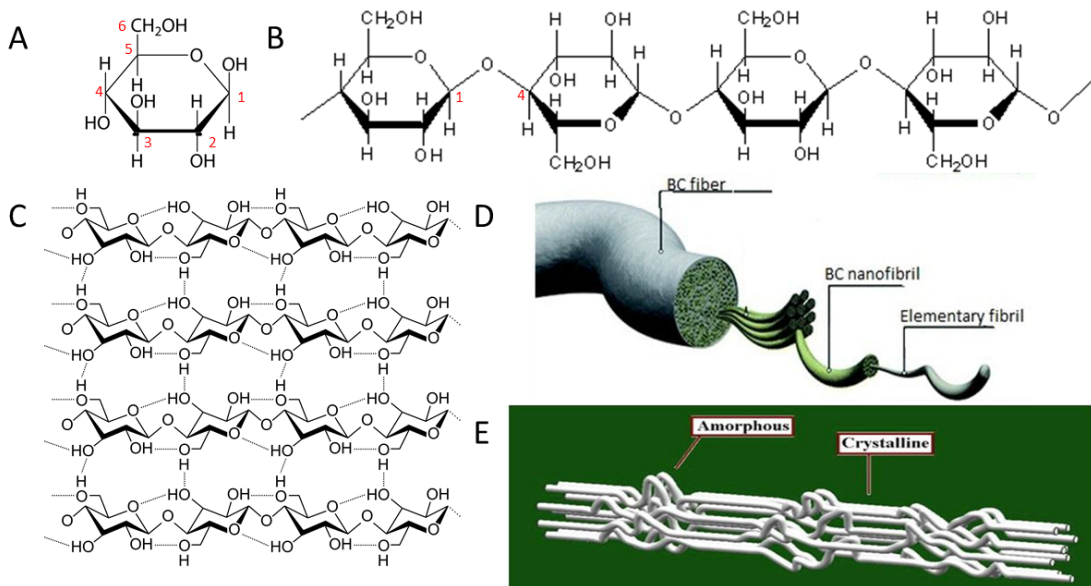


Figure 2.9: The building blocks and structure of bacterial cellulose: A) Chemical structure of β -glucose. B) Segment of a cellulose chain showing the 1,4 β -glycosidic bonds that link the glucose monomers together. C) The hydrogen bonding network that links adjacent cellulose chains together. They are formed by both intra and inter chain hydrogen bonds of hydroxyl groups. D) The hierarchical structure of BC. Elementary fibrils consist of several chains with a diameter of about 1.5 nm which in turn aggregate to form BC nanofibrils of diameter 6-20 nm. Again, they aggregate to form BC fibers with approximate diameter of 100 nm that form the macroscopic BC. Reproduced from [95]. E) BC nanofibril showing the crystalline regions that are connected by non-crystalline, amorphous regions. Reproduced from [96]

In order to form a straight polymer chain of glucose, every second monomer is rotated 180° and they bond together by a condensation reaction. Glucose monomers condense by 1,4 β -glycosidic bonds, named by the C1 and C4 pos-

tions participating in the reaction which is shown in figure 2.9B. Glycosidic bonds are types of covalent bonds that bond carbohydrates to another group that may or may not be another carbohydrate. The rotation of every second glucose monomer keeps the cellulose from rolling up, as is the case with starch and other carbohydrates. The degree of polymerisation (DP) (the number of repeating monomers in the polymer chain) of cellulose varies considerably depending on the cellulose source. For instance, BC is known for its high purity and excellent mechanical properties, as a result, it typically has a DP of 8000 or more.[97] This is in contrast to plant cellulose which has DP values in the range of 300-1700.[98, 80]

Adjacent cellulose chains bond together by both Van der Waals, inter and intra chain hydrogen bonding leading to the formation of elementary cellulose fibrils that have an approximate width of 1.5 nm.[99] Inter and intra chain hydrogen bonding is due to the high donor activity of the OH groups as shown in figure 2.9C. Each elementary fibril consists of about 10-15 bonded chains [86], which, in turn aggregate together with other elementary fibrils, again by Van der Waals and hydrogen bonding to form BC nanofibrils (BCN); that have diameters ranging from 6-20 nm and lengths of several microns.[100] The BCN then aggregate through the same processes to form macroscopic BC fibers with widths of approximately 100 nm.[101] This gives BC its hierarchical structure as shown in figure 2.9D. Since it was first isolated, BCN has been of much interest to researchers due to their excellent mechanical properties, such as reported Young's modulus as high as 78-160 GPa [102] and estimated tensile strength of 1500 MPa.[103] But as previously mentioned, BCN promising properties are limited due to their tendency to aggregate to BC fibers in the same way graphene and carbon nanotubes properties are limited by aggregation to graphite and nanotube bundles.

Like many other polymers, BC is not purely crystalline, but rather consists of a mixture of highly ordered, tightly packed crystalline regions, stabilised by a high density of strong inter and intra chain hydrogen bonds. These are connected together by amorphous regions caused by chain dislocations of segments along the elementary fibrils, where the nanofibrils are distorted by internal strain, causing them to tilt and twist as shown in figure 2.9E. The amorphous regions along the nanofibrils act as weak spots and are the most probable place where nanofibril fracture will occur. This means that the higher the crystallinity of cellulose, the

better the mechanical and chemical properties of it will have. BC is characterised by high crystallinity, up to 80% [104] and therefore, higher purity compared to that of plant cellulose, whose crystallinity can range from 23-53% depending on source.[105, 106, 107] The lower crystallinity of plant cellulose is attributed to defects such as hemicellulose, pectin or lignin, which are not found in BC.[108]

The crystal structure of cellulose has fascinated scientists for over 100 years [109, 110, 111, 112] due to being more complicated than first initially thought. The hydrogen bonding network and molecular orientation in cellulose can vary widely which gives rise to cellulose polymorphs which depends on its source, extraction method and treatments. So far, 6 polymorphs have been identified [113], of which 2 are widely studied (type I and II). Type I cellulose is native cellulose that includes plant and bacterial cellulose while type II is produced from chemically regenerated type I cellulose by dissolving it in solvent and then reprecipitating in water. [114, 115] Different sources of type I cellulose were once thought to have the same crystal structure but as it turned out, it had 2 sub-allomorphs, called type I_α and I_β ; discovered in 1984 [116] and studied in detail by Nishiyama *et al* in 2002 and 2003.[117, 118] It was discovered that cellulose I_α was primarily found in bacterial and algae cellulose while cellulose I_β is primarily found in plant based cellulose. Both I_α and I_β adopt parallel chain configuration but differ in their hydrogen bonding patterns, implying they have different crystal structures.[113] This was indeed the case as it was found that I_α corresponds to a triclinic unit cell ($a = 6.79 \text{ \AA}$, $b = 5.96 \text{ \AA}$, $c = 10.4 \text{ \AA}$, $\alpha = 118.08^\circ$, $\beta = 114.8^\circ$ and $\gamma = 80.37^\circ$) containing only one chain per cell [118], while I_β consists of a monoclinic unit cell containing 2 cellulose chains per unit cell ($a = 7.78 \text{ \AA}$, $b = 8.2 \text{ \AA}$, $c = 10.38 \text{ \AA}$, $\alpha = \beta = 90^\circ$ and $\gamma = 96.5^\circ$). This crystal structure of both is shown in figure 2.10. I_α is considered a metastable phase to the more thermodynamically stable I_β and can be converted from I_α to I_β by high temperature annealing in various media.[119]

2.5.2 Applications

BC has been widely used and is currently researched extensively, owing to its unique properties, such as its high mechanical strength, chemical robustness (BC is practically insoluble, with only a few exceptions), its high degradation temperature

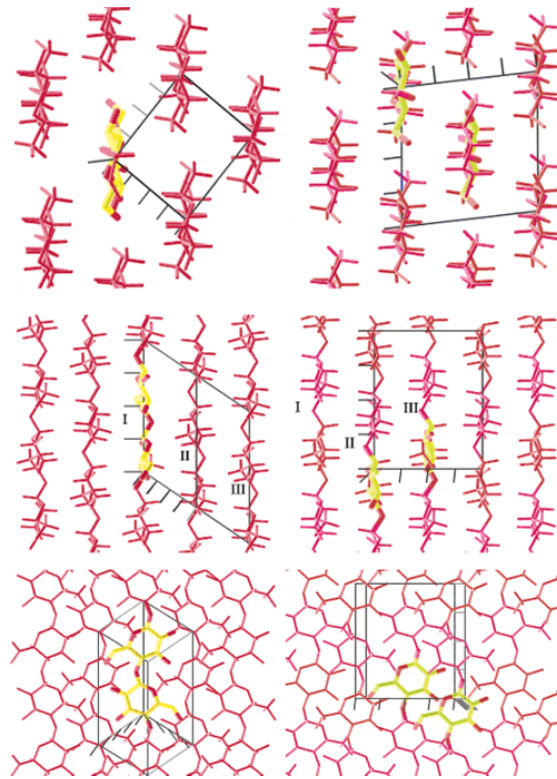


Figure 2.10: Projections of the crystal structures of cellulose I_α (left) and I_β (right) down the chain axes (top), perpendicular to the chain axis and in the plane of the hydrogen bonded sheets (middle), and perpendicular to the hydrogen bonded sheets (bottom). The cellulose chains are represented by red skeletal models. The unit cell of each structure is shown in white. Reproduced from [118]

and the fact that it's environmentally friendly in comparison to other materials with these traits. The main industries BC and BC nanofibrils are involved in are: food, medicine, composite and electronics.

The oldest known use of BC was as a raw material in nata de coco, a traditional dessert in the Philippines. Other food items where BC could be used were suggested by Okiyama *et al* that include thickening agents, salads and low calorie deserts.[120, 121, 122]

2.5.3 Medical

Research into using BC in medical applications has gained prevalence over the last few years [123] due to the combination of β -glucanases absence in human bodies, meaning that we can't break down BC due to BC's poor solubility in physiological media, making it potentially useful for applications such as patches, skin repair and in tissue engineering.[124]

BC's high mechanical strength, permeability to liquids and gases and low irritation of skin showed promise for use as an artificial skin for temporary use for covering wounds. Currently, there are two commercially available products that use BC, Biofill and Gergiflex which are widely used in surgery and dental implants. They have been used in the treatment of third degree burns [125] and as a temporary human skin substitute.[126] BC could also be used for artificial blood vessels as it carries a lower risk of blood clots than synthetic materials currently used in bypass operations.[127, 128, 129] Another obvious medical application is using BC as a scaffold material for tissue engineering, this is analogous to the function cellulose provides in plants. This could be applied to tissue engineering of cartilage, where scaffold is essential in order to support cell proliferation and to maintain cartilage function in addition to providing the shape of the new growing tissue.[130, 131, 128]

2.5.4 Composites

In the last few years, BC nanofibrils (BCN) have been investigated as an alternative, eco-friendly nanomaterial for composites. Nanocomposite materials combine the properties of its constituent parts, retaining the desired properties of each material to make a far more desirable material for potential applications. For example, BCN has been used as both a template and filler material in composites due to its high mechanical strength, and with the addition of other nanomaterials, this can provide composites with promising sensing, optical and electrical properties.[132]

BCN is an excellent material for the fabrication of high performance gas or moisture sensors due to it having a high specific surface area, water holding capacity and a large number of OH groups.[132] Hu *et al* coated a quartz crystal

micro-balance with BCN and tested it with water and other gases by measuring the shift in the resonance frequency of the micro-balance due to the additional mass from the adsorbed materials.[133] Results showed a two order of magnitude change in frequency from 5-97% humidity with excellent linearity between 20-70% humidity, while having good reversible behaviour and stability. This kind of device was further enhanced by adding other components for detection to the porous BCN substrate, producing a formaldehyde sensor with a detection limit of 1 ppm.[134] Other BC based sensors have been produced for the detection of glucose using a gold nanoparticle-BCN composite with a detection limit of 2.3mMol with potential for use to monitor glucose in blood samples.[135]

Optoelectronics is another field where BCN show promise as a composite material. BCN-electroconductive composites are prepared by combining conductive nanomaterials with BCN, such as with metal ions, carbon nanotubes (SWCNT or MWCNT) [136], graphene [137] and nanowires.[138] Yoon *et al* prepared a MWCNT-BCN composite by dipping BCN in MWCNT surfactant solution. Imaging showed the CNT's were well dispersed in the porous BCN matrix and had a conductivity of 1.4×10^{-1} S/cm.[136] One problem with the composites was a low transparency; this was improved by incorporating a silk fibroin solution into the membrane giving the composite at transmittance of 70% at 550 nm and a conductivity of 2.3×10^{-3} S/cm.[139] Later, a similar method was used to produce conductive films with a transmittance of 77%, with sheet resistance of 2.3 k Ω /sq [140] that showed excellent flexibility without loss of properties, making it ideal for transparent electrodes in devices like flexible displays and OLEDs.

BC films consist of a web like network of BCN that have excellent mechanical and thermal properties, making it ideal as a reinforcement material for transparent plastics.[103] Yano *et al* produced transparent BCN-epoxy and BCN-acrylic composites with BCN content as high as 70%, giving the composite a tensile strength of up to 325 MPa as well as excellent thermal stability and flexibility. Also, due to the aligned fibers, the composites had high transparency as shown in figure 2.11, these properties make the composites an ideal material for substrates in optoelectronic devices where high transparency, mechanical strength and thermal stability are required.



Figure 2.11: Flexible BCN-acrylic composite with 60% nanofiber content. Reproduced from Yano *et al.*[103]

2.6 Solubility Theory

As discussed previously, liquid phase exfoliation is an effective method to exfoliate low dimensional nanomaterials from their parent materials, e.g. graphite to graphene and BC to BCN. The exfoliation of graphene and the de-bundling of BC is based off previous work with CNT's [66, 141], where it was found that stable CNT dispersions could be obtained in certain solvents. This was later extended to the exfoliation of graphite by sonication in similar media as CNT by Hernandez *et al.*[142] More recently, Paton *et al* were able to scale graphene production by shear exfoliation of graphite, again, in similar media as before.[77] Since these materials could only be stabilised by certain solvents, it is important to understand the underlying solubility thermodynamics that govern the process. The next sections explore the thermodynamics behind the exfoliation of low dimensional nanomaterials.

Solution thermodynamics

The mixing of two chemical compounds, i.e. dispersed graphene sheets and solvent can be thought of as a binary mixture. In a thermodynamic sense, when two substances mix, it leads to a change in entropy (S) and enthalpy (H) of the system. In general terms, the solubility of materials in solvents is thermodynamically favourable if the Gibbs free energy of mixing (ΔG_{mix}) is favourable (negative) and

is given by:

$$\Delta G_{mix} = \Delta H_{mix} - \Delta S_{mix} \quad (2.1)$$

Where ΔH_{mix} and ΔS_{mix} are the enthalpy and entropy of mixing respectfully. ΔS_{mix} is the change in the level of disorder due to mixing and therefore is always positive. Generally, from equation 2.1, having a large ΔS_{mix} is beneficial for the formation of a solution. However, the materials examined in this thesis such as graphene, are large rigid macromolecules, therefore, ΔS_{mix} is very small and thus, ΔH_{mix} becomes the dominant term that describes solubility in equation 2.1 [65, 143]:

$$\Delta S_{mix} \approx 0 \quad (2.2)$$

$$\Delta G_{mix} \approx \Delta H_{mix} \quad (2.3)$$

Therefore, stable solvent dispersions can only occur if ΔH_{mix} is very small. An expression of ΔH_{mix} for graphene was derived by Hernandez *et al* that relates ΔH_{mix} to the surface energy of the solute and solvent [142], where the surface energy is considered the intersheet bonding energy per unit area. This calculation defines ΔH_{mix} as the difference in energy required to separate all solvent molecules and flakes to infinity and the energy required to form a graphene-solvent dispersion of re-stacked flakes of a different thickness than the original graphite. This gave an approximation for the energy cost of exfoliation per unit volume (V_{mix}):

$$\frac{\Delta H_{mix}}{V_{mix}} = \frac{2}{T_{flake}} (\partial_{graphene} - \partial_{solvent})^2 \phi \quad (2.4)$$

Where T_{flake} is graphene flake thickness, $\partial_i = \sqrt{\gamma_i}$, the square root of the surface energy of graphene and solvent and $\phi = \frac{V_{graphene}}{V_{solvent}}$ is the graphene volume fraction. Similarly for 1D nanomaterials, such as CNT, ΔH_{mix} is given by:

$$\frac{\Delta H_{mix}}{V_{mix}} = \frac{2}{R_{bundle}} (\partial_{CNT} - \partial_{solvent})^2 \phi \quad (2.5)$$

Where R_{bundle} is nanotube radius. From equation 2.4 and 2.5 we can see that ΔH_{mix} is minimised when the nanomaterials and solvents surface energy match,

this explains why these nanomaterials only form stable dispersions in certain solvents. These equations are very similar to the well known Hildebrand-Scratchard equation, the difference being that surface energy takes the role normally occupied by the cohesive energy density in molecular mixtures.[144]

Equation 2.4 implies that stable exfoliation can be achieved by minimising ΔH_{mix} . This method has been very successful in exfoliating a host of low-dimensional nanomaterials [72, 145, 74, 66, 146, 73] by producing solubility curves by sonicating the material in variety of solvents, thus varying surface energy, with the best solvents having a similar surface energy to that of the nanomaterial.

Strictly speaking, these studies measured solubility as a function of solvent surface enthalpy (H) and not solvent surface energy (Gibbs free energy, G). The Gibbs free energy and enthalpy are related by equation 2.1. The reason why these quantities are different is due to entropy (S) and can be thought of like so. In the case of a liquid-gas interface the entropic term comes from the fact that liquid-gas interfaces are disordered, brought on from when molecules go from being condensed (liquid) to gas via a transition region that is more disordered than the liquid. In equation 2.4, the surface enthalpy is used to describe the cost of making a liquid surface which will interface with the nanomaterial's surface. This interface will not (to a first approximation) have the same disorder associated with a liquid-gas interface (e.g. $\Delta S_{mix} \approx 0$). Therefore, the cost of making the liquid-nanomaterial interface is higher than making a liquid-gas interface. Therefore, a solvent's surface enthalpy is given by:

$$H = G + TS \quad (2.6)$$

Where G is the Gibbs surface free energy, i.e. solvent surface tension, T is temperature and S is the solvent surface entropy. Surface entropy is not a commonly quoted solvent property, but it has been shown to be of the order of 0.1 mJ/K for most solvents.[147, 148]

This explains the difference between solvent surface tension and energy used in solubility studies of nanomaterials [72, 145, 74], where, once again, solvent surface energy should really be quoted as surface enthalpy.

Shear Exfoliation Model

As discussed in section 3.5.2, shear exfoliation can be used to scale up production of liquid exfoliated graphene. Paton *et al* found that there was a minimum shear rate ($\dot{\gamma}$), below which very little graphene could be exfoliated.[77] To understand this, a simple model was devised that described the energy required to completely delaminate two platlets, this was found to be related to the surface energy of the material being exfoliated and the solvent and is given by:

$$\dot{\gamma}_{min} = \frac{(\sqrt{\gamma_P} - \sqrt{\gamma_L})^2}{\eta L} \quad (2.7)$$

Where γ_P and γ_L are the surface energy of the platelet and liquid, η is the liquids viscosity and L is the platelet length.

It is clear from this and the previous section that understanding the surface energy of these materials is very important to their exfoliation. Much of this thesis involves measuring and understanding the surface energy of materials like graphite, graphene and BC in order to help understand their exfoliation. Therefore, the origins and types of surface energy are explored in the next section.

2.7 Surface Energy

Surface energy is a fundamental property of solid materials, it is a measure of the difference in energy between surface and bulk atoms/molecule in a material. Surface atoms need to have a higher energy than bulk atoms in order to form a stable interface or surface; the excess energy is due to the fact that all bulk atoms are bonded to each other to minimise their energy, whereas surface atoms have a number of unfulfilled bonds. Take the example in figure 2.12, each bulk atom is bonded to six other atoms whereas surface atoms are bonded to less, meaning they have a number of unsatisfied bonds; this leaves the surface atoms at a higher energy state than the bulk. Another way of defining surface energy is the amount of work required to create a new surface, i.e. breaking the bonds in a material to create two new surfaces. Surface energy is an important property to understand as it dictates how materials interact with their environment.

The surface energy of a material, γ , is generally divided into two components:

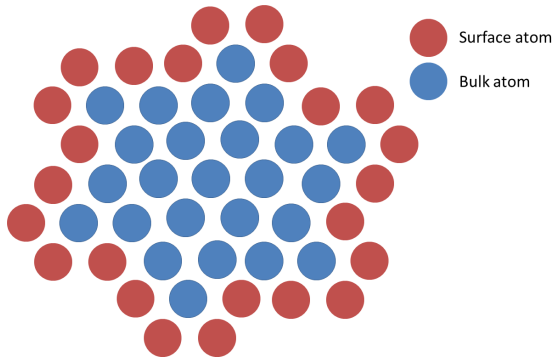


Figure 2.12: Differences between surface and bulk atoms. Bulk atoms are surrounded by 6 nearest neighbours whereas surface atoms are surrounded by less, therefore have unfulfilled bonds and hence a higher energy; this excess energy is defined as the surface energy.

The dispersive surface energy (γ_d), due to London dispersive force part of the Van der Walls interactions [149] and specific surface energy (γ_{sp}), due to all other types of intermolecular forces including the Debye induction force [149] (induced dipole), Keesom [149] (permanent dipole-dipole) and hydrogen bonding.[150] Knowledge of both components is important for many materials where both dispersive and specific interactions contribute to its surface properties, such as bacterial cellulose, but there are also materials whose surface properties are due to mainly dispersive interactions, as is the case for graphite and graphene.

As stated, γ_d is due to London dispersive forces between different molecules. The force arises from the spontaneous uneven distribution in electron density causing instantaneous polarisation of non-polar molecules. This in turn can induce polarisation in neighbouring atoms, causing them to be attracted to each other as shown in figure 2.13 A & B. The nature of the London dispersive component of the Van der Waals interaction can be described very well by the Lennard-Jones potential, a simple model that describes the interaction between neutral molecules and is given by:

$$V(r) = 4\epsilon \left[\left(\frac{\sigma}{r} \right)^{12} - \left(\frac{\sigma}{r} \right)^6 \right] \quad (2.8)$$

Where V is the Lennard-Jones potential, ϵ is the potential well depth, σ is the distance where inter particle potential is zero and r is the separation between

molecules. From equation 2.8, we can see that there are two components to this potential; the attractive and repulsive. The repulsive component results from the Pauli exclusion principle that stops the collapse of the molecule, while the attractive component is due to the London force as discussed. Figure 2.13C shows a typical Lennard-Jones plot. At large r , say >5 nm, there is very little attraction between molecules but as r decreases, they start to feel an attraction until they reach a minimum r , r_{min} . r cannot get any smaller due to the very strong, short range repulsive force. The London force is universal in all chemical groups/interactions and usually represents the main part of the total interaction force between molecules, even though they are weaker than specific interactions.[151, 152, 153] The magnitude of the London force scales with molecular weight due to the increased polarisability of large molecules, i.e. large molecules have more electrons that can add to the degree of non-uniform electron density distribution. This is seen in IGC measurements with the retention time of nonane being several multiples larger than smaller molecules, such as hexane.

The specific surface energy (γ_{sp}) is due to mainly polar interactions from permanent dipole-dipole and permanent dipole-induced dipole interactions and hydrogen bonding. Polar interactions originate from the electrostatic interactions between permanent dipoles due to the uneven distribution of electrons between atoms in a molecule. This occurs when the two atoms have substantially different electronegativity, where one atom attracts electrons more than the other. Figure 2.14A shows an example of a polar interaction, where two polar materials are attracted to each other. Sometimes, polar molecules can induce a dipole in non-polar media depending on its polarisability. Figure 2.14B shows a polar molecule coming close to a non-polar molecule, as they get closer electrostatic repulsion/attraction distorts the non-polar molecules electron cloud, causing it to polarise and hence, they are attracted to each other; this is also known as the Debye force.

A special case of polar interactions are hydrogen bonds, that differ from regular polar interactions due to their strength, being directional (a feature seen in covalent bonds) and produce smaller inter-atomic distances than Van der Waals interactions.[154, 155, 156] Hydrogen bonds are due to the attractions between groups when a hydrogen atom is bound to the highly electronegative atoms nitrogen, oxygen and fluorine. One of the best examples of this is in water molecules as

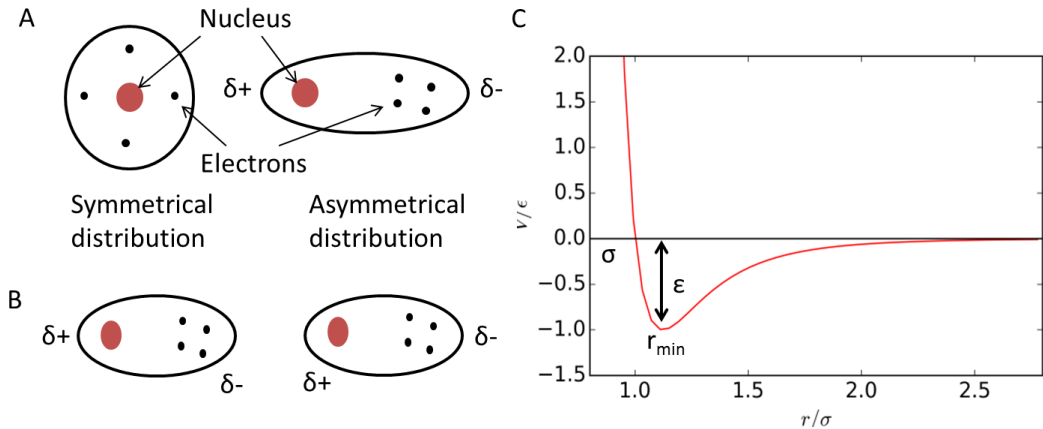


Figure 2.13: The London dispersive force. A) A non-polar molecule with symmetrical distribution of electrons, sometimes this distribution can become asymmetric, leading to the spontaneous polarisation of the molecule. B) The spontaneously polarised molecule can induce polarisation in nearby molecules causing them to be attracted to each other. C) Lennard-Jones potential that describes the attractive and repulsive component of the Van der Waals interaction. At long distances (>5 nm), adjacent molecules feel no attraction but as they get close they begin to attract each other by the London force until they feel repulsed at short distances due to the Pauli exclusion principle. As a result, there is minimum separation value at the point where the two components balance; called r_{min} .

shown in figure 2.14C. Since oxygen is very electronegative, the shared electrons are more likely to be situated closer to it than the hydrogen atoms. This leaves the hydrogen nucleus practically exposed from the effects of the electrons; this is why hydrogen bonds are typically stronger than other polar interactions, since polar molecules will still feel some shielding effects of electrons. This effectively causes the oxygen atoms to be negatively charged with the hydrogen atoms being positively charged, therefore, the molecules form bonds between adjacent oxygen and hydrogen in the form of hydrogen bonds. The presence of hydrogen bonds has great effects on materials; they explain why water has a higher boiling point compared to similar molecules without hydrogen bonding.

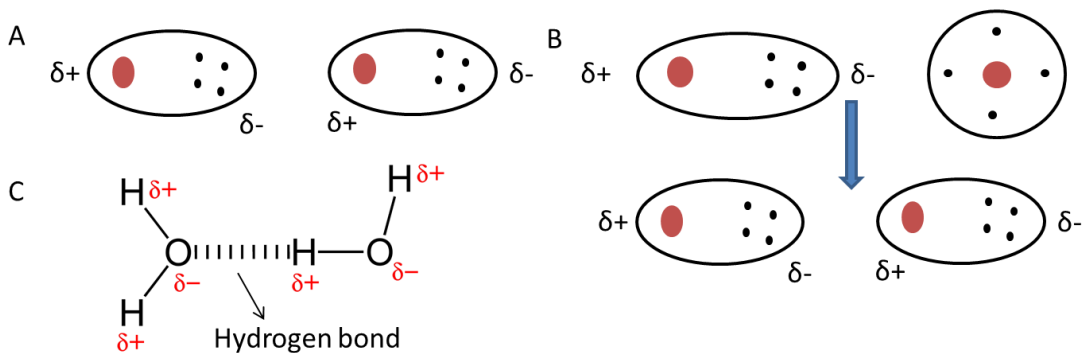


Figure 2.14: Types of specific interactions. A) polar interaction (permanent-permanent dipole). B) Polar material comes near a non-polar material and induces polarisation of that material causing electrostatic attraction between them. C) Hydrogen bonding in water. Due to the high electronegativity of oxygen, this leaves it practically negatively charged with the hydrogen positively charged. This causes the attraction between water molecules in the form of hydrogen bonds.

2.7.1 Surface Energy Measurements

This section explores some of the common methods of measuring surface energy from the literature, specifically inverse gas chromatography, contact angle and atomic force microscopy. A brief overview of each method is given, with their advantages and disadvantages considered.

Inverse Gas Chromatography

Inverse gas chromatography (IGC) is a gas vapour sorption technique that injects known probe solvents into a column containing the sample being investigated. The injected probes adsorb and desorb on and off the sample surface by dispersive and specific interactions; the time taken for the probes to elute through the column is used to calculate the samples surface energy. The theory and methods involved in IGC are discussed in detail in section 3.2. IGC is a versatile technique that is applicable to all types of materials, from powders to fibrous materials, porous and non-porous materials and surfaces with irregular topographies and inhomogeneities.[157] This gives IGC a clear advantage over contact angle and AFM as they generally require a flat, smooth surface to perform measurements. Traditionally, IGC was carried out at infinite dilution, where only minute

amounts of probe solvents are injected into the column. The main criticism of this method is that it only measures the highest energy sites on the surface; therefore, it isn't representative of the whole surface, giving inflated surface energy values in comparison to contact angle.[158, 159, 160]

This problem was addressed by the latest generation of IGC, called the surface energy analyser (SEA) which allows for the precise control of the amount of probe injected into the column, allowing the measurement of the surface energy heterogeneity of samples by controlling injected surface coverage.[161, 162, 163] This is illustrated in figure 2.15, showing how particular surface values are achieved; this depends on both the size of the probe molecule and the surface area of the sample. By injecting small amounts of probe that correspond to low surface coverage, it is possible to measure the infinite dilution surface energy; the surface energy due to the highest energy sites, due to the presence of defects on the sample surface.[164, 165] Coverage dependent IGC can also measure surface energy at higher coverage (finite dilution), which gives a more representative description of the samples surface energy since it covers more of the surface, giving access to lower energy sites in comparison to infinite dilution. The surface energy values measured using this method generally agree well with contact angle for this reason.[166, 167, 168, 169]

Contact Angle

Contact angle is another commonly used method to measure the surface energy of materials. It involves the measurement of the angle a known liquid makes with a solid film, i.e. the solid liquid interface. This can be described by Young's equation:

$$\gamma_{lv} \cos \theta_Y = \gamma_{sv} - \gamma_{sl} \quad (2.9)$$

Where γ_{lv} , γ_{sv} , γ_{sl} are the liquid-vapour, solid-vapour and solid-liquid interfacial surface energies respectfully, with θ_Y being the contact angle.

The contact angles of various solvents (dispersive and specific) are used to calculate the different components of the surface energy and therefore, the total surface energy can be calculated using the Neumann [171, 172], Fowkes [153] and

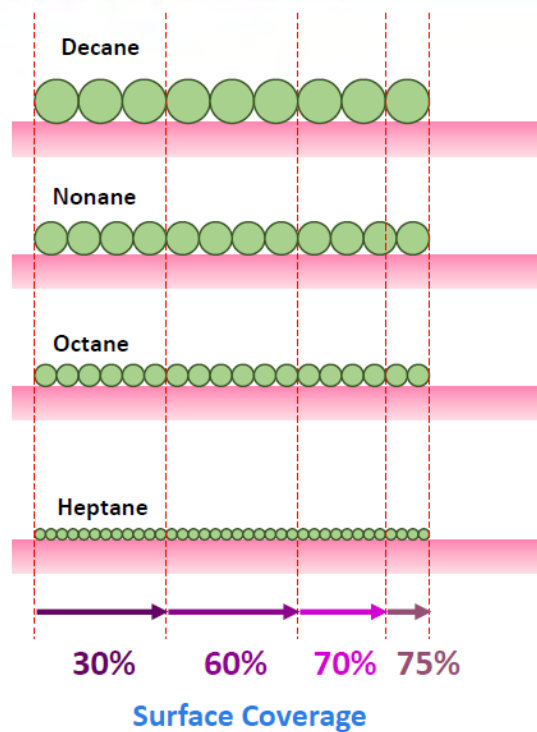


Figure 2.15: The surface coverage of various probe solvents. Knowing the specific surface area of the sample and probe means it is possible to inject amounts of probe that correspond to surface coverage.[170].

Owen-Wendt models.[173] Contact angle is also widely used for measuring wettability, for example, is a material hydrophobic or hydrophilic. Wettability and surface energy are linked as shown in figure 2.16; hydrophobic materials will exhibit a large contact angle due to having low surface energy. As the surface energy increases, the contact angle decreases and the droplets wet better to the surface. Sometimes, perfect wetting can be achieved with a contact angle of 0° . Here, the liquid-solid interactions are very strong in comparison to liquid-liquid interactions, forming a perfect liquid film on the surface. Altering the behaviour of surfaces has very important consequences. For example, low surface energy materials are used to coat rain jackets; since the jackets surface is coated with a hydrophobic material, rain water has a high contact angle and low wettability, meaning the rain just falls off the jacket, keeping the person dry. On the other hand, complete wetting is desirable for applications such as solution processed OLED's and solar cells where

complete wetting, forming nice films are required.[174, 175, 176]

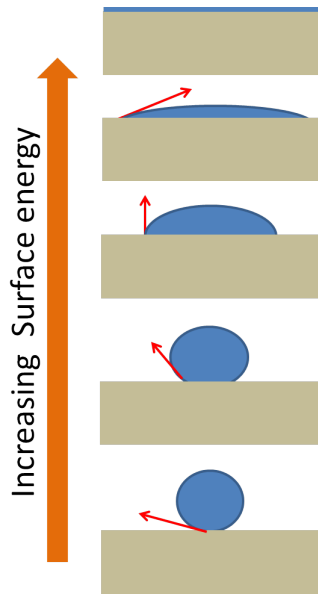


Figure 2.16: Contact angle and wettability as a function of surface energy. Liquid droplets on low surface energy surfaces have a high contact angle. As a result, the droplets don't wet to the surface. As surface energy of the surface increases, the contact angle decreases and wetting increases until the contact angle is zero, i.e. the liquid fully wets the surface.

One of the advantages of contact angle for measuring surface energy is that it is a widely used, relatively simple experiment that doesn't require expensive specialised equipment. However, it has substantial drawbacks; the method is only really suitable for smooth, flat surfaces. This rules out using it for powders, such as pharmaceutical materials and flaked particulates, like materials used in this thesis (graphite). Also, surface energy measurements from contact angle give a single, full coverage energy value. While being very useful, it doesn't fully reflect the energetics of the surface. This is a somewhat similar but opposite problem to that experienced with infinite dilution IGC, where it only measures the highest energy sites. Due to these differences, contact angle and ID-IGC often give dramatically different results.[177, 158, 157, 178, 179] This is why coverage dependent IGC is used in this thesis as it can measure both the infinite and finite dilution (similar result to contact angle) surface energy simultaneously by producing surface energy profiles.

Atomic Force Microscopy

Another method used to measure surface energy is by using atomic force microscopy (AFM). AFM is primarily used for imaging (as is the case for this thesis and is described in section 3.4.3) but it can also be used for measuring the adhesive forces between the AFM tip and sample surface. Surface energy is measured by measuring the force required to remove the tip from contact with the surface; this force can be related to the thermodynamic force of adhesion, which in turn is related to the surface energy of the material.[180, 181, 182, 183, 184] The drawbacks to this method are that it only provides a local measurement of the surface energy at that specific point on the surface. Therefore, many points have to be measured to get statistical significant values. This is a very time consuming and often expensive process. On the other hand, surface dependant IGC measures large numbers of flakes, powders and particulates simultaneously. AFM, like contact angle, is best preformed on smooth flat surfaces and therefore isn't very good for materials such as graphite. Surface energy mapping by AFM is possible but in reality isn't very practical due to data scatter and time taken to preform measurements.

For these reasons, coverage dependence IGC is the preferred method for measuring the surface energy of heterogeneous, low dimensional nanomaterials such as the ones characterised in this thesis; graphite, graphene and bacterial cellulose.

Chapter 3

Methods and Theory

3.1 Overview

This chapter explores the methods and some of the underlying theories used in this thesis to characterise the surface energy of various nanomaterials. Inverse gas chromatography is explained in detail, specifically: how it works, the methods used to calculate dispersive and specific surface energy and specific surface area of materials. Two methods used to exfoliate materials, sonication and shear mixing are described, along with how dispersions can be controlled by centrifugation. Other characterisation techniques used are introduced, such as: transmission and scanning electron microscopy, atomic force microscopy, Raman and absorption spectroscopy. The theory and methods involved in tensile testing are also examined as it was used to characterise the tensile properties of bacterial cellulose nanofibril films.

3.2 Inverse Gas Chromatography

Inverse gas chromatography (IGC) was extensively used throughout this thesis to characterise the surface energy and specific surface area (S_{BET}) of materials. IGC is a gas sorption technique where known probe solvents are injected into a glass column containing the sample. This is in contrast to traditional gas chromatography (GC), where a known stationary phase is used to separate compounds of a

mixture as shown in figure 3.1. The time taken for the probe to elute through the column, where probe molecules adsorb and desorb off the sample surface is used to calculate many surface and bulk properties of a material including surface energy and S_{BET} .

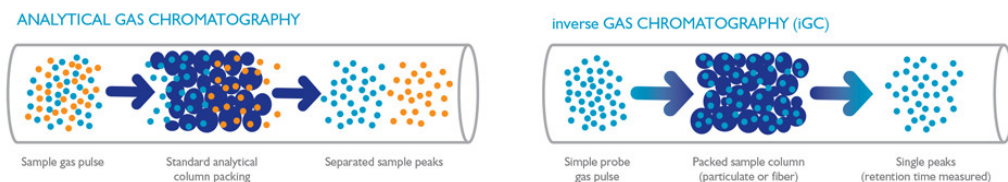


Figure 3.1: Differences between GC and IGC. GC uses a known stationary phase to separate compounds of a mixture while IGC uses known probe molecules to characterise a solid sample. Reproduced from [185]

3.2.1 Theory

All quantities calculated using IGC come from the measurement of the retention time t_r , that is the time taken for the probe to elute through the column. Traditionally, in the literature, experiments have been conducted under two chromatographic conditions. They are infinite dilution IGC (ID-IGC) and finite dilution IGC (FD-IGC). ID-IGC typically involves the injection of minute amounts of probe into the column where it is assumed that there are no probe-probe interactions due to the extremely low concentration of injected solvent.[186] Generally, the chromatograms (elution curves) are symmetric in nature (Gaussian) under these conditions.[187] FD-IGC involves the injection of a known probe concentration where usually the elution curves begin to tail and become asymmetric.[188] Since the SEA, the type of IGC used in this thesis can precisely control the amount of probe injected, it can measure in both the ID (low surface coverage region) and FD (high surface coverage region) in one experimental run. This is particularly advantageous here, since the materials studied in this thesis are extremely energetically heterogeneous [189], meaning there will be a range of surface energy values corresponding to different energy sites on the sample surface.[190] Using the SEA we can map the surface energetics of a solid by measuring its surface energy

profile.[191] The following sections will describe the theory and methods used to calculate the dispersive surface energy, specific surface energy and S_{BET} of solids.

Retention Time and Volume (t_N and V_N)

As stated, t_r , the retention time is the fundamental measurement in IGC. Figure 3.2 shows two sample elution curves, figure 3.2A shows an elution curve taken at low surface coverage (infinite dilution). In the infinite dilution range, we are in the Henry's law region of the isotherm where the amount adsorbed scales linearly with amount of probe injected.[192] For this type of elution curve, t_r is simply the time taken at max flame ionising detector (FID) signal. Figure 3.2B shows an elution curve at higher surface coverage (finite dilution). The curve is quite asymmetric due to 'tailing' which is due to the rate of change in the amount of probe adsorbed decreasing with amount injected. As a result, there is an additional complication in measuring t_r . In addition to the peak max method, there is the peak centre of mass method (peak COM). Often peak max and COM times can vary considerably; if this is the case peak COM is generally preferred since it is more representative of the interactions of the probe and sample than peak max.[193] Peak COM is calculated by:

$$t_{r,COM} = \frac{\sum(I_{FID}t)}{\sum I_{FID}} \quad (3.1)$$

where I_{FID} is the baseline corrected FID signal and t is time. t_r is subtracted from the dead time (t_0) as shown in figure 3.2A to get the net retention time ($t_N = t_r - t_0$). t_0 is the time taken for a non-interacting probe (methane) to elute through the column. This is done to insure that the retention time is only due to molecular interactions between the probe and sample.[194]

The specific net retention volume (V_N), a measure of the amount of carrier gas needed to elute the probe through the sample column and is calculated from t_N by:

$$V_N = \frac{j}{m}(t_r - t_0)F\frac{T}{273.15K} \quad (3.2)$$

Where m is the sample mass, F is the carrier gas flow rate, T is the temperature and j is the James-Martin correction factor [195] which corrects V_N by taking the compressibility of the gas and variation in packing density in the column into

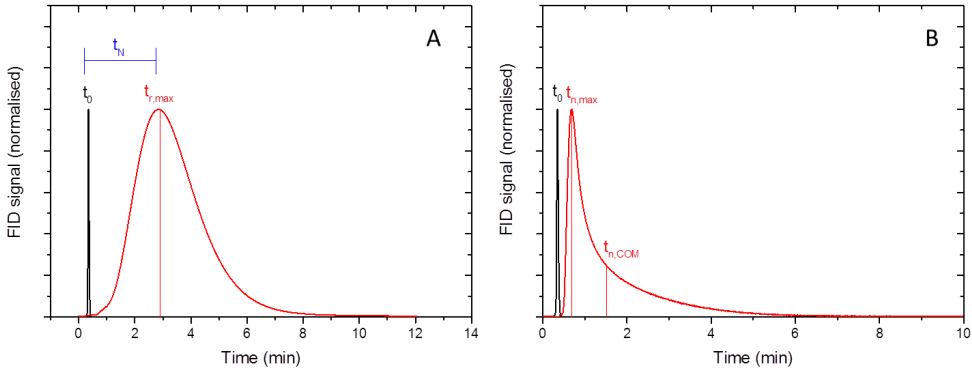


Figure 3.2: Sample elution curves at A) low coverage (infinite dilution) and B) high coverage (finite dilution) with the dead time (t_0) elution curve. The net retention time (t_N) is the difference between t_r and t_0 , where t_r is measured either using the peak max or peak COM method

account. [196] It is calculated by:

$$j = \frac{3}{2} \left[\frac{(p_{in}/p_{out})^2 - 1}{(p_{in}/p_{out})^3 - 1} \right] \quad (3.3)$$

Where p_{out} is atmospheric pressure (760 torr) and $p_{in} = p_{drop} + p_{out}$. p_{drop} is the pressure drop due to the injection measured by the SEA.

3.2.1.1 Dispersive Surface Energy

As discussed in section 2.7, the dispersive surface energy (γ_d) of a solid is due to dispersive Van der Waals interactions caused by London dispersive forces.[197] Two widely used methods for calculating γ_d are the Schultz-Lavielle (referred to as the Schultz method) [198] and Dorris-Gray [199] methods, both of which involve the injection of a series of n-alkanes into the column where it is assumed that they interact with the sample through dispersive interactions only.

Schultz Method

As stated, the Schultz method involves the injection of a series of n-alkane probes into the column. The Gibbs free energy of adsorption (ΔG) between probe and the sample is related to V_N by the thermodynamic relationship:

$$\Delta G = -RT \ln V_N \quad (3.4)$$

Where R is the real gas constant, T is the temperature. In the case of dispersive probes the Gibbs free energy of adsorption and desorption are equal, $\Delta G = \Delta G_{ads} = \Delta G_{des}$. ΔG is related to the thermodynamic work of adhesion (W_{adh}) by:

$$\Delta G = N_a a W_{adh} \quad (3.5)$$

Where N_a is Avogadro's constant and a is the cross sectional surface area of the alkane probe molecule. For dispersive probes, W_{adh} is described by the Fowkes relation [200]:

$$W_{adh} = 2\sqrt{\gamma_d^S \gamma_d^L} \quad (3.6)$$

where γ_d^S is the dispersive surface energy of the solid and γ_d^L is the dispersive surface energy of the liquid (probe molecule). Combining equations 3.4, 3.5 and 3.6 we get an expression relating V_N to γ_d^S :

$$RT \ln V_N = 2N_a a \sqrt{\gamma_d^S \gamma_d^L} + C \quad (3.7)$$

By plotting $RT \ln V_N$ against $a(\gamma_d^L)^{1/2}$, γ_d^S can be calculated from the slope of the line:

$$\gamma_d = \gamma_d^S = \left(\frac{slope}{2N_a} \right)^2 \quad (3.8)$$

An example of a Schultz plot is shown in figure 3.3A.

Dorris-Gray Method

The Dorris-Gray method is similar to the Schultz method in that a series of n-alkane probes are injected into the column and the retention parameters measured. The difference being, γ_d is calculated by measuring the dispersive Gibbs free energy of adsorption between a methylene group and the sample (ΔG_{CH_2}).[199] This is calculated by:

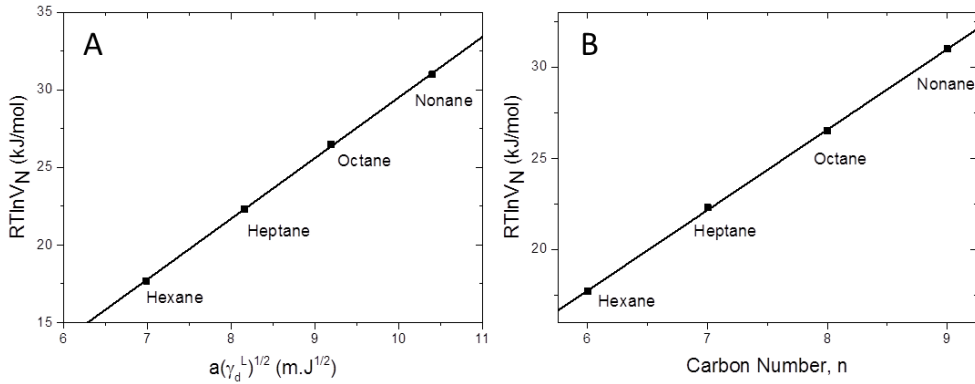


Figure 3.3: A) Example Schultz plot showing the fitted alkane line from Hexane-Nonane and a polar probe. γ_d for this method is calculated by using the slope of the fitted line using equation 3.8. B) Dorris-Gray plot showing $RT \ln V_N$ as a function of n-alkane carbon number. The slope of this line is used in equation 3.14 to calculate γ_d

$$\Delta G_{CH_2} = \Delta G_{n+1} - \Delta G_n \quad (3.9)$$

$$\Delta G_{CH_2} = -RT \ln \left(\frac{V_{N,n+1}}{V_{N,n}} \right) \quad (3.10)$$

Where n is the carbon number of the alkane probe. In a similar fashion to equation 3.5 and using the Fowkes relation (equation 3.6) we get:

$$\Delta G_{CH_2} = -N_a a_{CH_2} W_{CH_2} \quad (3.11)$$

$$W_{CH_2} = 2\sqrt{\gamma_d \gamma_d^{CH_2}} \quad (3.12)$$

Where $\gamma_d^{CH_2}$ is the dispersive surface energy of a methylene group. $\gamma_d^{CH_2}$ is calculated by:

$$\gamma_d^{CH_2} = 35.6 - 0.058(293.15 - T) \quad (3.13)$$

By combining equations 3.10, 3.11, 3.12 and 3.13 and rearranging, we get an expression for γ_d :

$$\gamma_d = \frac{1}{4\gamma_d^{CH_2}} \left[\frac{RT \ln(V_{N,n+1}/V_{N,n})}{N_a a_{CH_2}} \right]^2 \quad (3.14)$$

Where $RT \ln(V_{N,n+1}/V_{N,n})$ is the slope of the n-alkane line from the plot of $RT \ln V_N$ versus carbon number as illustrated in figure 3.3B.

3.2.1.2 Specific Surface Energy

Specific surface energy (γ_{sp}) is the surface energy of a material due to all types of non-dispersive interactions, including polar and hydrogen bonding interactions. Specific interactions are measured by injecting specific probes into the column, i.e. probes that have more than just a dispersive component and measuring the retention data. By carefully choosing the specific probe, it is possible to investigate the magnitude of a type of specific interaction, e.g. H-bonding.

It is difficult to get a direct measurement of specific interactions since these probes will interact with a sample by both dispersive and specific interactions. Therefore, a method to separate the two components must be used. If the Schultz method was used for calculating γ_d then this is relatively straight forward as this method allows both dispersive and specific probes to be displayed on the same scale. Figure 3.4A shows a Schultz plot including a specific probe. In order to measure the specific interactions we need to find the specific component of the Gibbs adsorption energy (ΔG_{sp}) by subtracting the effects of dispersive interactions. This is done by using the fitted n-alkane line as a reference (ΔG_{ref}). By taking the vertical difference between the specific probe's ΔG and ΔG_{ref} we get a value of ΔG_{sp} :

$$\Delta G_{sp} = RT \ln V_{N,sp} - RT \ln V_{N,ref} \quad (3.15)$$

Equation 3.15 is shown graphically in figure 3.3A.

If using the Dorris-Gray method for calculating γ_d there is no analogous method for calculating ΔG_{sp} as there is for the Schultz method since Dorris-Gray method only deals with dispersive probes. Therefore, other methods are required.

The polarisation method is a commonly used to measure ΔG_{sp} when Dorris-Gray was used for calculating γ_d . [194] Here, ΔG_{sp} is measured by plotting $RT \ln V_n$ versus the molar deformation polarisation of the probes (P_D) [150] as shown in figure 3.4B. P_D is an intrinsic characteristic and is independent of the probe [194] allowing them to be shown on the same scale in a similar manner to the Schultz

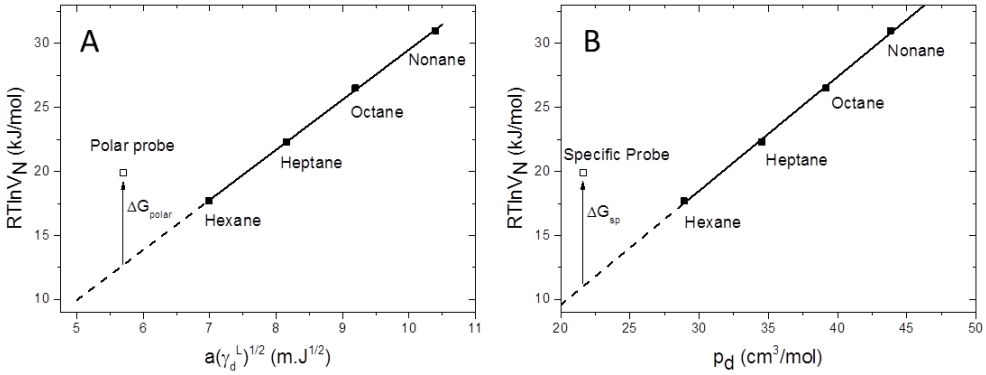


Figure 3.4: Method of calculating ΔG_{sp} using the A) Schultz method and B) Polarisation method

method:

$$RT \ln V_N = CP_D P_{Ds} \quad (3.16)$$

Where P_{Ds} is the deformation polarisation of the solid sample, C is a constant and P_D is given by:

$$P_D \approx \frac{4}{3}\pi N\alpha = \frac{n_r^2 - 1}{n_r^2 + 2} \frac{M}{\rho} \quad (3.17)$$

Where α is the polarisability, n_r is the refractive index, M is the molar mass and ρ is the density of the probe. As stated, this method allows all probe types to be shown on the same scale as shown in figure 3.4B. Therefore, we can apply the sample principle as used previously using the n-alkane line as a reference and using equation 3.15.

The unit of ΔG_{sp} is J/mol which is different to surface energy units, mJ/m^2 . There are several methods available that use ΔG_{sp} data to get γ_{sp} values such as the Van Oss method [201], where ΔG_{sp} can be divided into its Lewis acid (electron acceptor) and Lewis base (electron donor) components by injecting monopolar acid and base probes to find the acid and base components of γ_{sp} . From those values, the components are averaged to find γ_{sp} .

This work primarily deals with measuring the surface energy of graphite and

graphene. These materials surface energy is dominated by γ_d . As a result there are not many γ_{sp} measurements conducted throughout this thesis except in chapter 7 where H-bonding contributes a component of the surface energy of bacterial cellulose. For that work we used a simple method that harmonises the units of ΔG_{sp} (J/mol) to surface energy units (mJ/m^2):

$$\gamma_{sp} = \frac{\Delta G_{sp}}{aN_a} \quad (3.18)$$

Where a is the cross-sectional surface area of the specific probe molecule.[202]

3.2.1.3 Specific Surface Area

The specific surface area of a solid (S_{BET}) can be measured using IGC by injecting increasing concentrations of probe solvent to produce adsorption isotherms. [203] Adsorption isotherms show the relationship between the amount adsorbed (n) during elution of the probe and the partial pressure (p) or relative pressure ($p_{rel} = p/p_{sat}$, where p_{sat} is the saturation vapour pressure of the probe at temperature T) at constant temperature.

Knowing the S_{BET} of our sample is vital to measuring surface energy profiles since surface coverage is calculated from S_{BET}

S_{BET} values measured by IGC usually use octane as the probe molecule since it provides a reasonable compromise between sensitivity to the structure of the sample and retention time.[203] There is no reason why other n-alkanes couldn't be used, infact there can be slight variance in measured S_{BET} due to the different probe molecules depending on size [204] since different probes will have slightly different accessible surface areas. A example of a typical isotherm found in this work is shown in figure 3.5.

n is calculated from V_N by:

$$n = \frac{1}{RT} \int_0^p V_N dp \quad (3.19)$$

Where p is the partial pressure calculated from the chromatograph using:

$$p = \frac{n_i RH_{peak} 273.15}{FA_{peak}} \quad (3.20)$$

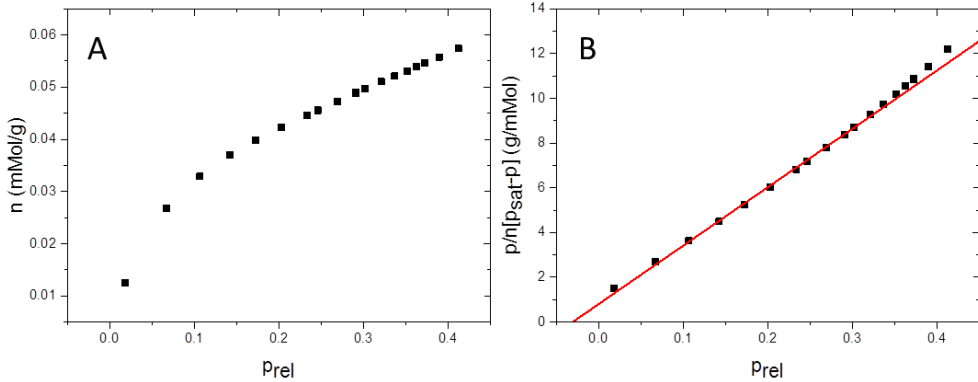


Figure 3.5: A) Typical adsorption isotherm that shows the amount of probe adsorbed onto the samples surface (n) as a function of relative pressure (p_{rel}) at constant pressure. B) BET plot using isotherm data with fitted line in the linear region of the BET range ($0.05 < p_{rel} < 0.35$)

Where n_i is the amount of probe injected into the column, H_{peak} is the FID intensity at the peak, F is the carrier gas flow rate and A_{peak} is the area of the chromatograph. The saturation vapour pressure (p_{sat}) used to calculate the relative pressure (p_{rel}) is calculated using the modified Antoine equation:

$$p_{sat} = \text{Exp}[C_1 + \frac{C_2}{T} + C_3 \ln(T) + C_4 T^{C_5}] \quad (3.21)$$

Where C_1, C_2, C_3, C_4 and C_5 are the Antoine coefficients.

To calculate S_{BET} , the isotherm data is applied to the Brunauer-Emmett-Teller (BET) equation [205]:

$$\frac{p}{n[p_{sat}-p]} = \frac{C-1}{n_m C} \frac{p}{p_{sat}} + \frac{1}{n_m C} \quad (3.22)$$

Where C is the sorption constant which is related to the enthalpy of adsorption of the probe and sample. n_m is the monolayer capacity of the sample. This is the theoretical amount of probe needed to form a monolayer on the sample surface and can be calculated by plotting $\frac{p}{n[p_{sat}-p]}$ against p_{rel} and fitting a line to the linear region of the BET range ($0.05 < p_{rel} < 0.35$) as shown in figure 3.5B. In order to ensure the accuracy of S_{BET} the trendline fit must exceed $R^2 \geq 0.995$. Using the slope and the intercept from this fitting we can calculate n_m :

$$n_m = \frac{1}{\text{slope} + \text{intercept}} \quad (3.23)$$

And n_m is related to S_{BET} by:

$$S_{BET} = N_a a n_m \quad (3.24)$$

Where a is the cross-sectional surface area of the probe molecule.

3.2.2 Equipment

The latest generation of IGC, the Surface Energy Analyser (SEA) made by Surface Measurement Systems, UK was used for all chromatographic measurements in this thesis. The SEA can precisely control the amount of probe injected into the column which allows surface energy measurements at different surface coverages.

The SEA has 12 solvent reservoir, 6 for alkane probe solvents (dispersive) and 6 for specific probe solvents. A photograph of the SEA is shown in figure 3.6A with schematic of the apparatus shown in figure 3.6B. The injection manifold carefully controls the amount of probe injected into the column and helium is used as the carrier gas. The sample is placed in the column and the time taken for the probe to travel through the column, the elution time is measured using a flame ionising detector (FID). The FID is highly sensitive at detecting organic species by measuring the current from the ions produced during combustion of organic molecules by a hydrogen flame as shown in figure 3.6C.

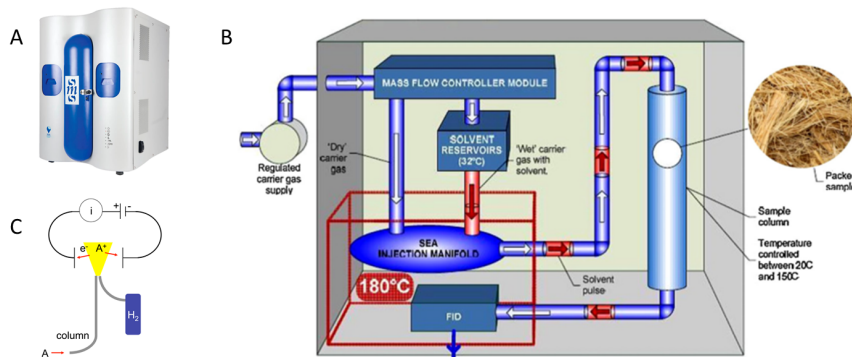


Figure 3.6: A) Photograph of the SEA. B) Schematic of SEA, reproduced from [204] C) FID flow path diagram

3.3 Spectroscopy

3.3.1 Absorption Spectroscopy

Theory

When light interacts with matter, there are several possibilities that can occur; photons can be absorbed by the material, reflected or refracted by an interface between media. Photons can be scattered, both elastically and inelastically; changing the direction of propagation. Absorption spectroscopy is a valuable tool used in this thesis to characterise materials. Absorption occurs when the incident photons' energy matches that of an electronic transition within the sample, causing an electron to be excited to a higher energy state, or when the photons energy matches that of a vibrational or rotational energy mode. For the regions of the spectrum examined in this work, UV (200-400nm) visible (400-700nm) and near IR (700-1000nm) only vibrational and excitation processes occur.

In this work, absorption spectroscopy is used to measure the concentration of nanomaterial dispersed in liquid media, using the Lambert-Beer law. The Lambert-Beer law relates the attenuation of light to properties of the material it is passing through as shown in figure 3.7.

If a beam of monochromatic light passes through a sample, the interaction of the incident light with the sample can be measured by the ratio of the intensity of the transmitted light detected to the incident light intensity.

$$T = \frac{I}{I_0} \quad (3.25)$$

Where T is the measured transmission of light. The Lambert-Beer law states the T decreases as a function of path length (L) such that:

$$I = I_0 10^{-\epsilon L} = I_0 10^{-\alpha CL} \quad (3.26)$$

Where α is the absorption coefficient. For this work, ϵ , the extinction coefficient is a more useful parameter since $\epsilon = \alpha C$, where C is the concentration of material in liquid. Rearranging equation 3.26 it becomes:

$$-\log_{10} \left(\frac{I}{I_0} \right) = \epsilon CL \quad (3.27)$$

This can be simplified further by the definition of absorbance of the sample, $A = -\log_{10} T$. Combining equations 3.25 and 3.27 we get most use statement of the Lambert-Beer law:

$$A = \epsilon CL \quad (3.28)$$

This is illustrated graphically in figure 3.7A.

Equipment

The absorbance measurements carried out in this thesis were done using a Cary Varian 6000i spectrophotometer which functions in the 190-1800 nm range. A schematic of the apparatus is shown in figure 3.7. This tool uses a dual beam system with a tungsten halogen lamp for visible and NIR wavelengths and a deuterium arc for ultraviolet wavelengths.[206] The spectrophotometer consists of a bulb whose beam which is split into two using a half mirror, which scan a reference sample (solvent without any material) and sample simultaneously to give a baseline corrected spectrum.

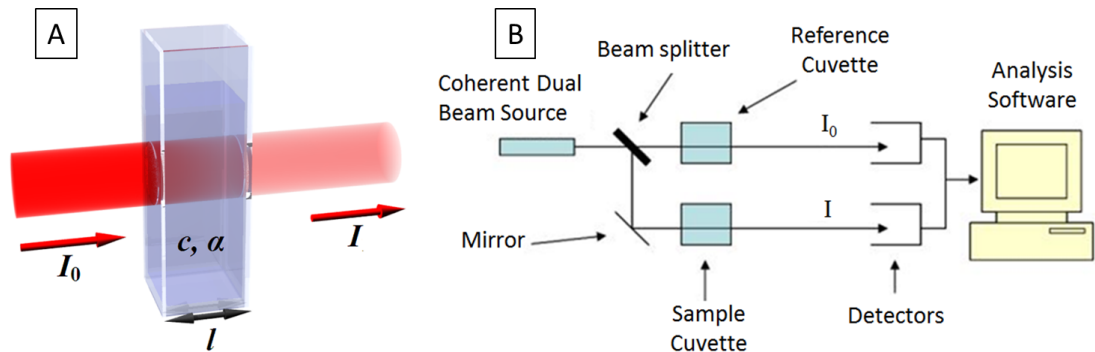


Figure 3.7: A) Illustration of the Lambert-Beer Law reproduced from [207] B) Schematic of Cary Varian 6000i reproduced from [208]

3.3.2 Raman Spectroscopy

Theory

Raman spectroscopy is a light scattering technique where incident photons (usually from a laser source) are scattered inelastically by phonons. This is in contrast to Rayleigh scattering (elastic scattering), where the scattered photon have the same energy as the incident photon, i.e. no energy is lost in the process. Almost all incident photons will be Rayleigh scattered, but a very small percentage of them will be inelastically scattered. The amount of inelastically scattered photons is proportional to the polarisability of the molecule.

Raman scattering occurs when a incident photon interacts with the electric dipole of the molecule resulting in the excitation of the ground state (the lowest rotational and vibrational energy level of the ground electronic state) to an excited virtual energy state. After a very short period of time in this state, an inelastically scattered photon is emitted. The inelastically scattered photon can have a lower energy (Stokes shift) or a higher energy (anti-Stokes shift) than the incident photon as shown in figure 3.8. After the scattering process the molecule of interest will be in a different rotational or vibrational state than before the interaction. The difference in the energy between the two states is equal to the energy difference between the incident and scattered photons.

Raman Spectroscopy of Graphite and Graphene

Raman Spectroscopy is a powerful tool for the characterisation of graphitic materials such as graphite [209], carbon fibers [210], carbon nanotubes [211] and graphene.[212] Raman spectroscopy is particularly useful in the characterisation of graphene as it is often used to determine length [213], number of layers [213, 214] and defect density.[215] Typical Raman spectra for graphite and graphene are shown in figure 3.9A.

The most intense peak in the graphite/graphene spectrum is the so called G-peak ($\approx 1580 \text{ cm}^{-1}$), it was first discovered in graphite [209] but is found in all sp^2 carbon systems.[214] It is due to inplane sp^2 C-C stretching mode and originates from phonons at the Γ point in the centre of the first Brillouin zone.

The next largest peak is the 2D-peak which is very important in graphene as

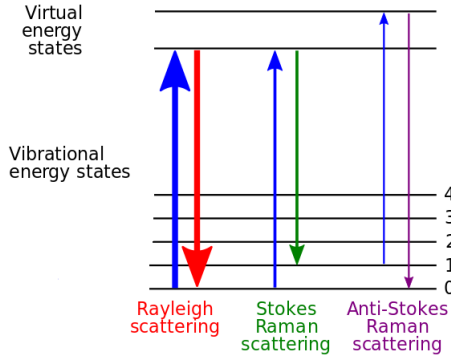


Figure 3.8: Energy level diagram showing the 3 possible scattering processes. Rayleigh scattering occurs when the incident and scattered photons have the same energy, accounting for almost all scattering events. Stokes scattering, where the scattered photon has a lower energy and anti-Stokes scattering, where the scattered photon has a greater energy than the incident photon are the possible Raman scattering interactions.

it gives information as to how many layers are present in a graphene nanosheet as discovered by Ferrari *et al* in 2006 [216] and shown in figure 3.8B. This figure shows that for graphite, the 2D-peak is made of 2 sub-peaks while single layer graphene consists of one sharp peak at 2640 cm^{-1} . This variation of the 2D-peak with nanosheet thickness was taken advantage of by Backes *et al* to define an empirical Raman spectroscopy graphene thickness metric for liquid exfoliated graphene [213] given by:

$$\langle N \rangle = 0.83e^{3.6M} \quad (3.29)$$

$$M = \frac{[I_{\omega_1}/I_{\omega_2}]_{G,ene}}{[I_{\omega_1}/I_{\omega_2}]_{G,ite}} \quad (3.30)$$

Where $\langle N \rangle$ is the mean nanosheet thickness in layers, $\omega_1=2720\text{ cm}^{-1}$ is the 2D-peak position in graphite and $\omega_2=\omega_1 - 30=2690\text{ cm}^{-1}$

The next peak of interest is the disorder induced peak (D-peak), the D-peak gets its name from the fact that it is only there in the presence of defects. The D-peak is a first order process unlike the 2D-peak; making it a one phonon process. Therefore, the energy shift is half that the 2D-peak. A defect in graphite/graphene is defined as any breaking of the symmetry in the graphene lattice, such as vacancy

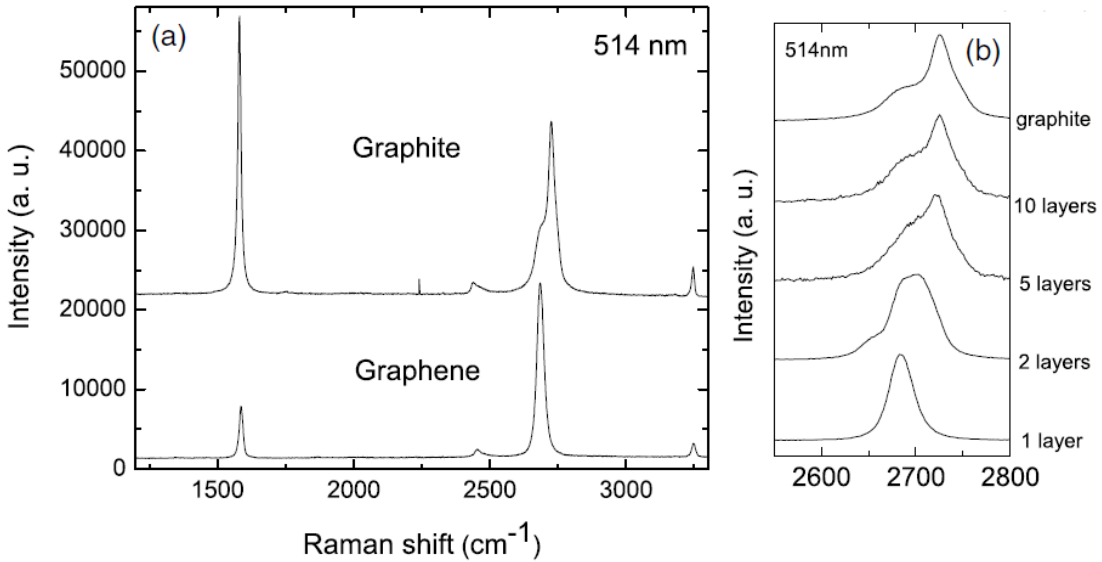


Figure 3.9: A) Raman spectra of graphite and graphene using a 514nm laser. B) 2D peak of graphite to single layer graphene showing the variation of the peak with number of layers. Graphite's 2D peak consists of 2 sub peaks with the creation of a shoulder at 2690 cm^{-1} while graphene has a single 2D peak. Modified from [216]

sites [217], sp^3 -defects [218], grain boundaries [219] and importantly edges.[215] Backes *et al* also devised an empirical mean flake length metric for liquid exfoliated graphene by using the (I_D/I_G) [213] but it is not explicitly used in this thesis. There are also minor peaks such as the D' peak (1620 cm^{-1}) which can appear in defective graphite/graphene.

Equipment

All Raman spectra were carried out using a Horiba Jobin Yvon LabRam HR800 spectrometer with a 532 nm excitation laser under ambient conditions. To avoid sample overheating and damage measurements were carried out at 10% laser power (2 mW). The spectra were taken using a 600 mm^{-1} diffraction grating, a 100X optical lens and a optical notch filter was used to remove the Rayleigh scattered light. The spectrometer was calibrated by using either a Silicon or HOPG (highly oriented pyrolytic graphite) source before measurements were taken.

Two main methods were used for spectra capture, single spectra capture and

Raman mapping. Raman mapping involves measuring many spectra over a defined area and getting an average spectrum for a sample.

3.4 Microscopy

3.4.1 Transmission Electron Microscopy (TEM)

Transmission electron microscopy (TEM) is a microscopy technique in which a beam of electrons is transmitted through the sample. As the electrons pass through the sample, they interact with it and form an image on a screen or CCD camera. TEM has been extensively used for the characterisation of nanomaterials such as graphene.[7] High resolution TEM has been able to get atomic resolution showing the hexagonal graphene structure as well as individual atoms such as dopants on the surface.[220] In this work TEM was used for measuring the physical dimensions of nanomaterials by statistical analysis.

The need to use TEM and more generally electron microscopy instead of optical methods is due to the diffraction limit. The diffraction limit states that the smallest object that can be resolved is proportional to the wavelength examining it, this can be approximated to $d \approx \frac{\lambda}{2}$, where d is the diffraction limit and λ is the sources wavelength. This means that for visible light (400-800 nm), the theoretical minimum resolved image is about 200 nm but in practise it is larger due to aberrations. This can be overcome using electrons, thanks to their wave-like properties, where the wavelength of an electron is given by the de Broglie wavelength:

$$\lambda = \frac{h}{p} = \frac{h}{mv} \quad (3.31)$$

Where λ is the electron wavelength, h is Planck's constant, p is the electrons momentum, m is electron mass and v is electron velocity. This means that the electrons wavelength can be controlled by a applied voltage, V :

$$eV = \frac{1}{2}mv^2 \quad (3.32)$$

where e is the electron charge. This leads to an expression for electron wavelength in terms of applied voltage:

$$\lambda = \frac{h}{\sqrt{2meV}} \quad (3.33)$$

This expression has to be modified for relativistic effects at high V:

$$\lambda = \frac{h}{\sqrt{2m_0eV \left(1 + \frac{eV}{2m_0c^2}\right)}} \quad (3.34)$$

Using 100 keV as an example, the theoretical resolution limit is ≈ 2 pm. Although, in reality, this is a lot lower due to aberrations in the magnetic lenses.

TEM Operation

There are 4 main parts to a standard TEM. They are the electron source, the electromagnetic lenses, the sample holder and the imaging system as shown in figure 3.10A. A coherent beam of electrons is emitted by thermionic emission from a heated filament (usually Tungsten or LaB₆) and are accelerated by a voltage through the TEM column according to equation 3.33. The beam then passes through a number of magnetic lenses, known as the condenser lens that focuses the beam before passing through the sample. The electrons interact with the sample through a variety of processes and are then focused as they pass through the objective lens on their way to the projector lens then the CCD. The interactions with the sample are measured by changes to the electron energy from the initial energy and the angles the electrons have been deflected. A schematic and image path of a standard TEM is shown in figure 3.10B.

As stated, when electrons interact with the sample there are a number of possible outcomes as shown in figure 3.11. There can be energy loss electrons where incoming electrons excite a core electron in the sample, reducing its energy which is then measured. The energy difference can provide details of the elements present in the sample. Zero-loss or small angle scattered electrons are used in bright field imaging, the most commonly used imaging technique. Here, image contrast is directly due to the absorption of electrons by the sample where thicker regions or regions of higher atomic number appear darker, while regions with no sample appear bright in the image. Diffracted or high angle scattered electrons, where the electrons undergo Bragg scattering causes electrons to disperse into discrete

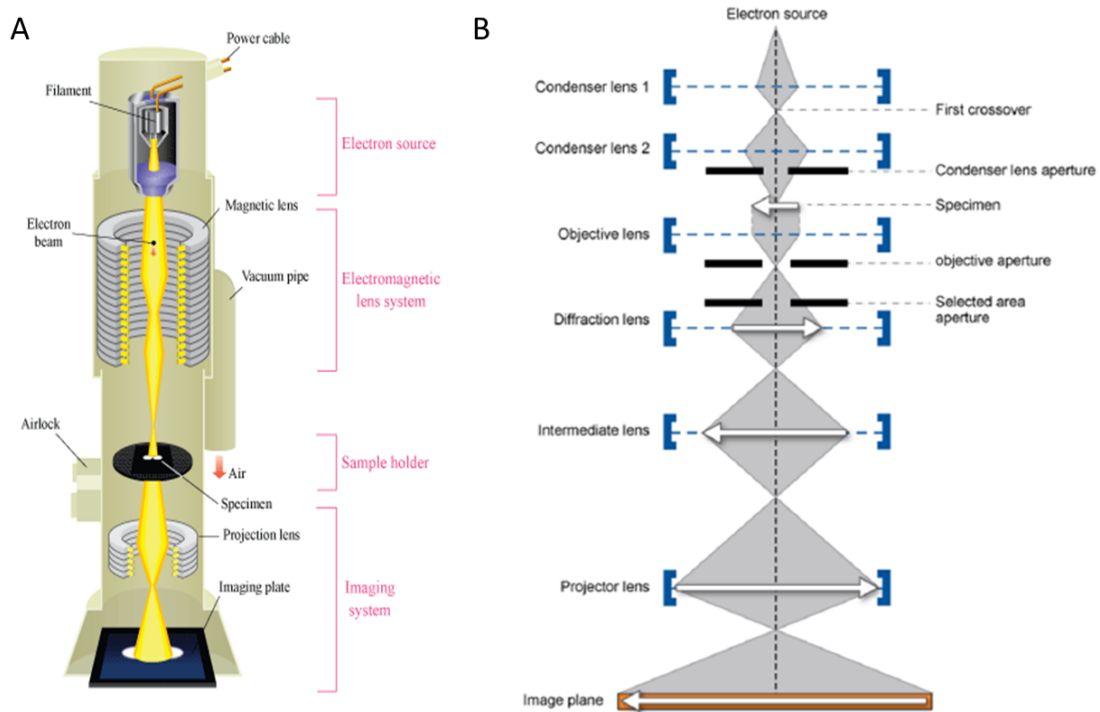


Figure 3.10: A) Schematic of TEM showing the main components. B) Electron beam path in a TEM showing the lenses and apertures used to focus the beam

locations on the back focal plane creating a diffraction patterns in crystalline samples. This can be achieved by either moving the objective aperture or by tilting the incident beam angle. This method is particularly useful for characterising the crystallographic structure of a sample.

Equipment

TEM images for this thesis were carried out on a Joel2100 TEM system which operates up to 200 kV. It uses a LaB₆ source that can operate between 80-200 kV with a maximum contrast resolution of 0.31 nm. The specimen holder could hold 5 samples in the column

Sample preparation and measurement

Samples were prepared by drop casting a few mL of dispersion onto a holey Carbon grid (CU 400 mesh) and were vacuum dried overnight to remove residual solvent.

Images were initially taken at low magnification (5000X) to survey the sample

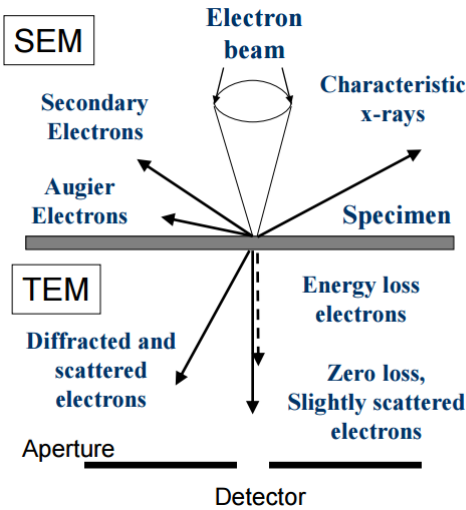


Figure 3.11: Possible electron-sample interactions in TEM and SEM. Reproduced from [208]

to see roughly how uniform the sample is, then images at higher magnification (20000X) were taken for nanosheet measurement. The exact magnification varied from sample to sample.

Statistical analysis of TEM images were done using the software ImageJ to measure the length and width of the nanosheet. The length was defined as the longest dimension of a sheet and the width was measured perpendicular to the length. A large number of samples need to be measured to get representative statistics of the sample (>100 counts).

3.4.2 Scanning Electron Microscopy (SEM)

Theory

Scanning Electron Microscopy (SEM) is a widely used method of imaging materials, both conductive and non-conductive, that gives high resolution images of solid samples that are easy to obtain. In this thesis, SEM was used to measure the dimensions of commercially available graphite. SEM is similar to TEM in that electrons are produced by thermionic emission and are accelerated and focused by electromagnetic lenses onto the sample as shown in figure 3.12A. However, this is

where the similarities end. SEM is used on thick solid samples where the electrons are not transmitted. The primary processes involved in SEM image formation used in this thesis are due to secondary and back scattered electrons.

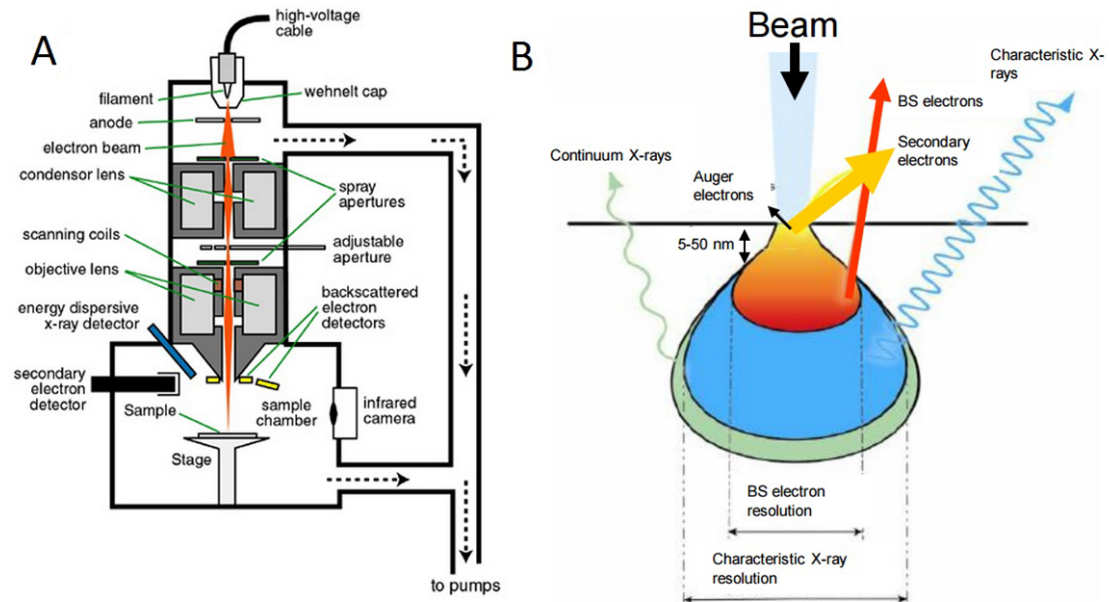


Figure 3.12: A) Schematic of a typical SEM showing the electron gun, apertures, objective lens, the different detectors each type of signal. B) SEM interaction volume showing the penetration depth of each type of beam-sample interaction. Modified from [208]

SEM images result from interactions with the electron beam and the atoms of various depths, depending on the signal source as shown in figure 3.12B. The most common imaging mode is from secondary electrons that are produced by the ejection of electrons from the sample surface due to the incoming electrons. These secondary electrons have a far lower energy, around 3-5 eV [221] resulting in a small escape depth of a few nanometers.[222] This gives secondary electrons excellent surface sensitivity and a resolution around 1 nm.

Backscattered electrons are also used for imaging, these are electrons that have been elastically scattered from the sample, as a result they have very high energies and emerge from deeper within the sample. This makes them less surface sensitive and have a lower resolution than secondary electrons.[221] However, the backscattered electrons are often used in analytical SEM because the intensity

of the backscattered signal depends on the atomic number of the atoms in the surface, giving rise to contrast differences between different elements in the sample. This is often used as a complementary method along with spectra made from characteristic X-rays to characterise the elemental make up of a sample. It should be noted that if the sample is non-conductive it should be coated by something metallic to prevent the build up of charge on the surface which causes excessive brightness and image distortion.

Equipment

SEM images were acquired using a Zeiss Ultra Plus SEM with a LaB₆ source and a accelerating voltage of 5 kV. Images were obtained by using a SE2 sensor that detects the secondary electrons.

Sample Preparation

Small amounts of sample were applied to a SEM stab using sticky Carbon tabs. No coating was required as all samples used were conductive.

3.4.3 Atomic Force Microscopy (AFM)

Theory

Atomic force microscopy (AFM) is a scanning probe technique that maps the topography of a surface by measuring the forces between a sharp tip and the sample surface.[223] The force interactions deflect the tip as it passes over the sample, the deflections are measured by using a laser and photo diode to produce an image/map of the sample surface. A schematic for a standard AFM is shown in figure 3.13A. The major components of an AFM are the tip, cantilever, piezoelectrics, laser and photodiode. The basic operation involves the tip and cantilever positioned very close to the sample (a few nanometers). At these distances, the tip can be attracted to or repulsed by the sample. These forces cause the cantilever to deflect, which can be measured using the laser and photodiode. The tip cantilever position change is used to form the image that can have a resolution of 0.1 nm in the z-direction (height), making it ideal for measuring the diameter of bacterial cellulose nanofibrils.

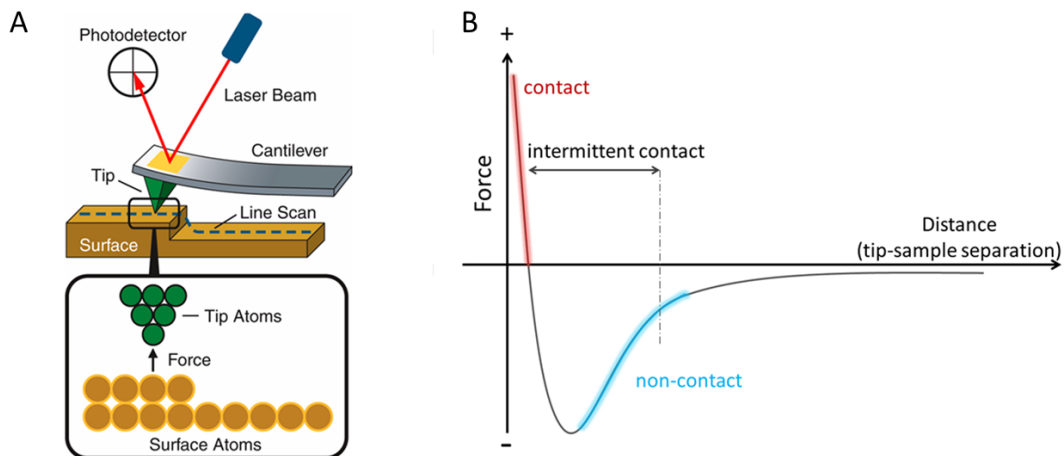


Figure 3.13: A) AFM schematic. B) Lennard-Jones potential

Van der Waals forces govern the interactions at the length scales involved with AFM, these attractive forces are interactions between molecules that leave their chemical identities unaltered. Repulsive forces, that prevents the complete collapse of matter due to the Pauli exclusion principle are also experienced by the tip at very short distances to the sample. This interaction can be modelled by assuming that one atom, say at the apex of the tip interacts with a particle at the surface. As their separation (r) changes so does the potential energy, which can be described by the Lennard-Jones potential:

$$V(r) = 4\epsilon \left[\left(\frac{\sigma}{r} \right)^{12} - \left(\frac{\sigma}{r} \right)^6 \right] \quad (3.35)$$

Where ϵ is the depth of the potential well and σ is approximately the diameter of the atoms involved, known as the hard sphere diameter. This is shown graphically in figure 3.13B. The first term in brackets, $(\frac{1}{r})^{12}$, represents the strong short range repulsive forces which accounts for the steep increase in $V(r)$ at small r . The second term, $(\frac{1}{r})^6$, is responsible for the weaker long range attractive forces at larger r .

AFM operational modes

There are 3 common imaging methods used in AFM. They are contact mode, non-contact mode and tapping mode. In contact mode, the tip is 'dragged' along the surface of the sample where contours in the sample are measured by the cantilever

laser, the feedback mechanism keeps the tip at a constant distance. Low stiffness cantilevers are used in the method to achieve a large enough deflection signal while keeping the interaction force low. Contact mode is almost always done in the repulsive force regime to prevent 'snap in' of the tip to the surface. This method is primarily used for smooth surfaced samples since it is easily to damage the tip in contact mode, which are expensive to replace.

Non-contact mode is used in situations when tip-sample contact can alter or damage the sample. In this mode, the tip is situated between 5-15 nm above the sample surface. The cantilever is set to oscillate at its resonant frequency (frequency modulation) or just above it (amplitude modulation) where the amplitude is usually <10 nm down to a few picometers.[224] At these tip-sample distances the attractive forces will decrease the frequency of the cantilever. A feed back mechanism is used to keep the cantilever oscillating at a constant rate by changing the tip-sample distance using the piezoelectrics. Unfortunately, this method has reduced resolution compared to contact mode. To overcome this, another mode called tapping mode is often used.

Tapping mode is a technique that allows high resolution topographical imaging of a sample surface without the negatives associated with contact mode. It is ideal for imaging samples that are loosely held to the substrate or for samples that damage easily. Tapping mode overcomes these problems by alternately placing the tip in contact with the surface to provide high resolution images and then lifting the tip off the surface to avoid 'dragging'. In tapping mode the cantilever oscillates at its resonant frequency by using the piezoelectric material where the amplitude of oscillation is typically >20 nm when the tip is not in contact with the surface. The oscillating tip is moved toward the surface until it begins to lightly 'tap' the surface, during the scanning the tip can oscillate between 50-500kHz. The oscillating reduces during tip-sample interactions, it is this reduction in amplitude that is used to measure topographical features of the surface. The amplitude is maintained constant by the feedback loop in tapping mode, when it comes near a 'bump' in the sample, the amplitude of oscillation will decrease. The decrease is detected by the feedback loops which in turn moves the tip further away from the sample to allow the cantilever to oscillate at its resonance frequency again. The opposite happens when it detects a 'hollow' in the sample.

Equipment

AFM measurements was carried out with a Digital Instruments Nanoscale IIIA from Veeco systems. All measurements were carried out under ambient conditions using tapping mode. Silicon tips were used with a resonance frequency of ≈ 300 kHz, force constant 40 Nm^{-1} and a tip radius of 8-10 nm.

3.5 Exfoliation Methods

3.5.1 Sonication

Theory

Ultrasonication, commonly known as sonication is a process that involves the use of ultrasonic energy to disperse [66] and exfoliate [146] nanomaterials in liquid. It is also commonly used in laboratories to clean equipment. Ultrasound is a term used to describe sounds greater than threshold of hearing for humans, usually >20 kHz. For de-bundling of 1D and exfoliation of 2D layered materials a ultrasonic probe is commonly used instead of the more well known sonic baths, due to higher energy density involved in probe sonication.[225] Although, exfoliation of these materials was first realised using sonic baths.[7]

In this work, sonication was used to disperse bacterial cellulose to its constituent nanofibrils in organic solvents. Upon application of sonic energy, the solvent molecules begin to oscillate about their mean position at the frequency of the applied sound wave. The sound wave propagates through the sample by compressions (high pressure) and rarefaction (low pressure). During rarefaction, high intensity sonic waves create small vacuum bubbles or voids in the liquid which collapse violently during compression releasing large amounts of energy in a form of a shockwave.[226] The shockwaves produced generate large shear stress which are able to overcome the intermolecular forces holding the layered/bundled materials together, thus exfoliating them. One drawback of this method is that it can produce large amounts of heat that can degrade the solvent and damage the material, this can be overcome by cooling using ice water. A graphical description of the sonication process is shown in figure 3.14A. Sonic tips produce high frequency sonic energy from electric energy from piezoelectric transducers. In the case of

sonic tips, the transducers supply energy to a titanium probe that is immersed in the sample.

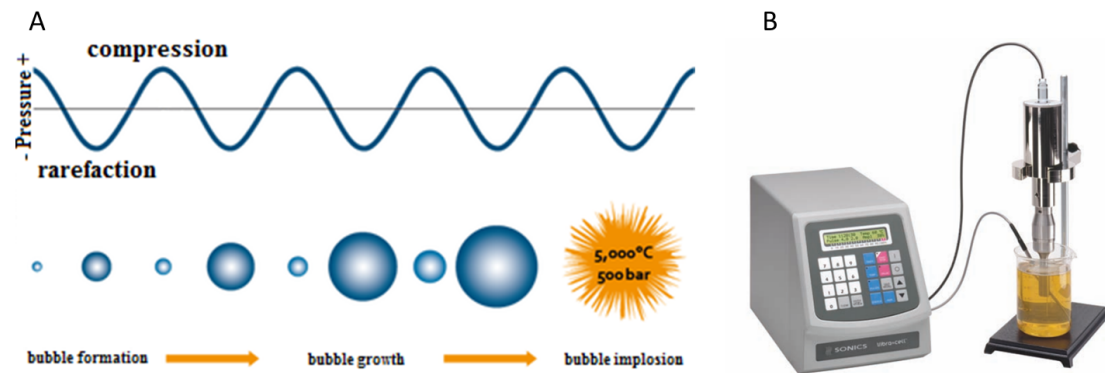


Figure 3.14: A) Graphic showing how ultrasonic energy is used to create voids in the liquid which in turn collapse releasing a large amount of energy that is able to disrupt the bonds holding layered materials together.[227] B) Picture of the sonic tip used in this thesis.[228]

Equipment

A Vibracell Gex750 (750 W) sonic tip was used in this work. The amplitude of the sonic tip, experiment time and pulse time were controlled using the control box as shown in figure 3.14B. A flathead probe was used for the sonication of large volumes while a taper tip was used for small volumes of solvent. The sonic tip was placed inside a noise reducing box which was stored in a fume hood.

3.5.2 Shear mixing

Theory

Shear mixing is another method of exfoliating 2D nanomaterials such as graphene. unlike sonication, it is a scalable process that isn't limited by volume and can produce as much as 5.3 g/h of pristine graphene.[77] Shear mixing was used in this thesis for the production of size selected graphene for surface energy characterisation.

Shear mixing exfoliates graphite to graphene by the application of shear rates above a shear minimum need to overcome the interlayer binding between nanosheets.[77].

In this work, an industrial shear mixer was used to exfoliate graphene in organic solvents, it should be noted that exfoliation can also be achieved by using a home blender and washing up liquid.[229] The exfoliation process for shear mixing has been described in section 2.6.

Figure 3.15A has 4 illustrations showing the shear exfoliation process. At first, during rotation, the shear mixer acts as a pump by pulling in both solid sample and liquid into the machine head. When inside the shear head it is pulled towards the edge of the rotor by centrifugal forces. It is at the edges that there are intense shear forces exerted on the material caused by the small gap between the rotor and the screen before passing out through a perforation in the stator and is driven back into the main volume. The approximate shear rate ($\dot{\gamma}$) is calculated by knowing the rotor rpm (N) and using the equation:

$$\dot{\gamma} = \frac{\pi ND}{\delta} \quad (3.36)$$

Where δ is the rotor-stator gap distance and D is the rotor diameter.

Equipment

The shear mixer used in this work was a LSM high shear laboratory mixer from Silverson Machines Ltd, UK and a picture of it is shown in figure 3.15B. It is equipped with a motor than can drive the rotor at speeds up to 8000 rpm. The mixing assembly used is shown in figure 3.15C which has a rotor diameter of 50 mm. The assembly has a frame, rotor with 4 plates, stator and base plate. All experiments used a square hole, high shear screen with a rotor-stator gap of 135 μm with 96 square holes, each of area 2 mm x 2 mm. The assembly was submerged in the solvent-material mixture to about 3 cm from the bottom of the container and slightly off centre to prevent the formation of a vortex during mixture. The mixture was cooled using a water bath connected to a circulating chiller set to 15 $^{\circ}\text{C}$ to prevent solvent overheating.

3.5.3 Centrifugation

Theory

After sonication or shear mixing, the resulting dispersion will be extremely poly-

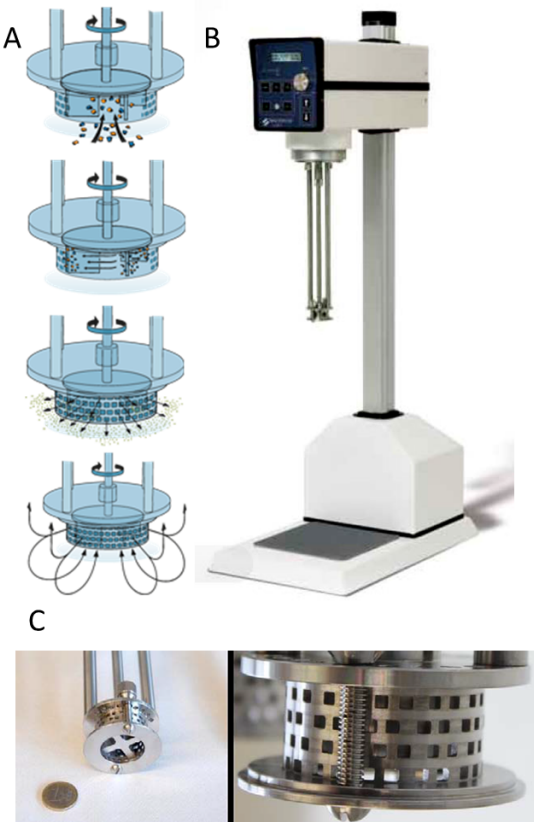


Figure 3.15: A) Illustration of the processes involved in shear exfoliation. The mixture is pulled into the head by the rotor rotation and pulled to the edges by centrifugal forces. At the edge there are high shear rates in the gap between rotor and stator, then the mixture leaves the head through a perforated hole in the stator.[230] B) Image of the Silverson shear mixer.[231] C) Close up of the shear mixer head.[77]

disperse; meaning there will be a wide distribution of nanosheet sizes. Flake types will be a mixture of large unexfoliated crystallites, large exfoliated flakes that are unstable in solution and small flakes that are stable in solution. The exfoliated flakes need to be separated from the unexfoliated flakes for characterisation. Flakes will naturally separate by sedimentation due to gravity but this process can be very slow. Centrifugation of the dispersions allows for quick and highly controllable method for separation based on size, where large flakes will sediment to the bottom of the vial due to centrifugal forces leaving the smaller exfoliated flakes in the supernatant, that can easily be extracted.

In centrifugation, the polydisperse samples in vials are put in the holder which rotates around a fixed point at speeds usually measured in revolutions per minute (rpm) (for convenience). The acceleration (a) experienced by materials in dispersion are related the radius and rotational speed of the centrifuge given by:

$$a = \omega^2 r = (2\pi N)^2 R \quad (3.37)$$

Where N is revolutions per second and R is the centrifuge radius. This acceleration is more commonly quoted in multiples of g called the relative centrifugal force (RCF) given by:

$$RCF = \frac{(2\pi N)^2 R}{g} \quad (3.38)$$

For example, a centrifuge of radius 5 cm spinning at 3000 rpm feels an acceleration of about 500 g

A centrifugation technique known as cascade centrifugation, developed by Backes *et al* [78] was used to size select specific size graphene sheets for surface energy characterisation. This is a technique that uses iterative cascades designed to achieve highly efficient nanosheet size selections in quantities necessary for IGC. Figure 3.16 shows the steps in cascade centrifugation to achieve size selected samples. It starts with a polydispersed graphene dispersion made from either shear mixing or sonication. It is initially centrifuged at low rpm to remove any large unexfoliated crystallites, the supernatant from this is called the stock solution, from which subsequent centrifugation runs will be done. The stock is centrifuged at a higher rpm and the sediment is kept for characterisation and is called for example '1500-2000 rpm', the supernatant is centrifuged again at higher speeds and sediment kept for characterisation. This process is repeated at much as needed or until there is no material left in the dispersion. The collected sediment can be re-dispersed to a desired concentration or filtered to form a film as is the case in this work.

Equipment

Two types of centrifuge were used in this thesis. A Hettich Mikro 220R with radius 9 cm, capable of holding 6 28 mL vials with operating speeds of 500-6000 rpm. The other centrifuge was a thermo scientific Heraeus Megafuge with a radius of

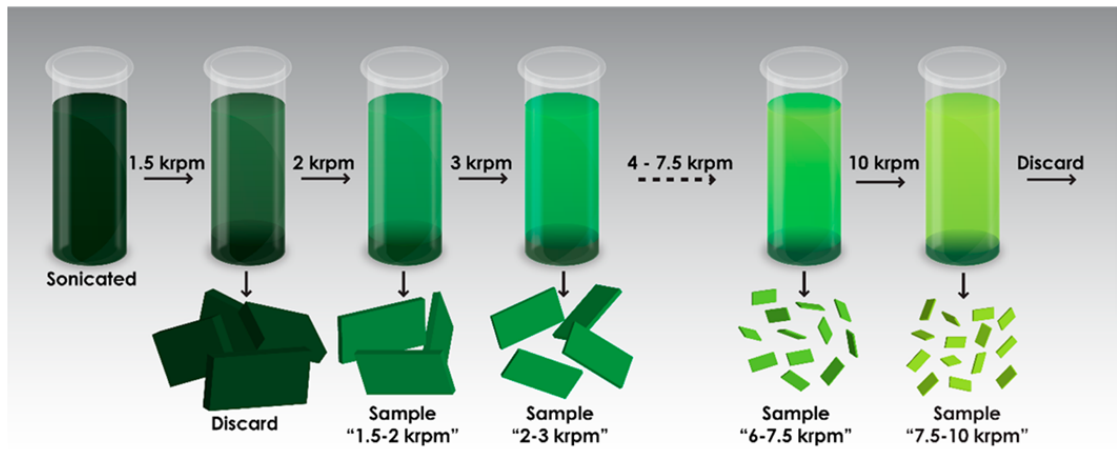


Figure 3.16: Schematic showing the steps in basic cascade centrifugation. The sediment after the initial centrifugation is discarded as it contains unexfoliated large crystallites, while the supernatant at the end contains small nanosheets. Image from Backes *et al.*[78]

16.8 cm, capable of holding up to 16, 50 mL vials operating at speeds from 300-5000 rpm. Both centrifuges have refrigeration units to keep temperature constant during experiments.

3.6 Tensile Testing

Theory

Tensile testing provides a wealth of information about a materials mechanical properties. It involves clamping a sample of known dimensions at either end and applying axial force (F) on the sample, elongating it and eventually breaking the material. The applied force to the sample is called stress (σ) which is taken as force per unit area.

$$\sigma = \frac{F}{A} \quad (3.39)$$

Where A is the cross sectional area of the sample. The applied stress results in the sample straining (elongation), ϵ , which is given by:

$$\epsilon = \frac{\Delta L}{L} \quad (3.40)$$

Where ΔL and L are the change in length and the original length respectfully.

Tensile test results are usually visualised using stress-strain curves where stress is a function of strain. An example stress-strain curve is shown in figure 3.17 which shows the key material characteristics that can be extracted from tensile testing. The stiffness of a material, referred to as the Young's modulus, E , is a measure of a materials resistance to deformation, or in other words its the force required to induce strain on the sample in the initial stage of tensile testing. It is calculated by the slope of the stress-strain curve in the linear region at low strain (elastic region).

$$E = \left(\frac{d\sigma}{d\epsilon} \right)_{Linear} \quad (3.41)$$

The ultimate tensile strength (UTS) is the highest point on stress-strain curve and corresponds to the maximum stress a material can withstand. The elongation at fracture, ϵ_B , is the strain at fracture. The yield point is the position in the stress-strain curve between linear and non-linear deformation and is discussed more below. The last important feature is the toughness, T , of a material. It is defined as the amount of energy per unit volume needed to fracture the material. It is equilivant to the area under the stress-strain curve which is calculated by integrating it, this means T is heavily influenced by the UTS and ϵ_B :

$$T = \int_0^{\epsilon_B} \sigma d\epsilon \quad (3.42)$$

A general description of stress-curves are as follows and uses figure 3.17 as an example. As stress is initially supplied, the material will undergo elastic deformation, meaning that it is a reversible process and is shown by the linear region of the stress-strain curve at low strain. The Young's modulus is measured in this region. Using an example of a polymer, the elastic region is due to elongation and realignment of the polymer chains from their initial configuration in the direction of the applied stress, since only the orientation is changed the process is reversible. Brittle materials fracture in this linear regime and are characterised by high E values meaning they are very hard to deform but have low ϵ_B .

For ductile materials, the yield point is where the material stops deforming

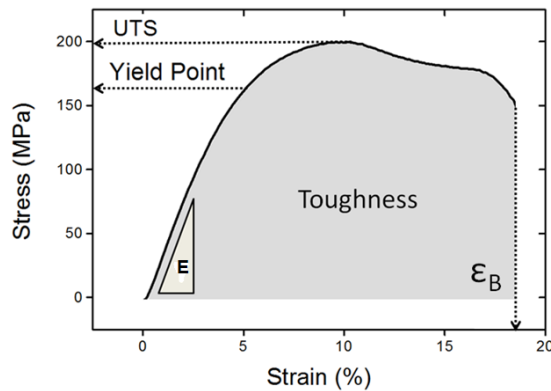


Figure 3.17: Example stress-strain curve showing the key features: Young's modulus (E), ultimate tensile strength (UTS), elongation at fracture (ϵ_B), the yield point and toughness (T). Figure modified from [232]

elastically and starts to deform plastically, meaning stress induced deformation causes permanent changes to the sample and it can't return to its previous state, as is the case in the elastic region. The material will continue to deform with increasing stress and reach its UTS. After this the material will have little or no strength left as it takes less stress to strain the material until eventually it fractures at ϵ_B .

Equipment

Tensile tests were carried out on a Zwick Roell Z005 equipped with a 100 N load cell. Specific experimental methods can be found in chapter 7

Chapter 4

Differentiating Defect and Basal Plane Contributions to the Surface Energy of Graphite Using Inverse Gas Chromatography

4.1 Overview

In this chapter, the surface energy of commercially available graphite is examined. Historically, reported values for the surface energy of graphite have covered a very wide range. Here, coverage dependant inverse gas chromatography is used to show that the measured surface energy of graphite has contributions from edge and basal plane defects as well as from the hexagonal carbon lattice. The surface energy associated with the defect-free hexagonal lattice is measured at high probe coverage to be $61 \pm 7 \text{ mJ/m}^2$, independent of graphite type. However, the surface energy measured at low probe coverage varied from $125\text{-}180 \text{ mJ/m}^2$ depending on the graphite type. Simulation of the coverage dependent IGC output for different binding site distributions allows us to associate this low-coverage surface energy with the binding of probe molecules to high energy defect sites. By analysing its dependence on flake size, it is possible to separate out the contributions of edge and basal plane defects, estimating the basal plane defect content to be 10^{15}

defects/m² for all graphite samples. All these results were achieved by developing a new framework for the analysis of the surface energetics of low dimensional nanomaterials by deriving both analytical and empirical observations.

4.2 Introduction

A detailed introduction to the structure and properties of graphite is given in section 2.2 but a brief summary of that section is that Graphite is a carbonaceous, crystalline, layered material consisting of an array of graphene sheets stacked in an orderly fashion. Within the graphene sheets, the carbon atoms are covalently bonded via sp² bonds while the graphene sheets are bound together by weak Van der Waals interactions.

Graphite has been studied scientifically for well over a century and is one of the best understood materials known to man. For example, its electronic properties have been studied exhaustively since 1947.[233] However, one property of graphite which is not so well understood is its surface energy. The reasons for this are twofold. Firstly, a very wide range of values have been reported in the literature for the surface energy of graphite, from \approx 27-875 mJ/m².[234, 235] A contributing factor is that graphite from different sources can display different surface energies. Secondly, it is known that graphitic surfaces are extremely energetically heterogeneous.[236] This means that the surface energy can vary spatially over the surface of a single graphite sample.

This is unfortunate as a knowledge of a materials surface energy is critical to the development of an understanding of its interactions with other materials. An example can be found in the production of graphene [8] by exfoliation of graphite.[33, 237, 7] One method in particular, liquid phase exfoliation (LPE), can be used to produce defect free graphene in a scalable manner. Theoretical studies have shown that the best solvents for exfoliating graphite to give graphene are those whose surface energy closely match that of graphene.[77, 238] However, without a proper understanding of the surface energies of either graphite or graphene, solvent optimisation remains completely empirical. Although the best solvents [7] are found to be those with surface energies close to 70 mJ/m², it is not clear that this value represents the true surface energy of graphene/graphite.

As discussed in section 2.7, the surface energy of a material is a measure of the energy required to produce a unit area of surface. Measuring surface energy of solids is important to a variety of applications or industries. For example, in pharmaceuticals, accurate knowledge of surface energy is important due to its influence on wet granulation and film coating.[239] In addition, surface energy measurements can be used to monitor product batch to batch variation.[167] However, measuring surface energy is non-trivial, with different measurement methods giving radically different values for the same material. The reasons for this are explored in section 2.7.1 but to summarise; contact angle measurements give a single surface energy value that doesn't take high energy surface sites into account. ID-IGC has the opposite problem where it only gives details of the highest energy sites. This is why coverage dependent IGC was used in this work as it allows the probing of both the high and low energy sites of material in a single measurement by producing surface energy profiles.

Surface energy measurements of graphite are further complicated by the fact that the material varies greatly depending on where it was mined and the processes used to refine it. In addition, most samples contain flakes with a wide range of sizes. Previous studies on the surface energetics of graphite using ID-IGC suggest that surface heterogeneities are partially due to active functional groups and contaminants [240] all of which are considered defects from the perfect graphitic surface. The population of such defects or other structural imperfections may vary with graphite source. These factors make its heterogeneous nature unsurprising and mean a spread of surface energy values can be expected regardless of the measurement technique. This combination of measurement inconsistency and the heterogeneous nature of graphite itself means that a new approach to study the surface energetics of graphite is required.

In this chapter, the surface energy profiles of a range of graphite types are measured using surface coverage dependent IGC. In all cases, high surface energy at low probe coverage were found. However, the measured surface energy falls off as the coverage is increased. We associate the high surface energy with the interaction of probe molecules with defects while the full-coverage, low surface energy values are linked to interactions with the defect-free basal plane. We find the full-coverage surface energies to be independent of graphite type. Conversely

the low-coverage surface energy scales with the flake size. This size-dependence can be explained by modelling the surface energy at low coverage (highest energy sites) as due to a combination of edge and basal plane defects with the edge contribution depending on graphite flake size.

4.3 Experimental Methods

Materials

Graphite samples were used from a variety of suppliers: Northern graphite, Timcal, Qingdao Henglide Graphite, Asbury Graphite, Future Carbon and Sigma-Aldrich.

Methods

The lateral dimensions of the graphite samples were measured by Zeiss Ultra Plus Field Emission SEM and software ImageJ was used to measure flake length.

Specific surface area and surface energy measurements were carried out on a Surface Energy Analyser (SEA) IGC (Surface Measurement Systems, UK). All IGC samples were packed into silanised glass columns of internal diameter (ID) of 2 mm and length 30 cm. Silanised glass wool was used to plug both ends of column the containing to sample to prevent machine contamination. For Specific surface area measurement 15-20mg of sample were packed into a 2mm ID column and preconditioned at 150 °C under helium with flow rate 20 mL/min to remove any loosely adsorbed surface containments, this is discussed more in appendix 8.2. The peak max method was used for the retention time. A series of increasing probe concentrations of octane at 20 °C and flow rate 20 mL/min were injected into the column to get an adsorption isotherm. Methane was used to calculate the column dead time. From this, the BET equation was applied using SMS Cirrus Plus software to get the samples specific surface area (see section 3.2.1.3).

The surface energy of samples was measured by packing columns with a mass that corresponds to a surface area of 0.5 m², this is known from specific surface area measurement. The samples were preconditioned in the same way as previously described. Alkane probes (nonane, octane, heptane, hexane) were used to measure the dispersive surface energy. Coverage values ranging from 0.0075 up to a maximum of 0.4 were used to measure surface energy profiles of the samples. The

peak centre of mass (COM) method was used to measure retention time. Surface energy measurements were performed at temperatures from 60-80 °C. SMS Cirrus plus software was used for all calculations with errors calculated from a python script. Chromatogram elution times were measured using a flame ionising detector (FID). The accuracy of the reported γ_d values depends heavily on the quality of the linear fit of the alkane line since the Dorris-Gray surface energy value depends on the square of the slope as shown in section 3.2.1.1. As a result we only used values where $R^2 > 0.99$ for alkane line fits. The uncertainty in measurements is explored in more detail by Ylä-Mäihäniemi *et al.*[241]

Raman spectroscopy was performed on the graphite samples using a Horiba Jobin Yvon LabRAM HR800 with 532 nm excitation laser in air under ambient conditions. The Raman emission was collected by 100x objective lens (N.A. = 0.8, spot size $\approx 1 \mu\text{m}$). To avoid sample heating we carried out all Raman experiments at 10% of maximum laser power ($< 2 \text{ mW}$). A mapping over a $20 \times 20 \mu\text{m}^2$ sample area was performed in each case in $2 \mu\text{m}$ steps. The spectra displayed are the baseline-corrected average of 120 individual spectra.

Computational Methods

In order to calculate the surface energy profiles, we use the method of Jefferson *et al* [242] as modified by Smith *et al.*[243] A full description is given in the two references. This model assumes the surface can be divided into one or more populations of binding sites. When probe molecules are introduced, they bind to the highest energy sites following a Boltzman distribution until the appropriate coverage is achieved. Then the surface energy can be calculated from the population-weighted mean of the binding energy.

The binding site populations are represented by normal distributions of the type shown in equation 4.11. In general, the total distribution can be the sum over a number of such Gaussians, each representing a different surface site. The total distribution is then transformed from continuous to discrete with bin size 0.005 mJ/m^2 and truncated for energies $< 0 \text{ mJ/m}^2$ to avoid introducing unphysical negative surface energies.

To account for the fact that probes preferentially adsorb to higher energy sites [244], we use a Boltzmann distribution to calculate the relative occupancy of each

site:

$$P_i = \frac{e^{-E_i/kT}}{\sum e^{-E_i/kT}} \quad (4.1)$$

where P_i is the number probability of a probe molecule adsorbing to site i, which has a probe-site binding energy of E_i . This binding energy is taken to be equal to the Gibbs free energy of adsorption, ΔG_{probe} :

$$E_i = \Delta G_{probe} = -a_{probe} 2\sqrt{\gamma_d \gamma_d^{probe}} \quad (4.2)$$

Where a_{probe} is the area occupied by each probe and γ_d^{probe} is the surface energy of the probe. Substituting equation 4.2 into equation 4.1 and multiplying by the total site distribution (generally a sum of discrete Gaussians distributions) gives the probability of a probe filling a site i/fraction of injected probes at each site. The surface energy at that coverage is then given by the mean of the surface energy contribution, weighted by the fraction of probe molecules at each energy (in each bin). However, it is known that this method gives values of surface energy which depend on the probe surface energy. This requires us to apply a correction procedure which is described in reference [243].

4.4 Results and Discussion

Basic Characterisation of Graphite Samples

In order to obtain a broad picture of the surface energy of graphite, we purchased graphite powder from several suppliers with the aim of comparing their surface energetics. First, we carried out some very basic characterisation of the various graphite types. To characterise the size of the graphite flakes used in this study, SEM was conducted on each sample to measure the mean flake dimensions. Figure 4.1A shows a representative SEM image of one of the graphite samples (9-Henglide). This image appears to show the graphite flakes to be particulate in nature. However, more detailed SEM examination shows that the flakes are not monolithic but rather are clearly made of stacked platelets as shown in figure 4.1B. These platelets were observed in all samples and were $<1 \mu\text{m}$ thick in all cases.

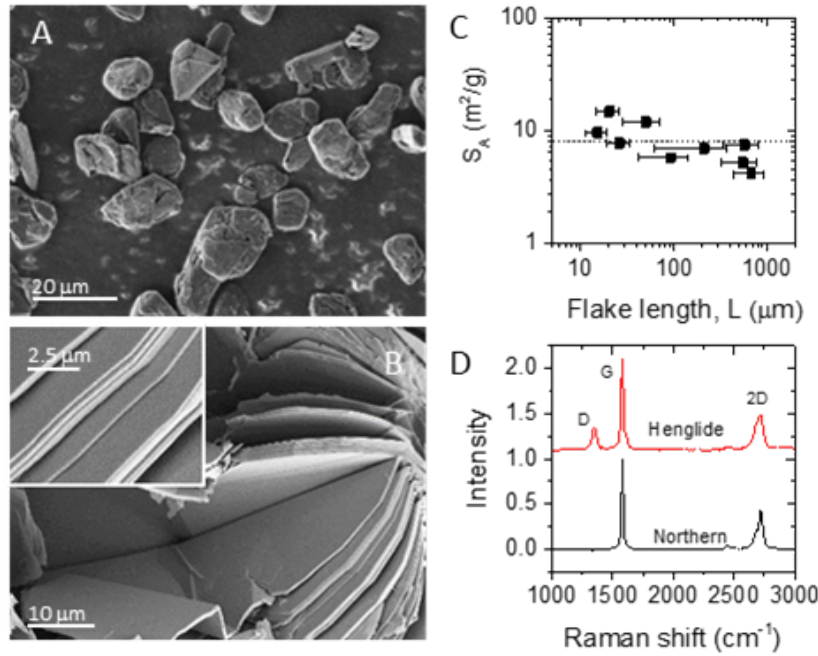


Figure 4.1: Initial characterisation of purchased graphite. A) SEM image of 9-Henglide graphite. B) Close up SEM image of 5-Timcal flake which shows that the flakes are not monolithic but are clearly made of thinner sub-structure. C) Plot of specific surface area versus graphite flake length. The dashed line represents the mean of $8.2 \text{ m}^2/\text{g}$. D) Raman spectra of 2 graphite samples with the main bands (D, G and 2D) indicated. This shows the ratio of D to G band intensities to vary among samples, implying a variation of defect contents.

From statistical analysis of the SEM images, we measured the mean length of the graphite flakes, finding values in the range $10\text{-}1000 \mu\text{m}$ as shown in figure 4.3 (we define L as the flakes maximum dimension, see below). We also measured the specific surface area of the graphite samples (see section 3.2.1.3). These values were clustered between 5 and $15 \text{ m}^2/\text{g}$, a much smaller range than observed for the flakes lengths (figure 4.1C). The specific surface area of a thin platelet of area, A , perimeter length, P , and thickness, t , is given by:

$$S_{BET} = \frac{2A + Pt}{\rho At} = \frac{2}{\rho t} + \frac{P}{\rho A} \quad (4.3)$$

where ρ is the platelet density. Here the first term represents the basal plane contribution while the second term represents the edge area. We do not have data

for A and P, only L and k, where L is the longest dimension of the flake and the width, $w=L/k$ is the dimension in the direction perpendicular to the direction of L. Then, k is the width/length aspect ratio, which was found to be independent of graphite type with $k=1.6$. We measure the dimensions in the long direction and its perpendicular as they are clearly easy to define and measure.

To calculate the ratio P/A, we model the platelets as rhombus-shaped as shown in figure 4.2. Therefore:

$$P = 2L\sqrt{1 + k^{-2}} \quad (4.4)$$

$$A = \frac{L^2}{2k} \quad (4.5)$$

Combining equations 4.4 and 4.5 we get:

$$\frac{P}{A} = \frac{4}{L}\sqrt{1 + k^2} \quad (4.6)$$

Combining equations 4.3 and 4.6

$$S_{BET} = \frac{2A + Pt}{\rho At} = \frac{2}{\rho t} + \frac{4\sqrt{1 + k^2}}{\rho L} \quad (4.7)$$

Because the data in figure 4.1C suggests S_{BET} to be roughly independent of L, this implies the edge contribution to be relatively small and the platelet thickness to be also independent of L. From the mean value of $\langle S_{BET} \rangle = 8.2 \text{ m}^2/\text{g}$, we can estimate the mean platelet thickness to be close to 100 nm for all graphite types.

To investigate the quality of the different graphite types, we conducted Raman spectroscopy. Spectra for the smallest and largest flaked graphite samples are shown in figure 4.1D with the rest shown in figure 4.4. Raman spectroscopy is a well-established technique for the characterisation of defects in carbon based materials.[212, 245, 211] We can use the ratio of the D-peak to G-peak intensity (I_D/I_G) as a measure of the defect content in a sample.[212] A more detailed discussion on the origin of Raman peaks is given by Beams *et al.*[214] Among the graphite samples studied, the I_D/I_G ratio varies from less than 0.01 for Northern to 0.26 for Henglide graphite. This variation can be linked to the variation in flake size, implying the basal plane defect concentration to be roughly constant over

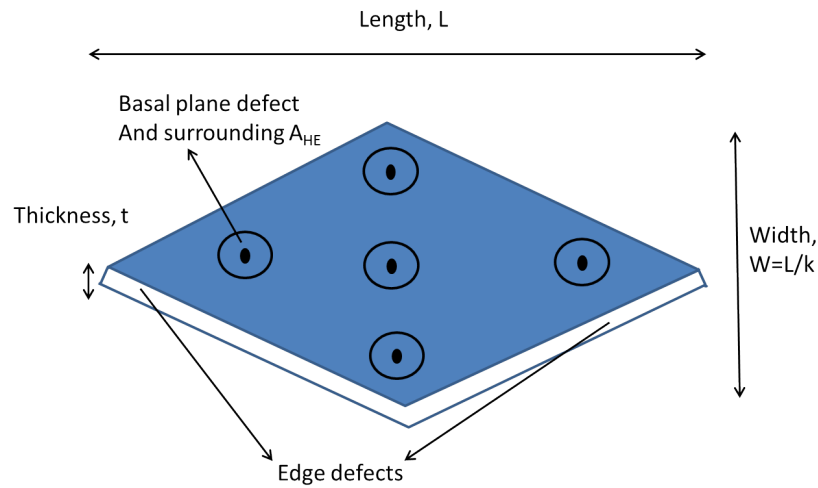


Figure 4.2: Modelling platelets as rhombuses with thickness, t .

these samples as shown in figure 4.5 where the data is fitted to the function:

$$\frac{I_D}{I_G} = \left(\frac{I_D}{I_G} \right)_{L=\infty} + \frac{k}{L} \quad (4.8)$$

Where $\left(\frac{I_D}{I_G} \right)_{L=\infty}$ is the contribution of basal plane defects to I_D/I_G and k is a constant. From the fitting of equation 4.8 to the data in figure 4.5 we can see that the basal plane defect concentration is roughly constant for all samples and therefore, the difference in I_D/I_G is due variations in flake size due to edge density.[213]

IGC measurements of graphite

In order to ascertain how the surface energy of different commercial graphites differ from each other, the dispersive surface energy (γ_d) profiles were measured using coverage-dependent IGC. Such γ_d profiles are measured by injecting a series of n-alkane probes from hexane to nonane at selected surface coverages. Surface coverage (ϕ) is calculated as a fraction of the monolayer capacity of the sample from specific surface area measurements (equation 3.24), of which the results are shown in figure 4.1C. Two alkane plots of the same sample (Timcal), one at low and high coverage which shows the Gibbs free energy of adsorption (ΔG) as a function of alkane carbon number are shown in figure 4.6A. At any coverage γ_d is calculated using the slope of the alkane plot and the Doris-Gray formula as shown

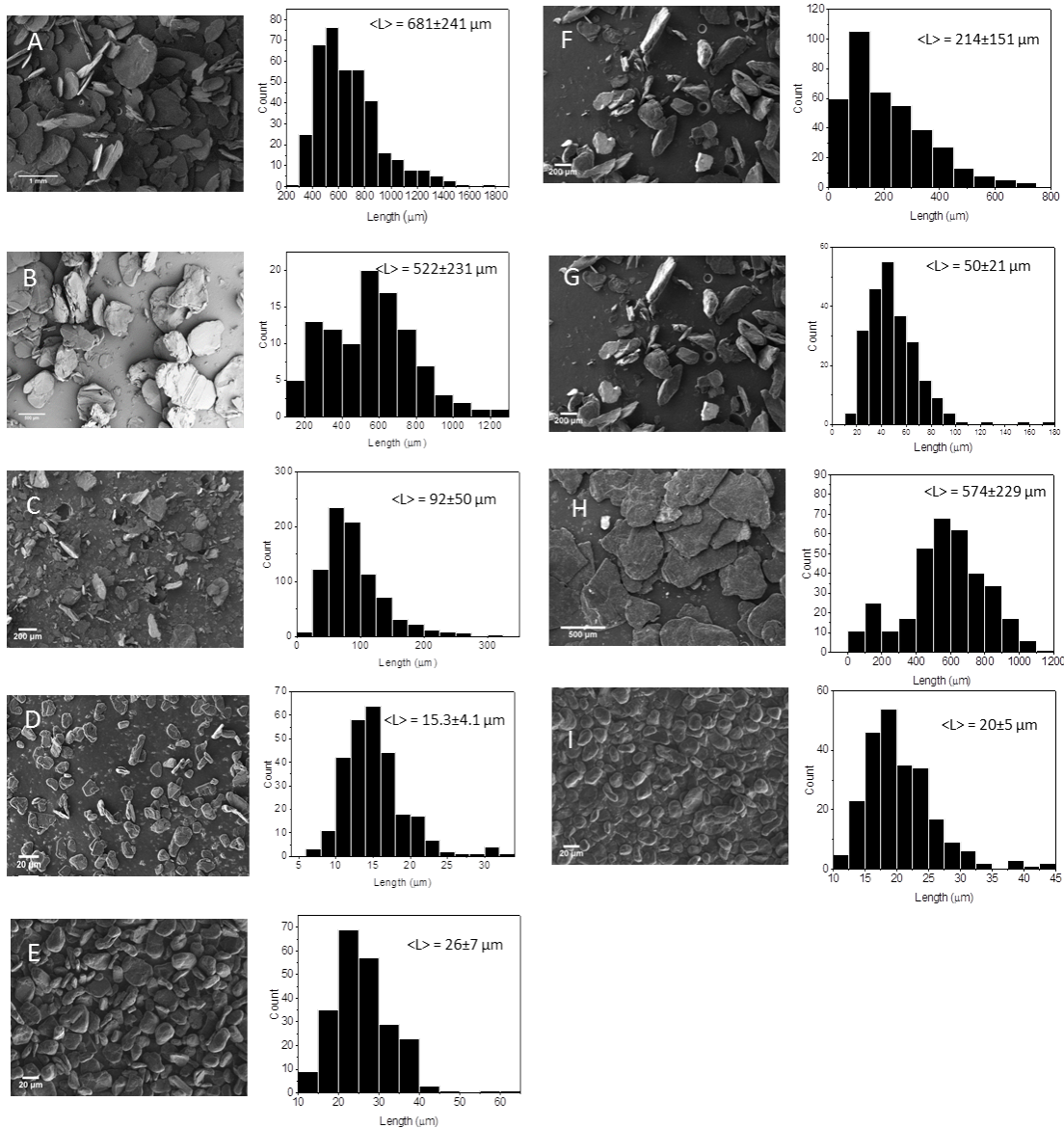


Figure 4.3: Representative SEM images of graphite samples used in the study with histograms showing flake length distributions. A) 1-Northern, B) 5-Timcal, C) 7-Timcal, D) 9-Henglid, E) 12-Henglid, F) 13-Asbury, G) 18-Asbury, H) Sigma-Aldrich, I) Future Carbon.

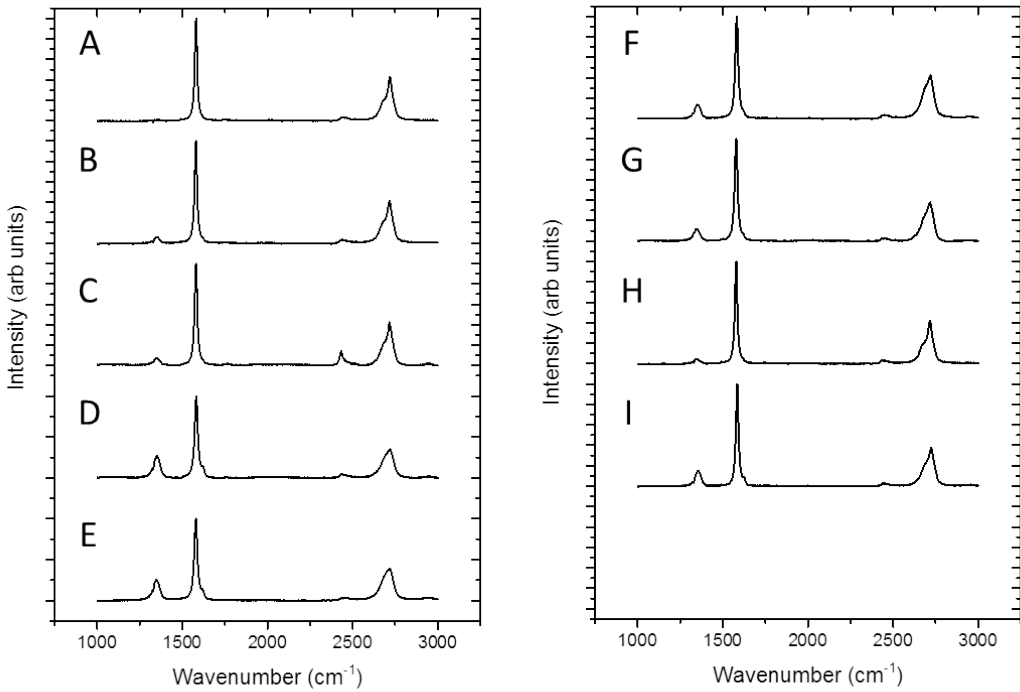


Figure 4.4: Raman Spectra of graphite samples. A) 1-Northern, B) 5-Timcal, C) 7-Timcal, D) 9-Henglide, E) 12-Henglide, F) 13-Asbury, G) 18-Asbury, H) Sigma-Aldrich, I) Future Carbon.

in equation 3.14. This process is repeated for all coverages to complete the γ_d profile.

Figure 4.6B shows the profiles of two of the graphite samples used in this study. The profiles have the expected concave shape with surface energy falling with increasing probe coverage [194, 246] from the low- ϕ value of γ_d before reaching a coverage-independent plateau at large coverage.[241, 190, 162, 247] This plateau value is defined as the full coverage surface energy, $\gamma_{d,\phi=1}$.[248] Significant variations in surface energy profiles were observed from sample to sample as shown in figure 4.3 which shows the γ_d profile of each sample used in the study. In some samples γ_d can increase past the plateau coverage. This is due to a phenomena known as column overloading where the chromatograms peak begins to front, i.e.

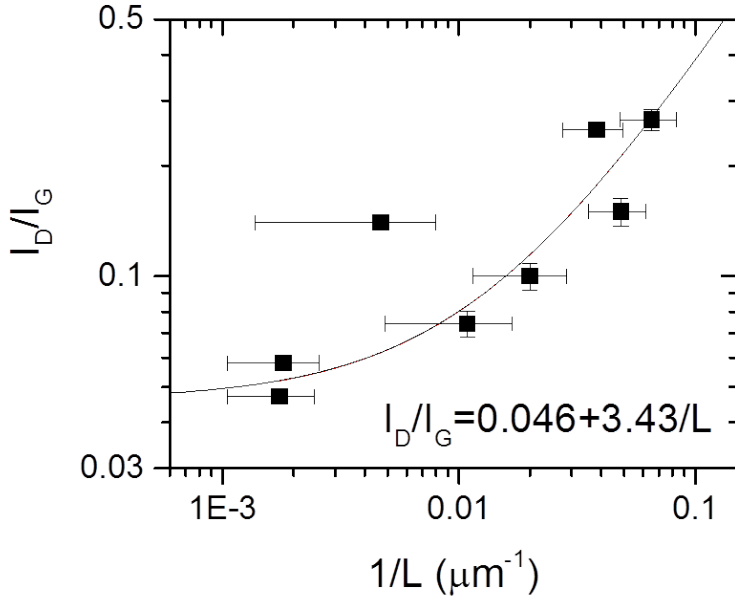


Figure 4.5: Raman I_D/I_G ratio plotted versus inverse flake length. A scaling of the form as shown in equation 4.8 is consistent with the variation in I_D/I_G between samples being due to variations in flake size and so edge content. Then, the basal plane defect density is roughly constant. Here, the vast majority of the data follow this trend (black line).

(t_r) increases.[249] This increase in t_r (and subsequently V_N and γ_d) is due to column effects and is not related to the sample. When this occurred (as shown by the red data points in figure 4.7) the last coverage value before the increase in γ_d is taken as $\gamma_{d,\phi=1}$.

For the graphites studied here, we observed values of γ_d at very low coverage ($\gamma_{d,\phi=0}$) in the range 125-175 mJ/m² while $\gamma_{d,\phi=1}$ values were in the range 50-75 mJ/m² (figure 4.6C). The measured values of $\gamma_{d,\phi=0}$ compare well to previous ID-IGC measurements of graphite. Balard *et al* found the infinite dilution for as-received commercial graphite to be 115 mJ/m² [250], while Papirer *et al* measured two commercial graphite samples and found their γ_d to be 105 mJ/m² and 279 mJ/m² [251], Donnet *et al* measured a γ_d value of 134 mJ/m² [252] and Park *et al* measured two graphite samples to be 119 mJ/m² and 120 mJ/m² [240] (adjusted for temperature). However, the values of $\gamma_{d,\phi=1}$ are far lower than the ID-IGC values quoted above and are more comparable to values of surface energy measured

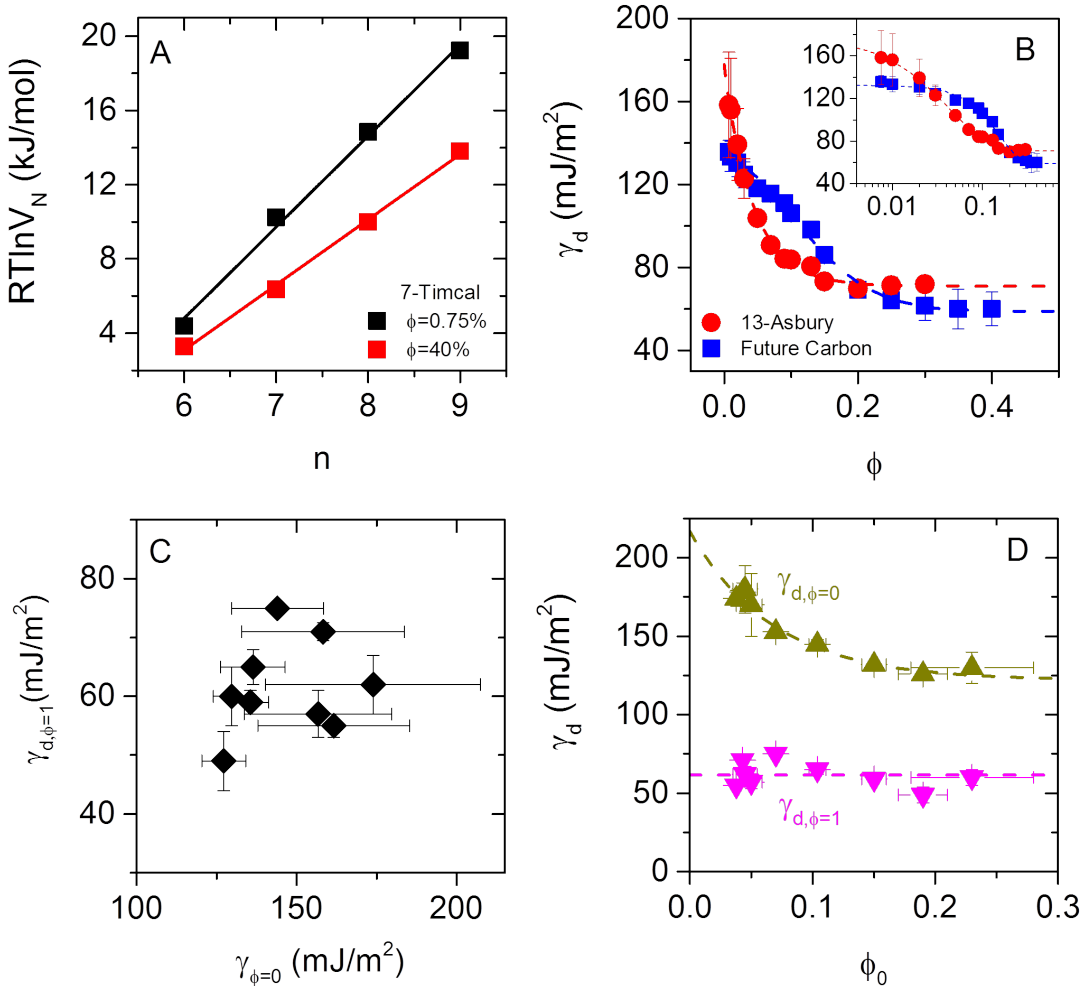


Figure 4.6: A) The Gibbs free energy of adsorption ($RT\ln V_N$) as a function of alkane number for two coverage values of the same sample (Timcal). The slope of the line is used for the calculation of γ_d using the Dorris-Gray formula (equation 3.14). B) γ_d as a function of surface coverage (ϕ) for two of the graphite samples used in the study (Northern and 18-Asbury). γ_d decreases with surface coverage until it reaches a plateau where it becomes coverage independent. The γ_d value at the plateau is defined as $\gamma_{d,\phi=1}$, the full coverage dispersive surface energy value. The γ_d profiles have been fitted to equation 4.10 which is similar to the standard exponential decay typically used for heterogeneous solids. Inset: Semi-log plot. C) $\gamma_{d,\phi=1}$ plotted against $\gamma_{d,\phi=0}$. This shows no correlation indicating that they are independent of each other. D) Dispersive surface energy at both zero coverage ($\gamma_{d,\phi=0}$) and full coverage ($\gamma_{d,\phi=1}$) as a function of the decay constant (ϕ_0). The upper line shows an exponential decay while the lower line represents the mean value of $\gamma_{d,\phi=1}$.

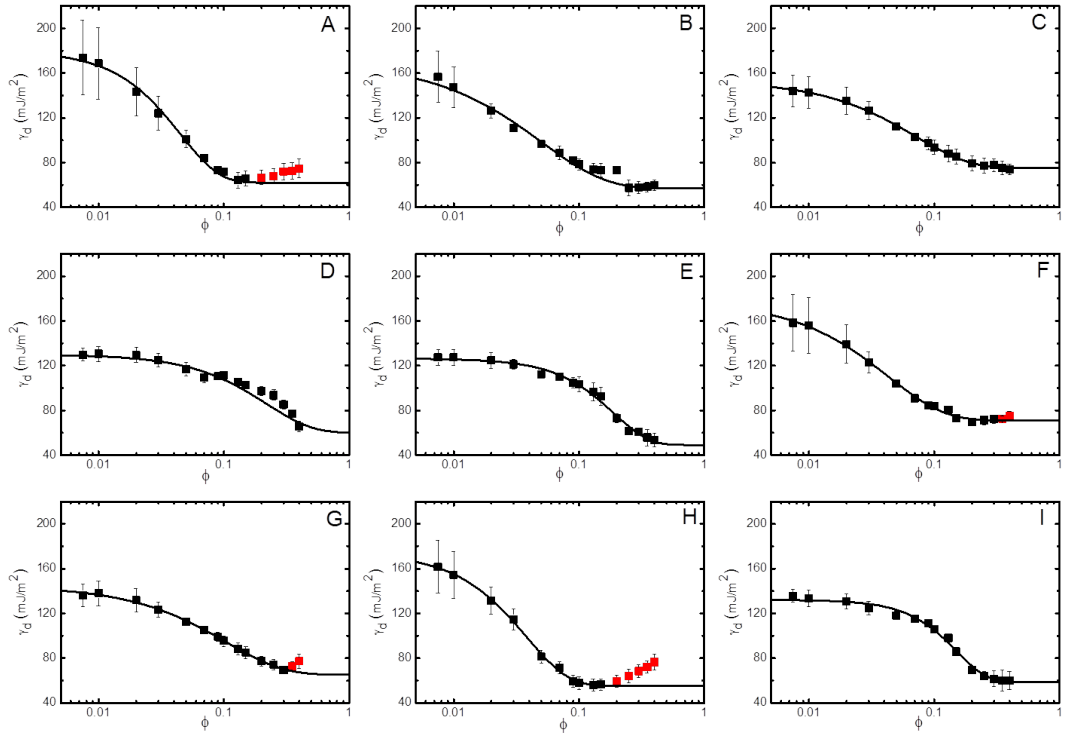


Figure 4.7: γ_d as a function of surface coverage (ϕ) for the graphite samples used in the study. γ_d decreases with surface coverage until it reaches a plateau where γ_d becomes coverage independent. The γ_d value at the plateau is defined as $\gamma_{d,\phi=1}$, the full coverage dispersive surface energy value. The γ_d profiles have been fitted to a characteristic exponential decay function shown in equation 4.10 which is typical for heterogeneous solids. The red data points where γ_d increases past the plateau are due to column overloading effects, as a result these points were removed from the exponential fittings of the γ_d profiles. The samples are (A) 1-Northern, (B) 5-Timcal, (C) 7-Timcal, (D) 9-Henglide, (E) 12-Henglide, (F) 13-Asbury, (G) 18-Asbury, (H) Sigma-Aldrich, (I) Future Carbon.

by contact angle [253] or suggested by solubility measurements [7] which tend to fall in the range 50-125 mJ/m².[254, 255, 256] This is consistent with the idea that these techniques give an average over the whole surface and not just the highest energy sites.

We note that it is difficult to compare literature values to one another in great detail due to the different experimental conditions used in each set of experiments. Such differences make it hard to differentiate the effects of different experimental conditions from those due to the inhomogeneous nature of graphite's surface.[236] We address these problems by insuring that all samples have the same total surface area (0.5 m²) in the column. In addition, the same coverage values and combination of alkane probes were used for all measurements. To the best of our knowledge this is the first paper to show a comprehensive comparison of the γ_d profiles of commercial graphites.

In the literature, γ_d profiles for energetically heterogeneous surfaces are often empirically fitted to an exponential decay function[257, 258]:

$$\gamma_d(\phi) = \gamma_{d,\phi=1} + (\gamma_{d,\phi=0} - \gamma_{d,\phi=1}) e^{-\frac{\phi}{\phi_0}} \quad (4.9)$$

where $\gamma_{d,\phi=1}$ is the dispersive surface energy at full coverage, $\gamma_{d,\phi=0}$ is the dispersive surface energy at zero coverage, and ϕ_0 is a constant which described how the surface energy decays with increasing coverage. However, we have found that a stretched/compressed exponential tends to match the data much better and give more consistent results (addressed in more detail below and in the appendix):

$$\gamma_d(\phi) = \gamma_{d,\phi=1} + (\gamma_{d,\phi=0} - \gamma_{d,\phi=1}) e^{-\left(\frac{\phi}{\phi_0}\right)^k} \quad (4.10)$$

where k is the stretching (when 0 < k < 1) or compression (k > 1) exponent. We have fitted all coverage dependent surface energy data in figure 4.7 to equation 4.10, extracting $\gamma_{d,\phi=1}$, $\gamma_{d,\phi=0}$, ϕ_0 and k, the results of which are shown in table 4.1. As shown in figure 4.6, good fits were obtained with values of k between 0.85 and 1.8 (see figure 4.7 and table 4.1). figure 4.6C is a plot of $\gamma_{d,\phi=1}$ versus $\gamma_{d,\phi=0}$, showing no correlation between these parameters indicating that they are independent of each other. This implies that high energy sites (probed at low coverage) on the sample surface are not representative of the surface as a whole (probed at high

coverage) and so carry little information about the intrinsic surface properties. This shows the importance of coverage dependent IGC compared to ID-IGC. We have plotted both $\gamma_{d,\phi=1}$ and $\gamma_{d,\phi=0}$ (both extracted from the fits to equation 4.10) versus ϕ_0 in figure 4.6D. Here, $\gamma_{d,\phi=1}$ appears to be independent of ϕ_0 . However, we see a clear correlation between $\gamma_{d,\phi=0}$ and ϕ_0 as shown in figure 4.6D. This implies that these two parameters are related and have their origins in the same phenomena.

Table 4.1: Fitting parameters of the γ_d profiles of graphite samples used in this study

Sample	$\gamma_{d,\phi=0}, \text{ mJ/m}^2$	$\gamma_{d,\phi=1}, \text{ mJ/m}^2$	ϕ_0	k
1-Northern	174 ± 33	62 ± 5	0.045 ± 0.010	1.40
5-Timcal	157 ± 23	57 ± 4	0.050 ± 0.009	0.85
7-Timcal	144 ± 14	75 ± 1	0.070 ± 0.002	0.99
9-Henglide	130 ± 6	60 ± 5	0.230 ± 0.050	1.20
12-Henglide	127 ± 7	49 ± 5	0.190 ± 0.020	1.56
13-Asbury	158 ± 25	71 ± 2	0.043 ± 0.003	0.97
18-Asbury	136 ± 10	65 ± 3	0.104 ± 0.007	0.95
Sigma-Aldrich	162 ± 24	55 ± 2	0.038 ± 0.002	1.30
Future Carbon	136 ± 6	59 ± 2	0.150 ± 0.010	1.83

Simulations of IGC profiles

In order to interpret the finite-dilution inverse gas chromatography data shown in figure 4.6B-D, it is important to understand the nature of the sites where the probe molecules bind to the graphitic surface. Such understanding will in turn shed light on the details of the heterogeneity of the surface chemistry of graphite. Recently, a method has been reported which allows the surface energy coverage profile to be simulated based on inputted energetic distribution of binding sites.[242, 243] Here we use such simulations to gain some broad insights into the relationships between $\gamma_{d,\phi=1}$, $\gamma_{d,\phi=0}$ and ϕ_0 and the energetic distribution of binding sites.¹

We begin by considering one population of binding sites whose contribution to the surface energy can be described by a normalised Gaussian distribution:

¹I would like to thank Ivan Caffrey for the IGC simulations.

$$N(\gamma_d) = \frac{1}{\Delta\gamma\sqrt{2\pi}} e^{-(\gamma_d - \gamma_0)^2/(2\Delta\gamma)^2} \quad (4.11)$$

which is centred at γ_0 with width $\Delta\gamma$. Three example distributions are shown in figure 4.8A. We used the simulation techniques initially described by Jefferson *et al* [242] and Smith *et al* [243] to calculate the surface energy versus coverage profiles for a range of such distributions with various combinations of γ_0 and $\Delta\gamma$ with examples in figure 4.8B corresponding to the distributions in figure 4.8A. In all cases, the simulated profiles took the same general form as experimental data with the surface energy decreasing with coverage. However, all simulated curves were convex in shape with none showing the exponential-like shape which tends to be found experimentally. Nevertheless, it is still possible to gain some insights from these single exponential coverage profiles. For example, we found the full coverage surface energy, $\gamma_{d,\phi=1}$ to be exactly equal to the centre of the distribution, irrespective of the distribution width (figure 4.8C). Perhaps more interestingly, we found the difference between the zero and full-coverage surface energies (figure 4.8D) to scale with distribution width approximately as

$$\gamma_{d,\phi=0} - \gamma_{d,\phi=1} \approx 0.045 \times \Delta\gamma^2 \quad (4.12)$$

Although this surface energy difference depends very weakly on the distribution centre, we find the approximation holds very well for all values of γ_0 between 60 and 200 mJ/m² with deviations of no more than 25%. This relationship reflects the fact that the deepest sites fill up first allowing us to make two simple observations: the value of $\gamma_{d,\phi=0}$ reflects the contribution to the surface energy of those sites which bind the probe molecules most strongly while $\gamma_{d,\phi=1}$ is a measure of the mean contribution to the surface energy.

Because of the lack of agreement between the shapes of simulated and experimental coverage profiles, we hypothesised that real experimental data is rarely, if ever, associated with a single population of binding sites. We thus carried out a range of simulations with two normalised Gaussians, representing populations $N_{LE}(\gamma_d)$ and $N_{HE}(\gamma_d)$ such that the total population of binding sites is given by $N_T(\gamma_d) = (1 - f_{HE})N_{LE}(\gamma_d) + f_{HE}N_{HE}(\gamma_d)$, where f_{HE} is the fraction of HE sites. Here the subscripts represent “High Energy” and “Low Energy” such that

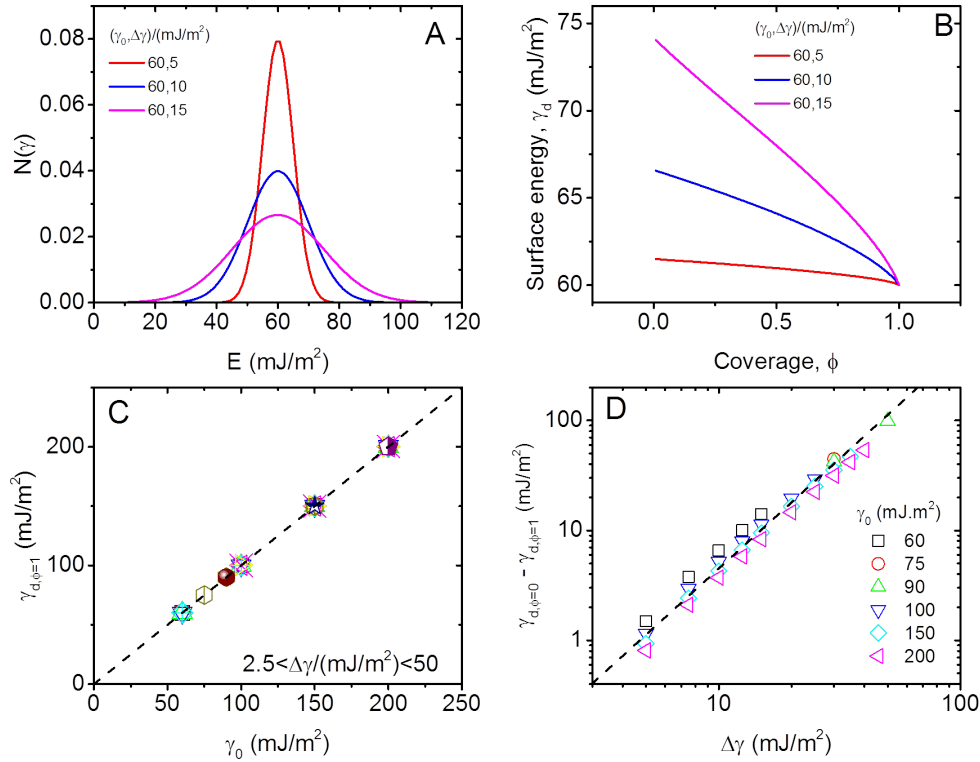


Figure 4.8: Simulation of surface energy vs. coverage data for one Gaussian distribution. A) Examples of Gaussian distributions of probe molecule-surface binding energies, expressed as energy per unit area (the distribution centres, γ_0 and widths, $\Delta\gamma$, are given in the panel). B) Simulated surface energy versus coverage profiles for the distributions shown in A). C) Calculated surface energy at full coverage ($\phi=1$) plotted versus distribution centre for a range of distributions with various widths. The different symbols represent different widths between 2.5 and 50 mJ/m². D) Difference between surface energy at zero coverage and that at full coverage plotted versus distribution width for various distributions with a range of centres. The line represents $\gamma_{d,\phi=0} - \gamma_{d,\phi=1} \approx 0.045 \times \Delta\gamma^2$.

$\gamma_{0,LE} < \gamma_{0,HE}$. An example of a pair of such Gaussians and their sum is given in figure 4.9A.

We first investigated whether such a two-Gaussian distribution can give an exponential-like concave surface energy vs. coverage profile by calculating a number of profiles for pairs of distributions with different combinations of γ_0 and $\Delta\gamma$. We found exponential-like coverage plots as long as the high energy distribution was relatively broad (roughly $\Delta\gamma_d > 0.3\gamma_0$), a condition that is fulfilled by the example distributions in figure 4.9A.

We then systematically calculated surface energy vs. coverage profiles for pairs of distributions, keeping the positions and widths constant for each pair but varying the fraction of high energy sites (f_{HE}). A typical sub-set of such profiles is given in figure 4.9B (calculated from the distributions in figure 4.9A). In general, such profiles are exponential-like (obviously except when $f_{HE} = 0$ or 1). However, we note that such simulated profiles cannot be well-fitted to exponential decays but are much better described by stretched exponentials ($k < 0$) as illustrated in figure 4.9B inset and the appendix. From the profiles, we have extracted $\gamma_{d,\phi=0}$, $\gamma_{d,\phi=1}$ and ϕ_0 (as well as k). Shown in figure 4.9C is a graph of $\gamma_{d,\phi=0}$ and $\gamma_{d,\phi=1}$, extracted from the profiles in figure 4.9B, plotted versus the fraction of high energy sites, f_{HE} . This data shows that $\gamma_{d,\phi=1}$ is just the weighted mean of the centres of the two Gaussian distributions such that: $\gamma_{d,\phi=1} = (1 - f_{HE})\gamma_{0,LE} + f_{HE}\gamma_{0,HE}$. However, $\gamma_{d,\phi=0}$ is slightly less straightforward to analyse, rising sharply as f_{HE} is increased, and approaching the value of $\gamma_{d,\phi=0}$ appropriate to the HE sites once the fraction of HE sites passes 40% in this case. We note that this result is consistent with the single Gaussian distribution case because it shows that $\gamma_{d,\phi=0}$ is largely controlled by the energy of the deepest sites. This of course means that $\gamma_{d,\phi=0}$ should be particularly sensitive to the width of the HE Gaussian distribution.

We have also plotted ϕ_0 (extracted from fits to equation 4.10) versus the fraction of high energy sites, f_{HE} , in figure 4.9D. This graph is particularly interesting as it shows a linear relationship between, $\phi_0 = \beta f_{HE}$, for $f_{HE} < 0.4$ in this case. Fitting the linear portion gives $\beta=1.1$ in this situation. This is potentially a very important relationship as it shows that, in principle, the population of high energy sites can be extracted directly from the stretched/compressed exponential fit of the data.

However, there is a significant discrepancy between the simulated two-Gaussian data and the real experimental data reported in figure 4.6. The data in figure 4.6D shows $\gamma_{d,\phi=0}$ to decrease with f_{HE} while the simulations (figure 4.9D inset) show the opposite trend. This trend in the simulation data arises because the higher energy distribution is broader than the low energy distribution, a necessary condition of finding concave, exponential-like coverage curves (see appendix figure 2). This strongly suggests that our experimental data cannot be described by two Gaussian distributions but actually require a third distribution. This can be seen by considering a low energy distribution (LE) and two high energy distributions, HE,1 and HE,2, such that HE,1 represents a small fixed population of deep sites while HE,2 represents somewhat shallower sites. When the population of HE,2 is small, the deep sites associated with HE,1 will dominate, resulting in a high value of $\gamma_{d,\phi=0}$. However, as the population of HE,2 is increased, this will reduce the overall value of $\gamma_{d,\phi=0}$, as observed in figure 4.6D.

We can see this quantitatively by simulating the surface energy versus coverage plots for three Gaussian distributions, labelled LE, HE,1 and HE,2, with a range of relative populations (figure 4.10). For reasons which will become clear below, we fix the population of HE,1 at approximately 5% of LE, but allow the population of HE,2 to vary. Because figure 4.6D show $\gamma_{d,\phi=1}$ to be roughly constant over all graphites, we set the means of the LE and HE,2 distributions as 60 mJ/m² (because the population of HE,1 is small its position will not significantly affect the overall value of $\gamma_{d,\phi=1}$). We then used trial and error to find values of the remaining parameters ($\gamma_{0,HE1}$, $\Delta\gamma_{LE}$, $\Delta\gamma_{HE1}$, $\Delta\gamma_{HE2}$) such that we could reproduce the experimental data shown in figure 4.6D.

We found good agreement using the distributions shown in figure 4.10A. The resultant low energy distribution had position and width of 60 and 5 mJ/m² while HE,1 and HE,2 had positions of 92 and 60 mJ/m² respectively with both widths equal at 20 mJ/m². Also shown in figure 4.10A (black curve) is an example of an overall distribution with fractions of each component: $f_{LE}=0.9$, $f_{HE1}=0.05$ and $f_{HE2}=0.05$. We calculated the surface energy versus coverage curves for combinations of these distributions, keeping the relative LE to HE,1 population ratio at 5% but varying the LE,2 population. Two example curves are given in figure 4.10B. As shown in the inset, such curves fit much better to stretched exponentials (equa-

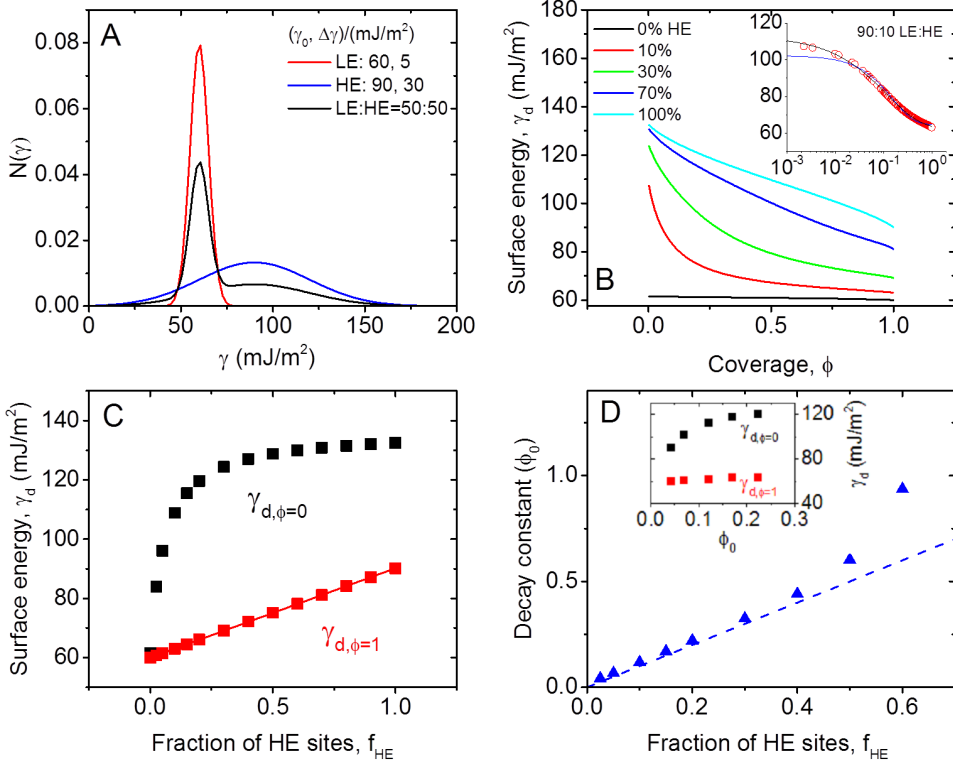


Figure 4.9: Simulations involving two Gaussian distributions A) An example of a narrow low-energy and a broad high energy distribution with an equally weighted sum shown in black (the distribution centres, E_0 and widths, $\Delta\gamma$, are given in the panel). B) Simulated surface energy versus coverage profiles for weighted combinations of the distributions shown in A. The weightings of the high-energy component are given in the panel. Inset: These distributions are not well fitted by exponential decays (blue line). Rather we find they are better described by stretched/compressed exponentials (black curve). C) Surface energy at zero- ($\phi=0$) and full-coverage ($\phi=1$), calculated for weighted sums of the distributions in A) plotted versus the fraction of high-energy sites. D) Decay constants (found by fitting curves such as those in B to stretched/compressed exponentials) plotted versus the fraction of high-energy sites. The dashed line shows that, so long as <45% of sites are of high energy, the decay constant is roughly equal to the fraction of high-energy sites. Inset: Plot of zero- ($\phi=0$) and full-coverage ($\phi=1$) surface energies versus decay constant. Note that this data does not match that in figure 4.6D.

tion 4.10) than exponential curves (equation 4.9). From the stretched exponential fits, we extracted $\gamma_{d,\phi=1}$ and $\gamma_{d,\phi=0}$, which we plotted versus the total fraction of high energy sites ($f_{HE} = f_{HE1} + f_{HE2}$) in figure 4.10C. This graph shows $\gamma_{d,\phi=0}$ to fall with fraction of high energy sites, fundamentally different behaviour to that observed for two Gaussians in figure 4.9C, but consistent with the data in figure 4.6D. We note that, although the data is plotted versus $f_{HE1} + f_{HE2}$, this decay in $\gamma_{d,\phi=0}$ is directly related to f_{HE2} . As shown in figure 4.10C (inset) $\gamma_{d,\phi=0}$ falls empirically with f_{HE2} as a single-exponential decay, a fact which will be important later.

From the fits, we also extracted the decay constant, ϕ_0 , which we plot against the total fraction of high energy sites ($f_{HE} = f_{HE1} + f_{HE2}$) in figure 4.9D. As with the two-Gaussian simulations described in figure 4.9D, we find linearity for low high energy fractions, described by $\phi = \beta f_{HE}$, although here $\beta=0.35$, significantly different to the value of $\beta=1.1$ found in figure 4.9D for the 2-Gaussian simulations. We believe the actual value of β is determined by the details of the overall binding energy distribution, essentially making it a material parameter. This result is important as it shows that, even for a 3-Gaussian system, the decay constant is a measure of the fraction of high energy sites. Shown in figure 4.10D inset is a graph of $\gamma_{d,\phi=1}$ and $\gamma_{d,\phi=0}$, plotted versus ϕ_0 , which matches very well to the experimental data in figure 4.6D. This clearly shows that the overall surface energy data for the set of nine graphite's studied experimentally is consistent with the probe molecules binding to three distinct types of binding site which can be simulated by the three distributions shown in figure 4.10D.

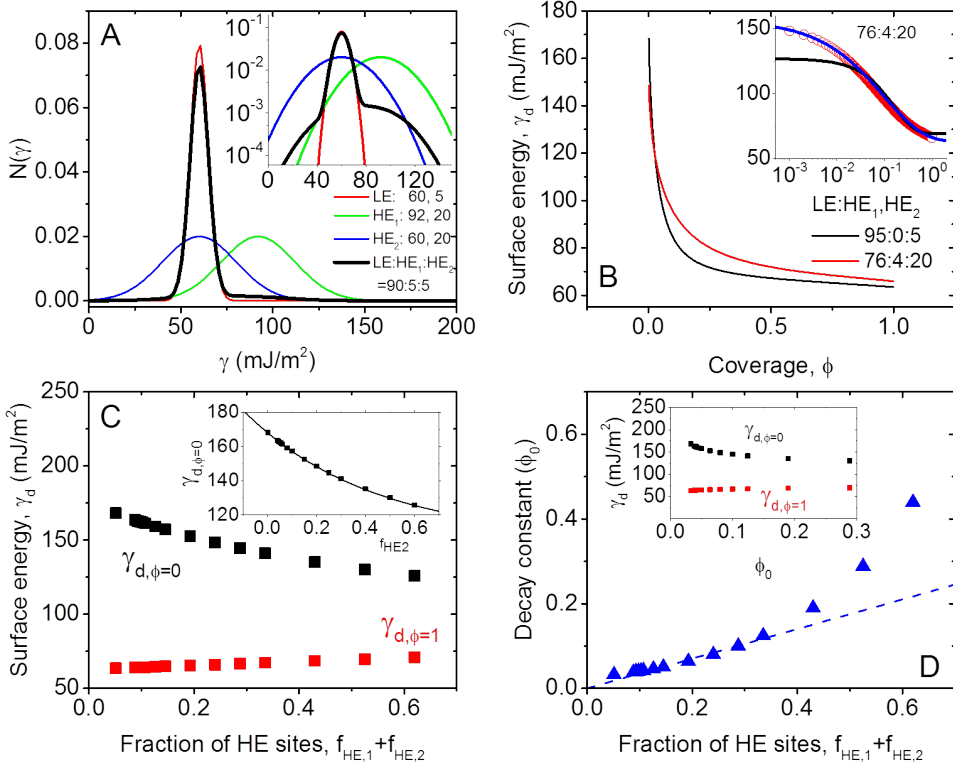


Figure 4.10: Simulations involving three Gaussian distributions. A) An example of a narrow low-energy and two broad high energy distributions with a weighted sum (90:5:5) shown in black (the distribution centres, γ_0 and widths, $\Delta\gamma$, are given in the panel). Inset: The same data plotted on a semi-log graph. B) Simulated surface energy versus coverage profiles for weighted combinations of the distributions shown in A. The weightings of the high-energy components are given in the panel. Inset: These distributions are not well fitted by exponential decays (blue line). Rather we find they are better described by stretched/compressed exponentials (black curve). C) Surface energy at zero- ($\phi=0$) and full-coverage ($\phi=1$), calculated for weighted sums of the distributions in A) plotted versus the total fraction of high-energy sites. Inset: $\gamma_{d,\phi=0}$ plotted against f_{HE2} . The line represents an exponential decay D) Decay constants (found by fitting curves such as those in B to stretched/compressed exponentials) plotted versus the fraction of high-energy sites. The dashed line shows that, so long as <35% of sites are of high energy, the decay constant is proportional to the total fraction of high-energy sites. Inset: Plot of zero- ($\phi=0$) and full-coverage ($\phi=1$) surface energies versus decay constant. Note that this data matches that in figure 4.6D extremely well.

Modelling of surface energy data

With this in mind, we can consider the physical nature of the three types of binding sites discussed above. We believe the high energy sites probed at low coverage are associated with defects in the graphitic lattice. These can either be associated with the flakes edges or basal plane defects, such as point defects. Conversely, the dominant low energy sites probed at high coverage represent the basal plane in the absence of defects. We would expect the population of basal plane defect binding sites to be low relative to the number of graphitic basal plane binding sites. In the ideal case where all graphite types were identical and varied only in flake size, we would expect the ratio of these populations to be fixed. Conversely, we would expect the number of edge binding sites to scale with flake size and so vary among the samples studied. Thus, we can associate the LE, HE,1 and HE,2 distributions with basal plane, basal plane defects and edge binding sites respectively.

If this model is correct, in the ideal case we would associate $\gamma_{d,\phi=1}$ with the intrinsic surface energy of graphite. However, this may not be the case here as the graphite used in this study was not exceptionally clean. In addition, the annealing process applied to the graphite was not particularly aggressive and was unlikely to result in a pristine graphitic surface. This means the values of $\gamma_{d,\phi=1}$ obtained may not correlate exactly with the true surface energy of graphite but more accurately reflect the surface energy of a graphitic surface contaminated with hydrocarbons.[256] In any case, within this model, we would expect $\gamma_{d,\phi=1}$ to be independent of the flake dimensions. This is shown in figure 4.11A where we plot $\gamma_{d,\phi=1}$ versus mean flake length for the nine samples of commercial graphite. We find the data to be size-independent with all data closely clustered around a mean of $\langle \gamma_{d,\phi=1} \rangle = 63 \pm 7 \text{ mJ/m}^2$.

We now turn to $\gamma_{d,\phi=1}$ and ϕ_0 . Within our model, we would expect the low coverage behaviour and so $\gamma_{d,\phi=1}$ and ϕ_0 to be controlled by the defect population. The decay constant (ϕ_0) represents the coverage where the high energy sites (defects) become saturated with probe molecules and as shown above, should scale with the number of defects in the system ($\phi_0 = \beta f_{HE}$). We can test the relationship between ϕ_0 and defect content by plotting the former parameter as a function of I_D/I_G . As described above, I_D/I_G is measured by Raman spectroscopy and is a measure of the graphite defect content. As shown in figure 4.11B, the linear trend

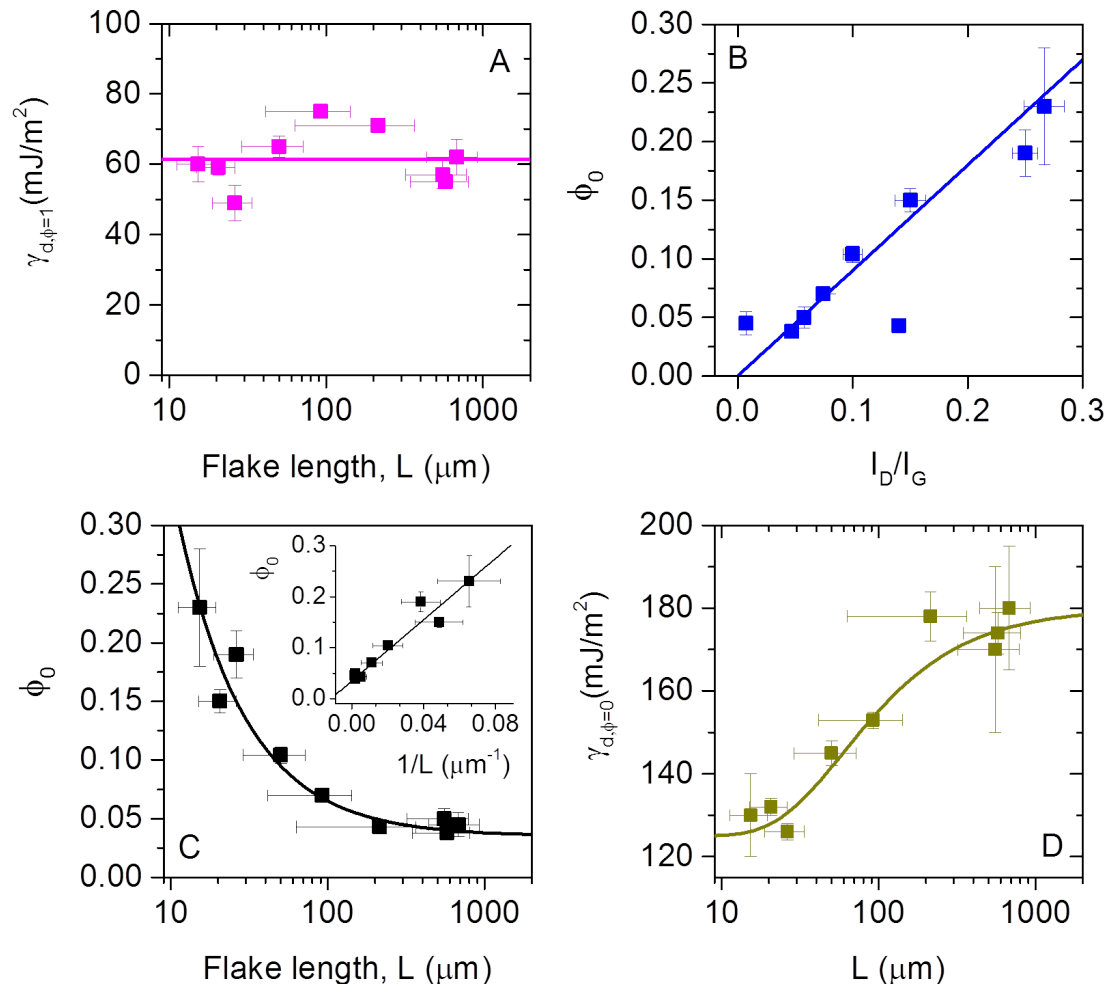


Figure 4.11: A) $\gamma_{d,\phi=1}$ plotted as a function of mean flake length (L) showing that $\gamma_{d,\phi=1}$ is size independent. B) Decay constant, ϕ_0 , plotted as a function of I_D/I_G , the linear trend indicates that ϕ_0 is related to the total amount of defects present in the sample. C) ϕ_0 plotted as a function of L with the inset showing linear trend of ϕ_0 with $1/L$. Using equation 7b this shows that ϕ_0 gives information about the nature of defects present in the sample and is able to differentiate between edge and basal plane defects. (D) $\gamma_{d,\phi=0}$ plotted as a function of L with equation y fitted to the data which indicates $\gamma_{d,\phi=0}$ is due to defects and is a combination of both edge and basal plane with edge defects contributing more in small flakes while basal plane defects contribute more to $\gamma_{d,\phi=0}$.

indicates that is indeed related to the amount of defects present.

If ϕ_0 scales with defect content, we would expect smaller flakes to have larger values of ϕ_0 , simply because smaller flakes have more edge defects. Figure 4.11C shows ϕ_0 versus mean flake length, L, for nine commercial graphite types. This graph clearly shows the expected behaviour with a well-defined fall-off of ϕ_0 with increasing L.

We can quantitatively model ϕ_0 as the fraction of graphitic surface area occupied by probe molecules when all defects have been saturated with probe molecules. We must consider a combination of both edge and basal plane defects. We assume that there are $N_{D,B}/A$ defects per unit area of basal plane and that an area, A_{HE} , surrounds each defect which acts as a high energy region for the probe molecules. In addition, the whole of the edge region of a flake also behaves as an array of high energy sites for probe molecules. Then, by treating the flake as a platelet of area, A, perimeter length, P, and thickness, t, as before we can write:

$$\phi_0 = \beta f_{HE} = \beta \times \frac{(N/A)_{D,B} A_{HE} 2A + Pt}{2A + Pt} \quad (4.13)$$

In the limit where the platelet area is much greater than its thickness, equation 4.13 simplifies to:

$$\phi_0 \approx \beta(N_{D,B}/A)A_{HE} + \beta \frac{Pt}{2A} \quad (4.14)$$

Using equation 4.6 from the rhombus model in figure 4.2, equation 4.14 becomes:

$$\phi_0 \approx \beta \frac{N_{D,B}}{A} A_{HE} + 2\beta \sqrt{1+k^2} \frac{t}{L} \quad (4.15)$$

The inset in figure 4.11C shows a linear relationship between ϕ_0 and $1/L$ as predicted by equation 4.15. Interestingly, the lack of scatter suggests all nine graphite types have similar values of t, k and A_{HE} ($N_{D,B}/A$) . The presence of a constant flake thickness is consistent with the specific surface area measurements, while the constancy of A_{HE} ($N_{D,B}/A$) is consistent with the length dependence of the Raman data (see figure 4.5). In addition, k is known to be constant from SEM with a mean value of k=1.6 over all samples. While it would be possible to use the mean value of t extracted from BET analysis to find β and A_{HE} ($N_{D,B}/A$) from

the linear fit, we demonstrate a better method below.

It is possible to perform a more quantitative analysis by combining equations 4.3 and 4.13 to eliminate t and then using the relationship in equation 4.6 to give:

$$\left[\frac{\rho S_{BET} \phi_0 L}{4\sqrt{1+k^2}} \right] = \beta \times (N_{D,B}/A) A_{HE} \times \left[\frac{\rho S_{BET} \phi_0 L}{4\sqrt{1+k^2}} - 1 \right] + \beta \quad (4.16)$$

Because all the parameters in the square-bracketed terms are known or have been measured in this work, it is possible to parametrise the data in accordance with equation 4.16 and plot a graph which should give linear behaviour. This is shown in figure 4.12 and does indeed show the expected behaviour with the line representing linearity. From this fit, we can extract a value of $\beta=9\pm2$ and $A_{HE}(N_{D,B}/A)=(0.4\pm0.1)\%$. As described above, we believe the value of β to be a material property which depends on the overall surface energy distribution including contributions from basal plane, basal plane defects and edges. We can use the value of $A_{HE}(N_{D,B}/A)$ to estimate the real basal plane defect density, $N_{D,B}/A$. We assume that the presence of a point defect effects the surface energy locally over a distance of ≈ 1 nm, giving $A_{HE} \approx 3 \text{ nm}^2$. This allows us to estimate $N_{D,B}/A \approx 10^{15}$ defects/m², close to the neutral point defect population measured for graphene by Barreiro *et al* (2.5×10^{15} defects/m²).[259] That the data is consistent with values of β and $A_{HE}(N_{D,B}/A)$ which are roughly constant over all the graphite samples implies that the nature of both edges and basal plane defects is the same for the range of graphite types studied.

Shown in figure 4.11D is a plot of $\gamma_{d,\phi=0}$ versus L which shows a well-defined monotonic increase. This is consistent with the data in figure 4.6D and 4.10C and can be understood as follows. When L is very large, flake edges are relatively uncommon and the fraction of edge defects ($f_{HE,2}$) becomes very low. This means that $\gamma_{d,\phi=0}$ is dominated by the relatively deep sites associated with the basal plane defect (HE,1) distribution. However, as L falls, the population of edge defects (f_{HE2}) increases until for very small flakes, the basal plane defect content becomes negligible and edge defects predominate. Then, the HE,2 (edge) distribution, with its shallower sites controls the low coverage surface energy, resulting in a reduction of $\gamma_{d,\phi=0}$. As a result, $\gamma_{d,\phi=0}$ increases steadily from its low-L, edge

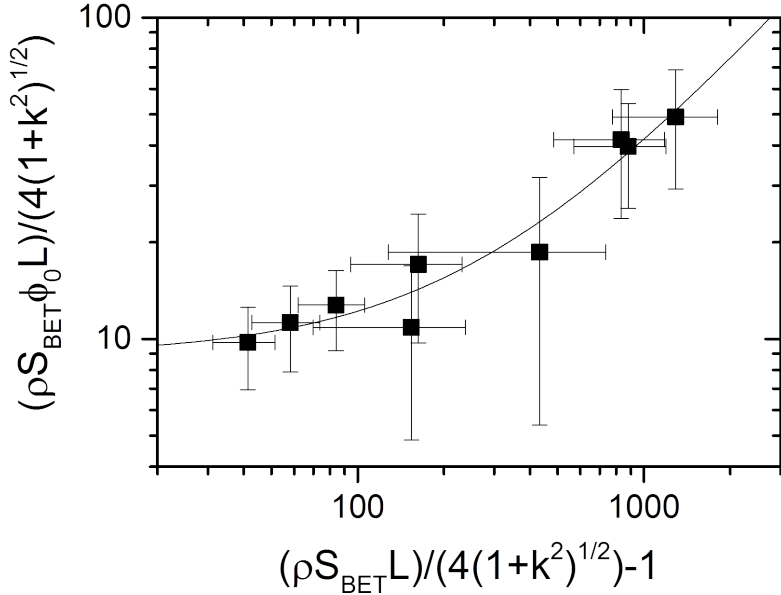


Figure 4.12: Combination of specific surface area and IGC data parameterised according to equation 4.16. The line is a linear fit.

defect dominated value of $\approx 130 \text{ mJ/m}^2$ to its high- L basal plane defect dominated value of $\approx 180 \text{ mJ/m}^2$. We believe that basal plane defects should have a higher energy than edge defects due to the fact that creating basal plane defects requires breaking more bonds than removing edge atoms.

Knowledge of the numerical value of $A_{HE}(N_{D,B}/A)$ allows us to test our understanding of the data in figure 4.11D. We have proposed that $\gamma_{d,\phi=0}$ is controlled by edge sites at low L and by basal plane defects at high L . If this is the case, we would expect the populations of edge and basal plane defects to be equal at intermediate values of L ($L_{BD=ED}$). We can express this by equating the basal plane area affected by defects with the edge area:

$$A_{HE} \left(\frac{N_{D,B}}{A} \right) \times 2A = Pt \quad (4.17)$$

Then using equation 4.6 for P/A and rearranging, equation 4.17 becomes:

$$L_{BD=ED} = \frac{2t\sqrt{1+k^2}}{A_{HE}\left(\frac{N_{D,B}}{A}\right)} \quad (4.18)$$

using $t \approx 100\text{nm}$, $k = 1.6$, $A_{HE}(N_{D,B}/A) = 0.4\%$ we can work out the length where the basal plane (BD) and edge defects (ED) populations are equal to be $L_{BD=ED} \approx 100\mu\text{m}$, a value that lies in the middle of the range where $\gamma_{d,\phi=0}$ is transitioning from a low to high value. This is exactly as expected given the explanation described above.

We can extend this analysis of the $\gamma_{d,\phi=0}$ by noting that, as shown in figure 4.10C (inset), simulated values of $\gamma_{d,\phi=0}$ fall empirically with $f_{HE,2}$ as a single-exponential decay. Because the fractional population of edge defects scales roughly with $1/L$, this implies that $\gamma_{d,\phi=0}$ should scale with L as:

$$\gamma_{d,\phi=0} = \gamma_{d,\phi=0}(L = 0) + [\gamma_{d,\phi=0}(L = \infty) - \gamma_{d,\phi=0}(L = 0)]e^{-L_{BD=ED}\ln 2/L} \quad (4.19)$$

We can justify the form of the exponential by noting that, when written this way, $L_{BD=ED}$ represents the flake length where $\gamma_{d,\phi=0}$ is midway between its small-L and large-L limits. This is consistent with the definition that $L_{BD=ED}$ is equal to flake length where the populations of edge and basal plane defects are equal. As shown by the solid line in figure 4.11D, the data is indeed consistent with this functional form with fitting parameters $\gamma_{d,\phi=0}[L = 0] = 125 \text{ mJ/m}^2$, $\gamma_{d,\phi=0}[L = \infty] = 180 \text{ mJ/m}^2$ and $L_{BD=ED} = 86 \mu\text{m}$. This value of $L_{BD=ED}$ is very close to the value calculated above. This analysis supports the association between the HE,2 defects and the nanosheet edges and highlights the agreement between simulation and experimental results.

This allows us to consider the surface energy profiles expected for graphene nanosheets. Because we expect the intrinsic basal plane surface energy to be similar to that of graphite, we expect $\gamma_{d,\phi=1} \approx 60 \text{ mJ/m}^2$. In addition, assuming $A_{HE}(N_{D,B}/A)$ is similar for graphene and graphite and taking $t \approx 2 \text{ nm}$ and $k \approx 1.6$, typical values for liquid exfoliated graphene nanosheets [77], we can work out $L_{BD=ED} \approx 2 \mu\text{m}$. As most liquid exfoliated graphene nanosheets are smaller than this, with lengths in the range 100-1000 nm, we expect $\gamma_{d,\phi=0}$ to be controlled by edge defects. This allows us to predict that graphene nanosheets will display values of $\gamma_{d,\phi=0}$ in the region of 125 mJ/m^2 . In addition, because the edge defect population will be relatively high, we expect ϕ_0 values to be higher for graphene samples than for graphite. This is explored more in the next chapter where the

surface energy of liquid exfoliated graphene is examined.

Comparison of measured $\gamma_{d,\phi=1}$ to literature values

To compare the $\gamma_{d,\phi=1}$ measurements in this study to literature values, we extracted literature data for graphite surface energies from contact angle measurements [234, 253, 254, 256, 260, 261, 262] liquid exfoliation [255], frictional sliding with adsorption measurements [263], crystal cleavage [264, 265], Krypton adsorption [189] and theoretical calculations.[235, 266, 267, 268] These are shown in ascending order of surface energy as shown in figure 4.13. Here we label the sample number as n, where n ascends from 1 to 34. It should be noted that the data in figure 4.13 doesn't necessarily differentiate between dispersive surface energy (γ_d) and total surface energy (γ_T) but the difference between these will be low for materials like graphite where specific interactions are minimal in comparison to γ_d . The energy values often used in crystal cleavage experiments quote the energy to cleave one crystal from another. If this was the case we divided the energy value by 2 to get the surface energy (from the definition of surface energy). This literature data extends over a very wide range, from 30 to 1000 mJ/m², with the data found here clustered at the low end.

We can analyse this data by assuming that these data points are a random selection from a hypothetical set of all possible graphite surface energy values. This hypothetical set of all possible graphite surface energy values can be represented by a distribution $g(\gamma_{graphite})$. Where g is large, there are many closely spaced values of $g(\gamma_{graphite})$. This means that a graph such as figure 4.11A will have many data points around values of $\gamma_{graphite}$ where g is large. Then such a graph of n vs $\gamma_{graphite}$ will increase sharply because the y increment is always fixed at 1 no matter how small the x increment gets.

On average, the slope of such a graph of n vs $\gamma_{graphite}$ will have a slope equal to

$$\frac{dn}{d\gamma_{graphite}} = \frac{1}{\langle \delta\gamma_{graphite} \rangle_{data}} \quad (4.20)$$

Where $\langle \delta\gamma_{graphite} \rangle_{data}$ is the local average spacing between data points in the data set extracted from the literature (including the data measured here). If these data points are a random selection from a hypothetical set of all possible graphite surface

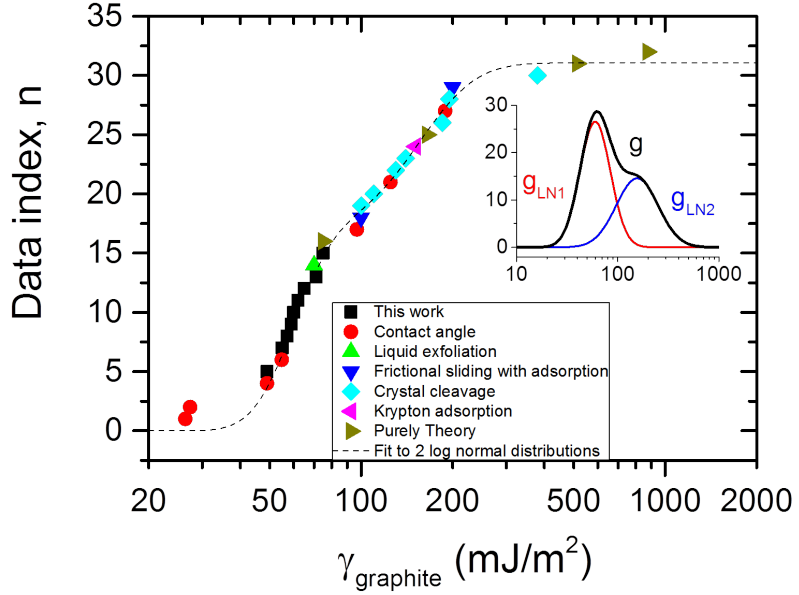


Figure 4.13: The measurements from this study compared to literature values in ascending order of γ_{graphite} . The values are taken from contact angle, liquid exfoliation, frictional sliding with adsorption, crystal cleavage, krypton adsorption and theoretical calculations. Our data is self-consistent and also consistent with some contact angle, liquid exfoliation measurements and a DFT calculation. The dashed line is a fit to equation 4.25 which allows us to reconstruct the over-all graphite surface energy distribution, g , as shown in the inset. From the fit in the main panel we can infer that the over-all graphite surface energy distribution is the sum of two log-normal distributions; g_{LN1} and g_{LN2} .

energy values, then $\langle \delta\gamma_{\text{graphite}} \rangle_{\text{data}} \propto \langle \delta\gamma_{\text{graphite}} \rangle_{\text{overall}}$ where $\langle \delta\gamma_{\text{graphite}} \rangle_{\text{overall}}$ is average spacing between data points in the hypothetical set of all possible graphite surface energy values. This means

$$\frac{dn}{d\gamma_{\text{graphite}}} = \frac{1}{\langle \delta\gamma_{\text{graphite}} \rangle_{\text{overall}}} \quad (4.21)$$

$\langle \delta\gamma_{\text{graphite}} \rangle_{\text{overall}}$ can be found from the surface energy range, $\Delta\gamma_{\text{graphite}}$, divided by the total number of data points in the distribution, $g(\gamma_{\text{graphite}})$, in the range $\Delta\gamma_{\text{graphite}}$. This means:

$$\langle \delta\gamma_{\text{graphite}} \rangle_{\text{overall}} = \frac{\Delta\gamma_{\text{graphite}}}{g(\gamma_{\text{graphite}})\Delta\gamma_{\text{graphite}}} = \frac{1}{g(\gamma_{\text{graphite}})} \quad (4.22)$$

This allows us to write:

$$\frac{dn}{d\gamma_{graphite}} = g(\gamma_{graphite}) \quad (4.23)$$

In principle this means we could differentiate the data in figure 4.13 to get the distribution of all possible graphite surface energy values. However, in reality the data is never truly a random selection from a hypothetical set of all possible graphite surface energy values. This introduces noise, which coupled with the fact that we will always be working with limited data sets makes such a differentiation impossible to achieve without introducing unacceptable levels of noise.

It is more practical to rewrite the equation as:

$$n(\gamma_{graphite}) = \int g(\gamma_{graphite}) d\gamma_{graphite} \quad (4.24)$$

The kink in the curve at $\gamma_{graphite} \approx 85 \text{ mJ/m}^2$ in figure 4.13 suggests the global distribution of graphite surface energies to include two components, one in the range 30-100 mJ/m^2 and the other in the range 70-1000 mJ/m^2 . We found that we could fit the $n(\gamma_{graphite})$ data to the sum of two cumulative distribution functions ($D(\gamma_{graphite,1})$ and $D(\gamma_{graphite,2})$) of log-normal distributions as shown by equation 4.25².

$$n(\gamma_{graphite}) = A \times D(\gamma_{graphite,1}) + B \times D(\gamma_{graphite,2}) \quad (4.25)$$

Where:

$$D(\gamma_{graphite,x}) = \frac{1}{2} \left[1 + \operatorname{erf} \left(\frac{\log(\gamma_{graphite}) - \log(\mu))}{\sqrt{2}\log(\sigma)} \right) \right] \quad (4.26)$$

where A and B are weighting factors, μ and σ are the mean and standard deviation of the distribution. As can be seen from figure 4.13, the fit is very good. From the fit parameters, we can reconstruct the two components of the log-normal distribution, g_{LN1} and g_{LN2} , and so the overall global distribution, $g(\gamma_{graphite})$. Figure 4.13 inset shows g , g_{LN1} and g_{LN2} . It is interesting that there is a clear division of data types over the two distributions. Over the energy range associated with

²Many thanks to Prof. Jonathan Coleman for assistance with this calculation

g_{LN1} , we have data from contact angle measurements, data extracted from liquid phase exfoliation experiments and the IGC data taken from $\phi=1$. These are all liquid based techniques associated with full coverage. Conversely, over the energy range associated with g_{LN2} , we have data from crystal cleavage, sliding as well as theory results. These techniques have in common the absence of liquid. It is not clear why this should be. However, it is clear that the spread of published surface energy data may have more structure to it than was previously thought.

4.5 Conclusion

In this chapter we have used coverage dependent inverse gas chromatography to measure the surface energy of a range of graphites as a function of the degree of coverage of the probe molecule. As the coverage is increased, the measured surface energy always falls before plateauing at high coverage. We find the high-coverage plateau to be invariant with graphite type with a value of $63 \pm 7 \text{ mJ/m}^2$, which we associate with the basal plane surface energy. The low coverage surface energy fell monotonically with graphite flake size, allowing us to associate it with defects which are located both at flake edges and as point defects in the basal plane. Using simple models, we could fit the data, allowing us to separate out the contributions of edge and point defects.

While this chapter has discussed the surface energy of graphite, the methods discussed here are applicable to the analysis of coverage dependent IGC data for any material. Most obviously, the ideas expressed here could be directly transferred to the measurement of the surface energy of other layered crystals such as Boron Nitride or MoS_2 . In addition, these methods will be useful for analysing the surface energy of exfoliated 2D materials such as graphene as shown in the next chapter.

Chapter 5

The Dependence of the Measured Surface Energy of Graphene on Nanosheet Size

5.1 Overview

In this chapter, the surface energy of size-selected, liquid exfoliated graphene is examined. In the literature, there have been very few detailed studies on the surface energy of graphene and no IGC studies on pristine graphene. This chapter follows on naturally from the previous chapter and applies the analysis developed for graphite to graphene. The surface energy associated with the basal plane graphene surface, measured at high coverage was found to be independent of nanosheet size with a mean value of $62 \pm 4 \text{ mJ/m}^2$; a finding consistent with graphite. The surface energy at low coverage was shown to be mainly due to the presence of graphene edges and was found to vary from $120\text{-}140 \text{ mJ/m}^2$.

5.2 Introduction

A detailed introduction into the structure and properties of graphene is given in section 2.4 but to recap; graphene is a carbonaceous, crystalline monolayer of graphite. Carbon-carbon bonding in graphene is due to covalent sp^2 bonds which

give graphene its unique properties. Since its discovery [8], graphene has gone on to be one of the most studied materials in the last few decades. It has been labelled the strongest, most conducting and absorbing of light material ever discovered and could lead to great advances in technology, such as in polymer composites, transistors and optoelectronics.

One aspect of graphene that hasn't been widely studied is its surface energy. There have been contact angle studies of graphene [253, 269, 270, 256, 260], but as we have shown previously, contact angle measurements don't fully describe the surface energy of materials but rather give an average value. There have been some infinite dilution IGC studies done on graphene oxide and reduced graphene oxide [271, 272] but to the best of our knowledge, this is the first study of the surface energy of graphene that has not been oxidised or reduced using IGC. A knowledge of graphene's surface energy is critical as it governs how it interacts with its environment. One of the most obvious examples is the exfoliation of graphite to graphene by liquid phase exfoliation; the method that is used in this chapter. Previous work within the group [7] have inferred the surface energy of graphene to be of the order 70 mJ/m^2 . Also, theoretical calculations have shown that optimum exfoliation is dependent on matching a solvents surface energy to that of graphene.[238] Therefore, a better understanding of the surface energy of graphene is required.

In this chapter, the surface energy of size selected, liquid exfoliated graphene is examined using coverage dependent IGC. The models initially developed for graphite from simulation and analytical models are applied to graphene, since the nature of the surface sites are the same as graphite, i.e. basal plane surface energy, basal plane defect energy and edge defect energy.

5.3 Experimental Methods

Timcal graphite was used as the starting graphite for exfoliation with N-methyl-2-pyrrolidone (NMP) (reagent plus 99%, Sigma Aldrich) being used as the solvent. Graphene was produced by shear exfoliation of graphite using a L5M high shear laboratory mixer (32mm rotor diameter) from Silverson Machines Ltd, UK.

The procedure for the production of size selected liquid exfoliated graphene was

as follows: 275 g of graphite was mixed with 2.5 L of newly opened NMP and this was shear mixed for 4 hours at 8000 rpm. This was let to settle overnight (approx 14 hours). After settling, the supernatant was removed and discarded, with fresh NMP (2.5 L) being added and the shear process being repeated. This is called sediment recycling and has been shown to increase graphene yield.[7, 75, 77] The final shear exfoliation step was the same as above (8000 rpm for 4 hours and settle overnight). Here, the supernatant was collected and put into 2 batches of 16, 50 mL vials and were centrifuged at 300 rpm for 2 hours using a Thermo Scientific Heraeus Megafuge. The supernatant from these was extracted and combined to form a stock solution. Part of the sediment from this was kept as the first size selected sample, called XXL. Further size selection of the graphene was done using a method called cascade centrifugation; a detailed description of this can be found in section 3.5.3 and Backes *et al.*[78] Here, the stock solution was centrifuged at 500 rpm (47 g) for 2 hours and the sediment was kept as the second size selected sample, called XL. The supernatant from this was used for the next cascade stage. This was repeated for 1000 rpm (188 g), 1500 rpm (422 g), 2500 rpm (1174 g) and 3500 rpm (2300 g), yielding samples: L, M, S, XS. The cascade was stopped at 3500 rpm due to low quantities of graphene at higher centrifugation speeds.

A small portion of each dispersion was kept for TEM analysis and Raman spectroscopy with the rest being vacuum filtered to make films using 0.45 μm pore size (47 mm diameter) Nylon membranes (Whatman) for samples containing large nanosheets. For the small nanosheet samples, 0.02 μm (47 mm diameter) alumina membranes (Whatman) were used to make sure all nanosheets were being collected during the filtration. Also, for the samples prepared at higher rpm, there was not enough material to make free standing films (using the 47 mm diameter membranes). Therefore, after the initial filtration, it was redispersed in a small volume (approx 30 mL) of fresh NMP by bath sonication for 15 minutes. This was then filtered using a 0.02 μm , 13 mm pore diameter alumina membrane (whatman) to produce films thick enough to be free standing. All films were dried in vacuum oven at 100 °C for 2 days.

Low-resolution bright field transmission electron microscopy (TEM) imaging was performed using a JEOL 2100, operated at 200 kV. Holey carbon grids (400 mesh) were purchased from Agar Scientific and prepared by diluting a dispersion

to a low concentration and drop casting onto a grid placed on a filter membrane to wick away excess solvent. Statistical analysis was preformed of the nanosheet dimensions by measuring the longest axis of the nanosheet and assigning it as “length”, L and the width, w (measured perpendicular to L).

SEM images were obtained using a ZEISS Ultra Plus (Carl Zeiss Group), 2 kV accelerating voltage, 30 μm aperture, and a working distance of approximately 1-2 mm. The samples were loaded onto the SEM stub using sticky carbon tape.

Samples were prepared for Raman spectroscopy by vacuum filtering a small quantity (2-5 mL) of dispersion onto 0.02 μm , 13 mm pore diameter alumina membranes (whatman) to make films and these were dried in the same manner discussed above. Raman spectroscopy was performed on the graphene samples using a Horiba Jobin Yvon LabRAM HR800 with 532 nm excitation laser in air under ambient conditions. The Raman emission was collected by 100x objective lens (N.A. = 0.8, spot size \approx 1 μm). To avoid sample heating we carried out all Raman experiments at 10% of maximum laser power (<2 mW). A mapping over a 20x20 μm^2 sample area was performed in each case in 2 μm steps. The spectra displayed are the baseline-corrected average of 120 individual spectra.

Specific surface area and surface energy measurements were carried out on a Surface Energy Analyser (SEA) IGC (Surface Measurement Systems (SMS), UK). All IGC samples were packed into silanised glass columns of internal diameter (ID) of 2 mm and length 30 cm. Silanised glass wool was used to plug both ends of the column containing the sample, preventing machine contamination. Methane was used to calculate the column dead time. For specific surface area measurements 10-15 mg of sample were packed into the column and preconditioned at 150°C under helium with flow rate 20 mL/min to remove any loosely adsorbed surface containments (such as residual solvent), this is discussed more in appendix 8.2. The peak max method was used for the retention time. A series of increasing probe concentrations of octane at 20 °C and flow rate 20 mL/min were injected into the column to get an adsorption isotherm. From this the BET equation is applied using the SMS Cirrus Plus software to get the samples’ specific surface area.

The surface energy of the samples was measured by packing columns with a mass that corresponds to a surface area of 0.5 mg/m^2 , this known from specific

surface area measurement. The samples were preconditioned in the same way as previously described. Alkane probes (octane, heptane, hexane) were used to measure the dispersive surface energy. The peak centre of mass (COM) method was used to measure retention time. Surface energy measurements were performed at 90 °C. The Cirrus plus software was used for all calculations. Chromatogram elution times were measured using a flame ionising detector (FID). The accuracy of the reported values depends heavily on the quality of the linear fit of the alkane line since the Dorris-Gray surface energy value depends on the square of the slope as shown in equation 3.14. As a result we only used values where $R^2 > 0.99$ for alkane line fits.

5.4 Results and Discussion

Basic Graphene Characterisation

We produced graphene nanosheet dispersions by liquid phase exfoliation [7] of graphite in the solvent N-methyl-pyrrolidone using high shear mixing [77] (see section 5.3). Such dispersions contain largely defect-free nanosheets with lateral sizes (defined in the same way as in chapter 4) between ≈ 50 nm and $\approx 5 \mu\text{m}$ and thicknesses (usually expressed as number of monolayers per nanosheet, N) between 1 and ≈ 15 layers. We used cascade centrifugation [78] to separate the as prepared dispersion into six fractions with different sizes and thicknesses and labeled: XS, S, M, L, XL and XXL in ascending order of nanosheet size as described in the methods section. Shown in figure 5.1A-B are example TEM images of nanosheets taken from the XS and XXL batches respectively.¹ The size difference between these fractions is clear. The lateral nanosheet size in each fraction was quantified by statistical analysis of TEM images with histograms for the largest and smallest fractions shown in figure 5.1C (with all distributions shown in figure 5.2). As observed previously, the size distributions are very close to lognormal distributions. [78, 213] The mean nanosheet length in each sample varied from 400 nm (XS) to $2.2 \mu\text{m}$ (XXL).

We also performed Raman spectroscopy of nanosheet films produced by vacuum

¹Many thanks to Andrew Harvey for the TEM images

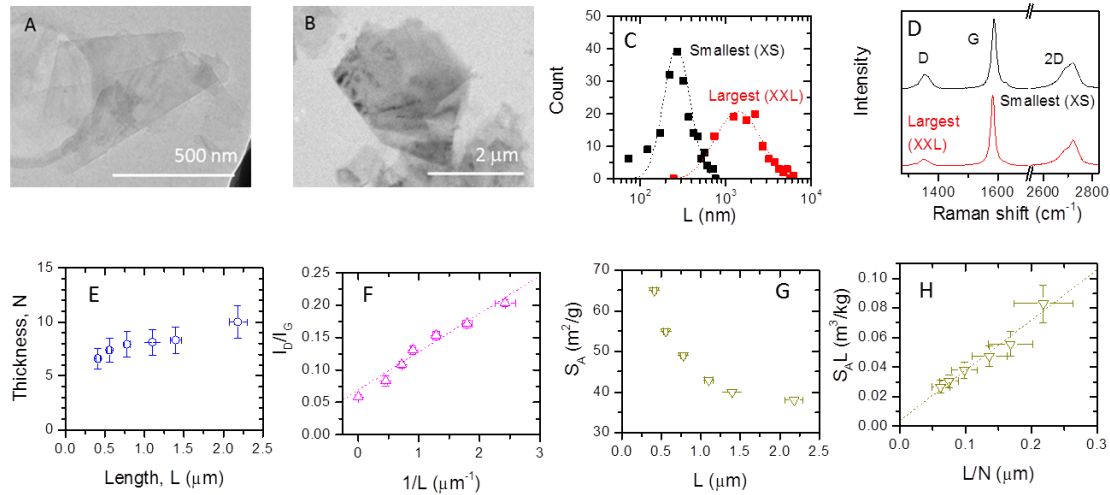


Figure 5.1: Basic characterisation of liquid exfoliated graphene. A-B) Representative TEM images of nanosheets from the smallest A) and largest B) samples. C) Histograms showing length distributions, the dashed lines are log-normal fits. D) Raman spectra for the smallest and largest samples. E) Map showing nanosheet thickness (i.e. monolayers per nanosheet, measured from Raman 2D band) and length (measured by TEM) for the six samples studied in this chapter. F) Raman I_D/I_G versus inverse nanosheet length. G) Specific nanosheet surface area plotted versus length. H) Linearised surface area plot. The line is a fit to equation 5.2.

filtration of the fractionated dispersions through porous membranes. The spectra of the smallest and largest samples are shown in figure 5.1D with each displaying the characteristic D, G and 2D bands.[216] All raman spectra are shown in figure 5.3. The 2D band is particularly interesting as it is very sensitive to the nanosheet thickness. Previous work from Backes *et al* [213] proposed a quantitative metric (as discussed in section 3.3.2) which allows the mean nanosheet thickness in the dispersion to be extracted from the shape of the 2D band. We have applied this metric, finding mean nanosheet thicknesses ranging from 6.6 ± 1 monolayers for the XS sample to 10 ± 2 layers for the XXL sample. We have plotted the mean nanosheet thickness versus the mean length in figure 5.1E. This graph clearly shows the nanosheet length to vary much more significantly over the fractions than the thickness. This makes these samples well suited to studying the effects of length on the nanosheet surface energy.

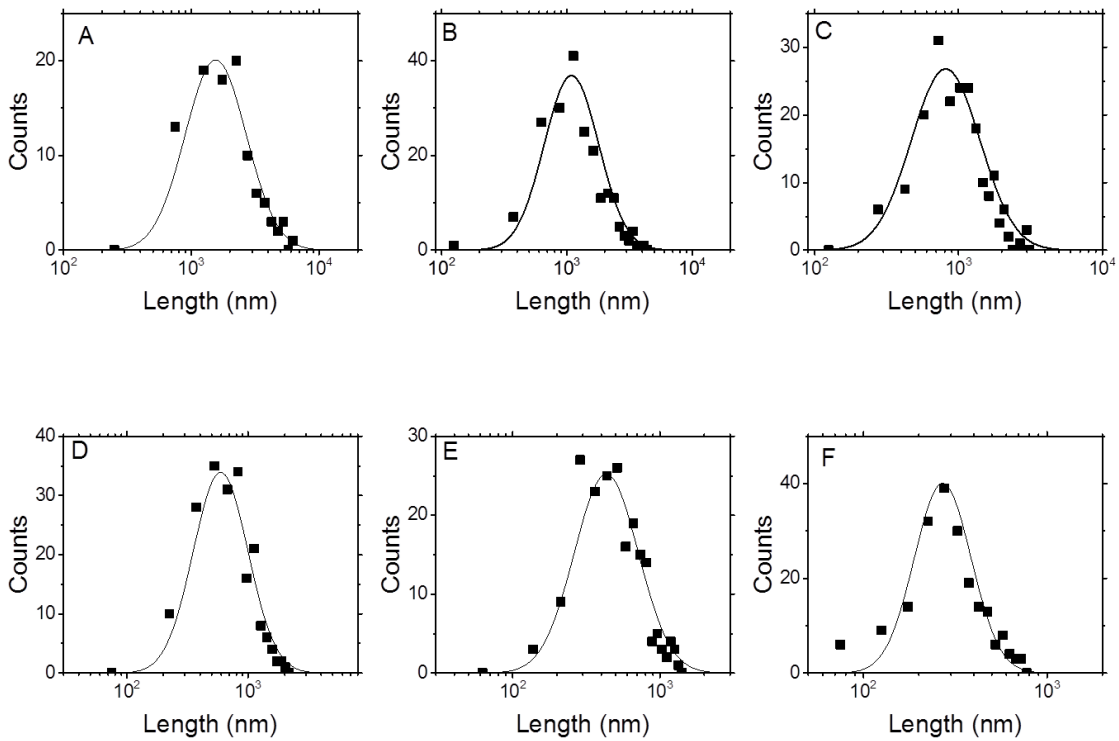


Figure 5.2: Graphene length distributions for each sample measured from statistical analysis from TEM images. The black lines are log-normal fits to the data. Samples A) XXL, B) XL, C) L, D) M, E) S and F) XS

The Raman D-band ($\approx 1360 \text{ cm}^{-1}$) is known to scale with the defect content.[218] For graphene nanosheets, it has been shown that the ratio of D-band to G-band ($\approx 1580 \text{ cm}^{-1}$) intensities scales linearly with $1/L$ due to the presence of nanosheet edges which act as defects.[213] This behaviour is shown in figure 5.1F for the nanosheets prepared here with the data close to $1/L=0$ representing the unexfoliated graphite. This graph suggests the basal plane defect content of the graphene to be similar to that of the graphite and shows the length-dependence of the defect content to be due to changes in the edge population.

For the IGC measurements, the solvent was removed by vacuum filtration to give a reaggregated powder. In order to facilitate the surface energy measurements and to learn more about the state of the material, we measured the specific surface area of these reaggregated powders (see methods and section 3.2.1.3). Shown in figure 5.1G is a graph of the specific surface area as a function of mean nanosheet

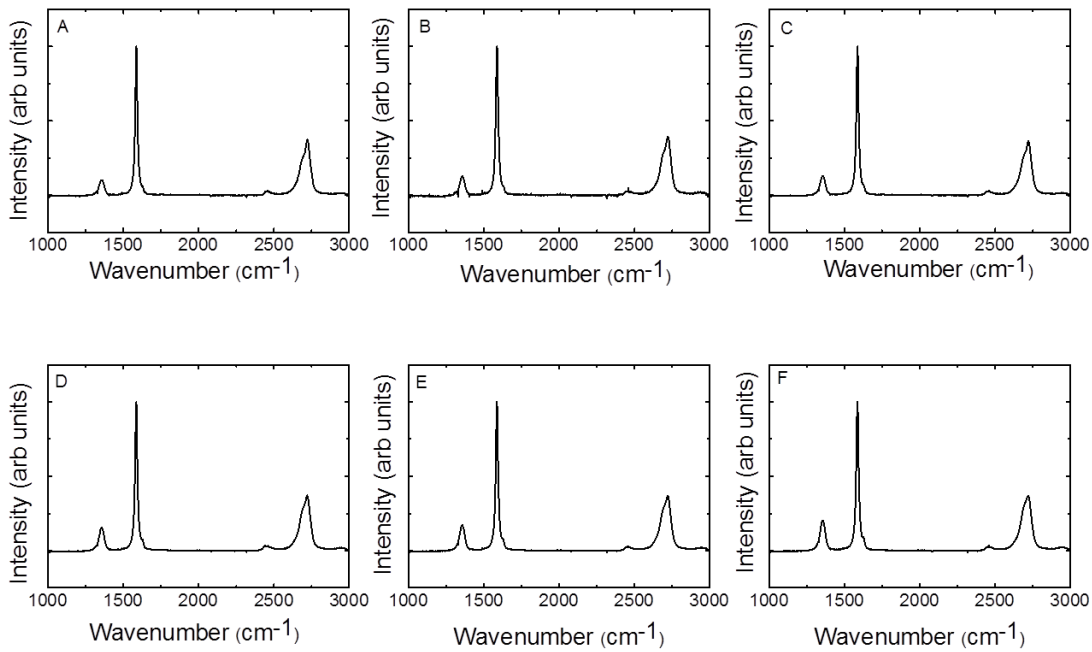


Figure 5.3: Raman spectra of size selected graphene used in this work. Samples A) XXL, B) XL, C) L, D) M, E) S and F) XS.

length. This graph clearly shows a significant length dependence. We can use the model introduced in equation 4.3 in chapter 4 that states that there are two contributions to specific surface area, one from the basal plane and the other edges, such that:

$$S_{BET} = \frac{2A + Pt}{\rho At} \quad (5.1)$$

where A is the basal plane area, P is the nanosheet perimeter length, ρ is density and t is the nanosheet thickness. Again, we use the same model used in chapter 4 that modelled a graphite platelet as a rhombus of length, L and aspect ratio, k . From this model, we defined $P/A = 4\sqrt{1+k^2}/L$. We also note reaggregation effects will mean that the nanosheets in the powdered sample may be significantly thicker than those in the dispersion. (We note that these aggregated nanosheets are probably consist of randomly stacked arrays of few-layer nanosheets, rather than Bernal-stacked monoliths, and so should not be considered to be graphite). This allows us to write the reaggregated nanosheet thickness as $t = R_N d_0 N$,

where $d_0=0.35$ nm is the monolayer thickness and $R_N = N_{agg}/N$ is the ratio of the mean number of stacked monolayers in an aggregated nanosheet, N_{agg} , to the mean number of monolayers in a few-layer nanosheet in the dispersed state (N). Combining these factors and rearranging gives:

$$S_{BET}L = \frac{2}{\rho R_N d_0} \frac{L}{N} + \frac{4\sqrt{1+k^2}}{\rho} \quad (5.2)$$

To test this, we have plotted $S_{BET}L$ versus L/N in figure 5.1H, finding good linearity. This supports our simple model and shows that the ratio $R_N = N_{agg}/N$ is constant over all fractions. Fitting the data with equation 5.2 gives $k=1.87$ and $R_N=7.6$. This value of k is very close to the value of $k=1.75$ found from statistical analysis of the TEM images. In addition, the value of R_N is consistent with recent data on WS₂ nanosheet supercapacitors which suggests the nanosheet thickness in filtered films to be approximately five times that in the liquid dispersion.[273]

IGC Measurements

In order to ascertain how the surface energy of different size selected graphene samples differ from each other, the dispersive surface energy (γ_d) profiles were measured using coverage-dependent IGC. These measurements were performed on reaggregated powders with SEM images of samples containing the smallest and largest nanosheets shown in figure 5.4A-B.² Surface energy profiles are measured by injecting a series of n-alkane probes from hexane to octane at selected surface coverages. Shown in figure 5.4C are two alkane plots, showing the Gibbs free energy of adsorption (ΔG_{probe}) as a function of alkane carbon number, n, measured at low and high probe coverage (from XL graphene). for a particular coverage, γ_d is calculated using the slope of the alkane plot and Doris-Gray formula.

Figure 5.4D shows the γ_d profiles of two of the graphene samples used in this study (the rest are shown in figure 5.5). The profiles have the usual concave shape, with surface energy falling with increasing probe coverage [246] from the low- ϕ value of $\gamma_{d,\phi=0}$, to the full coverage surface energy $\gamma_{d,\phi=1}$. Significant variations in surface energy profiles were observed from sample to sample. It is worth noting that some of these coverage curves are slightly different to those usually found

²Many thanks to Ian Godwin for the SEM images

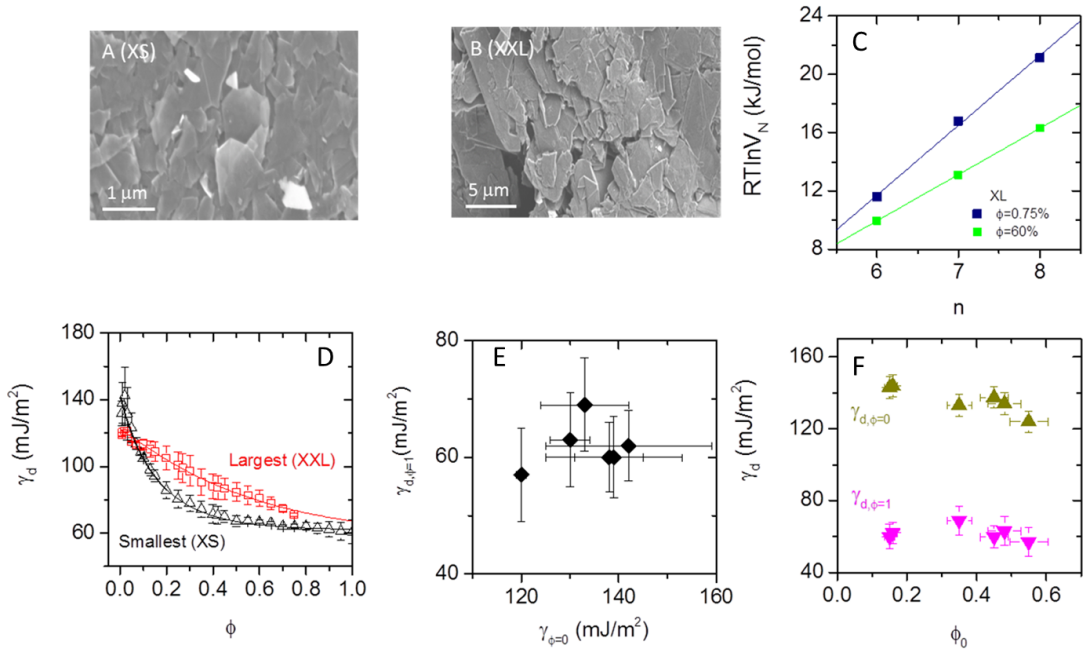


Figure 5.4: (A-B) SEM images of reaggregated solids used in the IGC measurements showing A) the smallest and B) the largest nanosheets. C) The Gibbs free energy of adsorption ($RT\ln V_N$) as a function of alkane number for two coverage values of the sample prepared by centrifuging at 300 and 500 rpm. D) Dispersive surface energy, γ_d , measured as a function of surface coverage, ϕ , for the largest and smallest nanosheet fractions. As coverage increases, the surface energy decreases from its zero-coverage value, $\gamma_{d,\phi=0}$, towards its asymptotic value of $\gamma_{d,\phi=1}$. The solid lines are fits to equation 5.3. E) Fit values of $\gamma_{d,\phi=1}$ plotted against $\gamma_{d,\phi=0}$. This shows no correlation indicating that they are independent of each other. F) $\gamma_{d,\phi=0}$ and $\gamma_{d,\phi=1}$ as a function of the decay constant (ϕ_0).

in that the surface energy does not saturate at high coverage (e.g. XS). As will become clear below, this is due to the large defect content associated with these edge-rich small nanosheets.

For the size selected graphene studied here, we observed values of $\gamma_{d,\phi=0}$ in the range 124-144 mJ/m² while $\gamma_{d,\phi=1}$ values were in the range 57-69 mJ/m² (figure 5.4E). To the best of our knowledge, there has been no reported IGC surface energy measurements done on pristine graphene. However, there have been ID-IGC studies on reduced graphene oxide (RGO) that show reasonable agreement with the measured values of $\gamma_{d,\phi=0}$ here. Dai *et al* have produced two studies

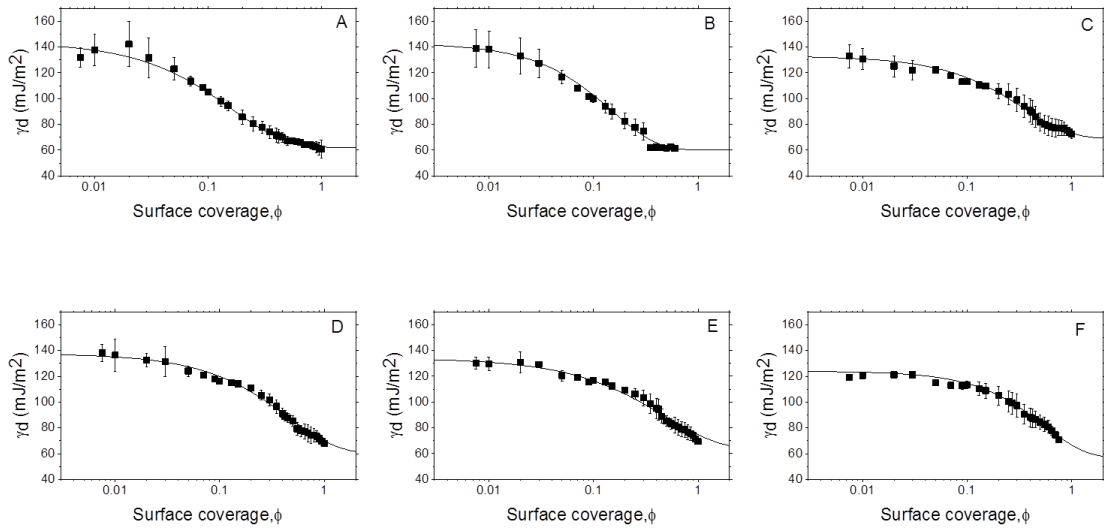


Figure 5.5: γ_d profiles of each size selected graphene sample used in this study. The black lines are fits to equation 5.3. Samples A) XXL, B) XL, C) L, D) M, E) S and F) XS.

on the γ_d of RGO and values that range from 89-106 mJ/m² measured using ID-IGC.[271, 272] However, $\gamma_{d,\phi=1}$ values are far lower than the literature ID-IGC values quoted above and are more comparable to values of surface energy measured by contact angle [253] or suggested by solubility measurements [7] which tend to fall in the range 35-85 mJ/m².[260, 256, 253] This is consistent with the idea that $\gamma_{d,\phi=0}$ involves the adsorption of molecules onto the whole surface and not just the highest energy sites, as also seen for graphite in the previous chapter.

As with the previous chapter we fit the γ_d profiles to a stretched/compressed exponential function as given by:

$$\gamma_d(\phi) = \gamma_{d,\phi=1} + (\gamma_{d,\phi=0} - \gamma_{d,\phi=1})e^{-(\phi/\phi_0)^k} \quad (5.3)$$

where once again ϕ_0 is the decay constant and k is the exponent. We have fitted all coverage-dependent surface energy data to equation 5.3, extracting $\gamma_{d,\phi=0}$, $\gamma_{d,\phi=1}$, ϕ_0 and k. As shown in figure 5.5, good fits of equation 5.3 were obtained with values of k between 0.8 and 1.1. See table 5.1 for all fit parameters.

Shown in figure 5.4E is a plot of $\gamma_{d,\phi=1}$ versus $\gamma_{d,\phi=0}$, showing no simple correlation between these parameters suggesting that they may be independent of

Table 5.1: Fitting parameters of the γ_d profiles of size selected graphene

Sample	$\gamma_{d,\phi=0}$, mJ/m ²	$\gamma_{d,\phi=1}$, mJ/m ²	ϕ_0	k
XXL	142 ± 17	62 ± 4	0.16 ± 0.01	0.90
XL	144 ± 14	58 ± 2	0.15 ± 0.01	1.00
L	133 ± 9	72 ± 4	0.35 ± 0.03	0.95
M	138 ± 7	71 ± 5	0.45 ± 0.03	0.90
S	134 ± 7	72 ± 6	0.48 ± 0.04	0.80
XS	124 ± 6	67 ± 4	0.55 ± 0.04	1.10

each other, as also seen for graphite (figure 4.6). This adds further weight to the argument that high energy sites (probed at low coverage) on the sample surface are not representative of the surface as a whole (probed at high coverage) and so carry little information about the intrinsic surface properties. Again, this highlights the importance of coverage dependent IGC compared to ID-IGC. We have plotted both $\gamma_{d,\phi=0}$ and $\gamma_{d,\phi=1}$ (both extracted from the fits to equation 5.3) versus ϕ_0 in figure 5.4F. Here, $\gamma_{d,\phi=1}$ appears to be independent of ϕ_0 with a value close to 60 mJ/m². This is very similar to the result found for graphite (figure 4.6). Similarly, the value of $\gamma_{d,\phi=0}$ does not vary strongly with ϕ_0 , with values lying roughly in the range 120-140 mJ/m². This is in contrast to the graphite data, where $\gamma_{d,\phi=0}$ fell smoothly with increasing ϕ_0 from ≈175 to ≈120 mJ/m² in the range 0.04 < ϕ_0 < 0.24. The reasons for these differences will be discussed below.

Modelling of Surface Energy Data

From the previous chapter, we believe the high-energy sites probed at low-coverage are associated with defects in the graphene lattice. These can either be associated with the flake edges or basal plane defects such as point defects. Conversely, the dominant low-energy sites probed at high-coverage represent the basal plane in the absence of defects. We would expect the population of basal plane defect binding sites to be low relative to the number of graphitic basal plane binding sites. In the ideal case, where all of the studied graphene samples were identical and varied only in flake size, we would expect the ratio of these populations to be fixed. Conversely, we would expect a significant number of edge binding sites with a population which scales with flake size.

If this model is correct, we would associate $\gamma_{d,\phi=1}$ with the intrinsic surface energy of graphene in the absence of defects or edges. However, as also the case with graphite, this may not exactly be the case, as the graphene used in this study was not exceptionally clean. This means the values of $\gamma_{d,\phi=1}$ obtained may not correlate exactly with the true surface energy of graphene but more accurately, reflect the surface energy of a graphitic surface contaminated with hydrocarbons.[256] In any case, within this model, we would expect $\gamma_{d,\phi=1}$ to be independent of the flake dimensions. This is consistent with the data in figure 5.1F and can be confirmed by plotting $\gamma_{d,\phi=1}$ versus mean flake length for each size selected graphene sample (figure 5.6A). We find the data to be size-independent with all data clustered around a mean of $\langle \gamma_{d,\phi=1} \rangle = 62 \pm 4 \text{ mJ/m}^2$, this is consistent with previous work by Shin *et al* [269] and Raj *et al* [260] who showed no thickness dependence on the contact angle of epitaxial and CVD grown graphene. This value is similar to the measured mean dispersive surface energy of commercial graphite found in the previous chapter, which was found to be $\langle \gamma_{d,\phi=1} \rangle = 63 \pm 7 \text{ mJ/m}^2$. This is also in agreement with Raj *et al* [260], who found that contact angle of their graphene was similar to HOPG graphite. Wang *et al* also found the surface energy of RGO and graphite to be similar with values of 47 and 55 mJ/m² respectively.[253]

We now turn to $\gamma_{d,\phi=0}$ and ϕ_0 . Within our model, we would expect the low coverage behaviour, and so $\gamma_{d,\phi=0}$ and ϕ_0 , to be controlled by the defect population. We address $\gamma_{d,\phi=0}$ first. Figure 5.6B shows $\gamma_{d,\phi=0}$ versus N/L showing a decrease from ≈ 145 to $\approx 120 \text{ mJ/m}^2$ with increasing N/L. This is consistent with the surface energy of graphite from the previous chapter which showed a steady increase in $\gamma_{d,\phi=0}$ from values of $\approx 125 \text{ mJ/m}^2$ for small graphite platelets with $L \approx 15 \mu\text{m}$ to $\gamma_{d,\phi=0} \approx 180 \text{ mJ/m}^2$ for much larger platelets with lateral dimensions approaching 1 mm.

From the graphite study, the behaviour was interpreted from computational studies and showed $\gamma_{d,\phi=0}$ to depend strongly on the position of the deepest sites in the surface energy distribution. The overall surface energy distribution has three components: normal basal plane carbons, basal plane defects and edge defects. Because both types of defect sites tend to be deeper (contribute higher surface energy values) than basal plane sites, they dominate the measured value of $\gamma_{d,\phi=0}$. When the graphite platelets are very large, there are very few edges and $\gamma_{d,\phi=0}$

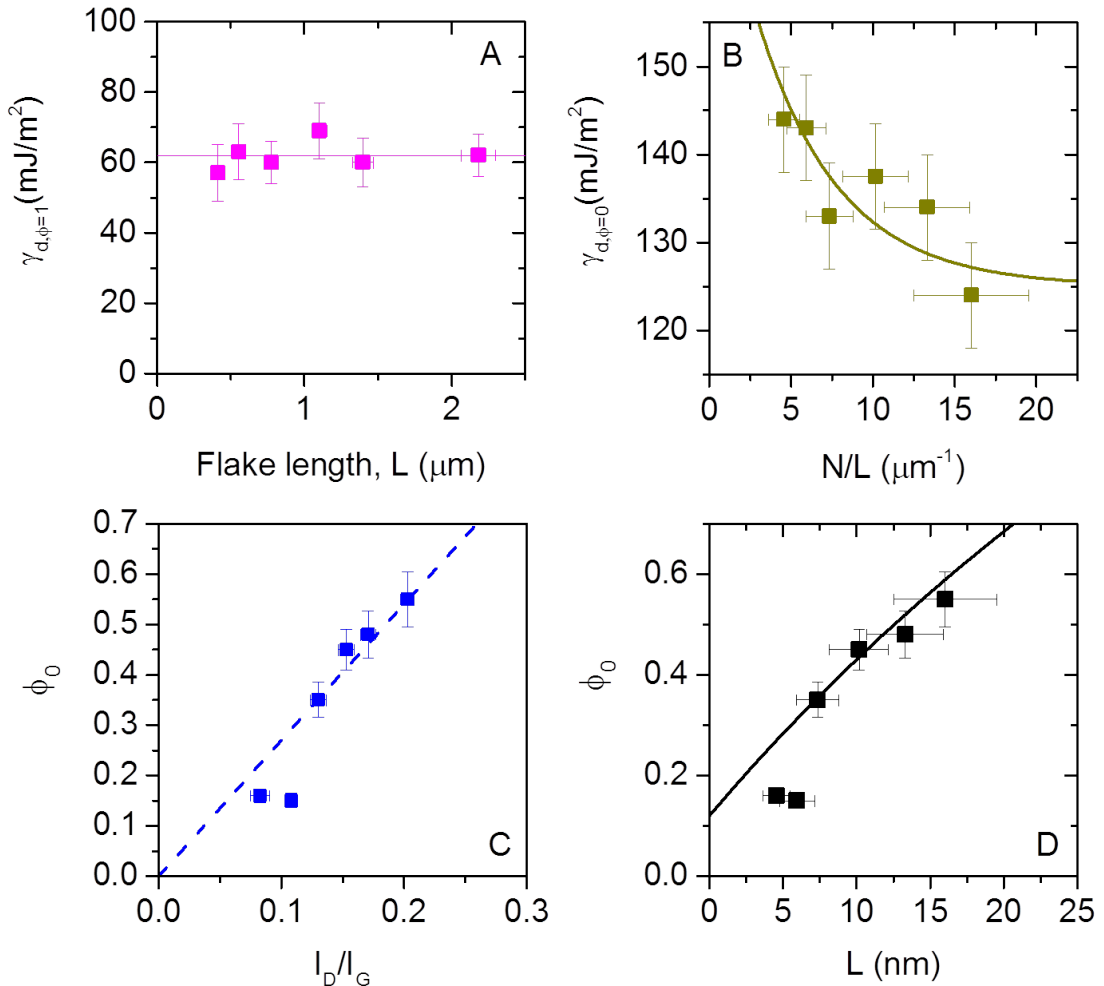


Figure 5.6: Full-coverage surface energy, $\gamma_{d,\phi=1}$, plotted as a function of mean flake length (L) showing $\gamma_{d,\phi=1}$ to be size independent. B) $\gamma_{d,\phi=1}$ as a function of N/L showing $\gamma_{d,\phi=1}$ decreasing with N/L . When N/L is small, i.e. larger nanosheets, $\gamma_{d,\phi=1}$ is higher due a higher contribution of basal plane defects, as sheets get smaller $\gamma_{d,\phi=1}$ decreases. The solid line is a fit of equation 5.6 to the data. C) Decay constant, ϕ_0 , plotted as a function of I_D/I_G , with the linear trend (dashed line) indicating that ϕ_0 is related to the total number of defects present in the sample. D) Decay constant plotted as a function of N/L . The line is a fit to equation 5.8

is predominately due to basal plane defects. In this case, the measured value of $\gamma_{d,\phi=0} \approx 180 \text{ mJ/m}^2$ indicates such basal plane defects to be relatively deep. On the other hand, when the graphite platelets are very small, there are many more edge defects compared to basal plane defects and so edges dominate $\gamma_{d,\phi=0}$. Again, because the small-platelet value of $\gamma_{d,\phi=0}$ measured for graphite is $\approx 125 \text{ mJ/m}^2$, considerably smaller than the large-flake limit, we suggest the edge defects to be shallower than basal plane defects (although deeper than the regular basal plane which tends to contribute $\approx 60 \text{ mJ/m}^2$ to the surface energy). We believe this interpretation also applies to the graphene data presented here.

From the graphite study, we showed a semi-empirical relationship between $\gamma_{d,\phi=0}$ and platelet dimensions:

$$\gamma_{d,\phi=0} = \gamma_{d,\phi=0}(L = 0) + [\gamma_{d,\phi=0}(L = \infty) - \gamma_{d,\phi=0}(L = 0)]e^{-\ln 2 \frac{L_{BD=ED}}{L}} \quad (5.4)$$

where, $L_{BD=ED}$ represents the flake size where the populations of edge and basal plane defects are equal and is given by:

$$L_{BD=ED} = \frac{2t\sqrt{1+k^2}}{A_{HE}(N_{D,B}/A)} \quad (5.5)$$

For graphene films, the nanosheet thickness is given by $t = R_N d_0 N$, allowing us to rewrite equation 5.4 as:

$$\gamma_{d,\phi=0} = \gamma_{d,\phi=0}(L = 0) + [\gamma_{d,\phi=0}(L = \infty) - \gamma_{d,\phi=0}(L = 0)]e^{-\ln 2 \frac{2R_N d_0 \sqrt{1+k^2}}{A_{HE}(N_{D,B}/A)} \frac{N}{L}} \quad (5.6)$$

While the data in figure 5.6B is too scattered to fit directly, we can fix $\gamma_{d,\phi=0}(L = 0) = 125 \text{ mJ/m}^2$ and $\gamma_{d,\phi=0}(L = \infty) = 180 \text{ mJ/m}^2$, i.e. at the values previously found for graphite, allowing only the decay constant to vary. We justify this by noting that we would expect both graphene and graphite to display similar values of $\gamma_{d,\phi=0}(L = 0)$ and $\gamma_{d,\phi=0}(L = \infty)$ because the nature of edge and basal plane defects should be similar. This procedure gives a reasonable fit as shown by the curve in figure 5.6B. This indicates that, like graphite, all graphene samples have a constant $A_{HE}(N_{D,B}/A)$ and k . A constant $A_{HE}(N_{D,B}/A)$ is consistent with figure

5.1F while a constant k value is consistent with TEM analysis and figure 5.1H. In theory, this method would allow us to calculate $A_{HE}(N_{D,B}/A)$ for graphene but since the data is fairly scattered, a better method is used in the next chapter.

We can also apply analysis to ϕ_0 . This parameter is related to the degree of coverage where the high energy sites (defects) become saturated with probe molecules and should scale with the number of defects in the system ($\phi_0 = \beta f_{HE}$, where β is a material constant of the order 1). We can test the relationship between ϕ_0 and defect content by plotting the former parameter as a function of I_D/I_G . As previously described, I_D/I_G is measured by Raman spectroscopy and is a measure of the graphene defect content. As shown in figure 5.6C, the linear trend indicates that ϕ_0 is indeed related to the amount of defects present; this is consistent with graphite which showed a similar relationship.

Assuming ϕ_0 scales with defect content, then we would expect smaller flakes to have larger values of ϕ_0 , simply because smaller flakes have more edge defects. Figure 5.6D shows a plot of ϕ_0 versus N/L for each size selected graphene samples. This graph clearly shows the expected behaviour with a well-defined increase of ϕ_0 with increasing N/L .

To model ϕ_0 as proportional to the f_{HE} , we use the same model as was used for graphite:

$$\phi_0 = \beta f_{HE} = \beta \times \frac{(N/A)_{D,B} A_{HE} 2A + Pt}{2A + Pt} \quad (5.7)$$

using the relations $P/A = 4\sqrt{1+k^2}/L$ and $t = R_N d_0 N$, equation 5.7 becomes:

$$\phi_0 = \beta f_{HE} = \beta \times \frac{(N/A)_{D,B} A_{HE} + 2d_0 R_N \sqrt{1+k^2} N/L}{1 + 2d_0 R_N \sqrt{1+k^2} N/L} \quad (5.8)$$

The data in figure 5.6C is fitted to equation 5.8 and shows good agreement, suggesting a constant value of $A_{HE}(N_{D,B}/A)$ and β for each sample. However, without explicit knowledge of either of them, this type of analysis is only qualitative in nature; a problem that is addressed in the next chapter.

5.5 Conclusion

In this chapter, IGC was used to measure the surface energy profiles of size selected, liquid exfoliated graphene. The measured γ_d profiles of graphene deviated significantly compared to graphite. Here, the γ_d profiles generally didn't plateau, this was due to the higher edge density of graphene. We found the full coverage surface energy to be size independent with a mean value of $\langle \gamma_{d,\phi=1} \rangle = 62 \pm 4$ mJ/m², which is consistent with previous models where we attribute this surface energy to the graphene basal plane. The low coverage surface energy, which we associate with defects, was found to vary monotonically with size from $\approx 120\text{-}145$ mJ/m² and was attributed mainly to edge defects.

The models that were originally developed for graphite from simulation and analytical work also held true for graphene, a promising result that should now be extended to other layered materials.

Chapter 6

Comparison of Graphite and Graphene Measurements

6.1 Overview

This chapter compares the measurements from the graphite and graphene studies and shows the consistency between the data sets and the models developed in the previous chapters. The main findings are that the basal plane surface energy ($\gamma_{d,\phi=1}$) of graphene and graphite are similar, with a mean value of $<\gamma_{d,\phi=1}>=63\pm6 \text{ mJ/m}^2$. We have shown that there is no relationship between the defect surface energy ($\gamma_{d,\phi=0}$) and $\gamma_{d,\phi=1}$, highlighting the importance of coverage dependent IGC over ID-IGC. It was found that graphite and graphene have the same values of $A_{HE}(N_{D,B}/A)$ and β , with calculated values of $0.7\pm0.2\%$ and 5 ± 1 respectively. The data and models developed describing the nature of $\gamma_{d,\phi=0}$ and ϕ_0 for both materials were shown to be consistent, highlighting the robustness of the models. To test if this type of analysis can be extended to other 2D-layered materials, more studies of this nature should be conducted on materials such as boron nitride and WS₂.

6.2 Results and Discussion

The surface energy of graphite and graphene were measured in the form of dispersive surface energy (γ_d) profiles, which maps γ_d as a function of surface coverage. Figure 6.1A shows the γ_d profiles of the largest graphite and smallest graphene samples. There are notable differences between the two, which can be explained by the relative amount of defect surface sites found on the surface. The graphite sample has a much larger value of γ_d at low surface coverage ($\gamma_{d,\phi=0}$) and decays quickly to a plateau, called the full coverage surface energy ($\gamma_{d,\phi=1}$). This is in contrast to the graphene sample which has a far lower value of $\gamma_{d,\phi=0}$ but decays very slowly to its $\gamma_{d,\phi=1}$ value. This can be explained by the larger edge area of graphene nanosheets in comparison to graphite flakes, which are associated with high energy sites on the surface. As graphite's edge area is far less than that of graphene, basal plane defects were found to control its $\gamma_{d,\phi=0}$ (for $L > 100 \mu\text{m}$ at least). As a result, its high energy sites are filled at low coverage and the profiles plateau to $\gamma_{d,\phi=0}$, the basal plane surface energy. On the other hand, for graphene, $\gamma_{d,\phi=0}$ is primarily due its higher edge defect content; as a result, graphene has a lower $\gamma_{d,\phi=0}$. However, both samples $\gamma_{d,\phi=1}$ are similar ($\approx 60 \text{ mJ/m}^2$), this is discussed more below. The profiles were fitted to a stretched/compressed exponential function as shown by equation 4.10, this function was used as simulations suggested γ_d profiles fitted better to it than standard exponentials, which are often used in the literature.[257, 258] From this, $\gamma_{d,\phi=0}$, $\gamma_{d,\phi=1}$, ϕ_0 were extracted and values are shown in tables 4.1 and 5.1.

Figure 6.1B shows $\gamma_{d,\phi=1}$ plotted against $\gamma_{d,\phi=0}$ for both graphite and graphene. As previously noted, these parameters show no correlation, indicating that $\gamma_{d,\phi=0}$ is not a measure of, or related to the intrinsic surface energy of heterogeneous materials. This is an important result, as traditional IGC measurements (at infinite dilution) quote $\gamma_{d,\phi=0}$ as the surface energy of the material, where in fact, it carries very little information about the majority of the surface sites.

Figure 6.1C shows both $\gamma_{d,\phi=1}$ and $\gamma_{d,\phi=0}$ as a function of ϕ_0 , with a clear trend showing $\gamma_{d,\phi=0}$ decreasing with ϕ_0 . This implies that they are related and their origins are in the same phenomena, i.e. defects. The dashed line is an exponential decay function, the origin of which is discussed below. On the other hand, $\gamma_{d,\phi=1}$

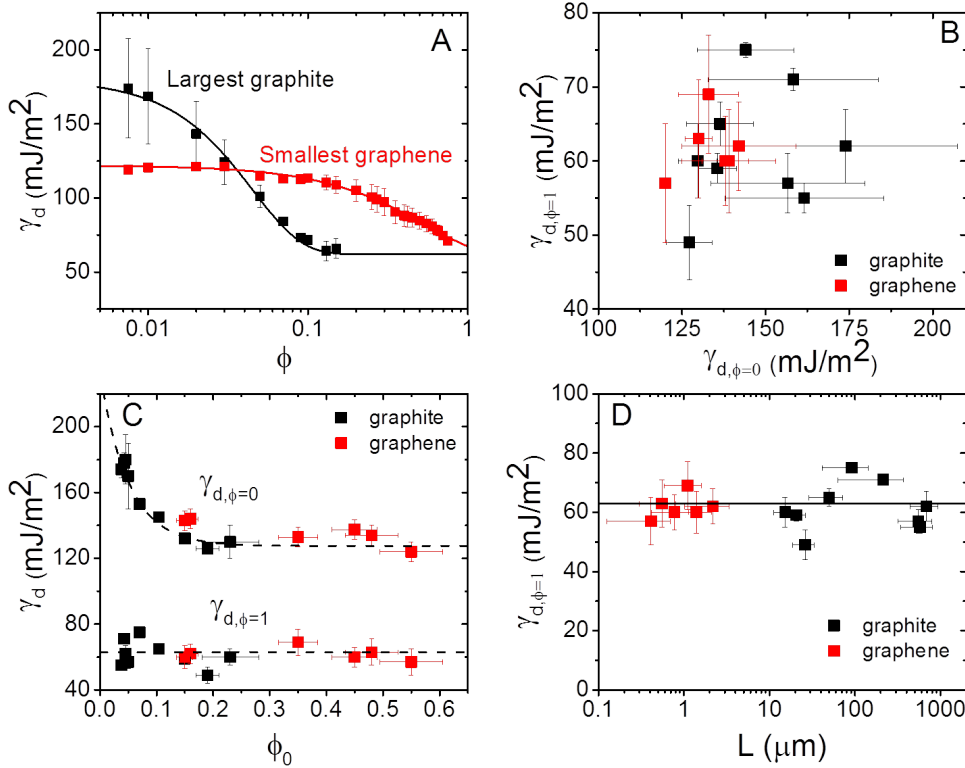


Figure 6.1: A) γ_d profiles for the largest graphite and smallest graphene sample (in terms of flake/nanosheet length). The solid lines are fits to stretched/compressed exponentials as shown in equation 4.10. B) $\gamma_{d,\phi=1}$ plotted against $\gamma_{d,\phi=0}$ which shows no relation between the quantities. C) $\gamma_{d,\phi=0}$ and $\gamma_{d,\phi=1}$ as a function of ϕ_0 . $\gamma_{d,\phi=0}$ is shown to decrease with ϕ_0 showing that they are related, the dashed line is a plot of equation 6.3. $\gamma_{d,\phi=1}$ is independent of ϕ_0 . D) $\gamma_{d,\phi=1}$ as a function of mean flake length, L . $\gamma_{d,\phi=1}$ for both graphite and graphene are shown to be size independent and consistent with each other with a mean of $\langle \gamma_{d,\phi=1} \rangle \approx 63$ mJ/m², as shown by the black line.

is shown to be independent of ϕ_0 . This figure shows that the data presented in the last two chapters is consistent.

Computer simulations in chapter 4 allowed us to assign $\gamma_{d,\phi=1}$ to the defect free basal plane surface energy of graphite/graphene, while $\gamma_{d,\phi=0}$ was attributed to defects; both edge and basal plane. Figure 6.1C implies that $\gamma_{d,\phi=1}$ is sample independent, this is confirmed in figure 6.1D where $\gamma_{d,\phi=1}$ is shown as a function of

mean flake/nanosheet length. This also shows that the basal plane surface energy of graphite and graphene to be the same, with mean value of $\langle \gamma_{d,\phi=1} \rangle \approx 63 \text{ mJ/m}^2$; an observation that has been shown several times in the literature.[253, 269, 260]

Following the analysis of the γ_d profiles from chapters 4 and 5, we were able to derive models describing the nature of $\gamma_{d,\phi=0}$ and ϕ_0 and derive expressions for $A_{HE}(N_{D,B}/A)$, the fractional surface area associated with basal plane defects and β , a material depended property that relates ϕ_0 to the fraction of high energy sites. In chapter 4, we were able to parametrise measured data to equation 4.16, this equation incorporates specific surface area, surface energy, SEM and TEM measurements. A plot of it is shown in figure 6.2A, for graphite and graphene, where the line is a linear fit to the data. The consistency of the data implies that graphite and graphene have the same values of $A_{HE}(N_{D,B}/A)$ and β . This is not a surprising result as the shear exfoliation of graphite to graphene generally doesn't induce basal plane defects [77] (also see figure 5.1F), therefore, they should have a similar basal plane defect content ($A_{HE}(N_{D,B}/A)$). The same β value is consistent with our understanding too, since we believe that it is determined by the details of the overall binding energy distribution, of which graphite and graphene have the same components, i.e. basal plane, edge and basal plane defects. From the fit of equation 4.16 to figure 6.2A we get, $A_{HE}(N_{D,B}/A)=0.7\pm0.2\%$ and $\beta=5\pm1$. Considering that the data presented here spans a greater flake size, specific surface area and ϕ_0 range than graphite alone (as presented in chapter 4), we believe that the values presented here give a better representation of the true values of $A_{HE}(N_{D,B}/A)$ and β . Using $A_{HE}(N_{D,B}/A)$, we can estimate the real basal plane defect density, $N_{D,B}/A$, by assuming, as before that $A_{HE} \approx 3 \text{ nm}^2$. This gives $N_{D,B}/A \approx 10^{15} \text{ defects/m}^2$, a value that is consistent with the previous measurement using graphite alone and from the literature.[259]

From this we are able to compare the data and models describing $\gamma_{d,\phi=0}$ and ϕ_0 developed for graphite and graphene. First, we deal with the modelling of $\gamma_{d,\phi=0}$. We were able to calculate a length, $L_{BD=ED}$, where the populations of edge and basal plane defects are equal; given by equation 4.18. Simulations have shown (figure 4.10C inset) that $\gamma_{d,\phi=0}$ falls-off with f_{HE2} , i.e. edges, as a single exponential decay. Since we know that edge population scales with $1/L$, this allows

us to write:

$$\gamma_{d,\phi=0} = \gamma_{d,\phi=0}(L = 0) + [\gamma_{d,\phi=0}(L = \infty) - \gamma_{d,\phi=0}(L = 0)]e^{-L_{BD=ED}\ln 2/L} \quad (6.1)$$

If the graphite and graphene measurements are consistent, then we would expect them both to sit on the curve described by equation 6.1, with $\gamma_{d,\phi=0}(L = 0) = 125$ mJ/m² and $\gamma_{d,\phi=0}(L = \infty) = 180$ mJ/m² (values were determined from chapter 4). To test this, $\gamma_{d,\phi=0}$ is plotted as a function of $L_{BD=ED}/L$ as shown in figure 6.2A and shows $\gamma_{d,\phi=0}$ to decrease with $L_{BD=ED}/L$ in a well defined manner. Equation 6.1 is also plotted in figure 6.2A using the values above and it follows the data very closely. This result highlights the consistency between graphite and graphene measurements and also the consistency between simulation and experiment.

Previously, we have shown ϕ_0 to be related to the defect content of graphite and graphene by relating it to I_D/I_G from raman spectroscopy (as shown in figures 4.11B & 5.6C). A quantitative model of ϕ_0 was also developed by relating it to the fraction of high energy sites found on the surface ($\phi_0 = \beta f_{HE}$) using the equation:

$$\phi_0 = \beta \times \frac{(N/A)_{D,B} A_{HE} + 2\sqrt{1+k^2}t/L}{1 + 2\sqrt{1+k^2}t/L} \quad (6.2)$$

Figure 6.2C shows ϕ_0 as a function of t/L ; where $t \approx 100$ nm for graphite and $t = d_0 R_N N$ for graphene. There is a clearly defined increase of ϕ_0 with t/L , where the black line is a plot of equation 6.2 using the values calculated above for $A_{HE}(N_{D,B}/A)$ and β . Again, this shows that the data and models are consistent for both graphite and graphene.

We are able to explain the relationship between $\gamma_{d,\phi=0}$ and ϕ_0 shown in figure 6.1C by combining equations 6.1 and 6.2 to get the expression:

$$\gamma_{d,\phi=0} \approx \gamma_{d,\phi=0}(L = 0) + 2[\gamma_{d,\phi=0}(L = \infty) - \gamma_{d,\phi=0}(L = 0)]e^{-\ln 2 \frac{\phi_0}{\beta A_{HE}(N_{D,B}/A)}} \quad (6.3)$$

This equation is plotted in figure 6.1C as shown by the dashed line using the values of $\gamma_{d,\phi=0}(L = 0)$, $\gamma_{d,\phi=0}(L = \infty)$, $A_{HE}(N_{D,B}/A)$ and β from above. This equation

shows excellent agreement with the measured data, once again highlighting the consistency of measurements from graphite and graphene studies as well as the models developed. The next steps are to test the robustness of the models developed by measuring the surface energy of different layered materials such as boron nitride and WS₂, this is discussed more in chapter 8.

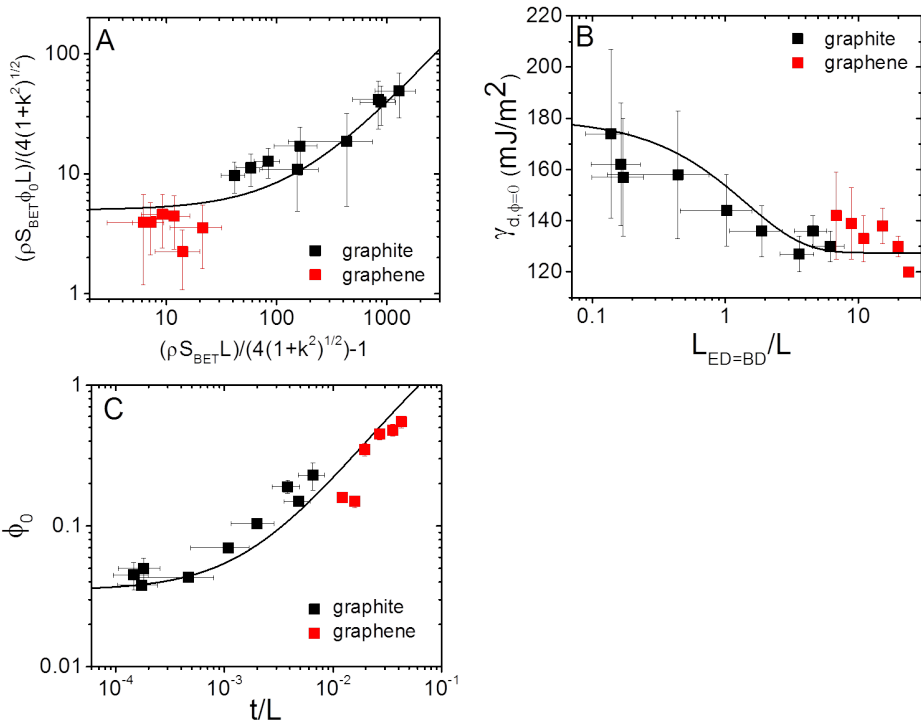


Figure 6.2: Comparison of graphite and graphene data with developed models. A) Specific surface area, surface energy, TEM and SEM data parametrised using equation 4.16, where the black curve is linear fit. This shows that graphite and graphene have the same values of $A_{HE}(N_{D,B}/A)$ and β . B) $\gamma_{d,\phi=0}$ as a function of $L_{BD=ED}/L$ showing a well defined fall off of $\gamma_{d,\phi=0}$ with $L_{BD=ED}/L$. The bold line is a plot of equation 6.1 using the values $\gamma_{d,\phi=0}(L = 0) = 125$ mJ/m² and $\gamma_{d,\phi=0}(L = \infty) = 180$ mJ/m². It should be noted that the curve is not a fit to the data. This result highlights the agreement between simulation and experiment. C) ϕ_0 as a function of t/L , the black line is a plot of equation 6.2 using the calculated values of $A_{HE}(N_{D,B}/A)$ and β .

Chapter 7

Understanding the Dispersion and Assembly of Bacterial Cellulose in Organic Solvents

7.1 Overview

The aim of this chapter is to show that low dimensional nanomaterials, in this case bacterial cellulose (BC), can be dispersed/exfoliated in liquid media to its constituent nanofibrils (BCN) by matching the measured surface energy of the material with that of a solvent. We show that the high coverage surface energy of BC measured with IGC agrees with the inferred surface energy from a solubility study, further validating our assertions from previous chapters that surface energy at high coverage is the intrinsic surface energy of the material. It was found that sonicating BC in various solvents produces BCN of various diameters. From this, BCN films were produced whose mechanical properties were shown to depend on nanofibril diameter and porosity. Since nanomaterial diameter was shown to depend on solvent and hence surface energy, we have shown a new method of controlling BCN films mechanical properties via the knowledge of its surface energy.

7.2 Introduction

A detailed introduction to the structure and properties of BC is given in section 2.5 but a brief summary of that section is that BC is a biopolymer of glucose molecules that is secreted by species of bacteria such as *Glucanobacter xylinum*.[93] During growth, adjacent molecules of cellulose aggregate through hydrogen bonding and dispersive Van der Waals interactions into BC nanofibrils (BCN).[82] Bacterial cellulose nanofibrils (BCN) are ribbon-shaped, with widths and thicknesses on the order of 10 nm, and lengths of several micrometers.[274] Structurally, BCN consist of stiff crystalline regions joined by more disordered amorphous segments, where the disordered domains form weak spots along a nanofibril. BCN has shown great promise as a environmentally friendly nanomaterial with the Young's moduli of individual BCN have been reported to be as high as 78-160 GPa.[102] These excellent mechanical properties and make BCN appealing for a variety of applications.[79] Furthermore, its ultrafine reticulated structure lends itself to applications including composite membranes [275, 91], artificial skin, and other medical applications.[274, 79, 276, 277] While the physical properties of BCN are extremely promising, their potential has been limited by their tendency to aggregate [88] through inter-BCN bonds to form larger and weaker fibers, typically \approx 100 nm wide.[101] The combination of intra- and inter-BCN bonding results in a stable hierarchical biopolymer.[82] Intra-BCN interactions are dominated by strong hydrogen bonds and dispersive Van der Waals forces [278], while inter-BCN interactions are a combination of weaker hydrogen bonds and dispersive forces.[279, 280, 118]

Deconstructing the hierarchical structure of BC fibers to individual BCN allows the high stiffness of the cellulose crystal to be exploited.[79] The bonds within an individual BCN are extremely strong and are responsible for the high axial chain stiffness of BC.[88] The bonds between neighbouring BCNs are weaker. While the inter-BCN network is more disordered, it is still relatively robust, making it extremely difficult to dissolve.[79] BC fibers are insoluble in water and in common organic solvents.[281] Despite this challenge, a number of methods to completely solubilise BC have been reported. Such routes include the use of lithium chloride/N,N-dimethylacetamide [282], NaOH/urea aqueous solutions [283], ZnCl₂ aqueous solutions [284], ionic liquids [285] and N-methyl morpholine-

N-oxide (NMMO) hydrate.[286] BC fibers can be reconstituted from these solutions using spinning techniques.[287] Unfortunately, these manufactured fibers were found to have lower degree of crystallinity (compared with the starting material) and, hence, lower mechanical properties.

To disrupt the hierarchical structure of BC to produce individualised BCN, we used liquid phase exfoliation which has been previously used to disperse similarly insoluble one-dimensional (1D) materials, such as single-walled carbon nanotubes (SWNTs) [288, 66] and nanowires (NWs).[289] Like BC, the properties of these materials are limited by their tendency to aggregate (through van der Waals interactions). Due to their rigidity and other factors, these macromolecules have very limited solubility in organic solvents. Nevertheless, solvents capable of producing stable dispersions of individual SWNTs and NWs were uncovered. The central finding of that work was that the concentration of exfoliated nanomaterial could be maximized by choosing solvents whose surface energies matched the surface energy of the nanomaterial. This chapter outlines how BC can also be dispersed to individualized BCN in a range of organic solvents and proposes a thermodynamic framework to predict dispersants for BC (based on BC's similarity to other rigid 1D nanomaterials). It should be noted that this technique does not dissolve BCN but rather it is dispersed by ultrasonication and stabilized in a suitable liquid. Neat films prepared from dispersed BCN show a clear correlation between the degree of dispersion and the mechanical properties of the BC films.

7.3 Experimental Methods

7.3.1 Materials

BC was kindly provided by fzmb GmbH (Forschungs- zentrum fur Medizintechnik and Biotechnologie, Bad Langensalza, Germany). The following organic liquids, N-methyl-2-pyrrolidone, ethylene glycol, dioxane, dichloromethane, ethanol amine, cyclohexyl-pyrrolidone, benzyl alcohol, N-dodecyl-pyrrolidone, cyclohexanone, and toluene (all HPLC grade), were purchased from Sigma-Aldrich. Inverse gas chromatography (IGC) probe molecules (decane, nonane, octane, heptane, hexane, ethanol, and 1-propanol) were purchased from Sigma-Aldrich (all HPLC grade).

Helium and methane (IGC carrier gas and dead-time probe gas) were purchased from BOC (research grade).

7.3.2 Methods

Freeze-Drying BC

The BC was supplied as wet pellicles containing 94 wt % water. The synthesis of BC pellicles used in this study is described in literature.[276] The BC pellicles were cut into small pieces and blended in to water for 2 min using a laboratory blender (LB20EG, Christison Particle Technologies, Gateshead, U.K.) at a concentration of 4 g/L. The suspension was then further homogenized (Polytron PT 10-35 GT, Kinematica, Lucerne, CH) for 2 min to produce a uniform suspension of BC in water. This suspension was then flash-frozen in a Petri dish by immersion in liquid nitrogen and subsequently freeze-dried (Heto PowerDry LL1500 Freeze-Dryer, Thermo Scientific, UK). The residual water content of the freeze-dried BC was determined using dynamic vapor sorption (DVS-Advantage, Surface Measurement Systems Ltd UK). A total of 30 mg of freeze-dried BC was loaded into the chamber of DVS held at 0% relative humidity for 5 h. During this period, the mass change of the sample was measured. The residual water content was obtained from the difference between the initial and final mass of the sample. The equilibrium water content post freeze-drying was 23 ± 6 mg g/L (mg of water per gram of BC)¹.[290]

BC Dispersion and characterisation

Aliquots (20 mL at concentrations of 1 mg/mL) of BC were dispersed in organic liquids using an ultrasonic tip (Sonics vibra cell 750 W tapered tip at 20% amplitude for 30 min with ice cooling) and centrifuged for 30 min at 4000 rpm. Tapping-mode atomic force microscopy (Bruker Multimode, silicon cantilever with radius of 10 nm) was used to assess the dispersion quality for each aliquot. Samples were prepared by taking a small drop from each dispersion and drop-casting it on a SiO₂ substrate and drying in a vacuum oven at 80 °C for 24 h. These conditions were chosen to minimize reaggregation on drying. The diameters of >50 nanofibrils were measured for each AFM sample.

¹The Freeze dried BC was supplied with thanks to Dr. Koon-Yang Lee

The concentration of dispersed BC in each solvent was determined spectroscopically. UV-Vis-NIR absorbance spectra were recorded with a Cary 6000i, Agilent. The extinction coefficient of BC at 600 nm (there are no absorption peaks in the spectrum in this range) was determined by measuring the absorbance of a series of stepwise dilutions whose precise concentrations were known. A stock mixture was prepared by adding 10.0 ± 0.3 mg of BC to 50.00 ± 0.01 mL of NMP and sonicating as described above. This stock solution was precisely diluted by 50% a number of times using volumetric flasks. The concentration of BC in dispersed media was calculated using the Beer-Lambert law ($A = \epsilon CL$, see section 3.3), relating the absorbance, A , of a species to its extinction coefficient, ϵ ; concentration, C ; and the path length of the sample cell, L .

BC Film Preparation

BC films were prepared from a range of organic liquids (see table 7.3). For each, two aliquots of 20 mg of BC in 87.5 mL of organic liquid were sonicated (750 W for 3 h, pulsing 5 s on/off with stirring and ice-cooling). The dispersion was vacuum filtered onto a nylon membrane (Whatman, 47 mm diameter and 45 μm pore size). The films were dried in a vacuum oven at 60 °C for 2 days. The tensile properties of each film were recorded using a Zwick Roell Z005 (equipped with a 100 N load cell). The porosity of the films (P) was calculated based on dimensional analysis and the mass of BC films using the equation:

$$P = 1 - \frac{\rho_{film}}{\rho_{BC}} \quad (7.1)$$

Where ρ_{film} is the film density and $\rho_{BC} = 1500 \text{ kg/m}^3$.[291] Two of the neat cellulose films were subjected to mild hot-pressing (10 min, 80 °C, 50 kN; Rondol Technology, UK) to assess the effect of increasing film density on tensile properties.

Inverse Gas Chromatography

The surface energy of BC was measured using inverse gas chromatography (IGC; Surface Energy Analyser, Surface Measurements Systems Ltd., UK). A total of 10 mg of freeze-dried BC was packed into a glass column of 2 mm internal diameter. Silanised wool was used to plug both ends. Samples were preconditioned at 150 °C

under helium with flow rate 20 mL/min to remove any loosely adsorbed surface containments, this is discussed more in appendix 8.2. Alkane probes (decane, nonane, octane, heptane, hexane) were used to measure the dispersive surface energy (γ_d) of the sample and specific probes were injected through the sample to measure specific interactions (γ_{sp}). A flow rate of 20 mL/min and a temperature 30 °C were used for all IGC measurements. Retention times were measured using a flame ionization detector (FID).

7.4 Results and Discussion

Can BC be dispersed to BCN in organic solvents

To determine if the network structure of BC could be disrupted by sonication to yield BCN, N-methyl pyrrolidone (NMP) was used as a dispersing medium due to its remarkable success at dispersing carbon nanotubes [66], graphene [7], and transition metal dichalcogenides.[74] It was found that the sonication of freeze-dried BC in NMP produced a clear, homogeneous dispersion as shown in figure 7.1A. A comparable experiment of BC sonicated in chloroform had little dispersive effect; BC remained aggregated and two phases were clearly visible (figure 7.1B). To assess the state of the BCN in NMP dispersion, AFM was used. A representative image for this sample is shown in (figure 7.1C) which shows a large population (figure 7.1D) of BCNs with average heights of 10.7 ± 0.5 nm (figure 7.1E) and lengths of several micrometers (figure 7.1C). Such measurements are consistent with the dimensions of BCNs previously reported.[274] These results suggest that the networked assembly of primary BC has been successfully disrupted. It is important to stress that these findings do not suggest that NMP dissolved BC molecules, as NMNO or ionic liquids do [79], forming a polymer solution.

The concentration of dispersed BCN in organic solvents was determined spectroscopically using the Lambert-Beer law ($A = \mathcal{E}CL$). A typical BCN absorption spectrum is shown in figure 7.2. The absorbance spectra of dispersed cellulose are dominated by a power-law scattering background at lower wavelengths ($\propto \lambda^{-n}$). A scattering exponent, n, of 3.97 ± 0.03 was obtained from a fit of the spectrum in figure 7.2. This exponent value is consistent with a Rayleigh scattering ($\propto \lambda^{-4}$), where the dimensions of the scattering particles are small, up to $\approx 10\%$ of the

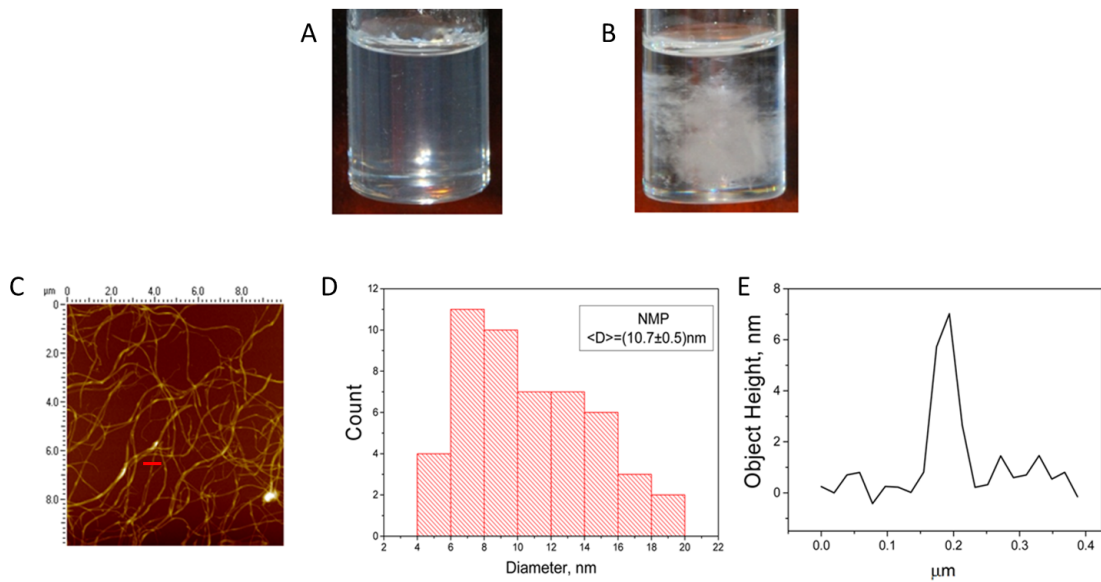


Figure 7.1: BC sonicated in A) N-methyl-2-pyrrolidone (NMP) showing a clear homogenised dispersion and B) chloroform: showing BC has not been dispersed. C) AFM image of BCN-NMP dispersion showing a large concentration of dispersed BCN. D) AFM statistics of BCN dispersed in NMP. E) AFM cross-section of a single BCN, marked with red line in C.

wavelength of the incident light. The exponents of multiple spectra were recorded and were found to be independent of concentration. This consistency suggests differences in absorbance between spectra are due only to differences in concentration of dispersed BCN.

To apply the Lambert-Beer law and determine the concentration of dispersed BCN, it was necessary to first determine the extinction coefficient (\mathcal{E}) of BCN. Plotting the absorbance per unit path-length of a serially diluted BCN NMP dispersion against concentration, as shown in the inset of figure 7.2, yielded an extinction coefficient of $200 \pm 6 \text{ mL/mg.m}$. To the best of our knowledge, there are no reported values of the extinction coefficient of BCN, but this result is reasonably consistent with reported value of 264 mL/mg.m for primary bacterial cellulose.[292] Using our measured extinction coefficient, the concentration of dispersed BCN in NMP was determined to be $0.13 \pm 0.04 \text{ mg/mL}$.

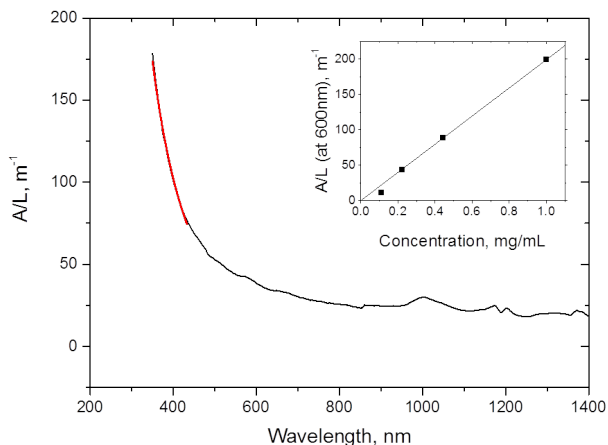


Figure 7.2: A typical UV-vis spectrum of BC. The red line is a fit of the scattering exponent ($n = -3.97$). The inset shows the absorbance at 600 nm of serially diluted BC dispersions. The line is a fit of the data, with the slope being the extinction coefficient from the Lambert-Beer law.

Thermodynamic Prediction of Organic Solvents for BC Dispersions

To investigate if other organic liquids enable dispersion of BC to BCN, it was sonicated in a wide range of organic liquids in an analogous way to the NMP dispersion described above. Organic liquids producing poor dispersions, where two distinct phases (liquid and BC) were clearly evident after sonication were discarded. Water was also shown to have no dispersive effect. The concentrations of dispersions of BCN in organic liquids that turned transparent upon sonication were determined spectroscopically and are shown in table 7.1. BC dispersions, with concentrations of up to 0.20 mg/mL, were obtained in a range of organic liquids. To investigate the make up of these dispersions, AFM measurements were conducted on samples prepared from the 10 solvent dispersions with the highest concentrations of dispersed BC.² These images were analyzed, measuring the heights of ≈ 50 BCN per dispersion, as shown in figure 7.3. Average object height measured for each solvent ranged from 10.7 ± 0.5 nm NMP to 16.2 ± 0.7 nm for cyclohexyl-pyrrolidone. This data suggest that a reasonable population of individual nanofibrils are present for samples dispersed in organic solvents as

² Many thanks to Dr Shane Bergin for carrying out the AFM measurements

shown in table 7.1. The solvents that were shown to have no dispersive effect are shown in table 7.2.

Table 7.1: Concentration of BCN in successful organic solvents

<i>Solvent</i>	<i>BCN concentration, mg/mL</i>
N-ethyl-2-pyrrolidone	0.20 ± 0.11
dioxane	0.16 ± 0.09
dichloromethane	0.16 ± 0.04
ethanol amine	0.16 ± 0.03
cyclohexyl-pyrrolidone	0.13 ± 0.04
benzyl alcohol	0.12 ± 0.03
N-dodecyl-pyrrolidone	0.11 ± 0.01
toluene	0.11 ± 0.01

Table 7.2: Solvents that were unable to disperse BC

<i>Solvent</i>
Water
Toluene
Propylene carbonate
Benzaldehyde
Benzonitrile
Pyridine
Heptane
Vinyl acetate
Acetone

In order to ascertain the qualities of a "good dispersion medium" for BC and predict effective liquids to disperse it, we turn to the considerable body of work on the dispersion of single walled carbon nanotubes (SWNTs) as both can be considered to be rigid 1D systems with limited dispersibility in most common solvents.[66] This is covered in more detail in section 2.6. The miscibility of any solute-solvent system is given by the Gibbs free-energy of mixing, ΔG_{mix} , a balance of enthalpic (ΔH_{mix}) and entropic (ΔS_{mix}) terms.[144]

$$\Delta G_{mix} = \Delta H_{mix} - T\Delta S_{mix} \quad (7.2)$$

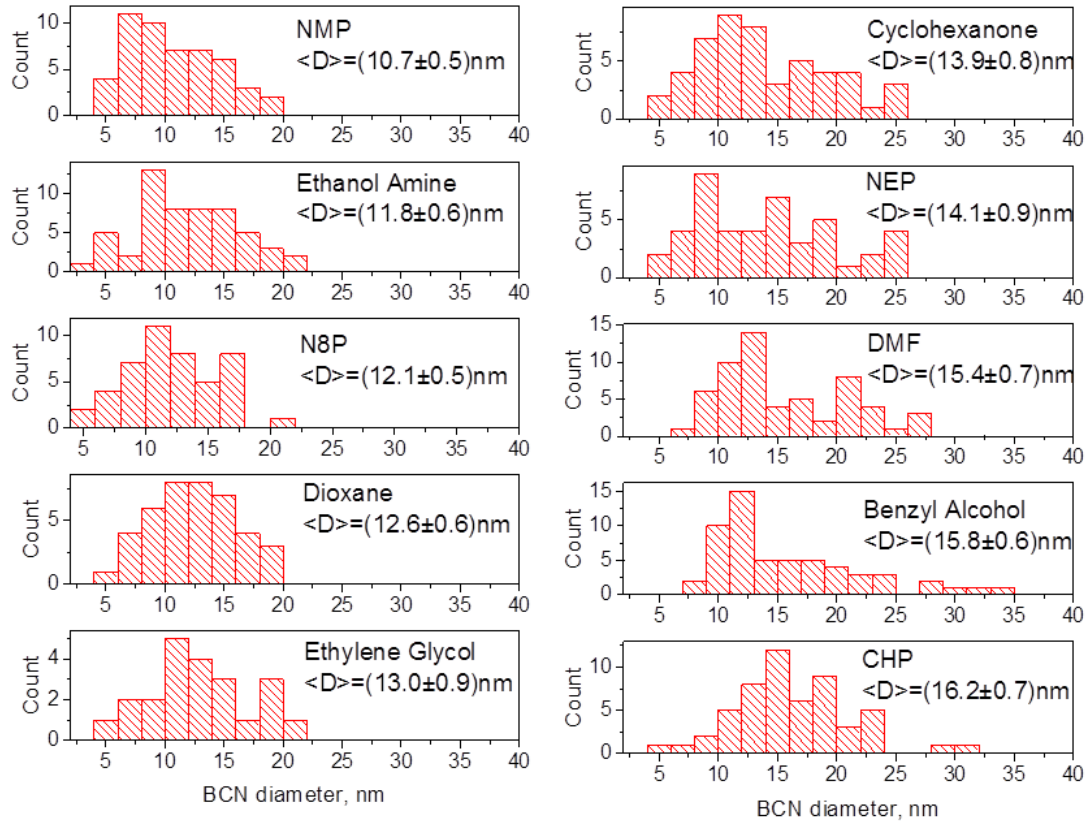


Figure 7.3: Height distributions of BCN from optimum solvents measured by AFM

A good dispersion medium implies a thermodynamically stable mixture over a range of concentrations and temperatures [293] (i.e. ΔG_{mix} is close to 0 or negative). Previous findings showed the challenge of dispersing rigid 1D rigid nanoparticles stems from the fact that the entropy of mixing, ΔS_{mix} , is very small for dispersions of rigid 1D macromolecules.[294] Thus, the enthalpy of mixing, ΔH_{mix} , must be small or negative, for mixing to occur. ΔH_{mix} for mixtures of solvents and SWNTs was found to be minimized when the surface energy (this, in fact should be called surface enthalpy) of the solvent, γ_l , matched that of the nanomaterial, γ_{NM} [66]:

$$\frac{\Delta H_{mix}}{\Delta V} = \frac{2}{R_{bun}} (\gamma_{NM} - \gamma_l)^2 \phi \quad (7.3)$$

where R_{bun} is the radius of the bundle of SWNTs and ϕ , the SWNT volume

fraction. The surface enthalpy of a solvent is related to its surface tension (surface free energy), σ , using the equation: $\gamma = \sigma + TS$, where S is the universal value for surface entropy of $\approx 0.1 \text{ mJ/m}^2\text{K}$.[147] The differences between surface tension and surface enthalpy of a solvent is discussed in detail in section 2.6. In solubility studies of this nature, surface energy of the solvent is used interchangeably with surface enthalpy. However, surface enthalpy is the correct term as shown in equation 2.6 but to be consistent with the nomenclature, the term solvent surface energy is used.

The route to discover a suitable dispersion medium for nanomaterials that aggregate through dispersive Van der Waals forces, summarised in equation 7.3, has been remarkably successful.[66, 295, 296] Solubility studies for SWNTs, graphene, and a range of other 2D nanomaterials show a peak in concentration of the dispersed material in organic liquids with surface energies close to 70 mJ/m^2 , where the surface energies for each of these nanomaterials are reported as being close to 70 mJ/m^2 . Figure 7.4 shows the concentration of dispersed BCN (in a range of solvents) plotted against the surface energy and surface tension of the dispersion medium. One can clearly see from figure 7.4 that optimum dispersion media have similar surface energies. Our findings suggest the physical properties of organic solvents used as dispersion medium of a range of low-dimensional nanomaterials, appear to also apply to the dispersion of BC, a material in which aggregation is due to a combination of dispersive and H-bonding forces.

Equation 7.3 implies that since stable dispersions of BCN are produced in organic solvents with surface energies close to 75 mJ/m^2 . Therefore, surface energy of BC must be close to 75 mJ/m^2 .[238, 65, 74] We note, however, that it is difficult to find suitable organic liquids to test BC dispersibility with higher surface energy values. Figure 7.4 shows that there is a clear trend of BC dispersibility with surface energy. Thus, an accurate measure of BC's surface energy is essential to ensure the dispersion route outlined in equation 7.3 is valid for BC and furthermore, to demonstrate that this route toward liquid-phase exfoliation can be applied to systems that are not bound solely by dispersive forces.

Inverse gas chromatography of BC

IGC was used to determine the surface energy of BC. While numerous techniques

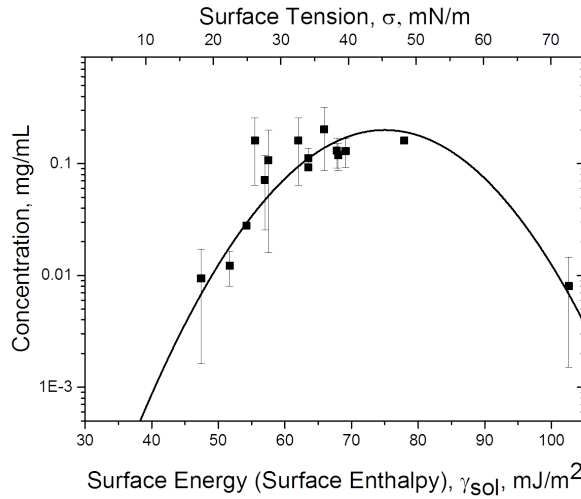


Figure 7.4: Concentration of BCN dispersed in various organic liquids plotted against liquid surface tension (σ) and surface energy (surface enthalpy) (γ).

have been reported to measure the surface tension of natural fibers, it seems that those based on the analysis of measured contact angles are unsuited to the natural fibers with an irregular geometry.[297] Using coverage dependent IGC, the surface energy of a packed bed of freeze-dried BC was determined from measured retention times, t_N (and corresponding retention volumes, V_N), for a series of known probe molecules eluting through a column). The dispersive surface energy (γ_d) of BC was measured using the Schultz method, which is discussed more in section 3.2.[198]

Figure 7.5A shows data recorded by IGC at 6% coverage of the BC surface. The dashed line is a fit to this data, which corresponds to a γ_d value of 42 mJ/m².

As outlined previously, BCNs aggregate through a combination of dispersive Van der Waals and H-bonding forces.[278] Thus, the total surface energy of BC will reflect the energies required to disrupt both dispersive and specific interactions. The dispersive component of surface energy, γ_d , of BC determined by IGC accounts for dispersive interactions and does not incorporate the contribution of specific interactions, such as H-bonds, to BC's surface energy. To measure the total surface energy of any material, we can crudely sum the dispersive term, γ_d , and the specific terms, γ_{sp} .[196] γ_{sp} was determined using the method described in section 3.2.1.2 and illustrated in figure 7.5A. However, this method gives a measurement of ΔG_{sp} which has units of kJ/mol, this can be crudely converted into units of mJ/m² by

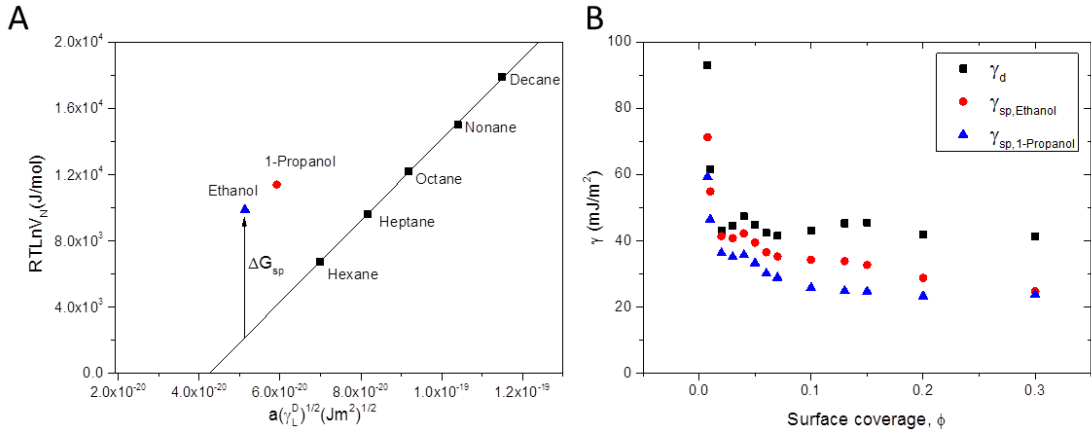


Figure 7.5: A) Free energy of adsorption ($RT\ln V_N$) as a function of dispersive energy of IGC probe vapor ($\gamma_{d,l}$) and the probes cross-sectional area (a). These data correspond to 6% coverage. B) Dispersive and specific surface energy (ethanol and 1-propanol) of BC as a function of BC surface coverage (ϕ).

using the equation: [202, 74]:

$$\gamma_{sp} = \frac{\Delta G_{sp}}{aN_A} \quad (7.4)$$

Where a is the cross sectional surface area of the probe molecule. We note however, that measured values of γ_{sp} are not intrinsic to the solid as they rely on interaction between the probe and the solid surface. They do, however, give an excellent indication of γ_{sp} . γ_{sp} profiles were measured for ethanol and 1-propanol as shown in figure 7.5B. One can sum γ_d and γ_{sp} terms to give a rather crude figure for the total solid surface energy.[298] Depending on the specific probe, the total surface energy for BC ranges from $\approx 72\text{-}79$ mJ/m² in the flat region of the surface energy profiles.

In general, published values of γ_d cellulose (as measured with IGC) are higher than those presented in this work. Papirer *et al* [299] report γ_d values up to 52.3 mJ/m² for microcrystalline cellulose and claimed dispersive and specific surface energies of cellulose scale with the degree of cellulose crystallinity. These authors also showed specific probes capable of H-bonding with cellulose to yield higher specific surface energy values ($\gamma_{sp} = 78.6$ mJ/m² for ethanol (16.7 kJ/mol)) than other specific probes that are not capable of such H-bonding. Elsewhere, γ_d val-

ues for BC of 61 [297] and 66 mJ/m² [91] have been reported. These values are higher than those for other forms of cellulose, a result attributed to the effects of crystallinity.[300] It is worth noting that, for these previous studies, IGC measurements were made at infinite dilution. As discussed previously, ID-IGC surface energy values are generally due to the highest energy sites on a sample surface, such as defects and aren't representative of the sample as a whole. To investigate the surface energy (both γ_d and γ_{sp}) of BC we measured its surface energy profile as shown in figure 7.5B which has the typical γ profile shape, with highest values at lowest coverage which reduces with coverage to a plateau value. Measured values of γ_d and γ_{sp} at low surface coverages are consistent with values for BC referenced above. Also, as previously discussed, the surface energy at the plateau region is a far more informative figure for dispersibility studies, where interaction with a liquid will be across most, if not all of the surface.[241] Assuming that the plateau value from Figure 7.5B of 79 ± 7 mJ/m² can be extrapolated to the fully solvated situation [241], there appears to be good agreement with the dispersibility study shown in figure 7.4, which suggested that solvents with surface energies of ≈ 75 mJ/m² were best for dispersing BC. The broad overlap of BC surface energy values (as measured by IGC) with the surface energies of solvents that yielded stable BC dispersions (as shown in Figure 7.4) suggests that the approach of matching the surface energy of the dispersion medium to that of BC, to disperse BC to their constituent BCN, is valid. While not every organic liquid that fulfils this criterion will produce BCN dispersions, the method is an excellent aid for identifying new dispersion media.

Mechanical properties of BCN Films

In order to ascertain the effect of BCN dispersant choice on the mechanical properties of the processed material, BC was dispersed in a range of organic liquids and processed to form pure BCN films (nanopapers) by vacuum filtration on a nylon membrane. Well formed, homogeneous, free-standing BCN films were obtained (typical photograph shown in figure 7.6A, with a porous nanofibrous architecture clearly visible via helium ion microscopy³ (figure 7.6B). The films were found to have a porosity in the range of 40-70%, directly after vacuum drying (see table

³Many thanks to Alan Bell from AML for the assistance in acquiring the helium ion images.

7.3). Typical stress-strain curves of the BCN films are shown in figure 7.7. Tensile strengths and moduli of films with a porosity of around 40% reached up to 114 ± 12 MPa and 2.2 ± 0.7 GPa, respectively. These values are lower than those reported elsewhere for films hot compacted against a hydrophobic surface during drying (which prevents the film from shrinking). Considering the low-density/high-porosity nature of the films reported here, however, the mechanical properties are within the range of mechanical responses for cellulose films, as reviewed by Moon *et al.*[82]

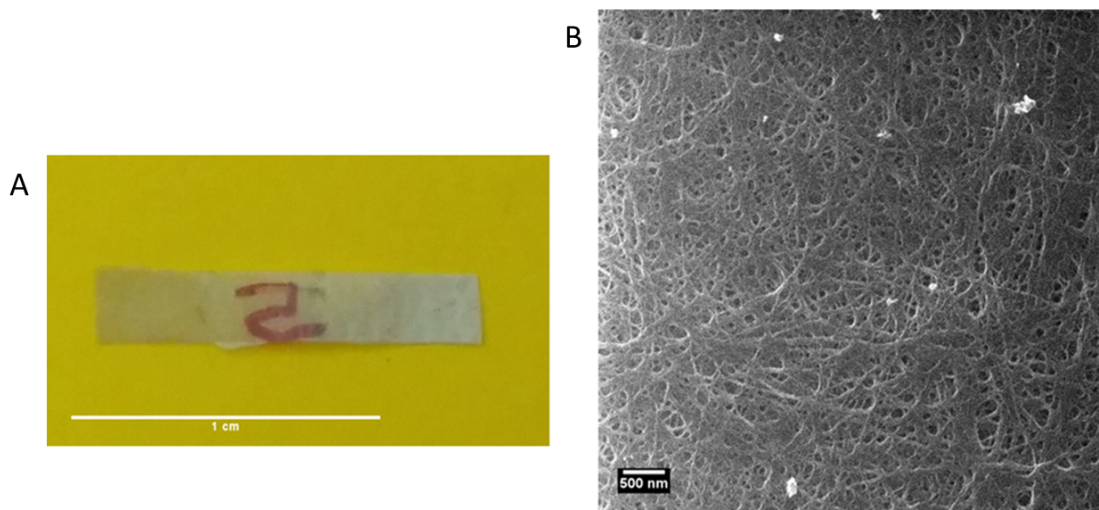


Figure 7.6: A) Photo of a typical BCN film. B) Helium ion image of the porous BCN network; both were prepared using NMP as the solvent.

Table 7.3: Density and porosity of BCN films

Solvent	Number of Samples	ρ_{film} (kg/m ³)	Porosity, % (P)
N-methyl-pyrrolidone (hot pressed)	8	1084 ± 113	28 ± 3
ethanol amine	7	929 ± 48	38 ± 2
N-methyl-pyrrolidone	7	909 ± 27	39 ± 4
cyclohexanone (hot pressed)	9	836 ± 102	44 ± 5
dimethylformamide	7	810 ± 36	46 ± 2
dioxane	7	570 ± 52	62 ± 6
cyclohexanone	7	462 ± 100	69 ± 15

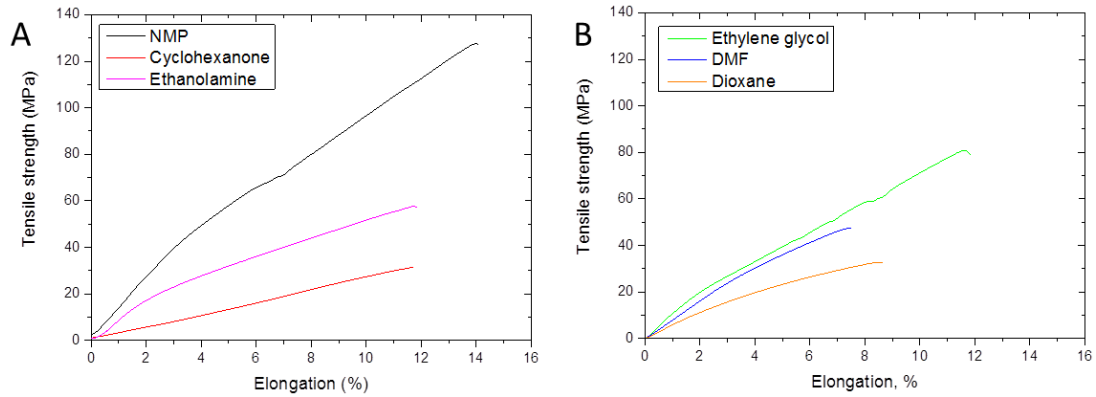


Figure 7.7: Representative stress-strain curves of individual BCN films prepared by A) N-methyl-pyrrolidone (NMP; black), cyclohexanone (red), and ethanol amine (magenta). B) Representative stress-strain curves of individual BC papers prepared by ethylene glycol (green), dimethylformamide (DMF; blue), dioxane (orange)

Several factors have been shown elsewhere to affect the mechanical response of pure cellulose films, including orientation of the constituent fibrils [301], porosity [302], the density of contact-points between fibrils [303, 304, 305], the fibril morphology, and moisture content.[82] This breadth of factors gives an excellent opportunity to engineer films as required for further applications.

For the BCN films in this study, the Young's moduli of the films scale with the square of the BC paper density (figure 7.8). Such a square-dependence is consistent with a well-ordered hierarchical structure as opposed to the $E \propto \rho^3$ trend observed for more disordered structures.[306] Recent work by Qui *et al* [307] on low-density graphene structures also observed a density-squared power law with Young's modulus.

If we consider BCN films to be random planar networks of rigid fibers, where exfoliation of the constituent fibrils is essential to their overall mechanical performance, we can draw analogies with the considerable body of work published for single-walled carbon nanotube (SWNTs) films. In this work it was shown that the mechanical behavior of SWNT films was correlated with the SWNT-SWNT junction-density [308]; accounting for the fact that mechanical properties of these films are most likely controlled by a combination of nanomaterial size and porosity. While the constituent SWNTs are extremely strong, the mechanical properties of

a film made from them will be limited by the properties of the weakest links, the junctions of criss-crossing nanotubes. Blige *et al* developed an expression linking the number of junctions per volume, N_J , to the diameter of the CNT's and the porosity of the film, given by:

$$N_J \approx \frac{16}{3\pi} \frac{(1-P)^2}{D^3} \quad (7.5)$$

where P is the porosity of the film and D the average diameter of the nanomaterial. The tensile strength, Young's modulus, and toughness of SWNT films were shown to scale with N_J . One might expect that films of neat BCNs should show a similar dependence if nanofibril junction density (where nanofibril junction is defined as the overlap region of two nanofibrils, analogous to SWNT junctions) controls their overall mechanical response.

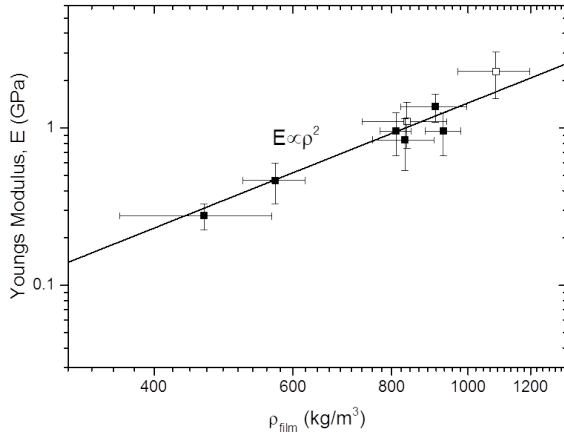


Figure 7.8: Young's modulus, E of BCN films prepared in a variety of solvents as a function of film density. The Young's modulus scales with density squared ($E \propto \rho_{film}^2$) which is consistent with BCN films being well ordered hierarchical structures. The open data points correspond to BC papers that have been hot pressed

To test this hypothesis, the mechanical response of BCN films was plotted against the number of junctions per volume, N_J , for each film as shown in figure 7.9. The bundle diameters from figure 7.3 were used as D. Figure 7.9A shows that Young's modulus of BCN films indeed scales with N_J . While it has been

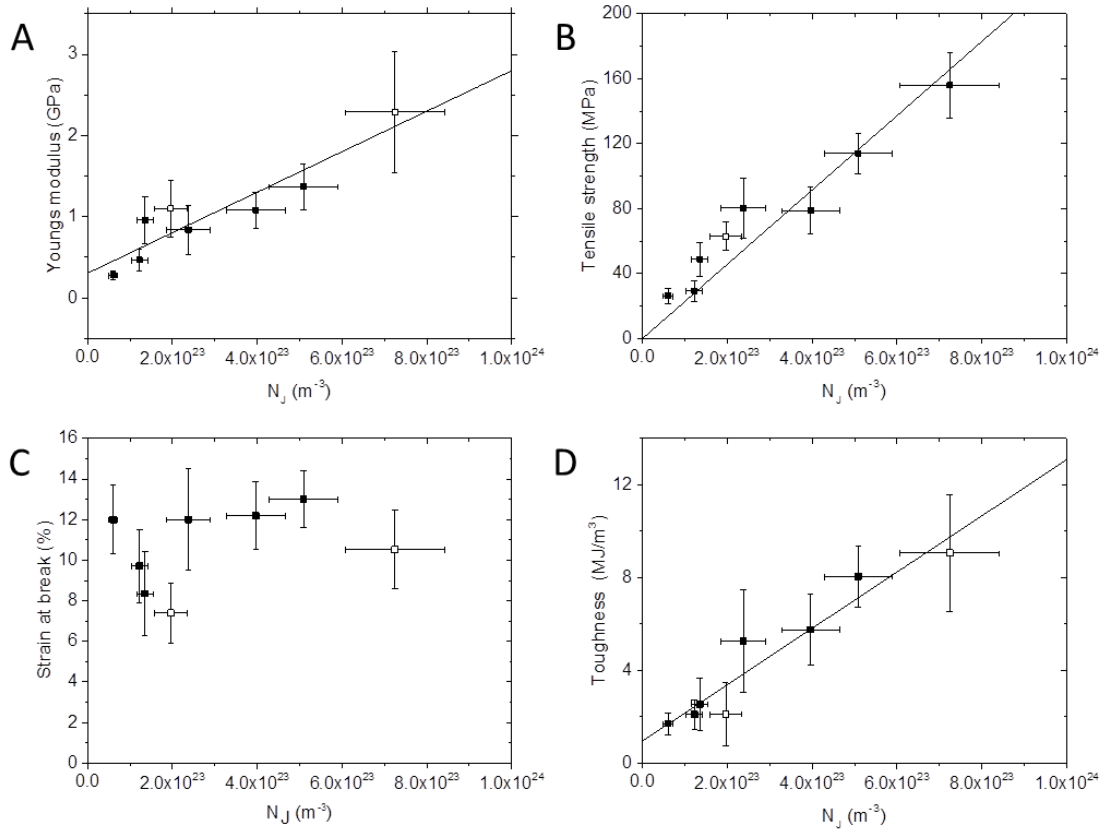


Figure 7.9: Tensile properties of BCN films as function of BCN junction density. A) Young's Modulus, B) Tensile strength, C) Toughness are all shown to scale with BCN junction density while D) Strain at break was found to be junction density independent. The open data points correspond to films that have been hot pressed

demonstrated that the Young's modulus of low-density films scales with the film density, this work shows that reducing the average diameter of the constituent BCN fibers dramatically improves the modulus of the film, by increasing the density fibril/fibril junctions.

The tensile strength of the BCN films also scaled with N_J (figure 7.9B). Blighe *et al* [308] also demonstrated that the average force required to break a junction in a SWNT film, f_J , could be determined from a fit of tensile strength against N_J . Speculating that any film fracture involves the breaking of junctions in a volume, $V_R \approx AL$, where A is the film cross- sectional area and L is the mean fiber length

and that, on fracture, every bundle in this volume breaks half its junctions, gave the film strength as:

$$\sigma \approx \frac{f_J L}{2} N_J \quad (7.6)$$

Fitting this equation to the data in figure 7.9B gives $f_J \approx 305 \pm 20$ pN where L was taken as $1.5 \mu m$ (measured L from AFM images in NMP gave $L = 1.4 \pm 0.4 \mu m$. For simplicity we take $L = 1.5 \mu m$) This value of f_J for the BCN film compares with that of $f_J \approx 113$ pN for a film of SWNTs.[308] The higher value of f_J for the BCN film is not surprising when one considers the combined effects of H-bonding and Van der Waals forces between BCNs. If we assume that the application of f_J leads to an opening of a gap between the bundles to ≈ 1 nm before breaking, we can calculate the fracture energy per junction to be ≈ 2 eV. This value should be comparable to the fracture energy calculated from the measured BC surface energy of 75 mJ/m² by IGC and the solubility study. By estimating the overlap area between junctions to be ≈ 3 nm² from contact mechanics of two crossed cylinders of equal radius (≈ 10 nm from AFM measurements) and a deformation depth of 1 nm, we can estimate the fracture energy to be ≈ 2.8 eV per junction. Considering the very approximate nature of these calculations, they show very good agreement.

Figure 7.9C shows that the strain at break is independent of N_J , as a result, the film toughness also scales with N_J as shown in figure 7.9D.

The relationship shown in figure 7.9 between the mechanical response of neat BCN films and N_J of the film, suggests that one can control the mechanical properties of a film by carefully controlling the extent of BCN dispersion from which the films/nanopapers are being produced. Moon *et al*'s extensive review [82] on cellulose nanomaterials shows the mechanical properties of neat BCN films to be strongly influenced by issues including pellicle purification, compaction pressure, drying temperature, and pellicle defibrillation. This chapter adds to that work showing the extent of BCN exfoliation (as given by the bundle junction density) to have significant impact on the film's mechanical behaviour.

7.5 Conclusion

In this chapter, BC was exfoliated from its primary fibers to its constituent nanofibrils (BCN) by liquid phase exfoliation in organic liquids. The highest concentrations of dispersed BCN were found for liquids whose surface energies matched the surface energy of BC (as measured by inverse gas chromatography). In this regard, the dispersibility of BC appears to follow a similar trend to the dispersibility of other low dimensional nanomaterials such as graphene and single-walled carbon nanotubes. While the predictive power of this route to exfoliated BCN is not absolute, it is a guide to uncovering new dispersion media for this intractable material. Notably, the ability of IGC to measure surface energy profiles and, hence, indicate the surface energy at higher coverages is an important advance in the current context and many others. Pure films of BCN produced from dispersions, in various solvents, showed a strong correlation between the mechanical response of the film and the degree of BCN exfoliation (expressed as a BCN bundle junction-density). These findings suggest a novel means to control the mechanical properties of BCN films, by considering and optimizing the junctions within the films.

Chapter 8

Conclusions and Further Work

8.1 Conclusions

The aim of this thesis was to further the understanding of the surface energy of low dimensional nanomaterials. Having knowledge of a materials surface energy is very important as it describes how materials interact with their environment. However, in the case of energetically heterogeneous solids, such as the ones studied in this thesis, are not very well known or understood. This task was largely achieved, however, like most research, there are still some questions that have to be answered. As a result, further research ideas are proposed that are a direct carry on from this work.

The surface energy of graphite was examined using inverse gas chromatography that can map the surface energy of a material with surface coverage via surface energy profiles. Using newly developed surface energy models it was possible to gain previously unknown insights into the make up of the surface energy of graphite. Preliminary tests on the specific surface area of several graphite samples found that the specific surface of graphite was largely flake length independent, implying that all graphite platelets had the same thickness of ≈ 100 nm. This was consistent with findings from SEM which showed that graphite samples were not monolithic in nature, but rather were made up of smaller stacked platelets, with thickness $< 1 \mu\text{m}$. Surface energy profiles showed high surface energy at low coverage which reduced with increasing coverage until a plateau value. This

allowed us to fit the profiles to a compressed/stretched exponential and extract the surface energy at low coverage ($\gamma_{d,\phi=0}$), full coverage surface energy ($\gamma_{d,\phi=1}$) and the decay constant (ϕ_0). Simulations of surface energy profiles provided details of the types of surface sites found in graphite; these were attributed to the graphitic basal plane, basal plane defects and edges. Simulations also showed that ϕ_0 is related to the amount of high energy sites, $\phi_0 = \beta f_{HE}$, with β believed to be a material dependent property due to the overall surface energy distribution of a material. With this in mind, we were able to attribute $\gamma_{d,\phi=1}$ as the intrinsic basal plane surface energy of graphite, which we found to be size independent with a value of $\gamma_{d,\phi=1} = 63 \pm 7 \text{ mJ/m}^2$ and $\gamma_{d,\phi=0}$ as the defect surface energy which ranged from 125-180 mJ/m². By modelling the graphite platelets as rhombuses, it was possible to differentiate between basal plane and edge defects by relating ϕ_0 to inverse flake length, which showed the amount of basal plane defects in graphite to be constant with the amount of edge defects depending on flake length. These results were completely consistent with simulations. By parametrising data from SEM, specific surface area and IGC it was possible to find that the basal plane defect density to be $\approx 10^{15} \text{ defects/m}^2$. From this, we showed $\gamma_{d,\phi=0}$ of large flakes ($> 100 \mu\text{m}$) to be dominated by higher energy basal plane defects and flakes $< 100 \mu\text{m}$ to be controlled by edges. This allowed us to predict that $\gamma_{d,\phi=0}$ for graphene to be $\approx 125 \text{ mJ/m}^2$.

The framework for the analysis of the dispersive surface energy of graphite was applied to size selected, liquid exfoliated graphene; seeing how successful exfoliation of graphite depends on surface energy, it was interesting to see differences, if any, between graphite and graphene. The basal plane surface energy, $\gamma_{d,\phi=1}$, of graphene was measured to be $62 \pm 4 \text{ mJ/m}^2$, while the defect surface energy, $\gamma_{d,\phi=0}$, was found to be between ≈ 120 -140 mJ/m², depending on flake size. This result is consistent with edge defects primarily contributing to $\gamma_{d,\phi=0}$, which is expected for graphene. The analytical models developed for graphite were shown to be qualitatively consistent with graphene measurements.

Graphite and graphene surface energy measurements were directly compared and were found to be consistent, finding $\langle \gamma_{d,\phi=0} \rangle = 63 \pm 6 \text{ mJ/m}^2$, independent of flake/nanosheet size. Using the models previously developed, we were able to calculate the percentage area of basal plane defects found on the graphite/graphene

surface to be $0.7 \pm 0.2\%$ and $\beta = 5 \pm 1$. From this, we proposed a model that describes the relationship between $\gamma_{d,\phi=0}$ and ϕ_0 , where the model and measurements show excellent agreement. The consistency found between graphite and graphene surface energy studies highlights the robustness of the models. It is hoped that this type of analysis can be extended to other types of materials as discussed below.

The dispersion of bacterial cellulose (BC) in organic solvents was examined. In this study, we showed how a knowledge of a materials surface energy can control the physical properties of exfoliated bacterial cellulose nanofibrils (BCN). As a result, we were able to control the mechanical properties of films made from them. BC was dispersed by sonication in a range of organic solvents with their diameters ranging from 10-16 nm. The inferred surface energy from a solubility shows agreement with the measured surface energy of BC by IGC, adding further evidence that $\gamma_{d,\phi=1}$ is a measure of the intrinsic surface energy of materials. Finally, films made from dispersed BCN mechanical properties showed clear correlation with BCN diameter and film porosity via N_J , the number of junction per unit volume. From this, we have discovered a new way of controlling the properties of BCN films. This could be important for the development of applications involving BCN.

8.2 Further Work

The most obvious next steps following on from the work in this thesis is to measure and understand the surface energy of other 2D layered materials such as boron nitride and MoS₂. The framework for the analysis of graphite and graphene should be applicable to all 2D systems and would give information such as defect content and intrinsic surface energy. Measuring material defect content would be beneficial to choosing a correct starting material for exfoliation, i.e. find the boron nitride powder with the least amount of defects. Measuring the intrinsic surface energy ($\gamma_{d,\phi=1}$) of other layered materials will make it easier to identify potential solvents for exfoliation. Also, analysing other 2D materials would give a better insight into the nature of β . We believe that it is a material parameter but more work needs to be done to confirm this.

Other possible studies include measuring the solubility parameters (both Hildebrand and Hansen) of 2D materials using IGC. There are many papers in the lit-

erature on measuring solubility parameters of materials using IGC but little work has been done on layered materials. Along with surface energy, solubility parameters are an excellent indicator whether a solvent will successfully exfoliate layered materials. Therefore, having a knowledge of a materials solubility parameters will help identify new solvents for exfoliation.

We showed a new method of controlling the mechanical properties of BCN films, this could be used for applications such as supercapacitors, optoelectronic devices and composites. The method developed here could be particularly advantageous because the porosity of the films can be tuned for a certain application, i.e. make a high porosity film where conducting materials can be embedded in the voids.

Appendix A: IGC Column Preconditioning

Preconditioning Process

A preconditioning step was used for all chromatographic measurements in this thesis to remove any loosely adsorbed contaminants, such as residual solvent in the case of liquid exfoliated graphene. The preconditioning step was the same for all samples and was as follows: The samples were heated to 150 °C for 2 hours under a helium flow rate of 20 mL/min. A typical preconditioning curve for exfoliated graphene is shown in figure 1 that shows an initial decrease in FID signal with time, which becomes invariant after approximately and hour. This shows that the preconditioning time of 2 hours used is sufficient to clean the sample of any loosely held adsorbates. We note however, that our samples will not be completely free of containments using this preconditioning process as it isn't aggressive enough to remove tightly bound contaminants, this is addressed in the main text. It is not possible to go higher than 150 °C due to hardware constraints of the SEA.

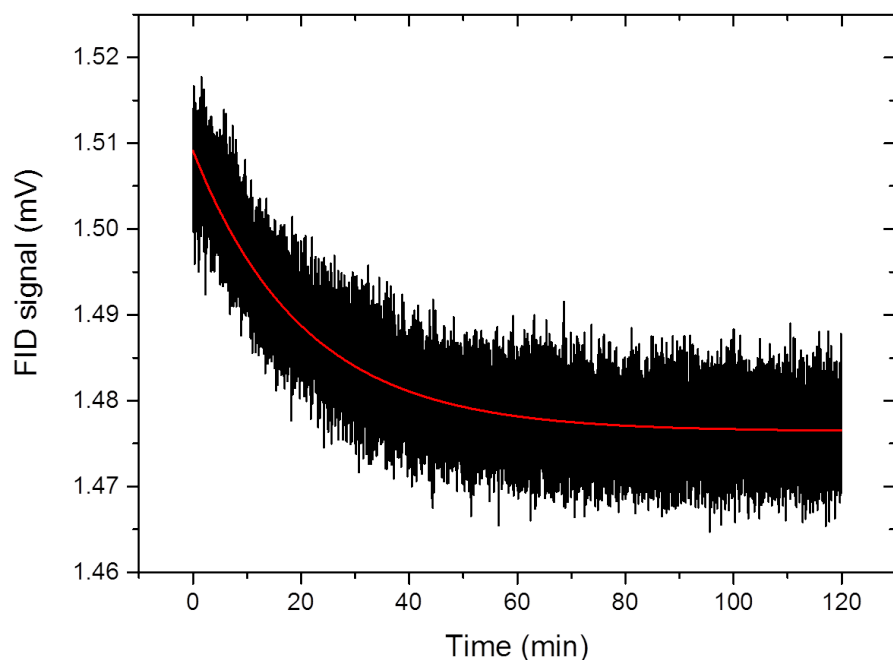


Figure 1: Graphene IGC preconditioning curve at 150 °C with helium flow rate of 20 mL/min with a fitted line showing mean signal with time.

Appendix B: Graphite IGC Study

Simulated Surface energy profiles

All experimental surface energy profiles were found to be exponential like. What we find in the simulations is that exponential like curves only arise when the high energy site (HE) distribution is broad and the low energy site (LE) distribution is narrow. This is because the very highest energy sites are adsorbed to preferentially. As those sites are used up, the probes start to adsorb to lower energy sites causing the γ_d profile to drop. Eventually once the HE sites are almost filled the probes adsorb to the LE sites which cause the γ_d profile to plateau (figure 2A). However, if the HE site distribution is narrow the γ_d remains high and fails to decrease until a much larger coverage (figure 2B) . If both distributions are broad they merge and the SE profile behaves like a single Gaussian distribution (figure 2C).

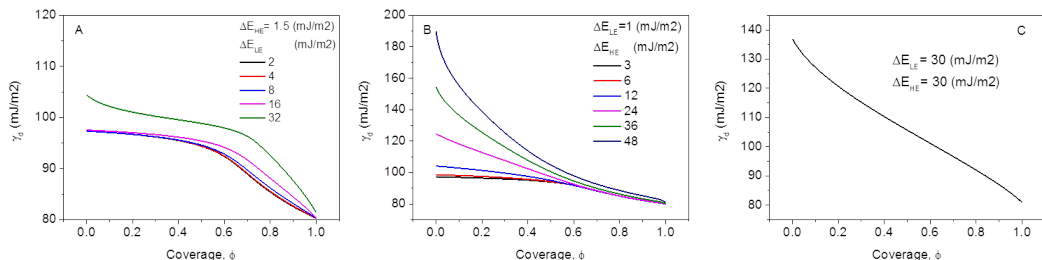


Figure 2: A) Simulated SE profiles for a narrow HE distribution with broadening LE distribution. B) Simulated SE profiles for a narrow LE distribution with broadening HE distribution. Notice how the profile becomes exponential-like as the HE distribution broadens. C) Simulated SE profile of broad HE and LE distributions. Notice how it behaves much like a single Gaussian SE profile.

Figure 3 Shows simulated surface energy versus coverage curves for two Gaussian distributions (see figure 4.9). These have been fit with both exponential distributions (dashed lines) and stretched exponentials (solid lines). We always find stretched exponentials to give better fits. As such, all fitting in this work was performed using stretched (or sometimes compressed) exponentials.

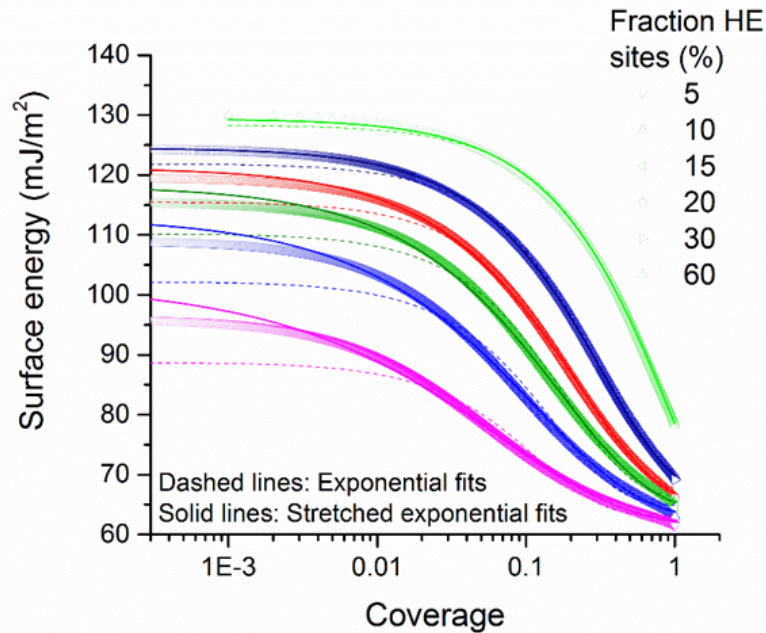


Figure 3: Simulations of γ_d profiles using two Gaussian distributions with increasing percentage of high energy sites ranging from 5-60%. These profiles have been fitted to exponential fits (dashed lines) and stretched exponentials (solid lines) showing that stretched exponentials give better fits to the data.

Bibliography

- [1] C. H. Online. the Cambridge Ancient History Volume III. III, 2008.
- [2] Old Cumbria Gazetteer.
- [3] A. Wainwright. *The Western Fells*. Frances Lincoln Limited, 2014.
- [4] *The Statutes at Large*. 1764.
- [5] S. Ritter. Pencils & Pencil Lead, 2001.
- [6] E. Otto. Electric Graphite, 2011.
- [7] Y. Hernandez, V. Nicolosi, M. Lotya, F. M. Blighe, Z. Sun, S. De, I. T. McGovern, B. Holland, M. Byrne, Y. K. Gun'Ko, J. J. Boland, P. Niraj, G. Duesberg, S. Krishnamurthy, R. Goodhue, J. Hutchison, V. Scardaci, A. C. Ferrari, and J. N. Coleman. High-yield production of graphene by liquid-phase exfoliation of graphite. *Nature nanotechnology*, 3(9):563–8, September 2008.
- [8] K. S. Novoselov, A. K. Geim, S. V. Morozov, D. Jiang, Y. Zhang, S. V. Dubonos, I. V. Grigorieva, and A. A. Firsov. Electric Field Effect in Atomically Thin Carbon Films. *Science*, 306(5696):666–669, October 2004.
- [9] H. W. Kroto, J. R. Heath, S. C. O'Brien, R. F. Curl, and R. E. Smalley. C₆₀: buckminsterfullerene. *Nature*, 318:162, 1985.
- [10] S. Iijima. Helical microtubules of graphitic carbon. *Nature*, 354(6348):56–58, 1991.

- [11] R. Tatar and S. Rabii. Electronic properties of graphite: A unified theoretical study. *Physical Review B*, 25(6):4126, 1982.
- [12] E. Taft and H. Philipp. Optical Properties of Graphite. *Physical Review*, 138(1A):A197–A202, 1965.
- [13] J. D. Bernal. The Structure of Graphite. *Proceedings of the Royal Society of London A: Mathematical, Physical and Engineering Sciences*, pages 422–451, 1924.
- [14] Diamond and graphite, allotropes of carbon.
- [15] P. R. Buseck and B. J. Huang. Conversion of carbonaceous material to graphite during metamorphism. *Geochimica et Cosmochimica Acta*, 49(10):2003–2016, 1985.
- [16] E. Peled. Improved Graphite Anode for Lithium-Ion Batteries Chemically. *Journal of The Electrochemical Society*, 143(1):L4, 1996.
- [17] A. V. Tamashausky. An Introduction to Synthetic Graphite, 2006.
- [18] H. P. Chang and A. J. Bard. Observation and characterization by scanning tunneling microscopy of structures generated by cleaving highly oriented pyrolytic graphite. *Langmuir*, 7(6):1143–1153, 1991.
- [19] G. Zhang, A. S. Cuharuc, A. G. Güell, and P. R. Unwin. Electrochemistry at highly oriented pyrolytic graphite (HOPG): lower limit for the kinetics of outer-sphere redox processes and general implications for electron transfer models. *Phys. Chem. Chem. Phys.*, 17(17):11827–11838, 2015.
- [20] K. Malik. Why Graphite?, 2012.
- [21] H. Sanderson. Material revolution: tech drives a new resource era, 2015.
- [22] W. Kratschmer, L. D. Lamb, K. Fostiropoulos, and D. R. Huffman. Solid C₆₀: a new form of carbon. *Nature*, 347(6291):354–358, September 1990.
- [23] A. Hirsch. The era of carbon allotropes. *Nature materials*, 9(11):868, 2010.

- [24] G. Dennler, M. C. Scharber, and C. J. Brabec. Polymer-fullerene bulk-heterojunction solar cells. *Advanced Materials*, 21(13):1323–1338, 2009.
- [25] GraphITA Graphene Conference, 2011.
- [26] G. Hummer, J. C. Rasaiah, and J. P. Noworyta. Water conduction through the hydrophobic channel of a carbon nanotube. *Nature*, 414(6860):188–190, 2001.
- [27] R. Zhang, Y. Zhang, Q. Zhang, H. Xie, W. Qian, and F. Wei. Growth of half-meter long carbon nanotubes based on Shulz-Flory distribution. *ACS Nano*, 7(7):6156–6161, 2013.
- [28] T. Ando. The electronic properties of graphene and carbon nanotubes. *NPG Asia Materials*, 1:17–21, 2009.
- [29] T. Dürkop, S. A. Getty, E. Cobas, and M. S. Fuhrer. Extraordinary Mobility in Semiconducting Carbon Nanotubes. *Nano Letters*, 4(1):35–39, 2004.
- [30] M.-F. Yu, B. S. Files, S. Arepalli, and R. S. Ruoff. Tensile Loading of Ropes of Single Wall Carbon Nanotubes and their Mechanical Properties. *Physical Review Letters*, 84(24):5552–5555, 2000.
- [31] H. P. Boehm, R. Setton, and E. Stumpf. Nomenclature and terminology of graphite intercalation compounds. *Carbon*, 24(2):241–245, 1986.
- [32] J. Sakamoto, J. Van Heijst, O. Lukin, and A. D. Schluter. Two-dimensional polymers: Just a dream of synthetic chemists? *Angewandte Chemie - International Edition*, 48(6):1030–1069, 2009.
- [33] A. K. Geim and K. Novoselov. The rise of graphene. *Nature Mater.*, 6(3):183–191, 2007.
- [34] C. Lee, X. Wei, J. W. Kysar, and J. Hone. Measurement of the Elastic Properties and Intrinsic Strength of Monolayer Graphene. *Science*, 321(18 July 2008):385–388, 2008.

- [35] R. R. Nair, P. Blake, A. N. Grigorenko, K. S. Novoselov, T. J. Booth, T. Stauber, N. M. R. Peres, and A. K. Geim. Fine Structure Constant Defines Visual Transparency of Graphene. *Science*, 320:1308, 2008.
- [36] K. I. Bolotin, K. J. Sikes, Z. Jiang, M. Klima, G. Fudenberg, J. Hone, P. Kim, and H. L. Stormer. Ultrahigh electron mobility in suspended graphene. *Solid State Communications*, 146(9-10):351–355, 2008.
- [37] K. S. K. S. Kim, Y. Zhao, H. Jang, S. Y. Lee, J. M. Kim, K. S. K. S. Kim, J.-H. Ahn, P. Kim, J.-Y. Choi, and B. H. Hong. Large-scale pattern growth of graphene films for stretchable transparent electrodes. *Nature*, 457(7230):706–10, 2009.
- [38] Y. Zhang, T. T. Tang, C. Girit, Z. Hao, M. C. Martin, A. Zettl, M. F. Crommie, Y. R. Shen, and F. Wang. Direct observation of a widely tunable bandgap in bilayer graphene. *Nature*, 459(7248):820–3, 2009.
- [39] K. S. Novoselov, A. K. Geim, S. V. Morozov, D. Jiang, M. I. Katsnelson, I. V. Grigorieva, S. V. Dubonos, and A. A. Firsov. Two-Dimensional Gas of Massless Dirac Fermions in Graphene. *Nature*, 438(7065):197–200, 2005.
- [40] M. I. Katsnelson, K. S. Novoselov, and A. K. Geim. Chiral tunnelling and the Klein paradox in graphene. *Nature Physics*, 2:1986, 2006.
- [41] S. Stankovich, D. A. Dikin, G. H. B. Dommett, K. M. Kohlhaas, E. J. Zimney, E. A. Stach, R. D. Piner, S. T. Nguyen, and R. S. Ruoff. Graphene-based composite materials. *Nature*, 442(7100):282–286, 2006.
- [42] J. Liang, Y. Huang, L. Zhang, Y. Wang, Y. Ma, T. Cuo, and Y. Chen. Molecular-level dispersion of graphene into poly(vinyl alcohol) and effective reinforcement of their nanocomposites. *Advanced Functional Materials*, 19(14):2297–2302, 2009.
- [43] M. D. Stoller, S. Park, Z. Yanwu, J. An, and R. S. Ruoff. Graphene-Based ultracapacitors. *Nano Letters*, 8(10):3498–3502, 2008.
- [44] X. Wang, L. Zhi, and K. Müllen. Transparent, conductive graphene electrodes for dye-sensitized solar cells. *Nano Letters*, 8(1):323–327, 2008.

- [45] R. Ruoff. Graphene: Calling all chemists. *Nat Nano*, 3(1):10–11, January 2008.
- [46] T. J. Booth, P. Blake, R. R. Nair, D. Jiang, E. W. Hill, U. Bangert, A. Bleloch, M. Gass, K. S. Novoselov, M. I. Katsnelson, and a. K. Geim. Macroscopic graphene membranes and their extraordinary stiffness. *Nano Letters*, 8(8):2442–2446, 2008.
- [47] K. S. Novoselov, V. I. Fal’ko, L. Colombo, P. R. Gellert, M. G. Schwab, and K. Kim. A roadmap for graphene. *Nature*, 490(7419):192–200, 2012.
- [48] C. Berger, Z. Song, T. Li, X. Li, A. Y. Ogbazghi, R. Feng, Z. Dai, N. Alexei, M. E. H. Conrad, P. N. First, and W. a. De Heer. Ultrathin epitaxial graphite: 2D electron gas properties and a route toward graphene-based nanoelectronics. *Journal of Physical Chemistry B*, 108(52):19912–19916, 2004.
- [49] T. Ohta. Controlling the Electronic Structure of Bilayer Graphene. *Science*, 313(5789):951–954, 2006.
- [50] C. Virojanadara, M. Syvajarvi, R. Yakimova, L. I. Johansson, A. A. Zakharov, and T. Balasubramanian. Homogeneous large-area graphene layer growth on 6H-SiC(0001). *Physical Review B - Condensed Matter and Materials Physics*, 78(24):1–6, 2008.
- [51] Z. Chen, W. Ren, L. Gao, B. Liu, S. Pei, and H. M. Cheng. Three-dimensional flexible and conductive interconnected graphene networks grown by chemical vapour deposition. *Nature materials*, 10(6):424–428, 2011.
- [52] S. Bae, H. Kim, Y. Lee, X. Xu, J. S. Park, Y. Zheng, J. Balakrishnan, T. Lei, H. Ri Kim, Y. I. Song, Y.-J. Kim, K. S. Kim, B. Özyilmaz, J. H. Ahn, B. H. Hong, and S. Iijima. Roll-to-roll production of 30-inch graphene films for transparent electrodes. *Nature Nanotechnology*, 5(8):574–578, 2010.
- [53] X. Li, W. Cai, J. An, S. Kim, J. Nah, D. Yang, R. Piner, A. Velamakanni, I. Jung, E. Tutuc, S. K. Banerjee, L. Colombo, and R. S. Ruoff. Large-area synthesis of high-quality and uniform graphene films on copper foils. *Science*, 324(5932):1312–1314, 2009.

- [54] H. Zhou, W. J. Yu, L. Liu, R. Cheng, Y. Chen, X. Huang, Y. Liu, Y. Wang, Y. Huang, and X. Duan. Chemical vapour deposition growth of large single crystals of monolayer and bilayer graphene. *Nature communications*, 4:2096, 2013.
- [55] S. Stankovich, D. A. Dikin, R. D. Piner, K. A. Kohlhaas, A. Kleinhammes, Y. Jia, Y. Wu, S. T. Nguyen, and R. S. Ruoff. Synthesis of graphene-based nanosheets via chemical reduction of exfoliated graphite oxide. *Carbon*, 45(7):1558–1565, 2007.
- [56] B. C. Brodie. On the Atomic Weight of Graphite. *Philosophical Transactions of the Royal Society of London*, 149(9):249–259, 1859.
- [57] W. S. Hummers and R. E. Offeman. Preparation of Graphitic Oxide. *Journal of the American Chemical Society*, 80(6):1339–1339, 1958.
- [58] Y. Zhu, S. Murali, W. Cai, X. Li, J. W. Suk, J. R. Potts, and R. S. Ruoff. Graphene and graphene oxide: Synthesis, properties, and applications. *Advanced Materials*, 22(35):3906–3924, 2010.
- [59] H. Y. He, J. Klinowski, M. Forster, and a. Lerf. A new structural model for graphite oxide. *Chemical Physics Letters*, 287(1-2):53–56, 1998.
- [60] D. R. Dreyer, R. S. Ruoff, and C. W. Bielawski. From conception to realization: An historial account of graphene and some perspectives for its future. *Angewandte Chemie - International Edition*, 49(49):9336–9344, 2010.
- [61] J. W. Suk, R. D. Piner, J. An, and R. S. Ruoff. Mechanical properties of monolayer graphene oxide. *ACS Nano*, 4(11):6557–6564, 2010.
- [62] Y. Xu, I. Hennig, D. Freyberg, A. James Strudwick, M. Georg Schwab, T. Weitz, and K. Chih-Pei Cha. Inkjet-printed energy storage device using graphene/polyaniline inks. *Journal of Power Sources*, 248:483–488, 2014.
- [63] A. Kamyshny and S. Magdassi. Conductive nanomaterials for printed electronics. *Small*, 10(17):3515–3535, 2014.

- [64] T. Dahlberg. *The first order Raman spectrum of isotope labelled nitrogen-doped reduced graphene oxide*. PhD thesis, 2016.
- [65] J. N. Coleman. Liquid exfoliation of defect-free graphene. *Accounts of chemical research*, 46(1):14–22, January 2013.
- [66] S. D. Bergin, V. Nicolosi, P. V. Streich, S. Giordani, Z. Sun, A. H. Winnable, P. Ryan, N. P. P. Niraj, Z. T. T. Wang, L. Carpenter, W. J. Blau, J. J. Boland, J. P. Hamilton, and J. N. Coleman. Towards solutions of single-walled carbon nanotubes in common solvents. *Advanced Materials*, 20(10):1876–1881, 2008.
- [67] U. Khan, A. O’Neill, H. Porwal, P. May, K. Nawaz, and J. N. Coleman. Size selection of dispersed, exfoliated graphene flakes by controlled centrifugation. *Carbon*, 50(2):470–475, 2012.
- [68] U. Khan, P. May, A. O’Neill, and J. N. Coleman. Development of stiff, strong, yet tough composites by the addition of solvent exfoliated graphene to polyurethane. *Carbon*, 48(14):4035–4041, 2010.
- [69] P. May, U. Khan, A. O’Neill, and J. N. Coleman. Approaching the theoretical limit for reinforcing polymers with graphene. *Journal of Materials Chemistry*, 22(4):1278, 2012.
- [70] P. J. King, U. Khan, M. Lotya, S. De, and J. N. Coleman. Improvement of transparent conducting nanotube films by addition of small quantities of graphene. *ACS Nano*, 4(7):4238–4246, 2010.
- [71] C. S. Boland, U. Khan, C. Backes, A. O’Neill, J. McCauley, S. Duane, R. Shanker, Y. Liu, I. Jurewicz, A. B. Dalton, and J. N. Coleman. Sensitive, high-strain, high-rate bodily motion sensors based on graphene-rubber composites. *ACS Nano*, 8(9):8819–8830, 2014.
- [72] D. Hanlon, C. Backes, T. M. Higgins, M. Hughes, A. O’Neill, P. King, N. McEvoy, G. S. Duesberg, B. Mendoza Sanchez, H. Pettersson, V. Nicolosi, and J. N. Coleman. Production of molybdenum trioxide nanosheets

- by liquid exfoliation and their application in high-performance supercapacitors. *Chemistry of Materials*, 26(4):1751–1763, 2014.
- [73] U. Khan, P. May, A. O'Neill, A. P. Bell, E. Boussac, A. Martin, J. Semple, and J. N. Coleman. Polymer reinforcement using liquid-exfoliated boron nitride nanosheets. *Nanoscale*, 5(2):581–7, 2013.
- [74] G. Cunningham, M. Lotya, C. S. Cucinotta, S. Sanvito, S. D. Bergin, R. Menzel, M. S. P. Shaffer, and J. N. Coleman. Solvent exfoliation of transition metal dichalcogenides: Dispersibility of exfoliated nanosheets varies only weakly between compounds. *ACS Nano*, 6(4):3468–3480, 2012.
- [75] M. Lotya, Y. Hernandez, P. J. King, R. J. Smith, V. Nicolosi, L. S. Karlsson, F. M. Blighe, S. De, Z. Wang, I. T. McGovern, G. S. Duesberg, and J. N. Coleman. Liquid phase production of graphene by exfoliation of graphite in surfactant/water solutions. *Journal of the American Chemical Society*, 131(10):3611–20, March 2009.
- [76] V. Nicolosi, M. Chhowalla, M. G. Kanatzidis, M. S. Strano, and J. N. Coleman. Liquid Exfoliation of Layered Materials. *Science*, 340(6139):1226419, 2013.
- [77] K. R. Paton, E. Varrla, C. Backes, R. J. Smith, U. Khan, A. O'Neill, C. Boland, M. Lotya, O. M. Istrate, P. King, T. Higgins, S. Barwick, P. May, P. Puczkarski, I. Ahmed, M. Moebius, H. Pettersson, E. Long, J. a. Coelho, S. E. O'Brien, E. K. McGuire, B. M. Sanchez, G. S. Duesberg, N. McEvoy, T. J. Pennycook, C. Downing, A. Crossley, V. Nicolosi, and J. N. Coleman. Scalable production of large quantities of defect-free few-layer graphene by shear exfoliation in liquids. *Nature materials*, 13(6):624–30, 2014.
- [78] C. Backes, B. M. Szydłowska, A. Harvey, S. Yuan, V. Vega-Mayoral, B. R. Davies, P.-l. Zhao, D. Hanlon, E. J. G. Santos, M. I. Katsnelson, W. J. Blau, C. Gadermaier, and J. N. Coleman. Production of Highly Monolayer Enriched Dispersions of Liquid-Exfoliated Nanosheets by Liquid Cascade Centrifugation. *ACS Nano*, page acsnano.5b07228, 2016.

- [79] S. J. Eichhorn, A. Dufresne, M. Aranguren, N. E. Marcovich, J. R. Capadona, S. J. Rowan, C. Weder, W. Thielemans, M. Roman, S. Renneckar, W. Gindl, S. Veigel, J. Keckes, H. Yano, K. Abe, M. Nogi, A. N. Nakagaito, A. Mangalam, J. Simonsen, A. S. Benight, A. Bismarck, L. A. Berglund, and T. Peijs. *Review: Current international research into cellulose nanofibres and nanocomposites*, volume 45. 2010.
- [80] D. Klemm, B. Heublein, H. P. Fink, and A. Bohn. Cellulose: Fascinating biopolymer and sustainable raw material. *Angewandte Chemie - International Edition*, 44(22):3358–3393, 2005.
- [81] A. Payen. Memoire sur la composition du tissu propre des plantes et du ligneux. *Comptes rendus*, 7:1052–1056, 1838.
- [82] R. J. Moon, A. Martini, J. Nairn, J. Simonsen, and J. Youngblood. *Cellulose nanomaterials review: structure, properties and nanocomposites.*, volume 40. 2011.
- [83] S. Khan, M. Ul-Islam, W. A. Khattak, M. W. Ullah, and J. K. Park. Bacterial cellulose–poly(3,4-ethylenedioxythiophene)–poly(styrenesulfonate) composites for optoelectronic applications. *Carbohydrate Polymers*, 127:86–93, 2015.
- [84] J. Shah and R. M. Brown. Towards electronic paper displays made from microbial cellulose. *Applied Microbiology and Biotechnology*, 66(4):352–355, 2005.
- [85] Z. Gui, H. Zhu, E. Gillette, X. Han, G. W. Rubloff, L. Hu, and S. B. Lee. Natural cellulose fiber as substrate for supercapacitor. *ACS Nano*, 7(7):6037–6046, 2013.
- [86] I. Sulaeva, U. Henniges, T. Rosenau, and A. Potthast. Bacterial cellulose as a material for wound treatment: Properties and modifications: A review. *Biotechnology Advances*, 33(8):1547–1571, 2015.
- [87] M. Pääkkö, J. Vapaavuori, R. Silvennoinen, H. Kosonen, M. Ankerfors, T. Lindström, L. a. Berglund, and O. Ikkala. Long and entangled native

- cellulose I nanofibers allow flexible aerogels and hierarchically porous templates for functionalities. *Soft Matter*, 4(Mcc):2492, 2008.
- [88] S. J. Eichhorn and G. R. Davies. Modelling the crystalline deformation of native and regenerated cellulose. *Cellulose*, 13(3):291–307, 2006.
- [89] A. J. Brown. XLIIL-On an acetic ferment which forms cellulose. *Journal of the Chemical Society, Transactions*, 49:432–439, 1886.
- [90] A. J. Brown. XIX-The chemical action of pure cultivations of bacterium aceti. *Journal of the Chemical Society, Transactions*, 49:172–187, 1886.
- [91] K. Y. Lee, G. Buldum, A. Mantalaris, and A. Bismarck. More than meets the eye in bacterial cellulose: Biosynthesis, bioprocessing, and applications in advanced fiber composites. *Macromolecular Bioscience*, 14(1):10–32, 2014.
- [92] W. S. Scott Williams and R. E. Cannon. Alternative environmental roles for cellulose produced by *Acetobacter xylinum*. *Applied and Environmental Microbiology*, 55(10):2448–2452, 1989.
- [93] M. Iguchi, S. Yamanaka, and A. Budhiono. Bacterial cellulose - a masterpiece of nature's arts. *Journal of Materials Science*, 35(2):261–270, 2000.
- [94] S. Hestrin and M. Schramm. Synthesis of Cellulose by *Acetobacter xylinum*. *Biochem. J.*, 58(1954):345–352, 1954.
- [95] H. Zhu, Z. Fang, C. Preston, Y. Li, and L. Hu. Transparent paper: fabrications, properties, and device applications. *Energy Environ. Sci.*, 7(1):269–287, 2014.
- [96] S. A. Bakar, A. A. Aziz, P. Marwoto, and S. Sakrani. Amorphous hydrogenated carbon films. *Carbon*, 77:311–320, 1987.
- [97] I. Siró and D. Plackett. Microfibrillated cellulose and new nanocomposite materials: a review. *Cellulose*, 17(3):459–494, February 2010.
- [98] G. Shanshan, W. Jianqing, and J. Zhengwei. Preparation of cellulose films from solution of bacterial cellulose in NMMO. *Carbohydrate Polymers*, 87(2):1020–1025, January 2012.

- [99] S. Bielecki, A. Krystynowicz, Marianna, and H. Kalinowska. *Bacterial Cellulose*. Wiley-VCH Verlag GmbH & Co. KGaA, 2005.
- [100] D. Klemm, F. Kramer, S. Moritz, T. Lindström, M. Ankerfors, D. Gray, and A. Dorris. Nanocelluloses: A new family of nature-based materials. *Angewandte Chemie - International Edition*, 50(24):5438–5466, 2011.
- [101] P. Ross, R. Mayer, and M. Benziman. Cellulose biosynthesis and function in bacteria. *Microbiological reviews*, 55(1):35–58, 1991.
- [102] S. Tanpichai, F. Quero, M. Nogi, H. Yano, R. J. Young, T. Lindstrom, W. W. Sampson, and S. J. Eichhorn. Effective young's modulus of bacterial and microfibrillated cellulose fibrils in fibrous networks. *Biomacromolecules*, 13(5):1340–1349, 2012.
- [103] H. Yano. Optically transparent composites reinforced with networks of bacterial nanofibers. *Sustainable Humanosphere*, (1):11, 2005.
- [104] B. V. Mohite and S. V. Patil. Physical, structural, mechanical and thermal characterization of bacterial cellulose. *Carbohydrate Polymers*, 106(1):132–141, 2014.
- [105] S. Andersson, R. Serimaa, T. Paakkari, P. Saranpaa, and E. Pesonen. Crystallinity of wood and the size of cellulose crystallites in Norway spruce (*Picea abies*). *Journal of Wood Science*, 49(6):531–537, 2003.
- [106] W. Chen, H. Yu, Y. Liu, Y. Hai, M. Zhang, and P. Chen. Isolation and characterization of cellulose nanofibers from four plant cellulose fibers using a chemical-ultrasonic process. *Cellulose*, 18(2):433–442, 2011.
- [107] A. Thygesen, J. Oddershede, H. Lilholt, A. B. Thomsen, and K. Stahl. On the determination of crystallinity and cellulose content in plant fibres. *Cellulose*, 12(6):563–576, 2005.
- [108] S. P. Lin, I. Loira Calvar, J. M. Catchmark, J. R. Liu, A. Demirci, and K. C. Cheng. Biosynthesis, production and applications of bacterial cellulose. *Cellulose*, 20(5):2191–2219, 2013.

- [109] S. Nishikawa and S. Ono. Transmission of X-Rays through Fibrous, Lamellar and Granular Substances. *Proc. Math. Phys. Soc. Tokyo*, 7(1):131–138, 1913.
- [110] K. Meyer and L. Misch. Positions des atomes dans le nouveau modele spatial de la cellulose. *helvetica chimica Acta*, 20:232–244, 1937.
- [111] K. Gardner and J. Blackwell. The structure of native cellulose. *Biopolymers*, 13(10):1975–2001, 1974.
- [112] A. Sarko and R. Muggli. Packing analysis of carbohydrates and polysaccharides. III. Valonia cellulose and cellulose II. *Macromolecules*, 7(4):486–494, 1974.
- [113] Y. Habibi, L. a. Lucia, and O. J. Rojas. Cellulose nanocrystals: Chemistry, self-assembly, and applications. *Chemical Reviews*, 110(6):3479–3500, 2010.
- [114] E. Schweizer. Das Kupferoxyd-Ammoniak, ein Auflösungsmittel für die Pflanzenfaser. *Journal für Praktische Chemie*, 72(1):109–111, 1857.
- [115] S. M. Hudson and J. A. Cuculo. The Solubility of Cellulose in Liquid Ammonia/Salt Solution. *J. Polym. Sci. , Polym. Chem.*, 18:3469–3481, 1980.
- [116] D. L. VanderHart and R. H. Atalla. Studies of microstructure in native celluloses using solid-state carbon-13 NMR. *Macromolecules*, 17(8):1465–1472, 1984.
- [117] Y. Nishiyama, J. Sugiyama, H. Chanzy, and P. Langan. Crystal structure and hydrogen bonding system in cellulose I β from synchrotron x-ray and neutron fiber diffraction. *Journal of the American Chemical Society*, 125(47):14300–14306, 2003.
- [118] Y. Nishiyama, J. Sugiyama, H. Chanzy, and P. Langan. Crystal structure and hydrogen bonding system in cellulose I(alpha) from synchrotron X-ray and neutron fiber diffraction. *Journal of the American Chemical Society*, 125(47):14300–14306, 2003.

- [119] F. Sugiyama, J. Okano, T. Yamamoto, H. Horii. Transformation of Valonia Cellulose Crystals by an Alkaline Hydrothermal Treatment. *Macromolecules*, 3198(7):3196–3198, 1990.
- [120] A. Okiyama, H. Shirae, H. Kano, and S. Yamanaka. Bacterial cellulose I. Two-stage fermentation process for cellulose production by *Acetobacter aceti*. *Food Hydrocolloids*, 6(5):471–477, 1992.
- [121] A. Okiyama, M. Motoki, and S. Yamanaka. Bacterial cellulose II. Processing of the gelatinous cellulose for food materials. *Food Hydrocolloids*, 6(5):479–487, 1992.
- [122] A. Okiyama, M. Motoki, and S. Yamanaka. Bacterial Cellulose .4. Application to Processed Foods. *Food Hydrocolloids*, 6(6):503–511, 1993.
- [123] A. J. Silvestre, C. S. Freire, and C. P. Neto. Do bacterial cellulose membranes have potential in drug-delivery systems? *Expert opinion on drug delivery*, 11(7):1113–1124, 2014.
- [124] M. L. Cacicudo, M. C. Castro, I. Servetas, L. Bosnea, K. Boura, P. Tsafrakidou, A. Dima, A. Terpou, A. Koutinas, and G. R. Castro. Progress in bacterial cellulose matrices for biotechnological applications. *Bioresource Technology*, 2015.
- [125] S. M. Keshk. Bacterial Cellulose Production and its Industrial Applications. *Journal of Bioprocessing & Biotechniques*, 04(02):1–10, 2014.
- [126] J. D. Fontana, A. M. De Souza, C. K. Fontana, I. L. Torriani, J. C. Moreschi, B. J. Gallotti, S. J. De Souza, G. P. Narciso, J. A. Bichara, and L. F. X. Farah. Acetobacter cellulose pellicle as a temporary skin substitute. *Applied Biochemistry and Biotechnology*, 24(1):253–264, 1990.
- [127] D. Klemm, D. Schumann, U. Udhardt, and S. Marsch. Bacterial synthesized cellulose - Artificial blood vessels for microsurgery. *Progress in Polymer Science (Oxford)*, 26(9):1561–1603, 2001.

- [128] G. Helenius, H. Backdahl, A. Bodin, U. Nannmark, P. Gatenholm, and B. Risberg. In vivo biocompatibility of bacterial cellulose. *Journal of Biomedical Materials Research - Part A*, 76(2):431–438, 2006.
- [129] F. K. Andrade, R. Costa, L. Domingues, R. Soares, and M. Gama. Improving bacterial cellulose for blood vessel replacement: Functionalization with a chimeric protein containing a cellulose-binding module and an adhesion peptide. *Acta Biomaterialia*, 6(10):4034–4041, 2010.
- [130] H. Backdahl, G. Helenius, A. Bodin, U. Nannmark, B. R. Johansson, B. Risberg, and P. Gatenholm. Mechanical properties of bacterial cellulose and interactions with smooth muscle cells. *Biomaterials*, 27(9):2141–2149, 2006.
- [131] J. M. Dugan, J. E. Gough, and S. J. Eichhorn. Bacterial cellulose scaffolds and cellulose nanowhiskers for tissue engineering. *Nanomedicine*, 8(2):287–98, 2013.
- [132] W. Hu, S. Chen, J. Yang, Z. Li, and H. Wang. Functionalized bacterial cellulose derivatives and nanocomposites. *Carbohydrate Polymers*, 101(1):1043–1060, 2014.
- [133] W. Hu, S. Chen, B. Zhou, L. Liu, B. Ding, and H. Wang. Highly stable and sensitive humidity sensors based on quartz crystal microbalance coated with bacterial cellulose membrane. *Sensors and Actuators, B: Chemical*, 159(1):301–306, 2011.
- [134] W. Hu, S. Liu, S. Chen, and H. Wang. Preparation and properties of photochromic bacterial cellulose nanofibrous membranes. *Cellulose*, 18(3):655–661, 2011.
- [135] W. Wang, H. Y. Li, D. W. Zhang, J. Jiang, Y. R. Cui, S. Qiu, Y. L. Zhou, and X. X. Zhang. Fabrication of Bionzymatic Glucose Biosensor Based on Novel Gold Nanoparticles-Bacteria Cellulose Nanofibers Nanocomposite. *Electroanalysis*, 22(21):2543–2550, 2010.

- [136] S. H. Yoon, H.-J. Jin, M.-C. Kook, and Y. R. Pyun. Electrically conductive bacterial cellulose by incorporation of carbon nanotubes. *Biomacromolecules*, 7(4):1280–4, April 2006.
- [137] Y. Feng, X. Zhang, Y. Shen, K. Yoshino, and W. Feng. A mechanically strong, flexible and conductive film based on bacterial cellulose/graphene nanocomposite. *Carbohydrate Polymers*, 87(1):644–649, January 2012.
- [138] L. F. Chen, Z. H. Huang, H. W. Liang, W. ang Yao, Z. Y. Yu, and S. H. Yu. Flexible all-solid-state high-power supercapacitor fabricated with nitrogen-doped carbon nanofiber electrode material derived from bacterial cellulose. *Energy & Environmental Science*, 6(11):3331–3338, 2013.
- [139] R. Jung, H. S. Kim, Y. Kim, S. M. Kwon, H. S. Lee, and H. J. Jin. Electrically conductive transparent papers using multiwalled carbon nanotubes. *Journal of Polymer Science Part B: Polymer physics*, 46(12):1235–1242, 2008.
- [140] Y. Kim, H. S. Kim, H. Bak, Y. S. Yun, S. Y. Cho, and H. J. Jin. Transparent conducting films based on nanofibrous polymeric membranes and single-walled carbon nanotubes. *Polymers and Polymer Composites*, 114(5):2864–2872, 2009.
- [141] S. D. Bergin, Z. Sun, D. Rickard, P. V. Streich, J. P. Hamilton, and J. N. Coleman. Multicomponent solubility parameters for single-walled carbon nanotube-solvent mixtures. *ACS Nano*, 3(8):2340–2350, 2009.
- [142] Y. Hernandez, V. Nicolosi, M. Lotya, F. M. Blighe, Z. Sun, S. De, I. T. McGovern, B. Holland, M. Byrne, Y. K. Gun’Ko, J. J. Boland, P. Niraj, G. Duesberg, S. Krishnamurthy, R. Goodhue, J. Hutchison, V. Scardaci, A. C. Ferrari, and J. N. Coleman. High-yield production of graphene by liquid-phase exfoliation of graphite. *Nature nanotechnology*, 3(9):563–568, 2008.
- [143] C. M. Hansen. *Hansen Solubility Parameters A User’s Handbook*. CRC press, 2007.

- [144] J. H. Hildebrand, J. M. Prausnitz, and R. L. Scott. *Regular and related solutions : the solubility of gases, liquids, and solids.* [s.n.], New York [etc.], 1970.
- [145] D. Hanlon, C. Backes, E. Doherty, C. S. Cucinotta, N. C. Berner, C. Boland, K. Lee, A. Harvey, P. Lynch, Z. Gholamvand, S. Zhang, K. Wang, G. Moynihan, A. Pokle, Q. M. Ramasse, N. McEvoy, W. J. Blau, J. Wang, G. Abellan, F. Hauke, A. Hirsch, S. Sanvito, D. D. O'Regan, G. S. Duesberg, V. Nicolosi, and J. N. Coleman. Liquid exfoliation of solvent-stabilized few-layer black phosphorus for applications beyond electronics. *Nature Communications*, 6:8563, 2015.
- [146] V. Nicolosi, M. Chhowalla, M. G. Kanatzidis, M. S. Strano, and J. N. Coleman. Liquid Exfoliation of Layered Materials. *Science*, 340(6139):1226419, 2013.
- [147] J. Lyklema. The surface tension of pure liquids. *Colloids and Surfaces A: Physicochemical and Engineering Aspects*, 156(1-3):413–421, 1999.
- [148] N. G. Tsiеркезос and A. C. Filippou. Thermodynamic investigation of N,N-dimethylformamide/toluene binary mixtures in the temperature range from 278.15 to 293.15K. *The Journal of Chemical Thermodynamics*, 38(8):952–961, 2006.
- [149] L. Lapčík, M. Otyepka, E. Otyepková, B. Lapčíková, R. Gabriel, A. Gavenda, and B. Prudilová. Surface heterogeneity: Information from inverse gas chromatography and application to model pharmaceutical substances. *Current Opinion in Colloid & Interface Science*, 24:64–71, 2016.
- [150] J. Donnet, S. Park, and H. Balard. Evaluation of Specific Interactions of Solid Surfaces by Inverse Gas Chromatography A New Approach Based on Polarizability of the Probes. *Chromatographia*, 31(9):434–440, 1991.
- [151] A. D. Buckingham. *Permanent and induced molecular moments and long-range intermolecular forces.* Wiley Online Library, 1967.
- [152] A. Stone. *The theory of intermolecular forces.* Oxford University Press, 2013.

- [153] F. M. Fowkes. Additivity of intermolecular forces at interfaces. I. Determination of the contribution to surface and interfacial tensions of dispersion forces in various liquids. *The Journal of Physical Chemistry*, 67(3):2538–2541, 1963.
- [154] E. Espinosa, E. Molins, and C. Lecomte. Hydrogen bond strengths revealed by topological analyses of experimentally observed electron densities. *Chemical Physics Letters*, 285(3-4):170–173, 1998.
- [155] P. Salucci, F. Stel, M. I. Wilkinson, N. W. Evans, G. Gilmore, R. P. Saglia, O. Gerhard, R. Bender, H. C. Ford, K. C. Freeman, M. A. Dopita, G. H. Jacoby, H. B. Dejonghe, D. Ballantyne, P. L. Schechter, R. P. Saglia, O. E. Gerhard, L. M. Lubin, C. S. Kochanek, E. V. Held, H. Lorenz, M. Vietri, C. M. Carollo, and K. Freeman. Ultrafast Hydrogen-Bond Dynamics in the Infrared. 1996.
- [156] U. Koch and P. L. A. Popelier. Characterization of C-H-O Hydrogen Bonds on the Basis of the Charge Density. *The Journal of Physical Chemistry*, 99(24):9747–9754, 1995.
- [157] R. Ho, S. J. Hinder, J. F. Watts, S. E. Dilworth, D. R. Williams, and J. Y. Y. Heng. Determination of surface heterogeneity of d-mannitol by sessile drop contact angle and finite concentration inverse gas chromatography. *International Journal of Pharmaceutics*, 387(1-2):79–86, 2010.
- [158] M. M. Chehimi, M.-L. Abel, C. Perruchot, M. Delamar, S. F. Lascelles, and S. P. Armes. The determination of the surface energy of conducting polymers by inverse gas chromatography at infinite dilution. *Synthetic Metals*, 104(1):51–59, 1999.
- [159] S. Reutener and F. Thielmann. The characterisation of cotton fabrics and the interaction with perfume molecules by inverse gas chromatography (IGC). *Journal of Materials Science*, 38(10):2205–2208, 2003.
- [160] D. F. Steele, R. C. Moreton, J. N. Staniforth, P. M. Young, M. J. Tobyn, and S. Edge. Surface energy of microcrystalline cellulose determined by capillary

- intrusion and inverse gas chromatography. *The AAPS journal*, 10(3):494–503, 2008.
- [161] L. Lapčík, E. Otyepková, B. Lapčíková, and M. Otyepka. Surface energy analysis (SEA) study of hyaluronan powders. *Colloids and Surfaces A: Physicochemical and Engineering Aspects*, 436:1170–1174, 2013.
- [162] L. Lapčík, B. Lapčíková, E. Otyepková, M. Otyepka, J. Vlček, F. Buňka, and R. N. Salek. Surface energy analysis (SEA) and rheology of powder milk dairy products. *Food Chemistry*, 174:25–30, 2015.
- [163] J. F. Gamble, M. Leane, D. Olusanmi, M. Tobyn, E. Supuk, J. Khoo, and M. Naderi. Surface energy analysis as a tool to probe the surface energy characteristics of micronized materials—a comparison with inverse gas chromatography. *International journal of pharmaceutics*, 422(1-2):238–44, 2012.
- [164] J. M. Felix, P. Gatenholm, and H. P. Schreiber. Controlled interactions in cellulose-polymer composites. 1: Effect on mechanical properties. *Polymer Composites*, 14(6):449–457, 1993.
- [165] I. A. Sacui, R. C. Nieuwendaal, D. J. Burnett, S. J. Stranick, M. Jorfi, C. Weder, E. J. Foster, R. T. Olsson, and J. W. Gilman. Comparison of the properties of cellulose nanocrystals and cellulose nanofibrils isolated from bacteria, tunicate, and wood processed using acid, enzymatic, mechanical, and oxidative methods. *ACS Applied Materials and Interfaces*, 6(9):6127–6138, 2014.
- [166] F. Thielmann, D. J. Burnett, and J. Y. Y. Heng. Determination of the surface energy distributions of different processed lactose. *Drug development and industrial pharmacy*, 33(11):1240–1253, 2007.
- [167] R. Ho, D. A. Wilson, and J. Y. Y. Heng. Crystal habits and the variation in surface energy heterogeneity. *Crystal Growth and Design*, 9(11):4907–4911, 2009.
- [168] S. C. Das, I. Larson, D. A. V. Morton, and P. J. Stewart. Determination of the polar and total surface energy distributions of particulates by inverse

- gas chromatography. *Langmuir : the ACS journal of surfaces and colloids*, 27(2):521–3, January 2011.
- [169] S. Ali, J. Heng, A. Nikolaev, and K. Waters. Introducing inverse gas chromatography as a method of determining the surface heterogeneity of minerals for flotation. *Powder Technology*, 249:373–377, 2013.
- [170] D. Williams. Vapor Sorption Characterisation of Materials.
- [171] A. W. Neumann, R. J. Good, C. J. Hope, and M. Sejpal. An equation-of-state approach to determine surface tensions of low-energy solids from contact angles. *Journal of Colloid And Interface Science*, 49(2):291–304, 1974.
- [172] D. Kwok and a.W. Neumann. *Contact angle measurement and contact angle interpretation*, volume 81. 1999.
- [173] D. K. Owens and R. C. Wendt. Estimation of the surface free energy of polymers. *Journal of Applied Polymer Science*, 13(8):1741–1747, 1969.
- [174] S. E. Shaheen, C. J. Brabec, N. S. Sariciftci, F. Padinger, T. Fromherz, and J. C. Hummelen. 2.5% Efficient Organic Plastic Solar Cells. *Applied Physics Letters*, 78(6):841–843, 2001.
- [175] F. C. Krebs, J. Fyenbo, and M. Jørgensen. Product integration of compact roll-to-roll processed polymer solar cell modules: methods and manufacture using flexographic printing, slot-die coating and rotary screen printing. *Journal of Materials Chemistry*, 20(41):8994, 2010.
- [176] T. R. Hebner, C. C. Wu, D. Marcy, M. H. Lu, and J. C. Sturm. Ink-jet printing of doped polymers for organic light emitting devices. *Applied Physics Letters*, 72(5):519–521, 1998.
- [177] N. M. Ahfat, G. Buckton, R. Burrows, and M. D. Ticehurst. An exploration of inter-relationships between contact angle, inverse phase gas chromatography and triboelectric charging data. *European Journal of Pharmaceutical Sciences*, 9(3):271–276, 2000.

- [178] J. W. Dove, G. Buckton, and C. Doherty. A comparison of two contact angle measurement methods and inverse gas chromatography to assess the surface energies of theophylline and caffeine. *International journal of pharmaceutics*, 138(2):199–206, 1996.
- [179] O. Planinsek, A. Trojak, and S. Srcic. The dispersive component of the surface free energy of powders assessed using inverse gas chromatography and contact angle measurements. *International journal of pharmaceutics*, 221(1-2):211–7, June 2001.
- [180] H. Awada, G. Castelein, and M. Brogly. Quantitative determination of surface energy using atomic force microscopy: The case of Hydrophobic/Hydrophobic contact and hydrophilic/hydrophilic contact. *Surface and Interface Analysis*, 37(9):755–764, 2005.
- [181] S. Cuenot, C. Frétigny, S. Demoustier-Champagne, and B. Nysten. Surface tension effect on the mechanical properties of nanomaterials measured by atomic force microscopy. *Physical Review B*, 69(16):1–5, 2004.
- [182] M. C. Perkins, M. Bunker, J. James, S. Rigby-Singleton, J. Ledru, C. Madden-Smith, S. Luk, N. Patel, and C. J. Roberts. Towards the understanding and prediction of material changes during micronisation using atomic force microscopy. *European Journal of Pharmaceutical Sciences*, 38(1):1–8, 2009.
- [183] G. A. Willing, T. H. Ibrahim, F. M. Etzler, and R. D. Neuman. New Approach to the Study of Particle–Surface Adhesion Using Atomic Force Microscopy. *Journal of Colloid and Interface Science*, 226(1):185–188, 2000.
- [184] T. H. Ibrahim, T. R. Burk, F. M. Etzler, and R. D. Neuman. Direct adhesion measurements of pharmaceutical particles to gelatin capsule surfaces. *Journal of adhesion science and technology*, 14(10):1225–1242, 2000.
- [185] P. Sciences. Inverse Gas Chromatography Technique, 2016.

- [186] A. Voelkel, B. Strzemiecka, K. Adamska, and K. Milczewska. Inverse gas chromatography as a source of physicochemical data. *Journal of chromatography. A*, 1216(10):1551–66, March 2009.
- [187] T. Hamieh, M. B. Fadlallah, and J. Schultz. New approach to characterise physicochemical properties of solid substrates by inverse gas chromatography at infinite dilution - III. Determination of the acid-base properties of some solid substrates (polymers, oxides and carbon fibres): A new model. *Journal of Chromatography A*, 969(1-2):37–47, 2002.
- [188] V. I. Bogillo, V. P. Shkilev, and a. Voelkel. Determination of surface free energy components for heterogeneous solids by means of inverse gas chromatography at finite concentrations. *Journal of Materials Chemistry*, 8(9):1953–1961, 1998.
- [189] F. A. Putnam and T. Fort. Physical Adsorption on Patchwise Heterogeneous Surfaces .1. Heterogeneity, 2-Dimensional Phase-Transitions, and Spreading Pressure of Krypton-Graphitized Carbon-Black System near 100 K. *Journal of Physical Chemistry*, 79(5):459–467, 1975.
- [190] J. F. Gamble, R. N. Davé, S. Kiang, M. M. Leane, M. Tobyn, and S. S. Y. Wang. Investigating the applicability of inverse gas chromatography to binary powdered systems: an application of surface heterogeneity profiles to understanding preferential probe-surface interactions. *International journal of pharmaceutics*, 445(1-2):39–46, March 2013.
- [191] L. Lapčík, M. Vašina, B. Lapčíková, E. Otyepková, and K. E. Waters. Investigation of advanced mica powder nanocomposite filler materials: Surface energy analysis, powder rheology and sound absorption performance. *Composites Part B: Engineering*, 77:304–310, 2015.
- [192] W. Henry. Experiments on the Quantity of Gases Absorbed by Water, at Different Temperatures, and under Different Pressures. *Philosophical Transactions of the Royal Society of London*, 93(1):29–274, 1803.

- [193] A. Kondor, C. Quellet, and A. Dallos. Surface characterization of standard cotton fibres and determination of adsorption isotherms of fragrances by IGC. *Surface and Interface Analysis*, 47(11):1040–1050, 2015.
- [194] S. Mohammadi-Jam and K. Waters. Inverse gas chromatography applications: A review. *Advances in Colloid and Interface Science*, 212:21–44, 2014.
- [195] A. T. James and A. J. P. Martin. Gas-liquid partition chromatography; the separation and micro-estimation of volatile fatty acids from formic acid to dodecanoic acid. *The Biochemical journal*, 50(5):679–690, 1952.
- [196] R. Ho and J. Y. Y. Heng. A Review of Inverse Gas Chromatography and its Development as a Tool to Characterize Anisotropic Surface Properties of Pharmaceutical Solids. *KONA Powder and Particle Journal*, 30:164–180, 2013.
- [197] M. Pérez-Mendoza, M. C. Almazán-Almazán, L. Méndez-Liñán, M. Domingo-García, and F. J. López-Garzón. Evaluation of the dispersive component of the surface energy of active carbons as determined by inverse gas chromatography at zero surface coverage. *Journal of chromatography. A*, 1214(1-2):121–7, December 2008.
- [198] J. Schultz, L. Lavielle, and C. Martin. The Role of the Interface in Carbon Fibre-Epoxy Composites. *The Journal of Adhesion*, 23(1):45–60, September 1987.
- [199] G. M. Dorris and D. G. Gray. Adsorption of n-alkanes at zero surface coverage on cellulose paper and wood fibers. *Journal of Colloid and Interface Science*, 77(2):353–362, October 1980.
- [200] F. M. Fowkes. Attractive forces at interfaces. *Industrial & Engineering Chemistry*, 56(12):40–52, 1964.
- [201] C. J. Van Oss, R. J. Good, and M. K. Chaudhury. Interfacial Lifshitz-van der Waals and polar interactions in macroscopic systems. *Chemical Reviews*, 88(6):927–941, 1988.

- [202] R. Menzel, A. Bismarck, and M. S. P. Shaffer. Deconvolution of the structural and chemical surface properties of carbon nanotubes by inverse gas chromatography. *Carbon*, 50(10):3416–3421, 2012.
- [203] S. Sharif, L. M. DiMemmo, M. Thommes, M. Hubert, and B. A. Sarsfield. A simplified approach to determine effective surface area and porosity of low bulk density active pharmaceutical ingredients in early development. *Advanced Powder Technology*, 26(2):337–348, 2015.
- [204] A. Legras, A. Kondor, M. T. Heitzmann, and R. W. Truss. Inverse gas chromatography for natural fibre characterisation: Identification of the critical parameters to determine the Brunauer-Emmett-Teller specific surface area. *Journal of Chromatography A*, 1425:273–279, 2015.
- [205] S. Brunauer, P. H. Emmett, and E. Teller. Adsorption of Gases in Multi-molecular Layers. *Journal of the American Chemical Society*, 60(2):309–319, 1938.
- [206] Cary Varian Technical Specification.
- [207] IIT-Spectrometry Notes.
- [208] J. N. Coleman. Trinity College Dublin Nanoscience Course Notes.
- [209] F. Tuinstra and L. Koenig. Raman Spectrum of Graphite. *The Journal of Chemical Physics*, 53(1970):1126–1130, 1970.
- [210] F. Tuinstra and J. L. Koenig. Characterization of Graphite Fiber Surfaces with Raman Spectroscopy. *Journal of Composite Materials*, 4:492–499, 1970.
- [211] M. Dresselhaus, G. Dresselhaus, R. Saito, and a. Jorio. Raman spectroscopy of carbon nanotubes. *Physics Reports*, 409(2):47–99, 2005.
- [212] A. C. Ferrari. Raman spectroscopy of graphene and graphite: Disorder, electron-phonon coupling, doping and nonadiabatic effects. *Solid State Communications*, 143(1-2):47–57, 2007.

- [213] C. Backes, K. Paton, D. Hanlon, S. Yuan, M. Katsnelson, J. Houston, R. Smith, D. McCloskey, J. Donegan, and J. N. Coleman. Spectroscopic metrics allow in-situ measurement of mean size and thickness of liquid-exfoliated graphene nanosheets. *Nanoscale*, 8(7):4311–4323, 2016.
- [214] R. Beams, L. G. Cançado, and L. Novotny. Raman characterization of defects and dopants in graphene. *Journal of physics. Condensed matter : an Institute of Physics journal*, 27(8):083002, 2015.
- [215] L. G. Cançado, M. A. Pimenta, B. R. A. Neves, M. S. S. Dantas, and A. Jorio. Influence of the atomic structure on the Raman spectra of graphite edges. *Physical Review Letters*, 93(24):5–8, 2004.
- [216] A. C. Ferrari, J. C. Meyer, V. Scardaci, C. Casiraghi, M. Lazzeri, F. Mauri, S. Piscanec, D. Jiang, K. S. Novoselov, S. Roth, and A. K. Geim. Raman spectrum of graphene and graphene layers. *Physical Review Letters*, 97(18):1–4, 2006.
- [217] L. G. Cançado, A. Jorio, E. H. M. Ferreira, F. Stavale, C. A. Achete, R. B. Capaz, M. V. O. Moutinho, A. Lombardo, T. S. Kulmala, and A. C. Ferrari. Quantifying defects in graphene via Raman spectroscopy at different excitation energies. *Nano Letters*, 11(8):3190–3196, 2011.
- [218] A. Eckmann, A. Felten, A. Mishchenko, L. Britnell, R. Krupke, K. S. Novoselov, and C. Casiraghi. Probing the nature of defects in graphene by Raman spectroscopy. *Nano Letters*, 12(8):3925–3930, 2012.
- [219] P. Lespade, A. Marchand, M. Couzi, and F. Cruege. Caracterisation de materiaux carbones par microspectrometrie Raman. *Carbon*, 22(4-5):375–385, 1984.
- [220] G. Wang, X. Shen, J. Yao, and J. Park. Graphene nanosheets for enhanced lithium storage in lithium ion batteries. *Carbon*, 47(8):2049–2053, 2009.
- [221] W. Zhou and Z. L. Wang. *Scanning Microscopy for Nanotechnology - Techniques and Applications*. Springer-Verlag, 2006.

- [222] Manual for the SUPRA and ULTRA Scanning Electron Microscopes V5.00. Zeiss, 2005.
- [223] G. Binnig and C. F. Quate. Atomic Force Microscope. *Physical Review Letters*, 56(9):930–933, 1986.
- [224] L. Gross, Z. L. Wang, D. Ugarte, F. Mohn, N. Moll, W. A. Heer, P. Vincent, P. Liljeroth, C. Journet, G. Meyer, V. T. Binh, M. Poot, H. S. J. V. D. Zant, A. Aguasca, A. Bachtold, K. Kim, A. Zettl, P. Hung, H. W. C. Postma, M. Bockrath, X. Blase, and S. Roche. only appears when looking at the I. *Science*, 325(August):1110–4, 2009.
- [225] U. Khan, H. Porwal, A. O'Neill, K. Nawaz, P. May, and J. N. Coleman. Solvent-exfoliated graphene at extremely high concentration. *Langmuir : the ACS journal of surfaces and colloids*, 27(15):9077–82, August 2011.
- [226] J. Lifka, B. Ondruschka, and J. Hofmann. Review The Use of Ultrasound for the Degradation of Pollutants. 3:253–262, 2003.
- [227] SONOTRONIC, Sonication of Biosolids SONOTRONIC; Document IG.
- [228] Sonics Product Database., 2015.
- [229] V. Eswaraiah, K. Paton, C. Backes, A. Harvey, R. Smith, J. McCauley, and J. N. Coleman. Turbulence-assisted shear exfoliation of graphene using household detergent and a kitchen blender. *Nanoscale*, 00:1–10, 2014.
- [230] Silverson. Labrotory Mixers - How it Works, 2016.
- [231] Silvers. Laboratory Mixers - Mixer Options, 2016.
- [232] W. Callister and D. Rethwisch. *Materials science and engineering: an introduction*. 2007.
- [233] P. R. Wallace. The band theory of graphite. *Physical Review*, 71(9):622–634, 1947.

- [234] G. Hammer and L. Drzal. Graphite fiber surface analysis by X-ray photo-electron spectroscopy and polar/dispersive free energy analysis. *Applications of Surface Science*, 4:340–355, 1980.
- [235] P. Bryant, P. Gutshall, and L. Taylor. A study of mechanisms of graphite friction and wear. *Wear*, 7(1):118–126, 1964.
- [236] F. Thielmann and D. Pearse. Determination of surface heterogeneity profiles on graphite by finite concentration inverse gas chromatography. *Journal of Chromatography A*, 969(1-2):323–327, 2002.
- [237] M. J. Mcallister, J.-l. Li, D. H. Adamson, H. C. Schniepp, A. Abdala, J. Liu, O. M. Herrera-alonso, D. L. Milius, R. Car, R. K. Prud, and I. A. Aksay. Single Sheet Functionalized Graphene by Oxidation and Thermal Expansion of Graphite. *Society*, 19(4):4396–4404, 2007.
- [238] J. M. Hughes, D. Aherne, and J. N. Coleman. Generalizing solubility parameter theory to apply to one- and two-dimensional solutes and to incorporate dipolar interactions. *Journal of Applied Polymer Science*, 127(6):4483–4491, 2013.
- [239] I. M. Grimsey, J. C. Feeley, and P. York. Analysis of the surface energy of pharmaceutical powders by inverse gas chromatography. *Journal of Pharmaceutical Sciences*, 91(2):571–583, 2002.
- [240] S. Park. London Dispersive Component of the Surface Free Energy and Surface Enthalpy. *Journal of Colloid and Interface Science*, 188(2):336–339, 1997.
- [241] P. P. Ylä-Mäihäniemi, J. Y. Y. Heng, F. Thielmann, and D. R. Williams. Inverse gas chromatographic method for measuring the dispersive surface energy distribution for particulates. *Langmuir : the ACS journal of surfaces and colloids*, 24(17):9551–9557, September 2008.
- [242] A. E. Jefferson, D. R. Williams, and J. Y. Heng. Computing the Surface Energy Distributions of Heterogeneous Crystalline Powders. *Journal of Adhesion Science and Technology*, 25(4-5):339–355, 2012.

- [243] R. R. Smith, D. R. Williams, D. J. Burnett, and J. Y. Y. Heng. A New Method To Determine Dispersive Surface Energy Site Distributions by Inverse Gas Chromatography. *Langmuir*, 30(27):8029–8035, 2014.
- [244] H. E. Newell and G. Buckton. Inverse gas chromatography: Investigating whether the technique preferentially probes high energy sites for mixtures of crystalline and amorphous lactose. *Pharmaceutical Research*, 21(8):1440–1444, 2004.
- [245] A. Ferrari and J. Robertson. Interpretation of Raman spectra of disordered and amorphous carbon. *Physical Review B*, 61(20):14095–14107, 2000.
- [246] S. Mohammadi-Jam, D. Burnett, and K. Waters. Surface energy of minerals – Applications to flotation. *Minerals Engineering*, 66-68:112–118, 2014.
- [247] A. Ferguson, U. Khan, M. Walsh, K.-Y. Lee, A. Bismarck, M. S. P. Shaffer, J. N. Coleman, and S. D. Bergin. Understanding the dispersion and assembly of Bacterial Cellulose in Organic Solvents. *Biomacromolecules*, 17(5):1845–1853, 2016.
- [248] Z. Yao, L. Ge, W. Yang, M. Xia, X. Ji, M. Jin, J. Tang, and J. Dienstmaier. Finite Dilution Inverse Gas Chromatography as a Versatile Tool To Determine the Surface Properties of Biofillers for Plastic Composite Applications. *Analytical Chemistry*, 87(13):6724–6729, 2015.
- [249] I. G. Zenkevich and A. A. Pavlovskii. Overloading control of gas chromatographic systems. *Journal of Separation Science*, 38(16):2848–2856, 2015.
- [250] H. Balard, D. Maafa, A. Santini, and J. B. Donnet. Study by inverse gas chromatography of the surface properties of milled graphites. *Journal of chromatography. A*, 1198-1199:173–80, July 2008.
- [251] E. Papirer, E. Brendle, F. Ozil, and H. Balard. Comparison of the surface properties of graphite, carbon black and fullerene samples, measured by inverse gas chromatography. *Carbon*, 37(8):1265–1274, January 1999.

- [252] J. Donnet, S. Park, and M. Brendle. The effect of microwave plasma treatment on the surface energy of graphite as measured by inverse gas chromatography. *Carbon*, 30(2):263–268, 1992.
- [253] S. Wang, Y. Zhang, N. Abidi, and L. Cabrales. Wettability and surface free energy of graphene films. *Langmuir*, 25(18):11078–11081, 2009.
- [254] R. J. Good. Contact angle, wetting, and adhesion: a critical review. *Journal of Adhesion Science and Technology*, 6(12):1269–1302, 1992.
- [255] M. Lotya, P. J. King, U. Khan, S. De, and J. N. Coleman. High-concentration, surfactant-stabilized graphene dispersions. *ACS nano*, 4(6):3155–62, June 2010.
- [256] Z. Li, Y. Wang, A. Kozbial, G. Shenoy, F. Zhou, R. McGinley, P. Ireland, B. Morganstein, A. Kunkel, S. P. Surwade, L. Li, and H. Liu. Effect of air-borne contaminants on the wettability of supported graphene and graphite. *Nature materials*, 12(10):925–31, 2013.
- [257] M. G. Huson, J. S. Church, A. A. Kafi, A. L. Woodhead, J. Khoo, M. S. R. N. Kiran, J. E. Bradby, and B. L. Fox. Heterogeneity of carbon fibre. *Carbon*, 68:240–249, 2014.
- [258] R. Ho, M. Naderi, J. Y. Y. Heng, D. R. Williams, F. Thielmann, P. Bouza, A. R. Keith, G. Thiele, and D. J. Burnett. Effect of milling on particle shape and surface energy heterogeneity of needle-Shaped crystals. *Pharmaceutical Research*, 29(10):2806–2816, 2012.
- [259] A. Barreiro, M. Lazzeri, J. Moser, F. Mauri, and A. Bachtold. Transport properties of graphene in the high-current limit. *Physical Review Letters*, 103(7):2–5, 2009.
- [260] R. Raj, S. C. Maroo, and E. N. Wang. Wettability of graphene. *Nano Letters*, 13(4):1509–1515, 2013.
- [261] P. Staszczuk. Determination of Water Film Pressure and Surface Free Energy on Graphite. *Materials Chemistry and Physics*, 14(3):279–287, 1986.

- [262] M. E. Schrader. Ultrahigh-vacuum techniques in the measurement of contact angles. 5. LEED study of the effect of structure on the wettability of graphite. *The Journal of Physical Chemistry*, 84(21):2774–2779, 1980.
- [263] H. Zaidi, F. Robert, and D. Paulmier. Influence of adsorbed gases on the surface energy of graphite: consequences on the friction behaviour. *Thin Solid Films*, 264(1):46–51, 1995.
- [264] J. Abrahamson. The surface energies of graphite. *Carbon*, 11(4):337–362, 1973.
- [265] W. Wang, S. Dai, X. Li, J. Yang, D. J. Srolovitz, and Q. Zheng. Measurement of the cleavage energy of graphite. *Nature Communications*, 6:7853, 2015.
- [266] N. Ooi, A. Raikar, and J. B. Adams. Density functional study of graphite bulk and surface properties. *Carbon*, 44(2):231–242, 2006.
- [267] L. A. Girifalco and R. A. Lad. Energy of Cohesion, Compressibility, and the Potential Energy Functions of the Graphite System. *The Journal of Chemical Physics*, 25(4):693–697, 1956.
- [268] R. O. Brennan. The Interlayer Binding in Graphite. *The Journal of Chemical Physics*, 20(1):40–48, 1952.
- [269] Y. J. Shin, Y. Wang, H. Huang, G. Kalon, A. T. S. Wee, Z. Shen, C. S. Bhatia, and H. Yang. Surface-energy engineering of graphene. *Langmuir*, 26(6):3798–3802, 2010.
- [270] A. Kozbial, Z. Li, C. Conaway, R. McGinley, S. Dhingra, V. Vahdat, F. Zhou, B. D’Urso, H. Liu, and L. Li. Study on the surface energy of graphene by contact angle measurements. *Langmuir : the ACS journal of surfaces and colloids*, 30(28):8598–606, 2014.
- [271] J. F. Dai, G. J. Wang, and C. K. Wu. Investigation of the Surface Properties of Graphene Oxide and Graphene by Inverse Gas Chromatography. *Chromatographia*, 77(3-4):299–307, 2014.

- [272] J. Dai, G. Wang, L. Ma, and C. Wu. Study on the surface energies and dispersibility of graphene oxide and its derivatives. *Journal of Materials Science*, 50(11):3895–3907, 2015.
- [273] Z. Gholamvand, D. McAtee, A. Harvey, C. Backes, and J. N. Coleman. Electrochemical Applications of 2-Dimensional Nanosheets: The Effect of Nanosheet Length and Thickness. *Chemistry of Materials*, 28(8):2641–2651, 2016.
- [274] C. Tokoh, K. Takabe, M. Fujita, and H. Saiki. Cellulose synthesized by *Aacetobacter xylinum* in the presence of acetyl glucomannan. *Cellulose*, 5:249–261, 1998.
- [275] A. Mautner, K. Y. Lee, P. Lahtinen, M. Hakalahti, T. Tammelin, K. Li, and A. Bismarck. Nanopapers for organic solvent nanofiltration. *Chemical communications (Cambridge, England)*, 50(43):5778–81, 2014.
- [276] K. Schlüter, H. P. Schmauder, S. Dorn, and T. Heinze. Efficient homogeneous chemical modification of bacterial cellulose in the ionic liquid 1-N-butyl-3-methylimidazolium chloride. *Macromolecular Rapid Communications*, 27(19):1670–1676, 2006.
- [277] M. Gama, P. Gatenholm, and D. Klemm. *Bacterial nanocellulose: a sophisticated multifunctional material*. CRC press, 2012.
- [278] R. Parthasarathi, G. Bellesia, S. P. S. Chundawat, B. E. Dale, P. Langan, and S. Gnanakaran. Insights into hydrogen bonding and stacking interactions in cellulose. *Journal of Physical Chemistry A*, 115(49):14191–14202, 2011.
- [279] Y. Nishiyama, G. P. Johnson, A. D. French, V. T. Forsyth, and P. Langan. Neutron crystallography, molecular dynamics, and quantum mechanics studies of the nature of hydrogen bonding in cellulose I β . *Biomacromolecules*, 9(11):3133–3140, 2008.
- [280] S. K. Cousins and R. M. Brown. Cellulose I microfibril assembly: computational molecular mechanics energy analysis favours bonding by van der Waals forces as the initial step in crystallization. *Polymer*, 36(20):3885–3888, 1995.

- [281] B. Lindman, G. Karlstrom, and L. Stigsson. On the mechanism of dissolution of cellulose. *Journal of Molecular Liquids*, 156(1):76–81, 2010.
- [282] X. Shen, Y. Ji, D. Wang, and Q. Yang. Solubility of a High Molecular-Weight Bacterial Cellulose in Lithium Chloride/N,N-dimethylacetamide Solution. *Journal of Macromolecular Science, Part B*, 49(5):1012–1018, 2010.
- [283] C. Guo, L. Zhou, and J. Lv. Effects of expandable graphite and modified ammonium polyphosphate on the flame-retardant and mechanical properties of wood flour-polypropylene composites. *Polymers and Polymer Composites*, 21(7):449–456, 2013.
- [284] X. Lu and X. Shen. Solubility of bacteria cellulose in zinc chloride aqueous solutions. *Carbohydrate Polymers*, 86(1):239–244, 2011.
- [285] S. Fischer, H. Leipner, K. Thümmler, E. Brendler, and J. Peters. Inorganic molten salts as solvents for cellulose. *Cellulose*, 10(3):227–236, 2003.
- [286] H. P. Fink, P. Weigel, H. J. Purz, and J. Ganster. Structure formation of regenerated cellulose materials from NMMO-solutions. *Progress in Polymer Science (Oxford)*, 26(9):1473–1524, 2001.
- [287] Q. Gao, X. Shen, and X. Lu. Regenerated bacterial cellulose fibers prepared by the NMMO·H₂O process. *Carbohydrate Polymers*, 83(3):1253–1256, 2011.
- [288] J. N. Coleman. Liquid-phase exfoliation of nanotubes and graphene. *Advanced Functional Materials*, 19(23):3680–3695, 2009.
- [289] V. Nicolosi, D. Vrbanic, A. Mrzel, J. McCauley, S. O’Flaherty, C. McGuinness, G. Compagnini, D. Mihailovic, W. J. Blau, and J. N. Coleman. Solubility of Mo₆S_{4.5}I_{4.5} nanowires in common solvents: A sedimentation study. *Journal of Physical Chemistry B*, 109(15):7124–7133, 2005.
- [290] K. Y. Lee and A. Bismarck. Susceptibility of never-dried and freeze-dried bacterial cellulose towards esterification with organic acid. *Cellulose*, 19(3):891–900, 2012.

- [291] K. Y. Lee, T. Tammelin, K. Schulter, H. Kiiskinen, J. Samela, and A. Bismarck. High performance cellulose nanocomposites: Comparing the reinforcing ability of bacterial cellulose and nanofibrillated cellulose. *ACS Applied Materials and Interfaces*, 4(8):4078–4086, 2012.
- [292] N. R. Gilkes, E. Jervis, B. Henrissat, B. Tekant, R. C. Miller, R. A. J. Warren, and D. G. Kilburn. The adsorption of a bacterial cellulase and its two isolated domains to crystalline cellulose. *Journal of Biological Chemistry*, 267(10):6743–6749, 1992.
- [293] G. Wypych. *Handbook of Solvents, Volume 1*. ChemTec Publishing, 2 edition, 2014.
- [294] M. Rubinstein and R. Colby. *Polymer Physics*. Oxford University Press, Oxford, 1 edition, 2003.
- [295] Y. Hernandez, M. Lotya, D. Rickard, S. D. Bergin, and J. N. Coleman. Measurement of multicomponent solubility parameters for graphene facilitates solvent discovery. *Langmuir*, 26(5):3208–3213, 2010.
- [296] J. N. Coleman, M. Lotya, A. O'Neill, S. D. Bergin, P. J. King, U. Khan, K. Young, A. Gaucher, S. De, R. J. Smith, I. V. Shvets, S. K. Arora, G. Stanton, H.-Y. Kim, K. Lee, G. T. Kim, G. S. Duesberg, T. Hallam, J. J. Boland, J. J. Wang, J. F. Donegan, J. C. Grunlan, G. Moriarty, A. Shmelev, R. J. Nicholls, J. M. Perkins, E. M. Grieveson, K. Theuwissen, D. W. McComb, P. D. Nellist, and V. Nicolosi. Two-dimensional nanosheets produced by liquid exfoliation of layered materials. *Science (New York, N.Y.)*, 331(6017):568–71, February 2011.
- [297] J. Y. Y. Heng, D. F. Pearse, F. Thielmann, T. Lampke, and A. Bismarck. Methods to determine surface energies of natural fibres: a review. *Composite Interfaces*, 14(7-9):581–604, 2007.
- [298] R. A. Bailey and K. C. Persaud. Application of inverse gas chromatography to characterisation of a polypyrrole surface. *Analytica Chimica Acta*, 363(2-3):147–156, 1998.

- [299] E. Papirer, E. Brendle, H. Balard, and C. Vergelati. Inverse gas chromatography investigation of the surface properties of cellulose. *J.Adhes.Sci.Technol.*, 14(3):321–337, 2000.
- [300] M. Pommet, J. Juntaro, J. Y. Y. Heng, A. Mantalaris, A. F. Lee, K. Wilson, G. Kalinka, M. S. P. Shaffer, and A. Bismarck. Surface modification of natural fibers using bacteria: Depositing bacterial cellulose onto natural fibers to create hierarchical fiber reinforced nanocomposites. *Biomacromolecules*, 9(6):1643–1651, 2008.
- [301] W. Gindl and J. Keckes. Drawing of self-reinforced cellulose films. *Journal of applied polymer science*, 103(4):2703–2708, 2013.
- [302] A. Retegi, N. Gabilondo, C. Peña, R. Zuluaga, C. Castro, P. Gañan, K. de la Caba, and I. Mondragon. Bacterial cellulose films with controlled microstructure-mechanical property relationships. *Cellulose*, 17(3):661–669, 2010.
- [303] H. Yano and S. Nakahara. Bio-composites produced from plant microfiber bundles with a nanometer unit web-like network. *Journal of Materials Science*, 39(5):1635–1638, 2004.
- [304] A. N. Nakagaito and H. Yano. Novel high-strength biocomposites based on microfibrillated cellulose having nano-order-unit web-like network structure. *Applied Physics A: Materials Science and Processing*, 80(1):155–159, 2005.
- [305] A. N. Nakagaito, S. Iwamoto, and H. Yano. Bacterial cellulose: the ultimate nano-scalar cellulose morphology for the production of high-strength composites. *Applied Physics A*, 80(1):93–97, July 2004.
- [306] L. J. Gibson and M. F. Ashby. *Cellular solids: structure and properties*. Cambridge university press, 1999.
- [307] L. Qiu, J. Z. Liu, S. L. Y. Chang, Y. Wu, and D. Li. Biomimetic superelastic graphene-based cellular monoliths. *Nature communications*, 3:1241, 2012.

- [308] F. M. Blighe, P. E. Lyons, S. De, W. J. Blau, and J. N. Coleman. On the factors controlling the mechanical properties of nanotube films. *Carbon*, 46(1):41–47, 2008.